

N71-14606
NASA CR-102984

**STUDY TO ESTABLISH CRITERIA FOR A
SOLAR CELL ARRAY FOR USE AS A PRIMARY
POWER SOURCE FOR A LUNAR-BASED
WATER ELECTROLYSIS SYSTEM**

PHASE III-FINAL TECHNICAL REPORT

09681-6007-R000

15 DECEMBER 1970

**CASE FILE
COPY**

Contract No. NAS 8-21189
Period covered: 15 November 1969 to 15 December 1970

Prepared for
NATIONAL AERONAUTICS AND SPACE ADMINISTRATION
George C. Marshall Space Flight Center
Huntsville, Alabama 35812

TRW
SYSTEMS GROUP

09681-6007-R000



STUDY TO ESTABLISH CRITERIA FOR A SOLAR CELL
ARRAY FOR USE AS A PRIMARY POWER SOURCE
FOR A LUNAR-BASED WATER ELECTROLYSIS
SYSTEM

PHASE III - FINAL TECHNICAL REPORT

15 November 1969 to 15 December 1970

A handwritten signature in dark ink, appearing to read "JEBoretz", written over a horizontal line.

J. E. Boretz, Project Manager
Lunar Surface Power System Project

A handwritten signature in dark ink, appearing to read "P. Goldsmith", written over a horizontal line.

P. Goldsmith, Ass't. Manager
Electrical Systems Laboratory

Prepared for:
National Aeronautics and Space Administration
George C. Marshall Space Flight Center
Huntsville, Alabama 35812
Contract No. NAS 8-21189

FOREWORD

This Phase III - Final Technical Report for the "Study to Establish Criteria for a Solar Cell Array for Use as a Primary Power Source for a Lunar-Based Water Electrolysis System" was prepared for the National Aeronautics and Space Administration, George C. Marshall Space Flight Center; Huntsville, Alabama. This effort, together with that documented in the Phase I and II Final Technical Reports (References 1.1 and 1.2), partially fulfills the requirements of Contract NAS 8-21189. This report covers the lunar surface solar array development work performed from 15 November 1969 to 15 December 1970. It documents and summarizes the results of this program during this fiscal period. This development work was conducted under the technical direction of J. L. Miller (COTR) of Astrionics Laboratory, Power Systems Branch of NASA/MSFC.

Distribution of this document is established by the Contracting Officer, Lawrence Garrison, or his authorized representative. Communications relative to this contract should be directed to the above Contract Specialist, Attention Code PR-SC, George C. Marshall Space Flight Center, Huntsville, Alabama, 35812.

ACKNOWLEDGEMENTS

This phase of the development program was conducted by the Electrical Systems Laboratory of the TRW Systems Group, which is under the direction of P. H. Greenler. The Project Manager and Principal Investigator was J. E. Boretz.

Acknowledgement is expressed to the various members of the TRW Systems Technical Staff named below for their valuable technical contributions to this effort.

W. R. Baron	W. Luft
W. I. Berks	E. E. Maiden
W. G. Binckley	T. J. Ockey
R. A. Boring	O. A. Phillips
D. G. Cross	A. Robertshaw
B. E. Franden	D. B. Scovill
J. M. Hefti	B. N. Smith
N. J. Judkins	W. R. Wannlund
W. M. Kendziorek	J. G. Wells
R. F. Kennedy	J. M. Woo
G. R. Luckey	J. F. Yurk

In addition the technical direction, guidance, reviews, and comments proved by J. L. Miller (COTR) and other members of the NASA/MSFC Power Systems Branch of the Astrionics Laboratory (C. Graff, C. Kirby, J. Willis, and L. Crabtree) are also gratefully acknowledged.

CONTENTS

	Page
FOREWORD	ii
ACKNOWLEDGEMENTS	iii
ILLUSTRATIONS.	viii
TABLES	xiv
1. INTRODUCTION	1-1
1.1 General.	1-1
1.2 Program Objectives	1-2
1.3 Program Approach	1-2
2. SUMMARY.	2-1
2.1 Engineering Test Model Designs	2-1
2.2 ETM Test Evaluation.	2-2
3. CONCLUSIONS AND RECOMMENDATIONS.	3-1
3.1 Conclusions.	3-1
3.2 Recommendations.	3-5
4. CELL-SUBSTRATE DESIGN CRITERIA	4-1
4.1 Cellstack Design Requirements.	4-1
4.1.1 Dynamic Environments	4-1
4.1.2 Thermal-Vacuum Environment	4-2
4.2 Candidate Components and Materials	4-10
4.2.1 Coverslides.	4-10
4.2.2 Coverslide Adhesive.	4-10
4.2.3 Solar Cell	4-10
4.2.4 Cell-to-Substrate Adhesive	4-15
4.2.5 Cell-to-Cell Interconnect.	4-15
4.2.6 Substrates	4-15
4.3 Candidate Cellstack Designs.	4-16
4.3.1 Solar Cell	4-16
4.3.2 Cell Spacing	4-16
4.3.3 Adhesive Bond Geometry	4-17
4.3.4 Interconnect Design.	4-18

	Page
4.4 Adhesive Considerations	4-18
4.4.1 Adhesive Types	4-18
4.4.2 Critical Adhesive Material Properties.	4-23
4.5 Module Materials	4-23
4.5.1 Substrates	4-23
4.5.1.1 Fiberglass Lattice	4-23
4.5.1.2 Kapton	4-24
4.5.1.3 Graphite Composite	4-24
4.5.1.4 Aluminum	4-24
4.5.2 Dielectric Insulation.	4-25
4.5.2.1 Fiberglass/RTV Silicone.	4-25
4.5.2.2 Kapton Film.	4-25
5. CELLSTACK DESIGN ANALYSES.	5-1
5.1 Structural Dynamic Induced Loads	5-1
5.2 Thermal-Vacuum Induced Loads	5-3
5.2.1 Analytical Model	5-4
5.2.2 Basic Assumptions.	5-4
5.2.3 Failure Mode and Effects Analysis.	5-5
5.2.4 Sensitivity of Cell Spalling Failures to Thermally Induced Loads.	5-6
5.2.5 Additional Parametric Analyses of Spalling Failures	5-12
5.2.5.1 Scope of Parametric Study.	5-13
5.2.5.2 Results of Analyses.	5-14
6. SUBSTRATE DESIGN CRITERIA.	6-1
6.1 Fiberglass - Aluminum Frame Configuration for ETM IA . .	6-1
6.2 Aluminum - Honeycomb End Plates with Intermediate Flexible Kapton Module for ETM IIA	6-1
6.3 Aluminum Honeycomb - Graphite/Epoxy Composite Substrate for ETM IIIA	6-2
7. MATERIAL PROPERTIES EXPERIMENTAL PROGRAM	7-1
7.1 Adhesive Materials Test Plan	7-1
7.2 Other Module Materials Test Plan	7-7
7.3 Materials Properties Test Evaluation	7-7
7.3.1 Coefficient of Expansion - Adhesives	7-7

	Page
7.3.2 Ultimate Tensile Strength and Modulus of Elasticity-Adhesives	7-19
7.3.3 Lap Shear Ultimate Strength and Shear Modulus of Elasticity - Adhesives.	7-21
7.3.4 Outgassing Characteristics - Adhesives	7-25
7.3.5 Other Module Material Properties	7-30
8. ENGINEERING TEST MODULE DESIGN	8-1
8.1 Aluminum Box Beam Frame/Fiberglass Facesheet Module (ETM IA)	8-1
8.2 Flexible Kapton Substrate - Aluminum Honeycomb Endplates (ETM IIA).	8-2
8.3 Aluminum Honeycomb-Graphite/Epoxy Composite (ETM IIIA)	8-2
8.4 Solar Cell Sub-Module Cellstack Design	8-2
9. ENGINEERING TEST MODEL FABRICATION	9-1
9.1 Manufacturing Considerations	9-1
9.1.1 Factors Effecting ETM IA	9-1
9.1.2 Factors Effecting ETM IIA.	9-4
9.1.3 Factors Effecting ETM IIIA	9-4
9.1.4 Factors Effecting the Interconnect and Bus Bars	9-4
10. ENGINEERING TEST MODEL TEST EVALUATION	10-1
10.1 Test Objectives.	10-1
10.2 Test Operations.	10-1
10.3 Test Evaluations	10-23
10.3.1 ETM IA Substrate Evaluation - Effects of Structural-Dynamic Tests	10-23
10.3.2 ETM IA Cellstack Evaluation - Effects of Structural-Dynamic Tests	10-23
10.3.3 ETM IIA Substrate and Cellstack Evaluations - Effects of Structural-Dynamic Tests.	10-25
10.3.4 ETM IIIA Substrate Evaluation - Effects of Structural Dynamic Tests	10-26
10.3.5 ETM IIIA Cellstack Evaluation - Effects of Structural-Dynamic Tests	10-26
10.3.6 Effects of Thermal-Vacuum Tests - General.	10-28
10.3.7 Evaluation of Bus Bar Tabs - Effects of Thermal-Vacuum Tests	10-28
10.3.8 Evaluation of Adhesive Bond - Effects of Thermal-Vacuum Tests	10-31

	Page
10.3.9 Evaluation of Spalling Phenomena - Effects of Thermal-Vacuum	10-51
REFERENCES	R-1
APPENDIX A - THERMAL STRESS ANALYSIS FOR SUB-MODULE COMMON INTERCONNECTS	A-1
APPENDIX B - DYNAMIC AND THERMAL ANALYSIS FOR PRE-STRESSED FIBERGLASS DIAPHRAGM FOR ENGINEERING TEST MODEL ETM IA.	B-1
APPENDIX C - TEST CURVES FROM X-Y PLOTTER FOR DETERMINATION OF EXPANSION FOR FOUR CANDIDATE ADHESIVE MATERIALS .	C-1

ILLUSTRATIONS

Figure No.		Page
4.1	Random Vibration Test Criteria	4-3
4.2	Acoustic Test Criteria	4-4
4.3	Sinusoidal Vibration Test Criteria	4-5
4.4	Shock Test Criteria	4-6
4.5	Typical Temperature Variation of the Lunar Surface	4-7
4.6	Theoretical Lunar Surface Temperature Variation for a Complete Luration at the Lunar Equator (where the lunar thermal inertia, $\gamma = (K\rho c)^{-1/2}$)	4-8
4.7	Theoretical Lunar Surface Temperature Variation for a Complete Luration on Lunar Central Meridian	4-9
4.8	Variation of Lunar Surface Temperature During a Complete Luration	4-11
4.9	Lunar Based 45° Lean-to Array Temperatures as a Function of Solar Heating for one Lunar Day	4-12
4.10	Lunar Based 45° Lean-to Array Temperature During the First Ten Hours of Solar Illumination	4-13
4.11	Thermal Test Profile Used to Simulate Array Lunar Surface Temperatures	4-14
4.12	Sub-Module, Solar Cell - Lunar Array Test Model	4-19
4.13	Connect, Common	4-20
4.14	Bus Bar, Positive	4-21
4.15	Bus Bar, Negative	4-22
5.1	Silicon Cell Adhesive Dot Design Chart	5-2
5.2	Model for Computer Analysis	5-7
5.3	Silicon Cell Axial Stress Distribution	5-8
5.4	Silicon Cell Effective Stress Distribution	5-9
5.5	Longitudal Silicon Cell Stress at a Level 0.00017 Inch from Interface Surface	5-10
5.6	Stress Distribution through Solar Cell Thickness - Modulus of Elasticity of Adhesive = 1×10^5 psi	5-11

Figure No.		Page
5.7	Effect of Adhesive Modulus of Elasticity on the Maximum Computed Stress	5-11
5.8	Plot of Function $\alpha = f/N_0$ for Simplified Stress Equation	5-15
5.9	Silicon Thermal Stress - RTV Adhesive Thickness, $t_2 = 0.005$ in., at 0.00017 Stress Level	5-16
5.10	Silicon Thermal Stress - RTV Adhesive Thickness, $t_2 = 0.010$ in., at 0.00017 Stress Level	5-17
5.11	Silicon Thermal Stress - RTV Adhesive Thickness, $t_2 = 0.015$ in., at 0.00017 Stress Level	5-18
5.12	Silicon Thermal Stress - RTV Adhesive Thickness, $t_2 = 0.020$ in., at 0.00017 Stress Level	5-19
5.13	Maximum Effective Stress in Silicon as Function of RTV Adhesive Thickness	5-20
7.1 A } 7.1 B }	Test Set-up for Obtaining Ultimate Shear and Tensile Strength	7-3
7.2	Test Set-up for Obtaining Ultimate Tensile Strength	7-4
7.3	Test Set-up for Obtaining Ultimate Tensile Strength	7-4
7.4	Lap Shear Specimen Configuration	7-9
7.5	Test Set-up for Obtaining Ultimate Overlap Shear Strength	7-10
7.6	Test Set-up for Obtaining Ultimate Overlap Shear Strength	7-10
7.7	Test Set-up for Obtaining Coefficient of Thermal Expansion	7-11
7.8	Dilatometer Used for Obtaining Coefficient of Thermal Expansion	7-12
7.9	X-Y Plotter Used in Conjunction with Coefficient of Thermal Expansion Testing	7-12

Figure No.		Page
7.10	Test Set-up for Obtaining Shear Modulus in Torsion	7-13
7.11	Change in Specimen Length as Function of Temperature - RTV 3145 Adhesive	7-15
7.12	Change in Specimen Length as Function of Temperature - RTV 511/577 (1:1)	7-16
7.13	Change in Specimen Length as Function of Temperature - RTV 118	7-17
7.14	Change in Specimen Length as Function of Temperature - PR 1538	7-18
7.15	Weight Loss Rate vs. Time for RTV 3145	7-26
7.16	Weight Loss Rate vs. Time for RTV 511/577	7-27
7.17	Weight Loss Rate vs. Time for RTV 118	7-28
7.18	Weight Loss Rate vs. Time for PR 1538	7-29
8.1	ETM Cellstack Bonding Matrix (typical for 3 different substrate materials)	8-3
8.2	Aluminum Box Beam Frame/Fiberglass Facesheet Module Design (ETM IA)	8-5
8.3	Flexible Kapton Substrate-Aluminum Honeycomb Endplates (ETM IIA)	8-6
8.4	Aluminum Honeycomb - Graphite Epoxy Composite (ETM IIIA)	8-7
9.1	Front View of Engineering Test Model IA (Fiberglass Substrate)	9-3
9.2	Rear View of Engineering Test Model IA (Fiberglass Substrate)	9-3
9.3	Front View of Engineering Test Model IIA (Kapton Substrate)	9-5
9.4	Top View of Engineering Test Model IIA Endplate (Aluminum Honeycomb with Aluminum Facesheets)	9-5
9.5	Front View of Graphite Composite Substrate for Engineering Test Model IIIA	9-7

Figure No.		Page
9.6	Rear View of Graphite Composite Substrate for Engineering Test Model IIIA	9-7
9.7	Front View of Engineering Test Model IIIA (Graphite Composite Substrate)	9-8
9.8	Common Interconnect for 2 cm x 2 cm Silicon Cells (3 in Parallel)	9-9
9.9	Positive Bus Bar for 2 cm x 2 cm Sub-Modules (3 in Parallel)	9-10
9.10	Negative Bus Bar for 2 cm x 2 cm Sub-Modules (3 cells in Parallel)	9-11
9.11	Improved Positive Bus Bar for 2 cm x 4 cm (2 in. Parallel) Silicon Cells	9-12
9.12	Improved Negative Bus Bar for 2 cm x 4 cm (2 in Parallel) Silicon Cells	9-13
10.1	Typical Location and Orientation of Accelerometers on ETM Modules during X, Y, and Z Axes Vibration Testing	10-3
10.2	ETM IA Mounted on Shake Table Fixture before being Subjected to Z-Axis Vibration	10-4
10.3	View of ETM IA Mounted on Vibration Test Fixture after Completion of Z-Axis Testing	10-5
10.4	ETM IIIA Mounted on Shake Table Fixture before being Subjected to X and Y Axes Vibration	10-6
10.5	ETM IIIA Mounted on Shake Table Fixture after being Subjected to X and Y Axes Vibration	10-7
10.6	Enlarged View of Failed Common Interconnects after Completion of Z-Axis Vibration Testing on ETM IA	10-8
10.7	Magnified View of Failed Common Interconnector on ETM IA at Completion of Vibration Test	10-9
10.8	Back of ETM IA Showing the Location of Temperature Sensors	10-10
10.9	Internal View of Thermal-Vacuum Chamber Showing LN ₂ Cooled Test Fixture	10-12
10.10	View Showing ETM IA Mounted in LN ₂ Cooled - Radiatively Coupled Fixture During Thermal-Vacuum Testing	10-13

Figure No.		Page
10.11	View of ETM IA in Thermal-Vacuum Chamber Radiatively Coupled Test Fixture	10-14
10.12	View Showing ETM IIA (unfolded) Mounted in LN ₂ Cooled - Radiatively Coupled Fixture During Thermal-Vacuum Testing	10-15
10.12A	Enlarged View of Spalling Failures on 2 cm x 4 cm Silicon Cells (Random Crystal Orientation-Solder Dipped)	10-15A
10.13	Partially Folded ETM IIA Configuration	10-27
10.14	Fully Folded ETM IIA Configuration	10-27
10.15	Solar Module Assembly Showing Configuration of Adhesive Bonds	10-33
10.16	Photomicrograph (100X) of Mudcracked Primer	10-34
10.17	Average Peel Strength of Primer Test Samples as a Function of Curing Time for Three Thick- ness of Primer	10-36
10.18	Average Peel Strength of Primer Test Samples as a Function of Two Primer Thicknesses for Three Humidity Levels	10-39
10.19	Average Peel Strength of Primer Test Samples as a Function of Relative Humidity for Two Primer Thicknesses	10-40
10.20	Average Peel Strength of Primer Test Samples as a Function of Cure Time for Three Conditions of Relative Humidity (Both Adhesive Thicknesses Combined)	10-41
10.21	Photomicrograph (100X) of Optimum Thickness Primer	10-43
10.22	Semiautomatic Primer Spray Equipment	10-45
10.23	Typical Temperature and Humidity Plot of Module Assembly Room	10-50
10.24	Variation of Adhesive Tensile Strength as Function of Specimen Temperature	10-52
10.25	Variation of Adhesive Modulus of Elasticity as Function of Specimen Temperature	10-53

Figure No.		Page
10.26	Variation of Adhesive Coefficient of Linear Expansion as Function of Average Temperature Range	10-54
10.27	Maximum Allowable Value of Adhesive Coefficient of Expansion to Prevent Spalling ($\Delta T = -193^{\circ}\text{C}$)	10-56
10.28	Maximum Allowable Value of " $E_2 \alpha_2$ " to Prevent Spalling ($\Delta T = -193^{\circ}\text{C}$)	10-57
10.29	Extrapolation of Effective Stresses in Surface of Silicon Cells	10-59

TABLES

Table No.		Page
5.1	Silicon Stress Summary	5-13
5.2	Allowable Adhesive Properties versus t	5-21
7.1	Test Matrix of Critical Adhesive Material Properties	7-6
7.2	Data Matrix of Desired Module Material Properties	7-8
7.3	Experimental Values of Coefficient of Linear Expansion, in/in/°F	7-20
7.4	Experimental Values of Ultimate Tensile Strength and Modulus of Elasticity, lb/in ²	7-22
7.5	Experimental Lap Shear Ultimate Strength, lb/in ²	7-23
7.6	Other Module Material Properties	7-24
10.1	ETM IA - Thermal-Vacuum Test Bonding Failures	10-16
10.2	ETM IIA Thermal-Vacuum Test Bonding Failures	10-17
10.3	ETM IIIA - Thermal-Vacuum Test Bonding Failures	10-18
10.4	ETM IA - Results of Pull Tests on Unconnected Cells	10-20
10.5	ETM IIA - Results of Pull Tests on Unconnected Cells	10-21
10.6	ETM IIIA - Results of Pull Tests on Unconnected Cells	10-22
10.7	Theoretical Thermal Stress	10-30
10.8	Nominal Values for Thermal Coefficient of Linear Expansion for Various Cellstack Materials	10-30
10.9	Critical Low Temperature Adhesive Properties	10-51

1. INTRODUCTION

1.1 GENERAL

This technical report encompasses the Phase III development work that was performed under Contract NAS 8-21189. It represents the extension to the original program entitled "Study to Establish Criteria for a Solar Cell Array for Use as a Primary Power Source for a Lunar-Based Water Electrolysis System" (References 1.1 and 1.2). The work was essentially carried out in accordance with the approved Work Statements of References 1.3 and 1.4 and the approved modifications outlined in References 1.5 and 1.6. This report fulfills the contractual requirement for preparation of a Phase III - Final Technical Report and covers the period from 15 November 1969 to 15 December 1970.

This overall program was initiated on 1 July 1967. Its original purpose was to generate parametric data for large area solar arrays to be used on the lunar surface. This work (Phase I) was completed on 30 June 1968 and reported in Reference 1.1. A follow-on effort to this work consisted of developing three prototype solar cell Engineering Test Models (ETM). These three ETM's utilized various substrate materials (fiberglass lattice, Kapton, and graphite composite) and a common, flat-laydown cell-stack configuration. They represented different degrees of technology refinement in the design of large area solar arrays and resulted in power-to-weight ratios of 12 to 18 watts per pound. This work (Phase II) was completed on 15 November 1969 and reported in Reference 1.2.

During the environmental testing of these modules certain development problems relating to the cellstack design were encountered. These consisted of cell spalling, cell cracking, and cell interconnect distortion. A cursory analysis and test evaluation of these failure modes was conducted and qualitative solutions proposed and reported in Reference 1.2. However, in order to establish a more comprehensive quantitative approach to these failure modes, a detailed evaluation was required. For example, it was necessary to identify and experimentally evaluate the materials and processes which were potential candidates for cellstack use and compare them against the lunar surface environmental requirements. Only in this way could the more promising materials and techniques be differentiated from those which are unacceptable. Accordingly, a follow-on effort to this

program was initiated.

During this follow-on activity (defined as Phase III), additional development work was conducted. Emphasis was placed upon establishing the required physical characteristics of various adhesives which could make them promising candidates for use in bonding silicon cells to solar array modules for lunar surface missions. Modified versions of the three ETM's developed during Phase II of this program were used as the baseline substrate structures to accomplish the cellstack development work.

1.2 PROGRAM OBJECTIVES

The overall objective of this program phase was to evaluate the adequacy of various candidate cell-to-substrate adhesive bond configurations with respect to the lunar surface thermal environment. The main emphasis was placed upon evaluating the cell spalling phenomenon which occurred during Phase II of this program. In accomplishing this it was necessary to establish the critical parameters and material properties associated with bonding silicon cells to various substrate materials. Furthermore, the critical adhesive material properties had to be experimentally evaluated over a wide temperature range (i.e. + 130°C to - 173°C). In addition, the candidate cell-to-substrate adhesive bond configurations were tested under the thermal-vacuum environmental conditions to be encountered on the lunar surface and an evaluation conducted to determine the structural adequacy and material compatibility of each bonding technique. Finally, the adhesive bond configurations were tested under the vibration and acceleration environments that they would experience during the launch operations phase. This was done to assure that the selected candidate adhesive bonding technique would also be compatible with the original mission requirements.

1.3 PROGRAM APPROACH

The approach taken during this program phase was to establish the critical material properties and bonding geometries that might possibly contribute to the cell spalling phenomenon that occurred during the Phase II thermal-vacuum testing. Thus, primary emphasis was placed upon establishing an analytical model which could best predict this failure mode. In addition, a cellstack matrix was devised to permit experimental verification of this failure mode over as wide a range of parameters and variables

that was permissible within the scope of this program. Finally, it was necessary to conduct environmental tests to confirm the validity of the analytical model, the adequacy of the adhesive bond geometry, and to aid in selection of the most desirable candidate cellstack design.

Three Engineering Test Models (ETM IA, IIA, and IIIA) were designed and fabricated. Each ETM utilized the same cellstack matrix but employed a different substrate design. These substrate designs simulated the materials and configurations of the three ETM's developed during Phase II of this program. This was done to determine the effect if any, of the substrate facesheet on the cell spalling problem.

An analysis was made of the test results. Failure modes, when they occurred were identified and evaluated. Recommendations for the final cellstack design were made and the technology readiness of these candidate ETM designs was assessed. Suggestions for future development activities were also provided.

2. SUMMARY

2.1 ENGINEERING TEST MODEL DESIGNS

The main emphasis during this program phase was to evaluate the spalling phenomenon which had occurred during thermal-vacuum testing during Phase II (Reference 1.2). A second objective was to design an improved cellstack interconnect and sub-module bus-bar since the Phase II configuration proved to be excessively sensitive to solder wicking action and fatigue. A third objective was to determine the adequacy of the cell-to-substrate adhesive bond strength with regard to both structural/dynamic and thermal-vacuum loads. Finally, an evaluation of the structural integrity of the overall candidate substrate/cellstack configuration was desired to assess the compatibility of the interactions between all the array module components.

The approach taken was to devise an Engineering Test Module (ETM) matrix (Figure 8.1) which would permit simultaneous evaluation of a variety of material property and geometric parameters. In order to accomplish this, theoretical analyses conducted during Phase II (Reference 1.2) together with additional analyses conducted during this phase (Section 5 and Appendices A and C) were utilized. These analyses not only identified the critical parameters associated with the spalling failure mode but also established the desirable range of values to be investigated. In addition, it also provided the design criteria and design margins required for selecting and implementing the final designs for the ETM candidate module configurations.

In addition to the foregoing, it was necessary to conduct a module material properties evaluation program (Section 7). This was particularly critical in the case of the selection of the candidate adhesives, since very little low temperature (to -173°C) data was available. Two test data matrices were prepared (Tables 7.1 and 7.2). The material properties evaluation program consisted of conducting both experimental tests and literature surveys to obtain the necessary data. The results of these activities are provided in Section 7 of this report.

By utilizing both the analytical and experimental data obtained during this program, it was then possible to arrive at the final ETM module

designs. The basic substrate designs were similar to the ETM I, II, and III candidate designs of Phase II. However, in order to stay within the scope of this program phase, a smaller module size (approximately 20 in. x 20 in. versus 30 in. x 48 in.) was utilized. In addition, a pre-tensioned fiberglass diaphragm substrate was used in place of the pre-tensioned lattice construction used for ETM I during Phase II. However, identical substrate materials were used in all three cases in order to insure similarity of material properties. The three test modules designed and built during this program phase were designated ETM IA, IIA, and IIIA respectively. A description of these designs, as well as the solar cell sub-module cellstack design which was common to all three configurations, is provided in Section 8. The design criteria utilized in arriving at these three ETM's is discussed at length in Sections 4 and 6 of this report.

The three ETM's were fabricated in accordance with the finalized designs (Figures 8.2, 8.3, and 8.4). Various views of the completed modules are shown in Section 9 (Figures 9.1 and 9.7). In addition, during the manufacturing operations, several compromises from the original design were found to be necessary. These are discussed in Section 9 also. The most significant of these was the necessity to relax the tolerances to which the various adhesive dot diameters and thicknesses would be held. In addition, at the inception of this program phase, all silicon cells were to be 2 cm x 2 cm. However, at the request of NASA/MSFC, two sub-modules of 2 cm x 4 cm cells (1 in parallel direction and 5 in series) were incorporated in each ETM module. These were installed only in the region where RTV 3145 adhesive was being utilized with a nominal adhesive dot diameter of 0.50 inches. This was done to evaluate the compatibility of these larger cells with the temperature extremes of the lunar surface environment.

2.2 ETM TEST EVALUATION

The environmental testing of the three ETM's was conducted in the facilities at NASA/MSFC with TRW Systems participating. The tests were conducted in accordance with TRW Systems Test Plan No. 09681-6004-R000 (Reference 7.2) to comply with the test objectives as outlined in Section 10.1 of this report. The test operations together with the documentation of the test data obtained are summarized in Section 10.2. However, only

that test data which was pertinent with respect to evaluation of the particular significant phenomena and failure modes encountered were included in this report. In addition to the anticipated silicon cell spalling, test evaluations were conducted regarding the structural integrity of the substrates, the fatigue characteristics of the common interconnector, the adequacy of the sub-module bus bar solder joints, and the factors effecting the cell-to-substrate adhesive bond strength. These are reported in Section 10.3. In all cases it was possible to draw meaningful qualitative assessments of the failure modes encountered. In the case of the silicon cell spalling failure mode, it was additionally possible to further quantify the significant parameters affecting this phenomenon. These were found to be adhesive modulus of elasticity (E_2), adhesive coefficient of linear expansion (α_2), adhesive thickness (t_2), a spalling parameter designated " $E_2 \alpha_2$ ", the ultimate tensile strength of the silicon cell, the surface finish of the silicon cell bonding surface, and substrate coefficient of linear expansion. The degree to which specific design criteria could be assigned to these various parameters was very much a function of the availability of material property data at low temperatures. In addition, since most of these properties change significantly with decreasing temperature, the quantity of material property data and the accuracy of this data are very critical in establishing adequate solar array adhesive design margins for the lunar surface temperature extremes.

An additional important factor, which could only be qualitatively assessed during this program was the possible variation of the candidate adhesive material properties. Not only are material property variations from batch-to-batch suspected, but also individual batch variations due to lack of homogeneity of these elastomers. Since the solar arrays on the lunar surface are subjected to such large temperature differentials, as well as long duration, low temperature conditions, the need for improved adhesive manufacturing process controls and quality control appears obvious.

Undoubtedly, additional analyses and environmental testing would be desirable to further quantify and provide statistical confirmation of the adequacy of the design criteria recommended in this program phase. However, if sufficient design margins are established and adequate quality control techniques are maintained during the material procurement and

manufacturing phases, the recommendations made in this report regarding solar array module design for lunar surface applications should be sufficient to insure a high probability of meeting overall design requirements.

3. CONCLUSIONS AND RECOMMENDATIONS

3.1 CONCLUSIONS

This phase of the lunar surface power system development program has resulted in establishing the critical design parameters associated with arriving at a satisfactory cell-to-substrate adhesive bond to prevent silicon cell spalling. This spalling phenomenon results primarily from the necessity for the solar array to survive the extremely low temperature (to -173°C) experienced during the long duration (14.75 Earth days) lunar night. This causes all the solar array module materials to be subjected to a very large temperature differential (i.e. $\Delta T = 193^{\circ}\text{C}$ for $T_1 = 20^{\circ}\text{C}$ and $T_2 = -173^{\circ}\text{C}$). The variations in the coefficients of expansion of the various materials used in the cellstack/substrate components are the prime stress producing factors. However, whether or not spalling will occur is directly related to the stress level reached in the adhesive/silicon cell bond region. This stress level in turn, is determined primarily by the low temperature properties of the adhesive and silicon cell and the thickness of the adhesive dot. In addition, the coefficient of linear expansion of the substrate facesheet material can also be a significant factor. All these properties vary considerably as a function of temperature for the various solar array module components. Hence, the rate at which these material properties change as the temperature is reduced also becomes an important consideration. This is due to the interaction between these material properties and their potential for inducing incipient failures which can ultimately result in excessive stresses and spalling at the extreme low temperatures involved.

Another important factor is the limited amount of low temperature data available for these materials. This is particularly critical for the typical adhesive bonding materials used (i.e. RTV 3145, RTV 511/577, RTV 118, PR 1538, etc.), where order of magnitude changes in modulus of elasticity and coefficient of linear expansion invariably occur in going from $+20^{\circ}\text{C}$ to -173°C . Experimental technique and data reduction methods become very critical in establishing accurate values for these elastomers. This is further compounded by the fact that, initially these materials are in the so-called plastic region where it is quite difficult to determine accurate material properties. When extremely low temperatures

and ultimately, hard vacuums, are applied to these adhesives, increased difficulty is encountered in precisely determining the critical material properties. Finally, when the additional complexities of potential material phase changes, lack of homogeneity in individual batches, and manufacturing process effects from batch to batch are considered, it becomes obvious that this represents a critical area where increased data could greatly contribute to a more comprehensive understanding of the spalling phenomenon.

The crystalline structure of the silicon cell (i.e. random, preferred, polycrystalline) also contributes greatly to the task of quantifying the cellstack design criteria to be used in preventing spalling. Not only does it effect the ultimate tensile and shear strength of this material, but it can also be a determining factor in controlling the silicon cell surface finish. This latter condition can be instrumental in creating scratches and cracks in the silicon cell surface which result in producing very high stress concentrations. In addition, because silicon is such a brittle material, it is possible to produce micro-cracks in the silicon cell surface if a bowed cell is excessively flattened during any of the manufacturing operations involved. These micro-cracks could also produce stress concentrations and lower the value of the ultimate tensile strength of the cell. This makes the determination of the allowable design margins for the cellstack more difficult to predict. In addition, it can impose additional limitations on the range of acceptable adhesive low temperature properties.

Because of the foregoing, it is essential that for lunar surface applications, where solar array temperatures as low as -173°C can be experienced, increased care must be taken in arriving at the design criteria for the module cellstack. It is important that the adhesive selected should have as low a value of modulus of elasticity at low temperature as possible. The adhesives selected for this program all fell within a range of 38,000 to 174,000 psi at approximately -173°C . Based upon the analyses conducted, these were all within an acceptable range as long as the correspondingly required low values of adhesive coefficient of linear expansion (see Figure 10.26) were actually achieved. However, because of the previously discussed uncertainties in both the adhesive and silicon material properties,

increased design margins with regard to the minimization or elimination of spalling can be established if the adhesive dot thickness is maintained at a nominal value of 0.005 inches. Use of a substrate facesheet material with a coefficient of linear expansion very nearly equal to that of silicon at low temperatures, can further enhance the probability of eliminating spalling. In addition, by utilizing higher quality preferred crystal orientation silicon cells with the adhesive bond surface free from excessive scratches or micro-cracks, the possibility for spalling occurring is even further reduced. Finally, by improving the process controls and quality control of the adhesives during their manufacture, the spread on the range of their material properties and hence their analogous behavior at low temperatures can be minimized.

The design of satisfactory cellstack common interconnectors for lunar surface applications invariably involves achieving a balance between providing a high spring rate, high natural frequency configuration (to avoid fatigue failures during vibration testing), while still permitting sufficient flexibility to preclude the possibility of overstressing the solder joints due to the large temperature excursions experienced. In addition, care must be taken during the cellstack manufacturing operations to prevent excessive solder wicking since this can contribute to increasing the possibility of fatigue failures and, by reducing interconnector flexibility, a higher probability of solder joint failure. These conclusions are equally applicable to the design of the sub-module bus bars. However, in the case where vertical tabs are used to simplify the soldering operation during manufacture, additional precautions must be taken to avoid causing stress concentrations in this solder joint. This can best be achieved by redesigning the tabs to minimize the tearing action produced at the solder joint by the thermal differential expansion or by eliminating the vertical tabs entirely. For a lunar surface application due to the large temperature excursions and the very high and very low temperatures involved, the latter approach appears to be the one that would result in a higher design margin and hence higher solder joint reliability configuration.

With respect to improving the cell-to-substrate adhesive bond strength, in order to minimize adhesive bond failures, two approaches should be considered. For those adhesives requiring primers (i.e. RTV 511/577 and PR 1538), increased primer thickness control and humidity and cure-time control

during cellstack production should completely eliminate this failure mode. For unprimed adhesives, such as RTV 3145, improved process and quality control during its manufacture is required to assure a homogeneous adhesive whose material properties remain consistent from batch to batch and within a given batch as well. In addition, because the failure of the silicon oxide coatings on zone-soldered cells can further contribute to adhesive bond failures, these type of cells are not recommended for use on lunar surface applications.

The three candidate substrates used during this program phase used cellstack-to-facesheet bonding materials similar to those used during Phase II of this program. These were fiberglass epoxy (ETM IA), Kapton (ETM IIA), and graphite composite (ETM IIIA). All three substrates demonstrated adequate structural integrity during vibration testing. However, the large deflections experienced with the pre-tensioned fiberglass epoxy diaphragm of ETM IA directly contributed to many of the common inter-connector fatigue failures. In addition, the fiberglass diaphragm developed a granular appearance upon completion of the thermal-vacuum testing. Because of these factors and the increased complexity associated with manufacturing a pre-tensioned type substrate, this configuration does not appear to be too attractive for lunar surface applications. Both the Kapton substrate configuration (ETM IIA) and the graphite composite design (ETM IIIA) are structurally superior and impose minimum adverse dynamic effects on the cellstack components. However, from the standpoint of eliminating the spalling phenomenon, the graphite composite design appears to be more desirable since its coefficient of linear expansion at low temperatures more nearly matches that of the silicon cell. This was further confirmed during thermal-vacuum testing when only one spalling failure (out of a total of 46) occurred on the module using this substrate. While this is a fairly small test sample and many other factors previously discussed could have contributed to this result; at this program phase, the ETM IIIA substrate is to be preferred for lunar surface applications. However, if solar array stowage height is critical in a given application, the use of a Kapton substrate should also prove acceptable, if the previously recommended cellstack design criteria are adhered to.

3.2 RECOMMENDATIONS

This program phase has served to establish an analytical approach for identifying the critical parameters involved in silicon cell spalling. In addition, within the limits of the scope of this effort, it has provided experimental confirmation of the validity of the analytical model. Furthermore, it has established a basis for providing improved design criteria to increase the reliability of cellstack designs for lunar surface applications. However, in accomplishing these objectives, this development work has identified a need to obtain further corroboration of the qualitative conclusions drawn and increased statistical data to provide further confirmation of the cellstack design criteria established. The following recommendations are provided to identify these technology areas.

- (a) The analytical model for evaluating the spalling failure mode should be expanded to include a quantitative evaluation of the impact of the substrate on this phenomenon. This work should be done parametrically over a judiciously selected range of values compatible with the low temperature properties of the graphite composite (0/90 and 0/ \pm 60 orientation types), Kapton, and the fiberglass epoxy laminate. In addition, since the silicon cell is a brittle material with variable surface imperfections, micro-fracture analyses should also be conducted to assess the impact of these stress concentrations on the spalling failure mode. Finally, since the material properties of the adhesives, and to a lesser degree the other cellstack and substrate components, vary greatly with changing temperature, parametric analyses should be conducted for various low temperature regimes and temperature differentials, to determine if the inception of the spalling failure is initially induced at higher levels in the low temperature regime.
- (b) The low temperature properties of all the cellstack and substrate materials were found to be very critical with regard to the spalling phenomenon. This was particularly true of the various candidate adhesives utilized. It is felt that a much larger and more comprehensive set of experimental data should be obtained to provide a higher degree of confidence in

1

achieving adequate design margins for establishing cellstack design criteria for lunar surface applications. This should include the development of improved specifications for procuring solar array adhesives, silicon cells, interconnects, solders, and substrate facesheets. Techniques for improving the process and quality control in the manufacturing of all the cellstack/substrate materials should also be included in this effort.

- (c) Consideration should be given to the redesign of the negative and positive bus bars. The use of vertical tabs and the resulting solder joints do not appear to be compatible with the large temperature excursions to be experienced on the lunar surface. A modified common interconnector looks attractive as a possible replacement for the bus bar designs, but additional analytical and experimental investigations should be conducted to preclude the occurrence of any adverse solder wicking action and to establish adequate fatigue strength design margins.
- (d) The four candidate adhesives (RTV 3145, RTV 511/577 , RTV 118 and PR 1538) evaluated during this program phase all had acceptable low temperature material properties (i.e. modulus of elasticity and coefficient of linear expansion). However, both RTV 511/577 and PR 1538 require priming of the bonding surface. This adds increased complexity and cost to the manufacturing operation and if adequate quality control is not maintained a decrease in the reliability of the cell-to-substrate adhesive bond strength could occur. Despite these shortcomings, there were no occurrences of spalling in those module regions where RTV 511/577 was used. Hence this adhesive is worthy of further consideration. From an overall point of view, the self-priming Dow Corning RTV 3145 and G. E. RTV 118 appear to be the more desirable adhesives to use for a lunar surface application. However, in the case of the use of RTV 3145, the potential material property variations from batch-to-batch and lack of homogeneity within a given batch

must be minimized and its impact on adhesive bond reliability evaluated. In addition, process control techniques must be utilized to assure meeting required outgassing limits. Similarly, care must be taken with the use of RTV 118, since it contains an acetic acid constituent which can cause corrosion of the silver titanium contacts to occur on zone-soldered cells. Use of fully solder backed cells should eliminate this problem, but additional experimental data is required to assure that this adhesive is compatible with the other cellstack/substrate materials. However, RTV 118 is capable of meeting NASA/MSFC outgassing limits and is on their approved list in this category. In addition, during this program phase, it demonstrated the highest adhesive bond strength reliability of all the four candidate adhesives. In view of the foregoing, it would appear to be technologically prudent to conduct additional adhesive bonding, outgassing, and material compatibility tests with at least three of the four candidate adhesives. This would provide a larger statistical base for estimating adhesive bond design margins and reliability before committing a particular application for a lunar surface solar array to a specific adhesive.

- (e) The structural integrity of all three candidate substrates has been adequately demonstrated during both Phase II and the current phase of this program. However, both the Kapton and graphite composite substrates (ETM IIA and IIIA) are more easily manufactured and reproducible than the pre-tensioned fiber-glass lattice configuration (ETM IA). In addition, the cell area utilization as determined during Phase II was only 74% for the ETM IA design, while ETM IIA and ETM IIIA were both capable of providing a value of 84.4%. Because of this either the ETM IIA (Kapton substrate) or the ETM IIIA (graphite composite substrate) configurations are the preferred module designs for lunar surface application. The ultimate factor in selection of a particular design would be contingent upon whether a flexible roll-up or fold-up configuration (ETM IIA) would be required to meet stowage height limitations or whether

a rigid, fold-up type (ETM IIIA) would be more compatible with solar array deployment and retraction requirements in the 1/6 g lunar surface environment.

- (f) The work conducted to date has resulted in resolving all the major technology problems associated with the design of solar array modules for use on the lunar surface. This has included the establishing of design criteria for the elimination of silicon cell torsional vibration, silicon cell spalling, common interconnector fatigue failures, sub-module bus bar tab solder joint failures, and cell-to-substrate adhesive bond failures. In all cases this has been achieved by a combination of analysis, design, and experimental verification. However, these development results have been accomplished individually in several phases of this program. In order to achieve complete technology readiness, it now is essential that all these criteria be incorporated into an overall prototype Engineering Test Model. This prototype ETM design should be based upon incorporating the proper materials and design techniques, whose compatibility with the lunar surface environment has been established on this and earlier phases of this program. This prototype design should then be subjected to the entire spectrum of environmental tests as definitized in Reference 7.2. In this manner, the overall technology readiness of the prototype Engineering Test Model can be demonstrated and its suitability for future lunar surface solar array applications confirmed.

4. CELL-SUBSTRATE DESIGN CRITERIA

4.1 CELLSTACK DESIGN REQUIREMENTS

Solar arrays designed for operation on the lunar surface will experience all of the environmental conditions which are common to spacecraft solar arrays; however, in addition, they must be designed to survive some relatively "new" conditions. These "new" conditions include:

- lunar landing shock
- manual deployment by gloved astronauts
- 1/6 gravity static load on structure
- new temperature extremes of operation
- long term temperature soak at each extreme

Present solar array designs have not specifically been required to consider these conditions, either in the selection of interconnect and bonding materials, or configurations. In addition, material interfaces on the completed array, adhesive bond geometry, and consideration of solar cell crystal orientation can be important if the array is to survive the lunar night low temperature soak.

This section defines the launch, cislunar coast, and lunar landing short duration loads, as well as the thermal-vacuum environment to which the solar array will be subjected. In addition, specification of solar cell types, adhesives, adhesive patterns and substrate types to be considered during this program phase are provided.

4.1.1 Dynamic Environments

Solar arrays for lunar surface applications will be subjected to dynamic excitation during pre-launch, boost, flight, lunar landing and post-landing phases of the mission. The dynamic excitation will result from transient acceleration (shock) and mechanically and acoustically induced vibration environments imposed by a Saturn V SLV and a LEM-type landing vehicle.

The shock, vibration and acoustic levels have been defined by the Apollo/Saturn V - Lunar Module Criteria of (1) TRW Systems IOC 7440.68-40, Appendix IV, dated 22 July 1968, and (2) Grumman Aircraft Engineering Corporation Specification No. LSP-520-0018, dated 4 September 1967. The

respective level for each condition is given in Figures 4.1 to 4.4.

The tolerance limits indicated are those allowable by standard practice and/or practical test considerations.

4.1.2 Thermal-Vacuum Environment

The lunar surface environment is the dominant factor in effecting the material selection, performance, and operation of lunar-based solar arrays. The various environmental parameters affecting solar array system operation are:

- temperature
- radiation levels
- micrometeoroid bombardment
- dust
- vacuum level (10^{-13} to 10^{-23} Torr.)
- g-level (1/6 that of Earth)

By far the most critical of these, from the standpoint of affecting solar array performance, is the thermal-vacuum environment and the resultant effect on array operating temperature. This has been amply demonstrated by the parametric analysis in Reference 1.2. Data obtained in laboratory tests, and operation data obtained from Earth orbital and interplanetary spacecraft, have verified that analysis to some extent.

The average day/night variation in lunar surface temperature due to the presence or absence of the solar constant (I_{sol}) of approximately 140 mw/cm^2 is shown in Figure 4.5. This is the range of operation for long-term lunar missions. Sub-surface temperatures are expected to be considerably more moderate due to the insulating effect of the surface materials. Theoretical lunar surface temperature variation parametric curves are shown in Figure 4.6 for a point at the lunar equator where the lunar material thermal inertia (γ) varies from 20 to $1000^\circ\text{C-cm}^2\text{-sec}^{1/2}/\text{cal.}$; Figure 4.7 depicts the lunar surface temperature variation with latitude.

The equation $T = T_{\text{subsolar point}} \cos \psi/4$ was used to establish these curves (ψ is the latitude angle) and since radiation is the principle heat transfer mechanism, variation in surface material properties can cause hot spots of re-reflected solar energy. The light scattering properties

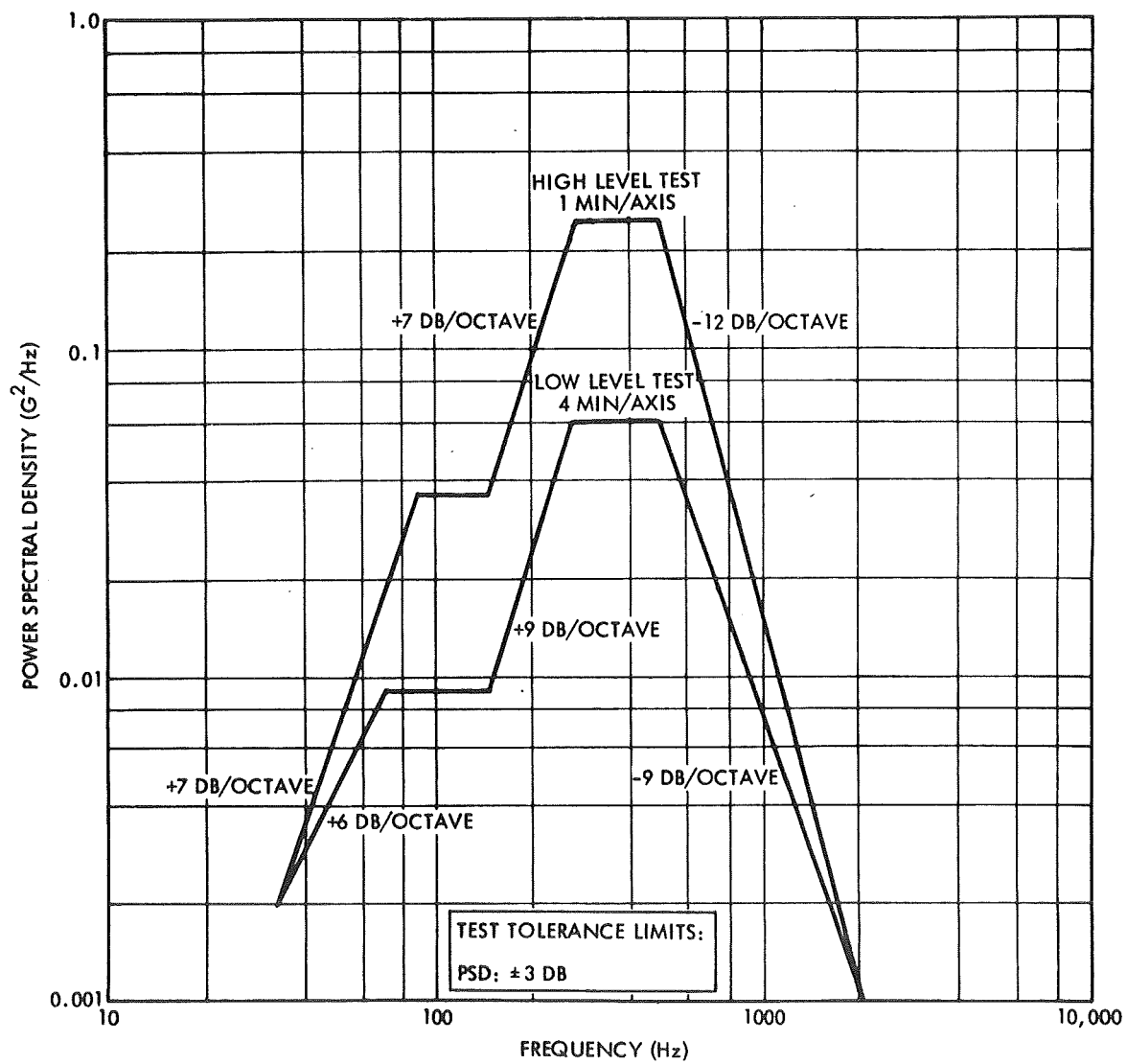


Figure 4.1 Random Vibration Test Criteria

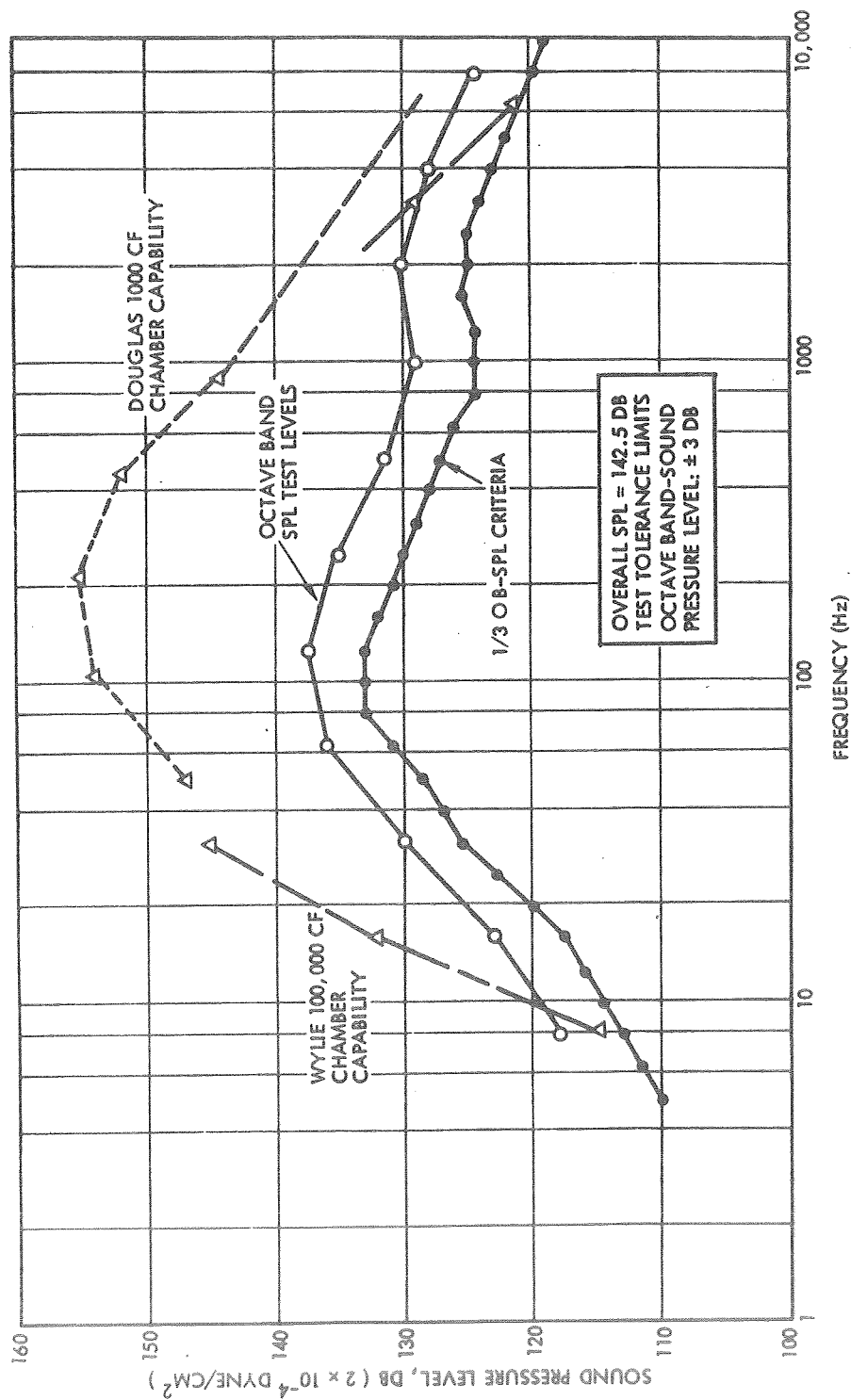


Figure 4.2 Acoustic Test Criteria

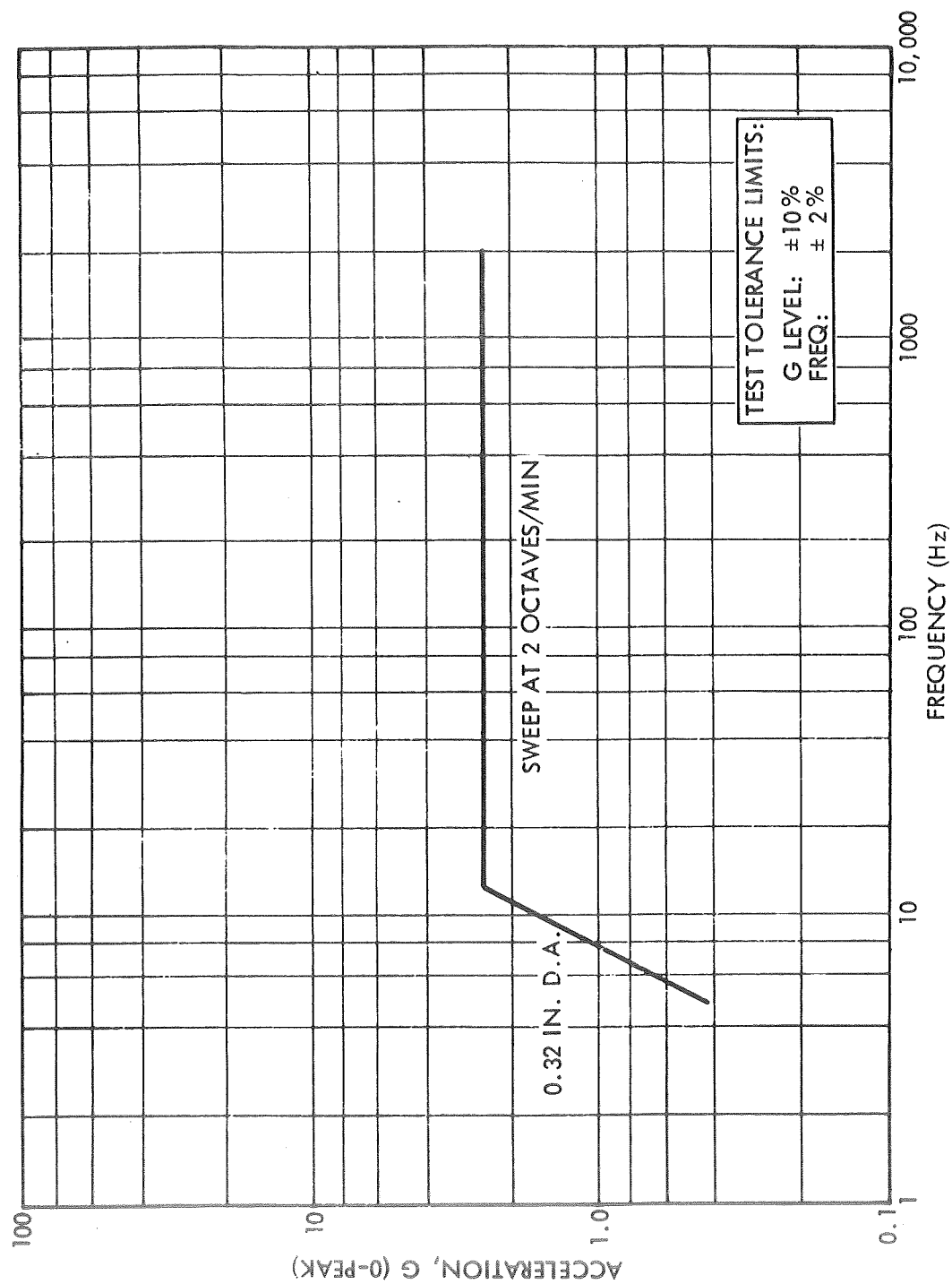


Figure 4.3 Sinusoidal Vibration Test Criteria

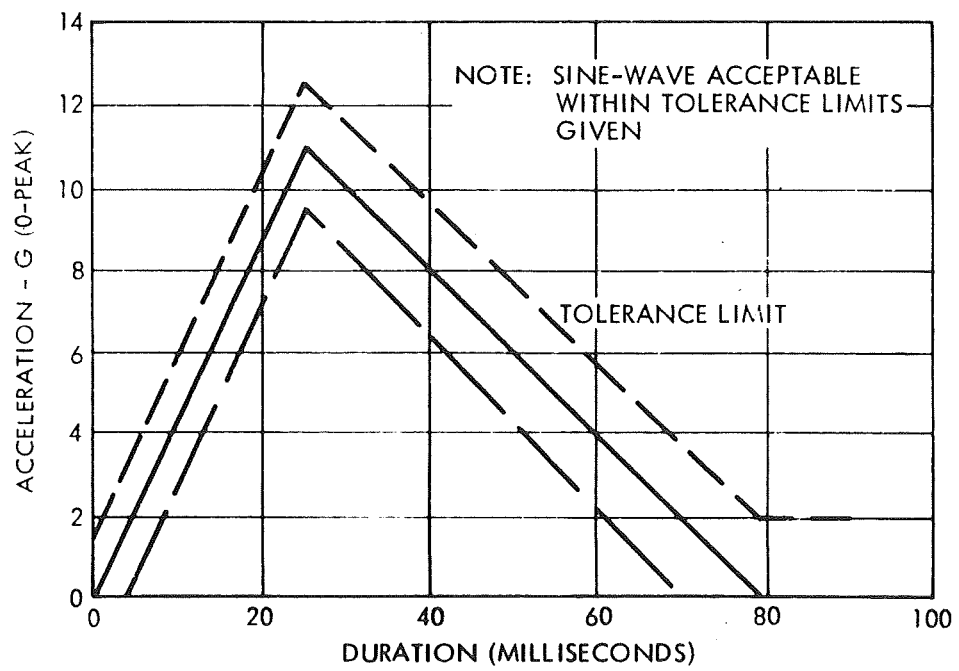


Figure 4.4 Shock Test Criteria

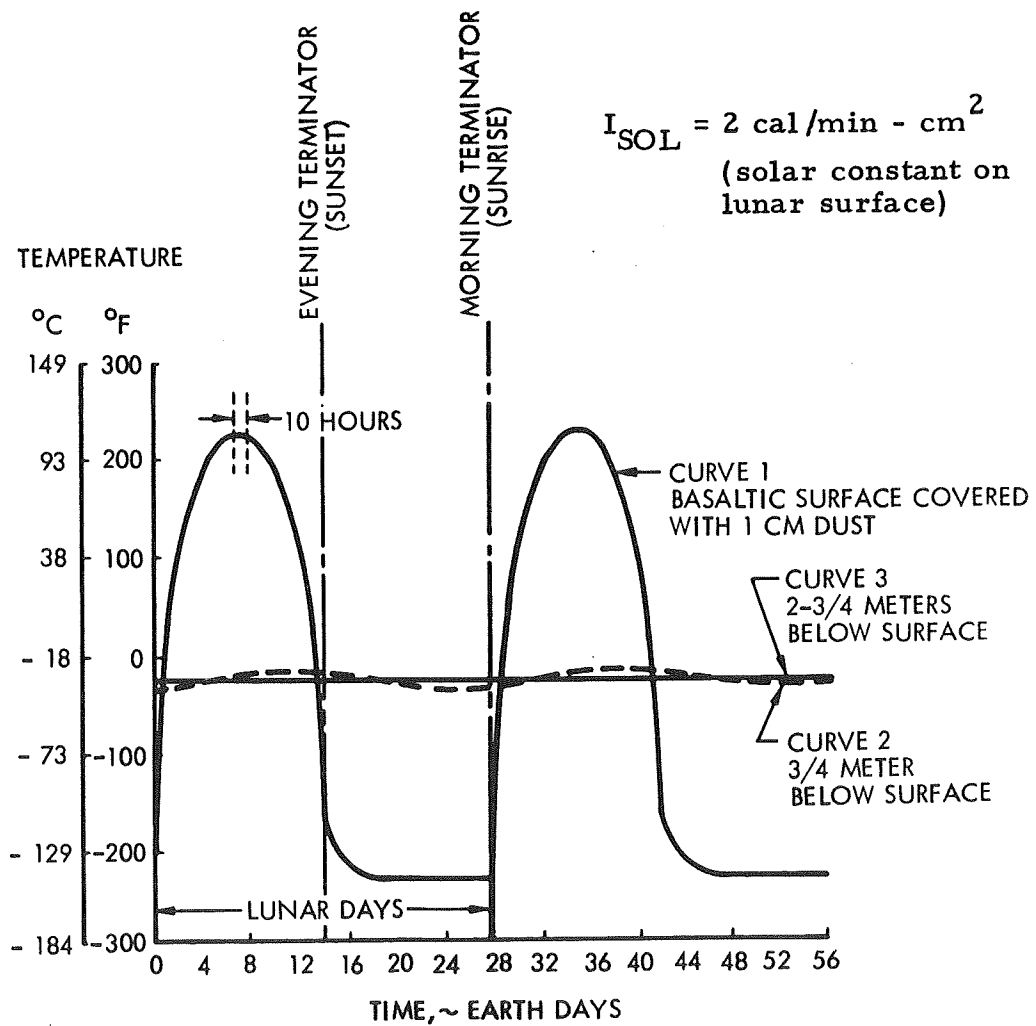


Figure 4.5 Typical Temperature Variation of the Lunar Surface

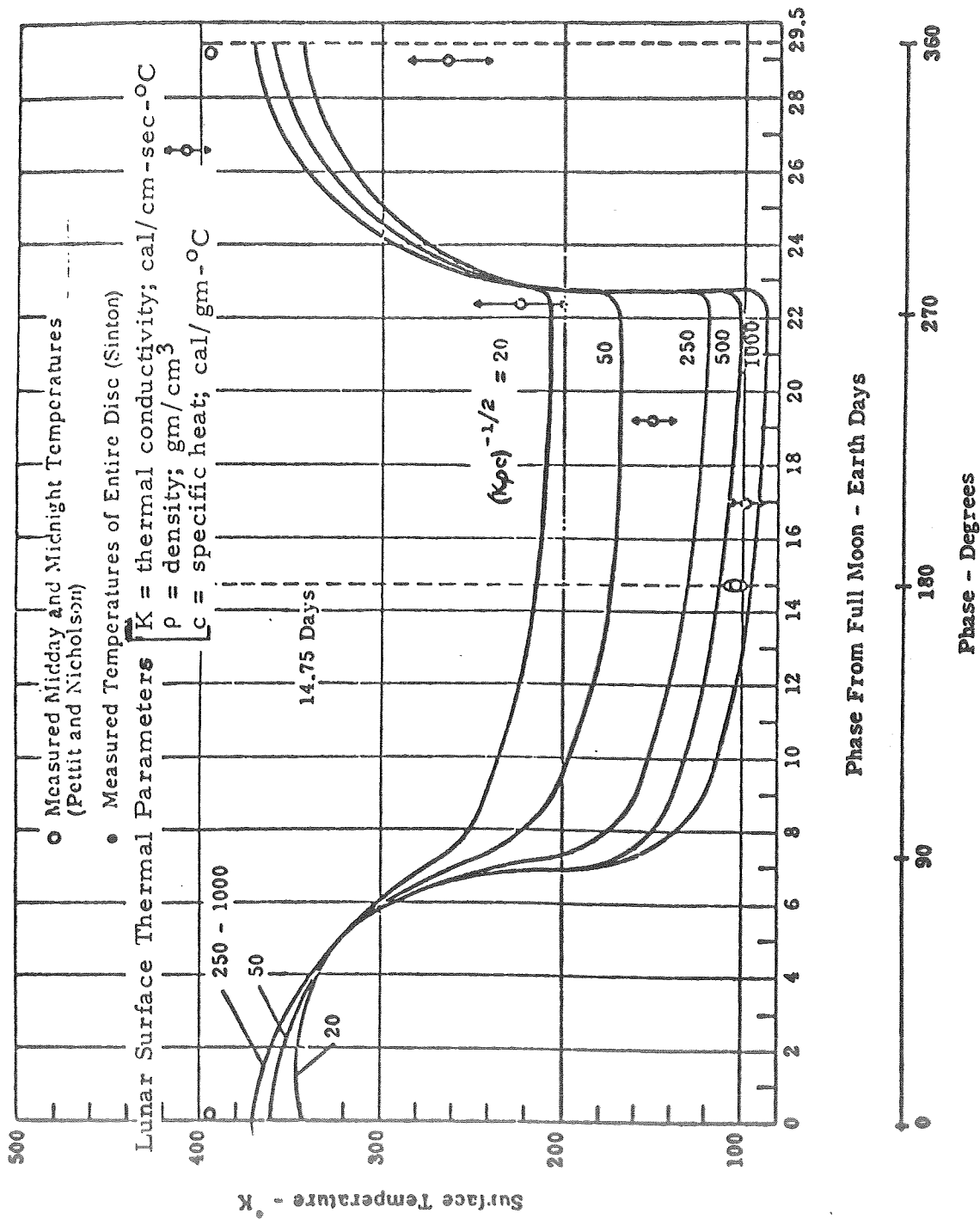


Figure 4.6 Theoretical Lunar Surface Temperature Variation for a Complete Lunation at the Lunar Equator (where the lunar thermal inertia, $\gamma = (K\rho c)^{-1/2}$)

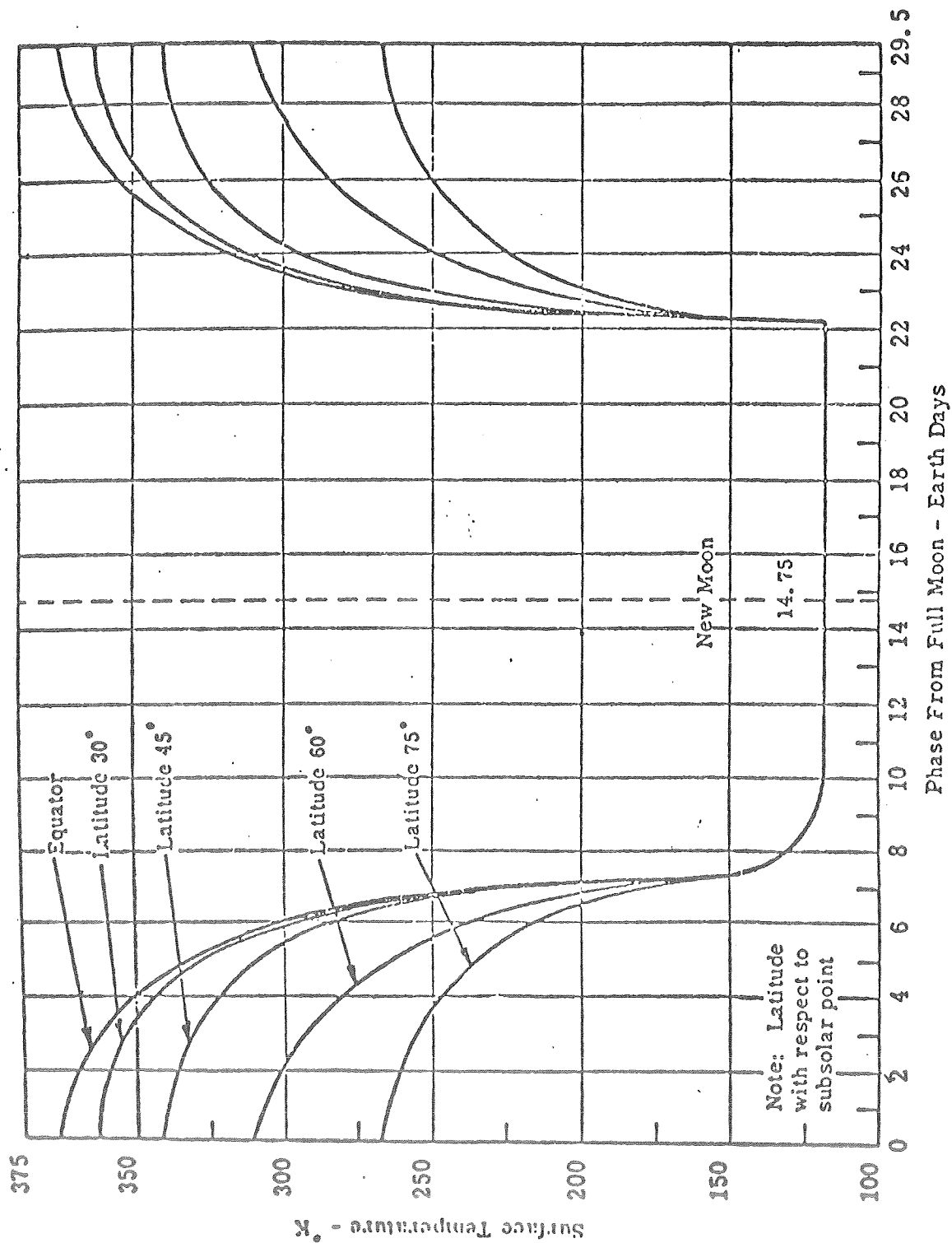


Figure 4.7 Theoretical Lunar Surface Temperature Variation for a Complete Lunation on Lunar Central Meridian

of the moon are such that there is no limb darkening regardless of latitude or longitude during a full moon, at which time each part attains maximum brightness.

Figure 4.8 is considered a best estimate only of a lunar thermal model since it is based on experimental laboratory data, rather than actual measurement. The data from Surveyor and Apollo have somewhat verified this experimental data. The range of thermal parameters of surface materials is:

K (thermal conductivity) = 1.676 to 2.514 w/°C-m

ρ (density) = 350 to 2500 kg/m³

c (specific heat) = 838 w-sec°C/kg

γ (thermal inertia) = 1.43×10^{-2} to 4.3×10^{-2} °C-m²/w-sec^{1/2}

Figures 4.9 and 4.10 indicates the predicted temperature profile for a lean-to type lunar surface solar array during the illuminated portion of the lunar day. The lunar night is a 14.75 earth day soak at a temperature near -173°C. Actual temperatures are highly dependent on array constructions, material and consideration of active array heating during the eclipse period. The thermal test profile to simulate these temperature conditions is shown on Figure 4.11.

4.2 CANDIDATE COMPONENTS AND MATERIALS

4.2.1 Coverslides

Coverslides can be either Dow Corning 0211 microsheet (0.006 inches thick) or 7940 fused silica (0.012 inches thick). However, the microsheet is the most desirable and would be representative of that which would be used for an actual mission.

4.2.2 Coverslide Adhesive

There are three adhesive candidates for this application, they are: RTV-602, Sylgard 182 and R 63-489 (highly refined Sylgard 182). The RTV-602 is the least desirable since the AgTi contacts are susceptible to corrosion from some of the volatiles. However, Sylgard 182 and R 63-489 are both equally acceptable for lunar surface system applications.

4.2.3 Solar Cell

The cells selected were 2 cm x 2 cm, single crystal, silicon of 0.010

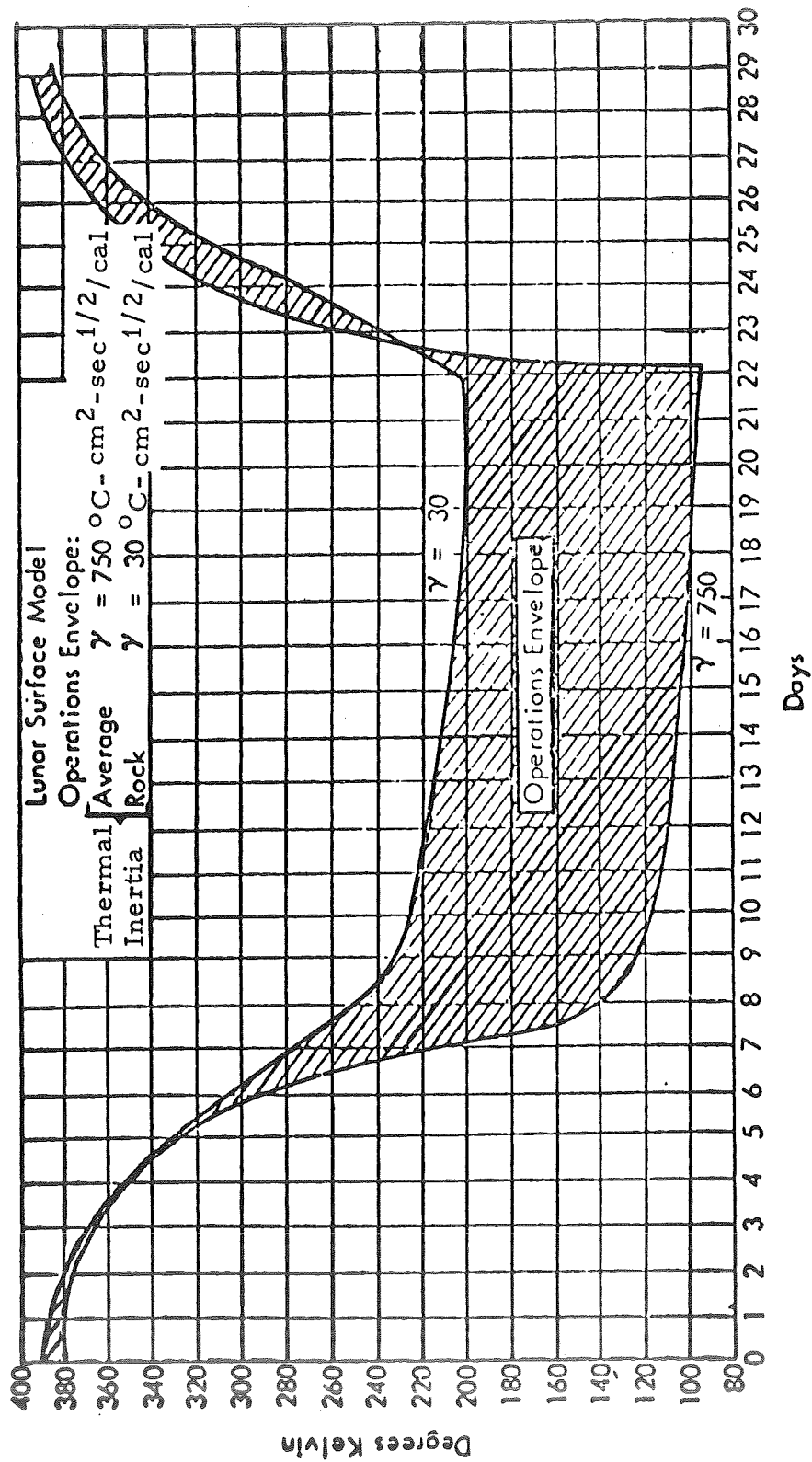


Figure 4.8 Variation of Lunar Surface Temperature During a Complete Lunation

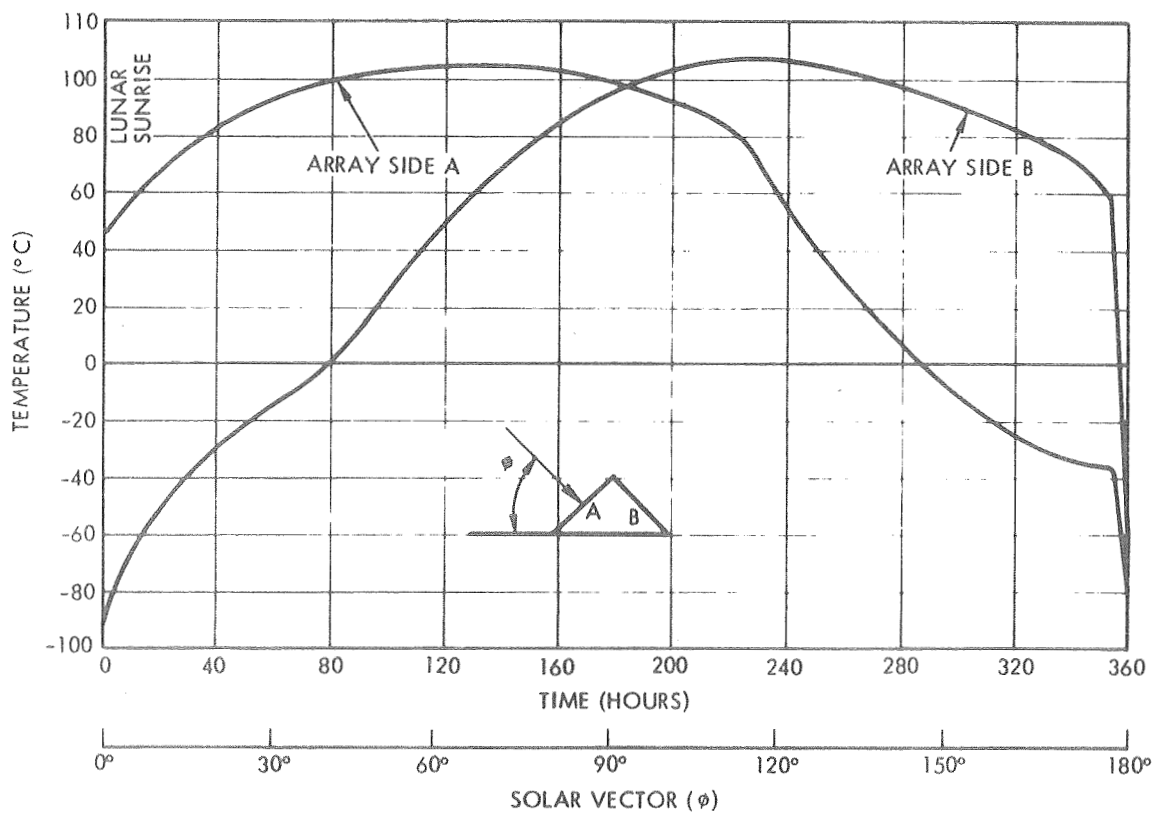


Figure 4.9 Lunar Based 45° Lean-to Array Temperatures as a Function of Solar Heating for one Lunar Day

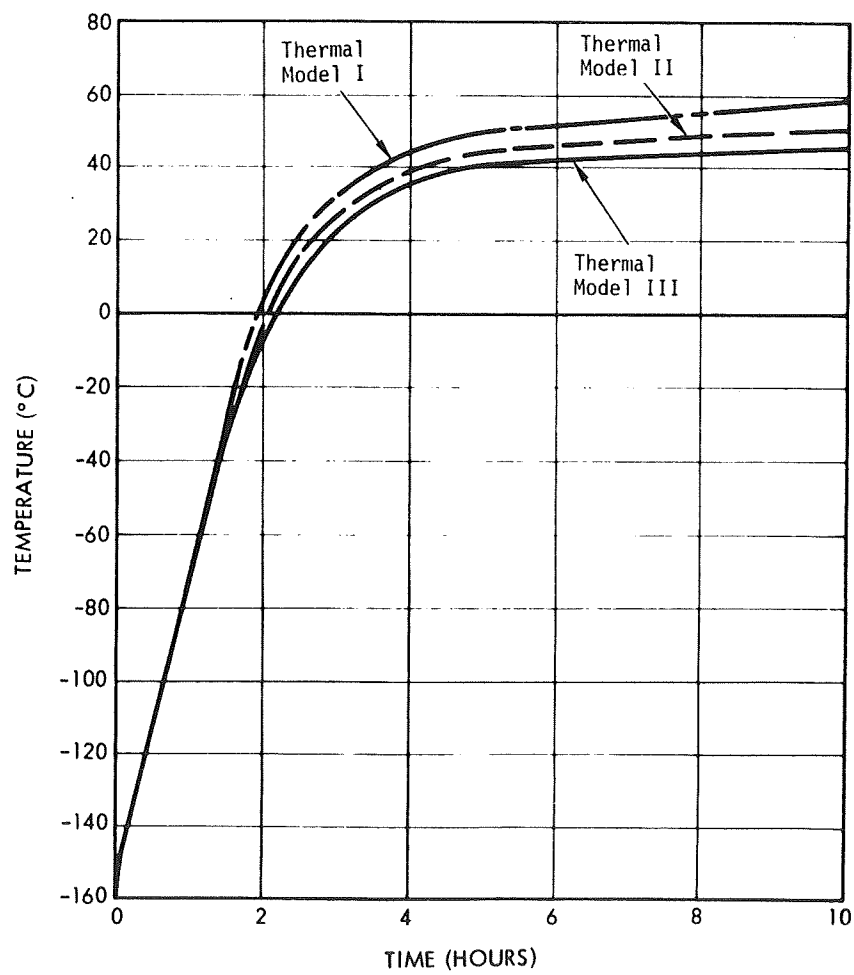


Figure 4.10 Lunar Based 45° Lean-to Array Temperatures During the First Ten Hours of Solar Illumination

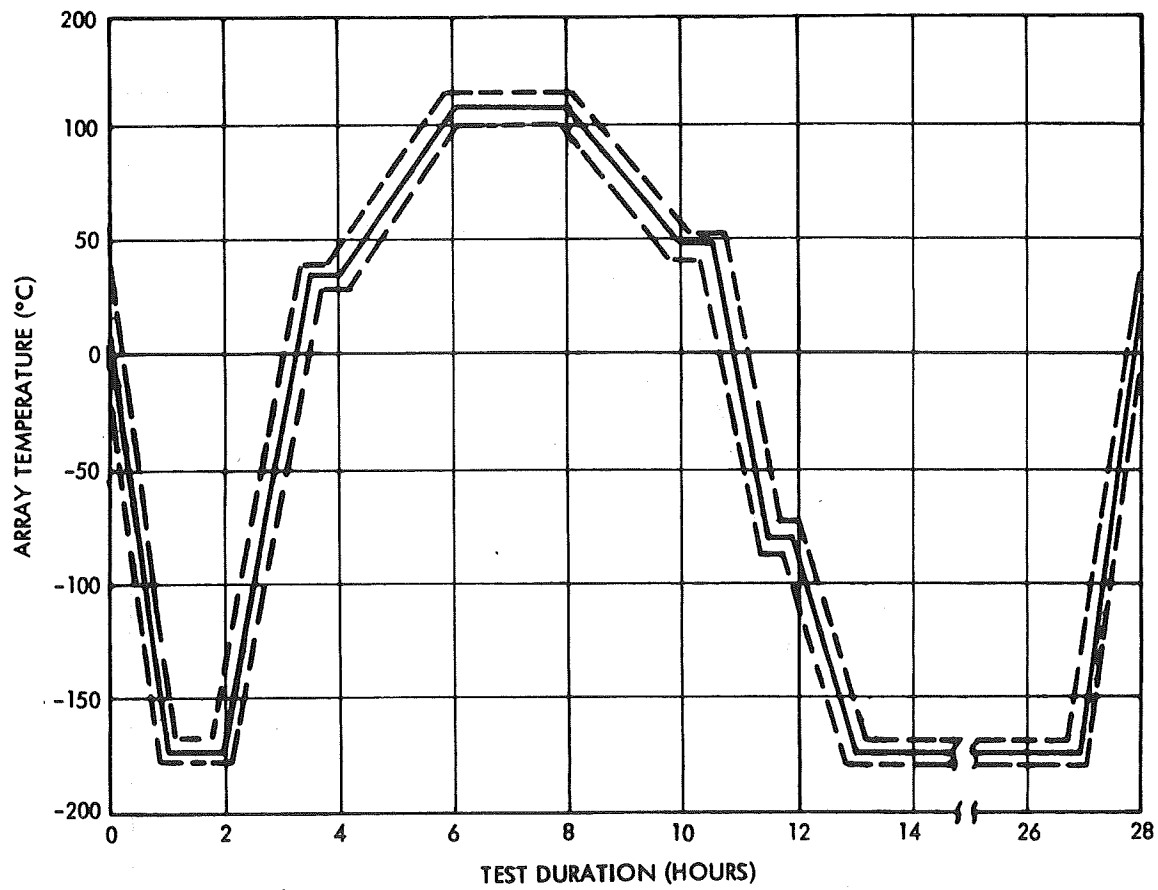


Figure 4.11 Thermal Test Profile Used to Simulate Array Lunar Surface Temperatures

inch thickness. Base resistivity should not affect test results and thus is arbitrary. Cells should include both fully-soldered and zone-soldered (not solderless) types with each type applied to both preferred and random cut crystal orientation wafers.

4.2.4 Cell-to-Substrate Adhesive

The selection of adhesives for cell bonding quickly narrows when long term, low temperature soaks are considered. There are four candidates in the RTV category; 1) RTV 3145, 2) RTV 118, 3) RTV 511/577 (50-50 mix), and 4) Silastic 140. RTV 118 is an acetic acid producer and may only be useable with fully solder-backed solar cells. Promising Urethanes which should be considered are Crest Products No. 7343/7139, and Products Research PR 1538. The adhesive thickness should be 0.010 ± 0.005 inches applied in either a single dot (large diameter) or a multiple dot pattern and diameter consistent with data derived during Phase II of this program (Figure 5.1). Three adhesive patterns are worthy of consideration and include:

- full adhesive coverage
- single dot per M35 and Program 777
- three dot pattern 120 degrees apart

The single dot diameter pattern was selected for this program phase as the most cost-effective. It should be consistent with surviving the g-levels imposed by the dynamic loads curves given earlier, coupled with the resulting levels predicted for the various substrate designs being considered.

4.2.5 Cell-to-Cell Interconnect

Solar cells were interconnected using 0.001 inch thick solder-plated Kovar material. The geometry should offer stress relief in both series and parallel cell directions and be compatible with flat laydown designs. Each solar cell should have a minimum of two solder joints per contact.

4.2.6 Substrates

The three substrate types developed during Phase II of the LSPS effort were used so the effects of the material properties of the face-sheets on the spalling phenomenon could be determined. These were:

- ETM IA - Fiberglass lattice/box beam
- ETM IIA - Kapton sheet between end plates of aluminum face-sheet/honeycomb panels
- ETM IIIA - Graphite composite/aluminum honeycomb sandwich

Facesheets having electrical conductivity (such as the graphite composite) should be coated with a dielectric material interface between cells and the conducting surface of the substrate. The dielectric material should be compatible with the thermal environment defined earlier and be capable of being bonded to the substrate using the adhesives being considered. Consideration was given to perforated Kapton sheet as that insulating layer.

4.3 CANDIDATE CELLSTACK DESIGNS

4.3.1 Solar Cell

The baseline cellstack design consisted of 2 cm. x 2 cm. silicon cells. The cell dimensions were nominally 0.788 x 0.788 inch and have an active area of 0.589 in^2 (3.80 cm^2). The cells had a thickness of $0.010" \pm 0.002$. The base resistivity of these cells was not considered to be a critical parameter during this program phase. Hence, both 2 ohm-cm and 10 ohm-cm cells were considered acceptable and specific use depended upon cell availability.

The impact of cell crystalline structure on the spalling failure mode could not be deduced analytically. This was also true of the cell underside coating. These material property effects however, were evaluated on an experimental basis. Both fully-soldered and zone-soldered cells were included in each ETM cellstack design. In addition, based upon their availability, both preferred and random cut crystal orientation cells were utilized.

To insure structural similarity with flight type cellstack designs all test cells included 0.006 inch thick Dow Corning 0211 microsheet coverslides. These were bonded to the silicon cells with Dow Corning XR 6-3489 adhesive (a highly purified version of Sylgard 182).

4.3.2 Cell Spacing

For flat laydown cellstack designs, the cell spacing is an important

design parameter. It is this parameter which greatly determines the achievable packing factor or cell area utilization. However, thermal differential contraction and torsional deflections due to in-plane vibration and acceleration loads place constraints on minimizing the cell spacing. In addition, interconnect design and sub-module manufacturing techniques can further limit reduction of cell clearances. Based upon these considerations a cell spacing of 0.010 inches (min.) in the parallel direction and 0.030 inches (min.) in the series direction was selected. A typical solar cell sub-module using these values is shown in Figure 4.12, and represents the arrangement that was utilized during this program phase.

4.3.3 Adhesive Bond Geometry

The use of various cell-to-substrate adhesive patterns as discussed in Section 4.2.4 was considered. However, for 2 x 2 centimeter silicon cells only full adhesive coverage or single dot designs are practical with regard to minimizing cellstack fabrication costs. In addition, the complexity of the analytical model is greatly increased if multiple dot patterns are utilized. Since the spalling failures during Phase II of this program resulted from single dot configurations, it was deemed advisable to limit the adhesive bond geometries to single circular spot designs. Four diameters were selected, each representing a different percentage of cell area coverage. These were:

<u>Nominal Spot Diameter, inches</u>	<u>Percent of Cell Area</u>
0.250	8%
0.375	18%
0.500	32%
0.750	70%

In addition to adhesive spot diameter, it appeared desirable to assess the effect of adhesive spot thickness. Two nominal thicknesses were selected, namely; 0.010, and 0.005 inches. An initial assessment indicated that holding these thicknesses to close tolerances with plastic adhesives would be quite difficult. However, it was an objective of this program to see if a practical manufacturing technique can be developed to hold and inspect these thicknesses to within ± 0.003 inches. However, a constant adhesive thickness of 0.010 ± 0.005 inches was considered acceptable for the ETM cellstack designs.

4.3.4 Interconnect Design

The 0.001 inch thick Kovar interconnector design (Reference 1.2) utilized on the Engineering Test Models during Phase II of this program proved vulnerable to vibration loads. The comparatively long expansion loops yielded during Z-axis vibration tests. This was partly due to the long unsupported lengths of the expansion loops. In addition, wicking action during soldering operations deposited solder on these expansion loops which further contributed to their yielding. Because of these factors, the cell module interconnectors were redesigned for this program phase.

The new interconnector designs are shown on Figures 4.12, 4.13, 4.14, and 4.15. Analysis indicated that this new design would be considerably stronger with respect to sustaining the imposed vibration loads. In addition, the use of this interconnector design would simplify cellstack submodule manufacturing operations, thus contributing to reduced fabrication costs.

4.4 ADHESIVE CONSIDERATIONS

4.4.1 Adhesive Types

There are a wide variety of cell-to-substrate adhesives that are currently in use. These include Silastic 140, RTV-560, RTV-580, RTV-602, Sylgard 182, RTV 3145, RTV 511/577 (50-50), RTV 118 and PR 1538. An initial assessment of their properties revealed that four of these adhesives could be attractive candidates for this low temperature (-173°C) application.

Based upon existing material properties data, four (4) elastomeric adhesive systems were selected for test evaluation. These were:

- Dow Corning RTV 3145
- General Electric RTV 511/577 (50-50 mix)
- General Electric RTV 118
- Products Research PR 1538

It was felt, that the low temperature properties of these adhesives would vary sufficiently to determine the criticality of adhesive selection to the cell spalling phenomenon.

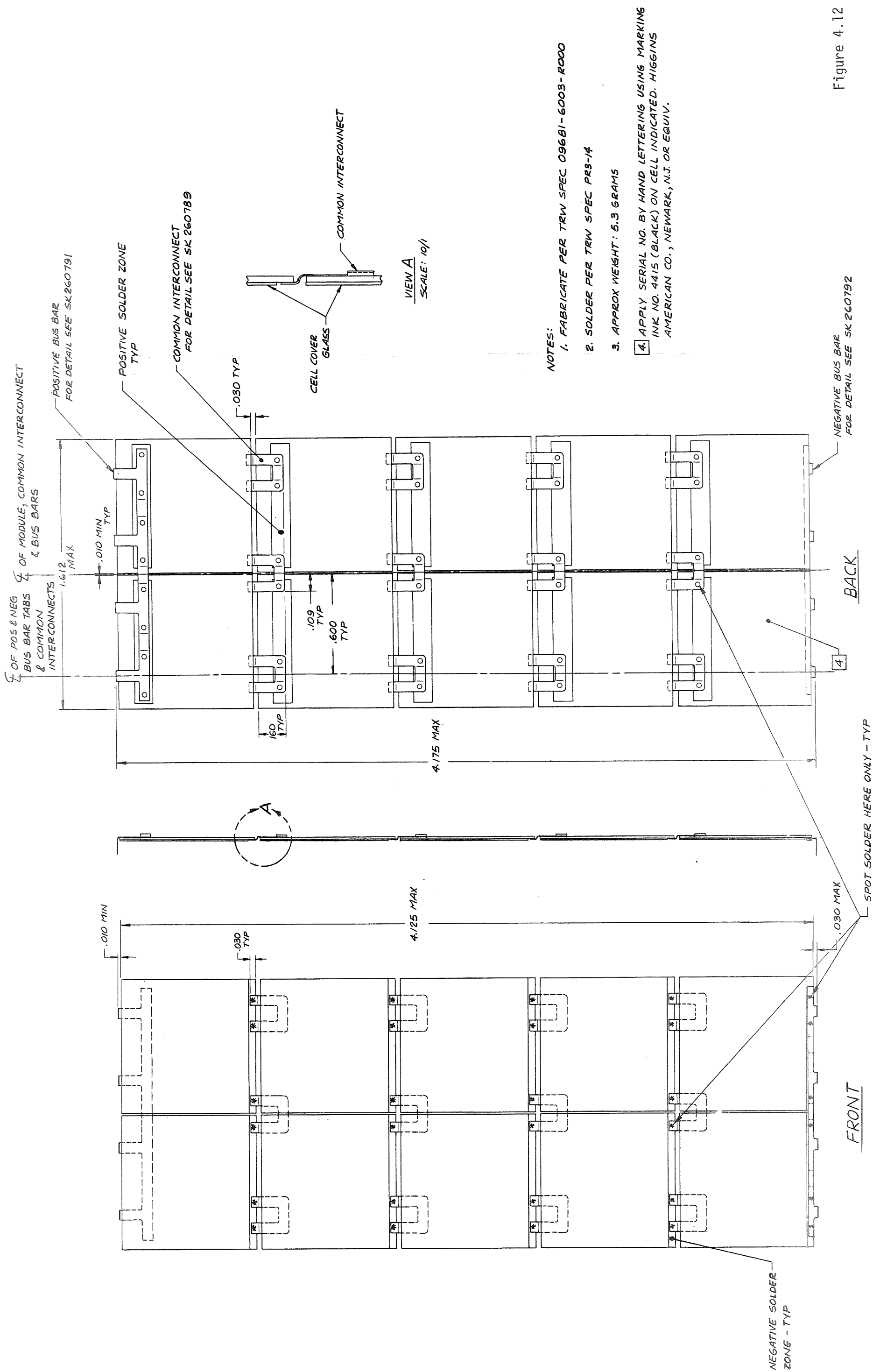
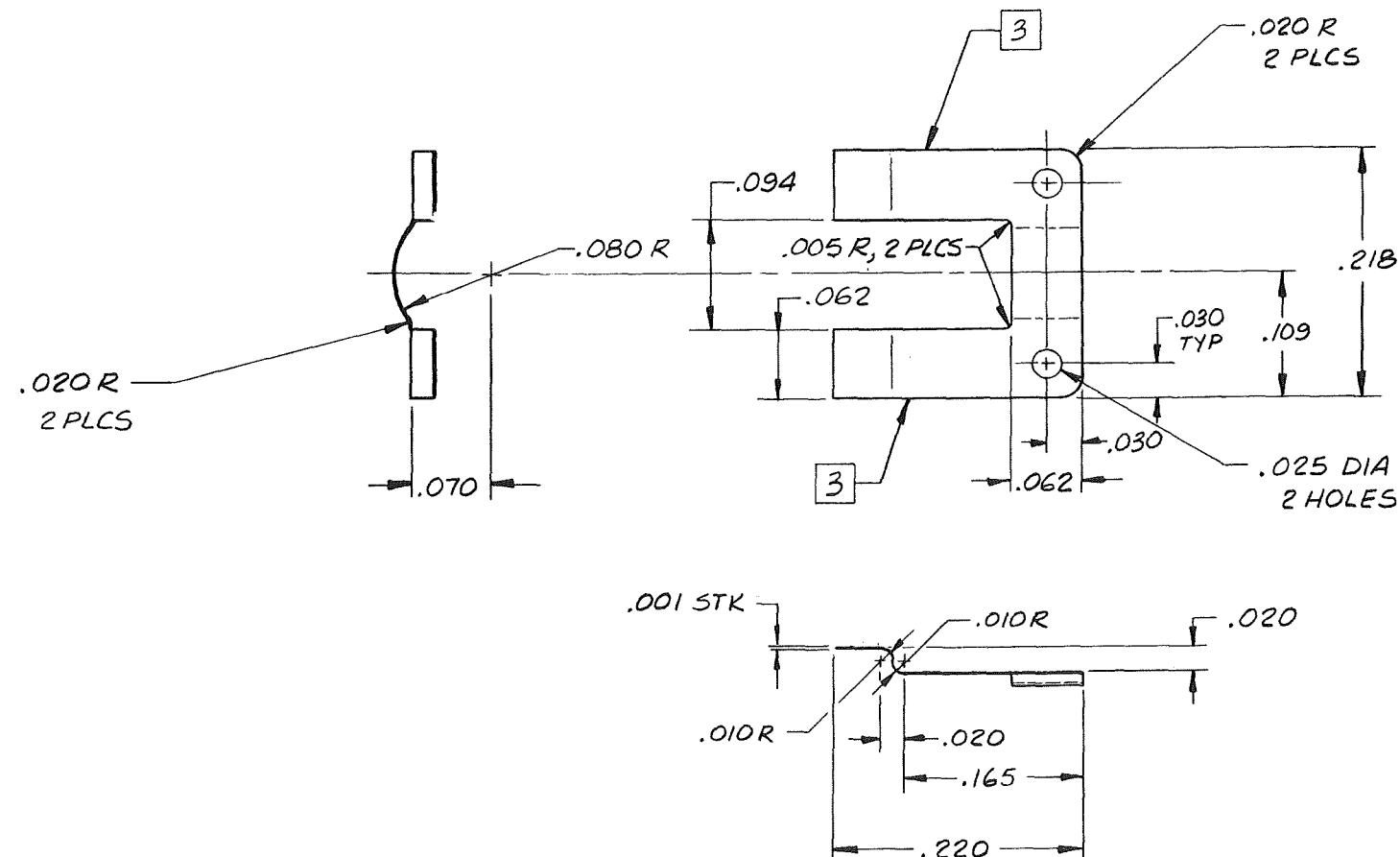


Figure 4.12

REVISIONS			
LTR	DESCRIPTION	DATE	APPROVED

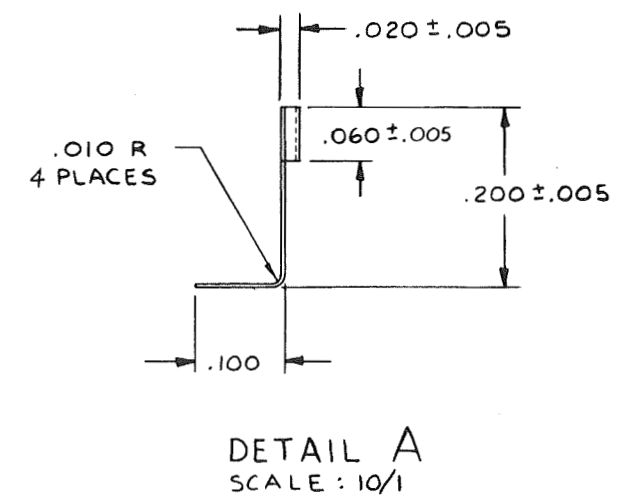
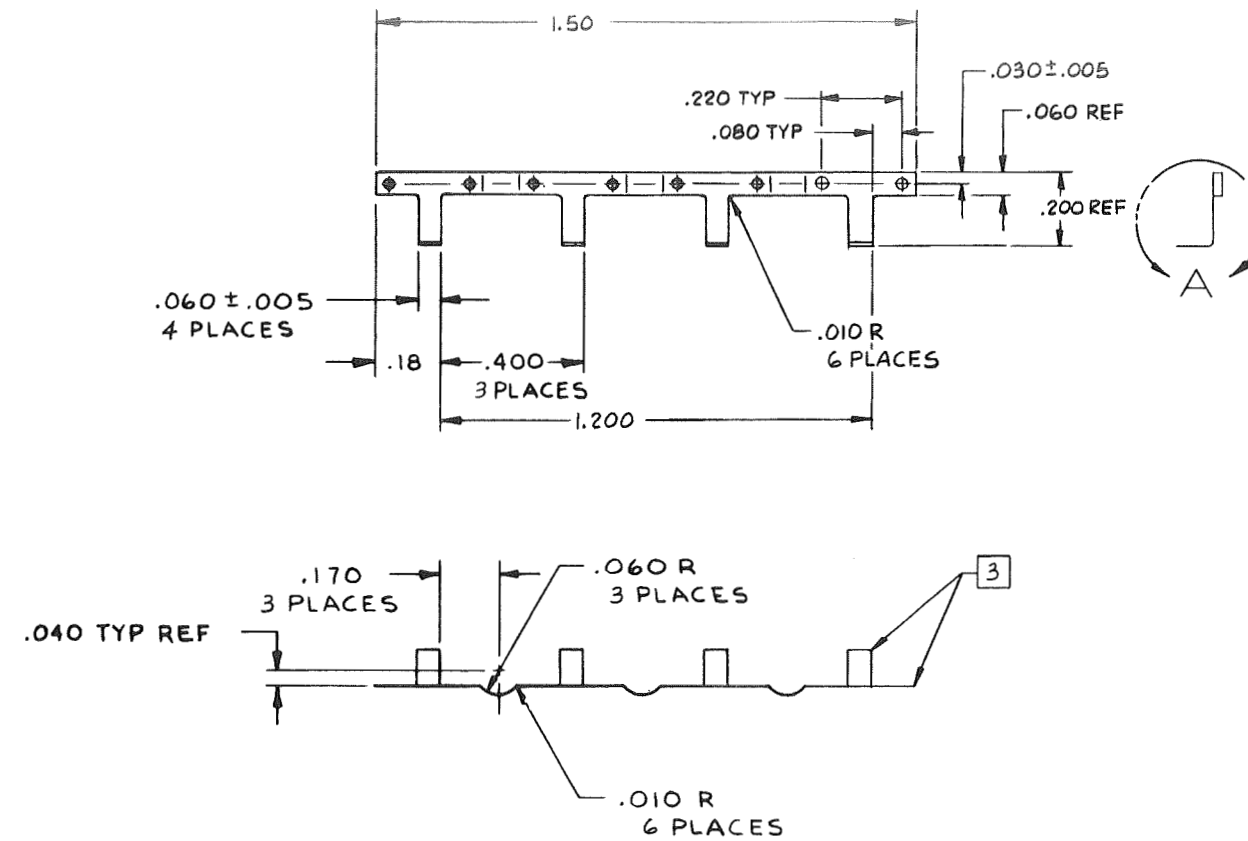


- 4 NO PHASE TRANSFORMATION SHALL OCCUR IN THE MATERIAL BETWEEN 1100°C AND -190°C.
- 3 ONLY PIECE PART SEPARATION EDGES MAY REMAIN UNPLATED.
- 2 SOLDER PLATE AND FUSE PER PR6-5-2, EXCEPT PARA 3.3 AND PARA 3.4.2 NICKEL STRIKE .00003 MAX AND COPPER PLATE .00005 TO .00015 PER MIL-C-14550 USING CYANIDE TYPE PYROPHOSPHATE OR ROCHELLE COPPER UNDER PLATING BATH. SOLDER PLATE .00008 TO .0002, MEASURED BEFORE FUSING.

1. IDENTIFICATION MARKING PER PR 12-1
TYPE 2 CLASS 1G
PART NUMBER _____

NOTES: UNLESS OTHERWISE SPECIFIED

SHALL OCCUR IN THE AND -190°C. ON EDGES MAY REMAIN			-1 INTERCONNECT .001-THK, IRON-NICKEL-COBALT ALY SHEET, CL-1 [4]			MIL-I-23011														
CODE IDENT NO.			PART OR IDENTIFYING NO.			NOMENCLATURE OR DESCRIPTION			MATERIAL			SPEC.			REF DES			ITEM NO.		
QTY REQD PER ASSY CONFIGURATION			PARTS LIST																	
FINISH 2			UNLESS OTHERWISE SPECIFIED 1. INTERPRET PER MIL-STD-100. 2. DIMENSIONS ARE IN INCHES 3. SURFACE TEXTURE SHALL BE 4. DIMENSIONS APPLY BEFORE PLATING OR CONVERSION COATING. 5. REMOVE BURRS & SHARP EDGES			DO NOT SCALE DRAWING CONTRACT NO.			THE FOLLOWING EQ'S HAVE BEEN ATTACHED TO THIS PRINT											
HEAT TREAT			TOLERANCES - ALL HOLE DIA			DRAWN D. SCOVILL 1/14/70			TRW SYSTEMS GROUP ONE SPACE PARK • REDONDO BEACH, CALIFORNIA											
			TOLERANCES ON DECIMAL DIMENSIONS: XXX ± .010 XX ± .03 X ± .1			CHECKED			STRUCTURES			INTERCONNECT, COMMON								
			TOLERANCES ON ANGULAR DIMENSIONS: MACHINED & LOCATING ± 0°30' FORMED ± 2° CHAMFERS ± 5°			SUPERVISOR J. BOETZ 27 JAN 70			MAT'L & PROCESS ENGR H. WELLS 21 JAN 70											
LSPS			PRG-5 PR 12-1			OTHER APPROVALS R. B. 1-27-70 J. K. 1-27-70			SIZE CODE IDENT NO. C 11982 SK 260790											
USED ON NEXT ASSY NEXT ASSY QTY REQD			APPLICABLE SPECIFICATIONS THE ABOVE TRW SYSTEMS GROUP SPECS FORM A PART OF THIS DRAWING						SCALE 10/1						SHEET					

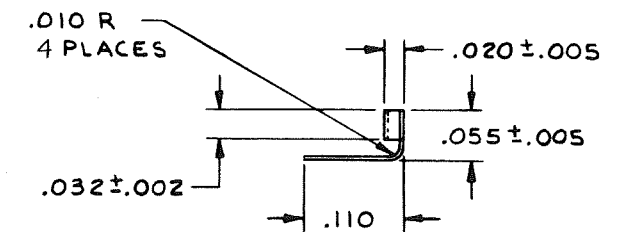
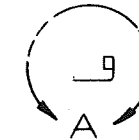
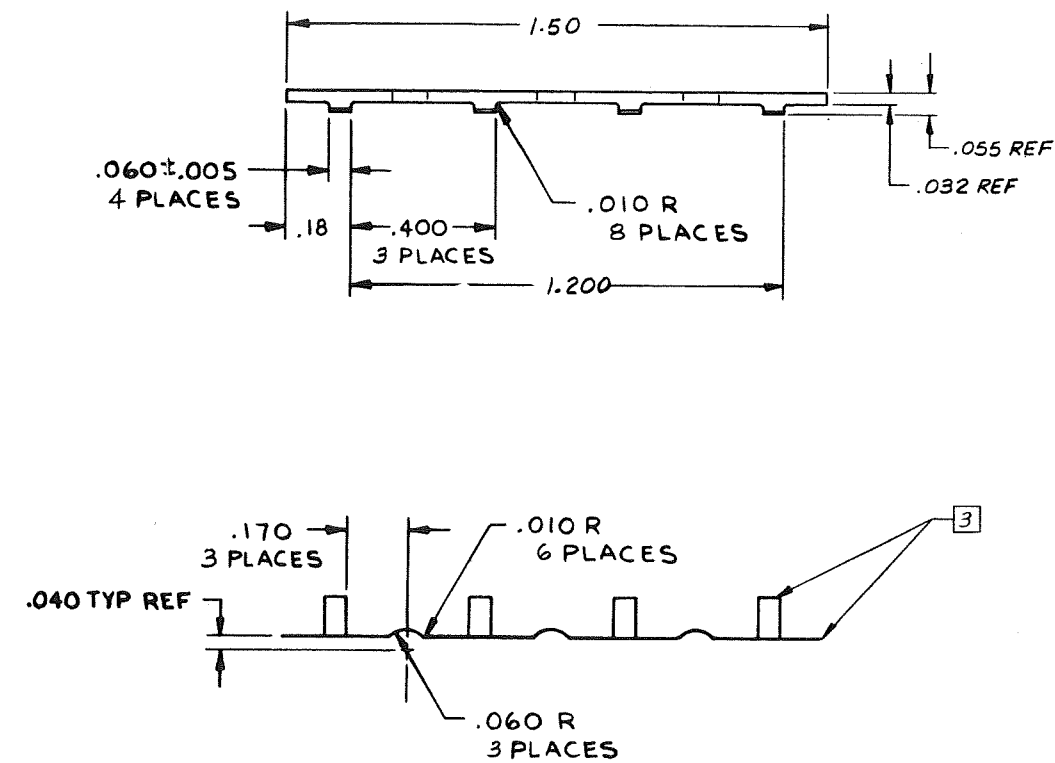


- ④ NO PHASE TRANSFORMATION SHALL OCCUR IN THE MATERIAL BETWEEN 1100°C AND -190°C
- ③ ONLY PIECE PART SEPARATION EDGES MAY REMAIN UNPLATED
- ② SOLDER PLATE AND FUSE PER PRG-5-2, EXCEPT PARA 3.3 AND PARA 3.4.2, NICKEL STRIKE .00003 MAX AND COPPER PLATE .00005 TO .00015 PER MIL-C-14550 USING CYANIDE TYPE PYROPHOSPHATE OR ROCHELLE COPPER UNDER PLATING BATH. SOLDER PLATE .00008 TO .0002, MEASURED BEFORE FUSING

1. IDENTIFICATION MARKING PER PR 12-1
TYPE 2 CLASS 10 PART NUMBER

NOTES: UNLESS OTHERWISE SPECIFIED

Figure 4.14



DETAIL A
SCALE: 10/1

- 4 NO PHASE TRANSFORMATION SHALL OCCUR IN THE MATERIAL BETWEEN 1100°C AND -190°C
- 3 ONLY PIECE PART SEPARATION EDGES MAY REMAIN UNPLATED
- 2 SOLDER PLATE AND FUSE PER PR6-5-2, EXCEPT PARA 3.3 AND PARA 3.4.2. NICKEL STRIKE .00003 MAX AND COPPER PLATE .00005 TO .00015 PER MIL-C-14550 USING CYANIDE TYPE PYROPHOSPHATE OR ROCHELLE COPPER UNDER PLATING BATH. SOLDER PLATE .00008 TO .0002 MEASURED BEFORE FUSING

1. IDENTIFICATION MARKING PER PR 12-1
TYPE 2 CLASS 1G PART NUMBER

NOTES: UNLESS OTHERWISE SPECIFIED

Figure 4.15

4.4.2 Critical Adhesive Material Properties

An assessment of the critical adhesive material properties revealed that only four parameters were of prime consideration. These were:

- ultimate tensile strength
- ultimate shear strength
- Young's modulus of elasticity
- coefficient of linear expansion

The shear modulus of elasticity was of lesser importance since torsional deflections are not involved in the low temperature induced spalling problem. Finally, thermal conductivity and dielectric strength were not considered critical properties for the failure mode under investigation.

The adhesive material properties to be obtained during this test program are outlined in Section 7.

4.5 MODULE MATERIALS

This section describes the various materials that comprise the elements which make up a solar array module substrate. The basic elements of the substrate are the facesheets, core (if utilized), frame, and dielectric insulator. The substrate materials evaluated during this Phase III program are described below.

4.5.1 Substrates

Cell spalling at low temperature can be induced by shrinkage action of an adhesive spot on the cell without attachment to a substrate. Because of this the mathematical model for cell stress analysis described in Section 5.2 does not contain effects of substrate thermal contraction. However, substrates identical to those of Phase II are included in the present module designs. The inclusion of these substrates provided identical conditions as existed in Phase II and permitted experimental determination of the effects, of the various substrates.

4.5.1.1 Fiberglass Lattice

This concept is similar to Engineering Test Model No. I as described in Section 6.1.1 of the Phase II Final Report (Reference 1.2) and consists of an aluminum extrusion box beam frame welded at the corner and fitted

with 0.007 thick fiberglass diaphragm. The diaphragm was epoxy bonded to one side of the box beam frame under a preload and capped with an aluminum strip which was bonded and riveted in place.

The solar cells were arranged in rows on the diaphragm. (Figure 7.1).

4.5.1.2 Kapton

The substrate for this concept corresponds to the flexible portion of Engineering Test Model No. II as described in Section 6.1.2 of the Phase II Final Report (Reference 1.2) and consists of a sheet of 0.003 thick "Kapton" polyimide plastic. As a non-conductor, the silicon cells may be bonded directly to it.

The Kapton sheet was bonded to edge frames of aluminum. Although not identical to the flight concept, the frames were included in the test model for convenience in handling of the flexible array and to conduct the structural dynamic vibration tests.

4.5.1.3 Graphite Composite

This concept was identical to the Engineering Test Model No. III, as described in Section 6.1.3 of the Phase II Final Report, (Reference 1.2) and consists of a conventional aluminum honeycomb core with high-modulus graphite fiber facesheets. The graphite fibers are cross-plyed in two layers to provide the necessary bi-directional stiffness. Each ply of the graphite is approximately 0.003 inch thick. A fiberglass scrim cloth, 0.003 thick, is required between the two plies to distribute differential thermal expansion stresses which occur during curing. The two plies plus the scrim give a facesheet thickness of approximately 0.009 inch.

4.5.1.4 Aluminum

This concept corresponds to the rigid end plate portion of Engineering Test Model No. II, as described in Section 6.1.2 of the Phase II Final Report (Reference 1.2). As stated in the report, the aluminum honeycomb core, aluminum facesheet concept is not considered a likely structural concept for weight effectiveness; therefore, a test module with this substrate concept will not be fabricated. However, the characteristics of the material were included in the material tables as a baseline for comparison.

4.5.2 Dielectric Insulation

The solar cells contain electrical connection points on both their front and back faces. These consist of zones with a thin solder coating. The interconnect straps are soldered to these areas. The interconnect straps are designed with loops to the adjacent cells. The purpose of the loops is to provide for differential thermal expansion between the cells and the substrate. Thus, the solder and strap combinations form protrusions from the flat backside of the cell. These protrusions must be kept electrically insulated from each other to prevent circuit shorting.

Some types of substrates are self-insulating by the nature of their construction material, whereas other types of substrates consisting of metallic or conductive materials require coatings or films between the substrate and cell interconnects.

4.5.2.1 Fiberglass/RTV Silicone

The fiberglass substrates are by their nature in the class of self-insulating material. No coatings or films are required between the substrate and cell interconnects. On this type of substrate, the only requirement is to provide space between the substrate surface and the backside of the cell to accommodate the interconnect loops. This is accomplished by bonding the cell to the substrate with an RTV silicone elastomer spot of sufficient thickness to provide the clearance necessary.

4.5.2.2 Kapton Film

The Kapton film insulation method is applicable to the class of substrates that are electrical conductors. These include aluminum or other metallics, and graphite or boron fiber composites. This latter category may be self-insulating if the matrix resin has formed a sufficiently thick coating on the conductive fibers; however, as the laminates are designed with a minimum amount of resin to achieve structural coherence, self-insulation may not be achieved, and a positive insulating film or coating would be required.

In this method, a 0.001 thick Kapton polyimide film is perforated with holes slightly larger than the diameter of the cell bond spot. The holes are located in a regular pattern to coincide with the centers of the cells in the array. The film is laid onto the substrate, and the

cells are bonded with RTV through the holes to the substrate beneath. No other adhesive is used to retain the trapped film.

5. CELLSTACK DESIGN ANALYSES

The failure modes that were experienced by the cellstack during the Phase II environmental testing fell into two broad categories, namely:

- failures due to structural dynamic induced loads
- failures due to thermal-vacuum induced loads

The types of failures and the technical approach taken to eliminate them during this Phase III Program are summarized below.

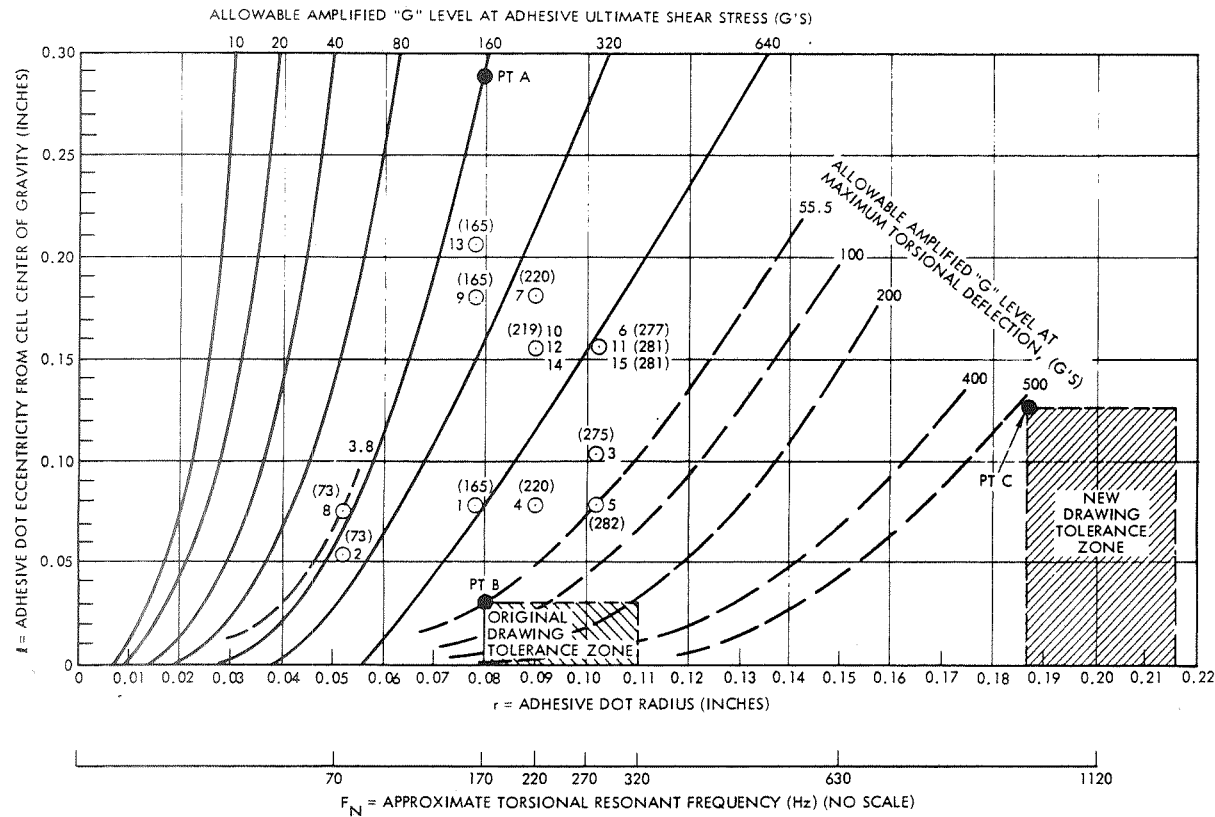
5.1 STRUCTURAL DYNAMIC INDUCED LOADS

The structural dynamic induced loads caused four basic types of failures. These were:

- cracking of the silicon cells due to excessive torsional deflection
- yielding of interconnect expansion loops
- breakage of interconnect expansion loops
- shear failure of the single RTV adhesive spot due to out-of-tolerance diameter and/or eccentric location

An evaluation of these failures was carried out during Phase II and documented in Section 8.4.4 of Reference 1.2. As a result of this analysis, a design criteria was established for the silicon cell adhesive dot diameter. This is shown in the Figure 5.1 Adhesive Dot Design Chart. From this chart, it was established that any adhesive spot diameter greater than 0.400 inches would be adequate to meet the structural dynamic induced loads (torsional shear and deflection). However, for this Phase III Program, in order to evaluate the Phase II failure modes, a range of adhesive spot diameters were selected for the Adhesive Bond Geometry Matrix (see Figure 7.1) including values less than 0.400 inches. The adhesives spot diameters are designated by percent area on Figure 8.1. The equivalent nominal diameters are as follows:

<u>% Area</u>	<u>Nominal Diameter, inches</u>
8%	0.250
18%	0.375
32%	0.500
70%	0.750



LEGEND:

CELL WEIGHT, $W = 0.001$ LBTRANSMISSIBILITY, $T_R = 5$ ULTIMATE SHEAR STRESS, $S_{SULT} = 325$ PSIMAXIMUM ALLOWABLE DEFLECTION, $\theta_{MAX} = 0.025$ RADIAN

MINIMUM CELL CLEARANCE = 0.010 INCHES

○ = l AND r VALUES FOR 15 ETM I FAILED CELLS
WITH F_N INDICATED (XXX)

— SEE TABLE B.1 OF APPENDIX B

- - - SEE TABLES B.2 AND B.3 OF APPENDIX B

Figure 5.1 Silicon Cell Adhesive Dot Design Chart

The use of this broad range of adhesive spot diameters permitted an in-depth assessment of adhesive bond geometries for both the thermal-vacuum testing and the structural dynamic induced loads.

To further minimize the possibility of interconnect and solder joint failure, the interconnector was redesigned for this program phase. This redesign and the technical reasons for its selection are outlined in Section 4.3.4.

5.2 THERMAL-VACUUM INDUCED LOADS

Silicon solar cells (primarily zone-soldered) resulted in a high rate of spalling type failures when subjected to -160°C and lower temperature testing of the interface between the adhesive dot and the silicon cell. This type of failure was the most predominant during testing of the Engineering Test Models at NASA/MSFC and was subsequently reproduced in a test program conducted at TRW Systems during Phase II.

The thermal-vacuum induced loads caused spalling or "pull-out" of the silicon or SiO coating from the underside of the silicon cells. This failure mode was common to all three ETM's and appeared to be independent of substrate facesheet material. However, during the Phase II testing, cell spalling failures occurred only with the zone-soldered cells. No difficulties of this type were experienced with the fully solder backed cells or the simulated aluminum chips. It is postulated that these spalling failures were the result of a large mismatch between the coefficients of expansion of the silicon cells, the adhesive, and possibly the substrate materials.

For example, G.E. RTV 511/577 (50-50 mix) has a coefficient of linear expansion of 72.5×10^{-6} in/in/ $^{\circ}\text{C}$ between -100°C and -180°C . Assuming this value is similar for RTV 3145 (used during Phase II), a thermal differential expansion between the adhesive and silicon of 0.0076 in/in would occur over a temperature range of -65°C to -173°C . This is based upon the silicon cell exhibiting a coefficient of expansion of 3×10^{-6} in/in/ $^{\circ}\text{C}$ at 0°C and declining to a value of zero at -173°C . These properties and conditions could induce high tensile stresses at the circumferential interface between the outer diameter of the adhesive dot and the plane of the underside of the silicon cell. These tensile stresses can be of sufficient magnitude to cause cracking at the interface and

eventually spalling will occur. The analytical model described in Section 5.2.1, combined with a TRW Systems computer program was used to predict this failure mode. During this Phase III program an effort was made to obtain experimental confirmation of this failure mode as a function of various types of adhesives, adhesive bond geometries, and cellstack material properties. This has been reported in Section 10.3.

5.2.1 Analytical Model

To obtain further insight into the failure mechanism a study was conducted to estimate these thermally induced stresses. During Phase II of this program it was noted that the spalling failures occurred only in those cells which were bare or SiO back-coated and appeared to be independent of bond diameter and substrate geometry or material. The model, Figure 5.2, therefore utilizes only a 0.008" thick 2 x 2 cm. cell and a 0.25 in. diameter by 0.020 in. thick adhesive spot. Division of the model into the discrete sections shown was selected to obtain the maximum benefit of a finite element difference computer program.

5.2.2 Basic Assumptions

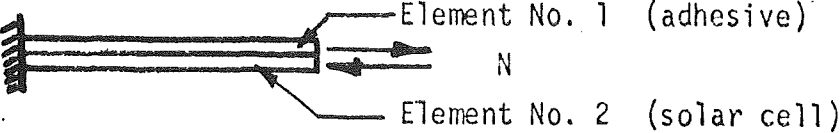
The program used was a two dimensional, linear, thermal elastic routine of handling 550 elements and therefore was well suited to investigate local stress distributions within planar structures. The assumption of a two dimensional model representing a radial section thru a three dimensional stress problem is rational considering the need to identify critical parameters and their interactions.

Available data on the modulus of elasticity of class 500 silicon rubbers (RTV) terminate at -84°C with indicated brittle points below -101°C. To be able to run the program a conservative estimate of 0.5×10^6 psi was taken for the adhesive's modulus. A summary of the material properties assumed for this analysis at -173°C is tabulated below:

	E (psi)	α (in/in/°C)	α_{UTS} (psi)
Silicon cell	16.1×10^6	1.5×10^{-6}	19,000
RTV Adhesive	0.5×10^6 (est)	163×10^{-6}	Variable

A comparison between these values and those determined experimentally during this program are given in Section 7 and confirm their conservative levels.

No attempt was made initially to parametrically study the effects of adhesive diameter or thickness on the stress distribution or its peaking magnitude. Potential contributions were inferred by considering the simple analogy of a bimetallic strip and its classical load equation. Subsequently, it was found desirable to conduct limited parametric analyses and these are reported in Paragraphs 5.2.4 and 5.2.5 of this section.



$$N = \frac{\alpha_1 - \alpha_2 (\Delta T)}{\frac{1}{t_1 E_1} + \frac{1}{t_2 E_2}} \quad \text{(pound per inch width)}$$

The average load (N) induced in each element is directly proportional to the difference in coefficients of expansion ($\alpha_1 - \alpha_2$) and related to the stiffness ration (tE) of the materials involved. Thus, in theory, a reduction in adhesive thickness would be one geometric technique to lower thermal stresses. Additional benefits could be realized by selection of an adhesive that exhibits larger flexibility (low modulus of elasticity) at the minimum (-173°C) operating temperature involved.

5.2.3 Failure Mode and Effects Analysis

The results of the computer run are shown in Figures 5.3 and 5.4. Figure 5.3 depicts the silicon cell axial stress distribution adjacent to the adhesive/cell interface, and Figure 5.4 shows the effective stress in the same region using Von Mises Shear Distortion Theory (Reference 5.1) to combine axial, normal, and shear stresses. The high local peaking stresses at the edge of the adhesive dot interface, are typical of those found in any lap joint subjected to axial loads.

The magnitude of the theoretical peaking tensile stress (70800 psi at the 0.00017 level) in the silicon cell, whose allowable ultimate tensile stress is 19,000 psi, is sufficient to cause the type of failure as witnessed by the previous Phase II testing. It was concluded based upon this

analysis, that spalling type failures at temperatures at -160°C and lower are induced primarily by adverse material properties of the adhesive.

5.2.4 Sensitivity of Cell Spalling Failures to Thermally Induced Loads

It was found that the experimentally determined values of the modulus of elasticity (E) and the coefficient of linear expansion (α) for the various candidate adhesive materials varied over a considerable range (see Tables 7.3 and 7.4). For example, one of the most promising adhesives selected to minimize thermally induced loads was RTV 3145. This had an experimentally determined modulus of elasticity that ranged from less than 0.4×10^5 to 1.0×10^5 psi at -173°C . It also had a variation in coefficient of linear expansion of from 130×10^{-6} to 2.4×10^{-6} in/in/ $^{\circ}\text{C}$ for a temperature range between 20°C and -173°C . In view of this, a stress analysis of the silicon cell based upon this range of material properties was made to determine the sensitivity of the stress levels to these parameters. The same finite difference computer model as was delineated in Reference 1.5 was used.

Results of these computer runs have been plotted in Figure 5.5 for both the original estimated properties and the newly obtained experimental values. As can be noted, the peak stress levels drop off sharply with reduced adhesive modulus of elasticity. Hence, the possibility of spalling is closely coupled to the actual value of this parameter. If this value varies considerably from batch to batch on a given adhesive it could result in spalling taking place in some instances and not in others.

Figure 5.6 presents the axial and effective stress distributions through the thickness of the cell at the critical interface radius for an arbitrary adhesive modulus of elasticity of 1×10^5 psi. Both figures 5.5. and 5.6 show the highly localized effect of the maximum stress peaking and suggests the possibility of even higher surface stresses at values computed at distances of less than 0.00017 inches from the surface. A new computer model would be required to determine this, which was beyond the scope of this program phase.

Figure 5.7 was plotted using data from the computer runs and the bimetallic strip analogy equation indicated in Para. 5.2.2. This equation

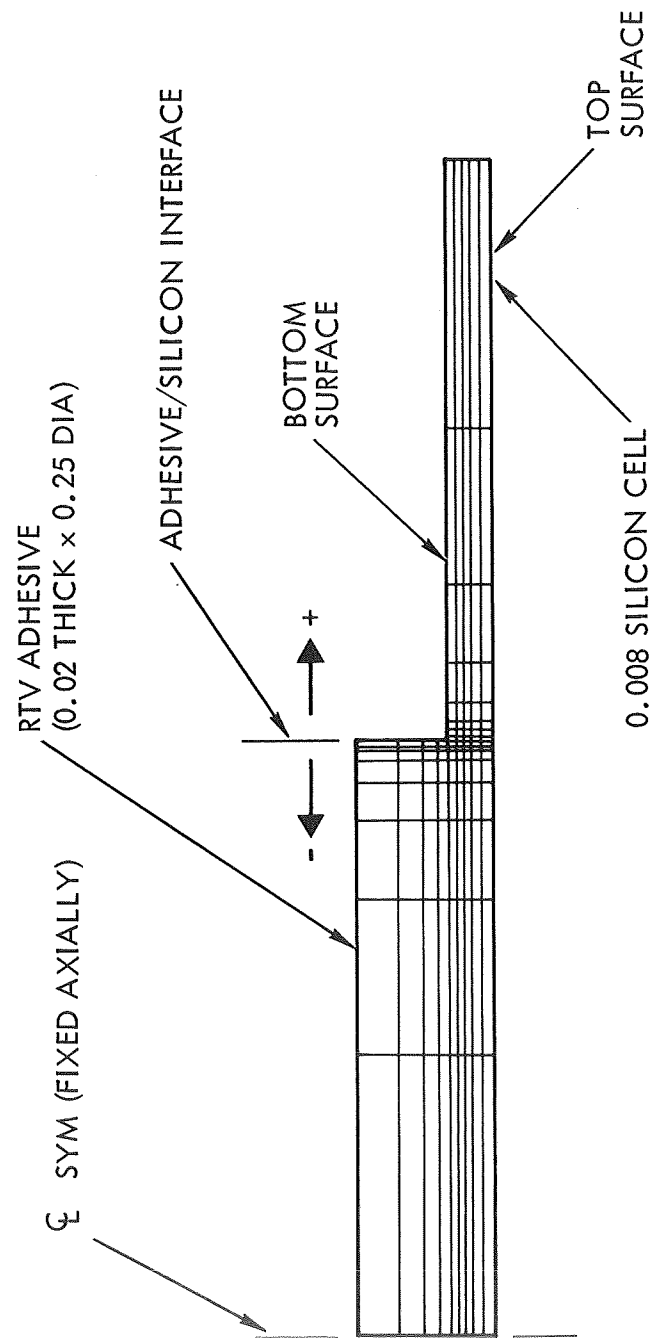
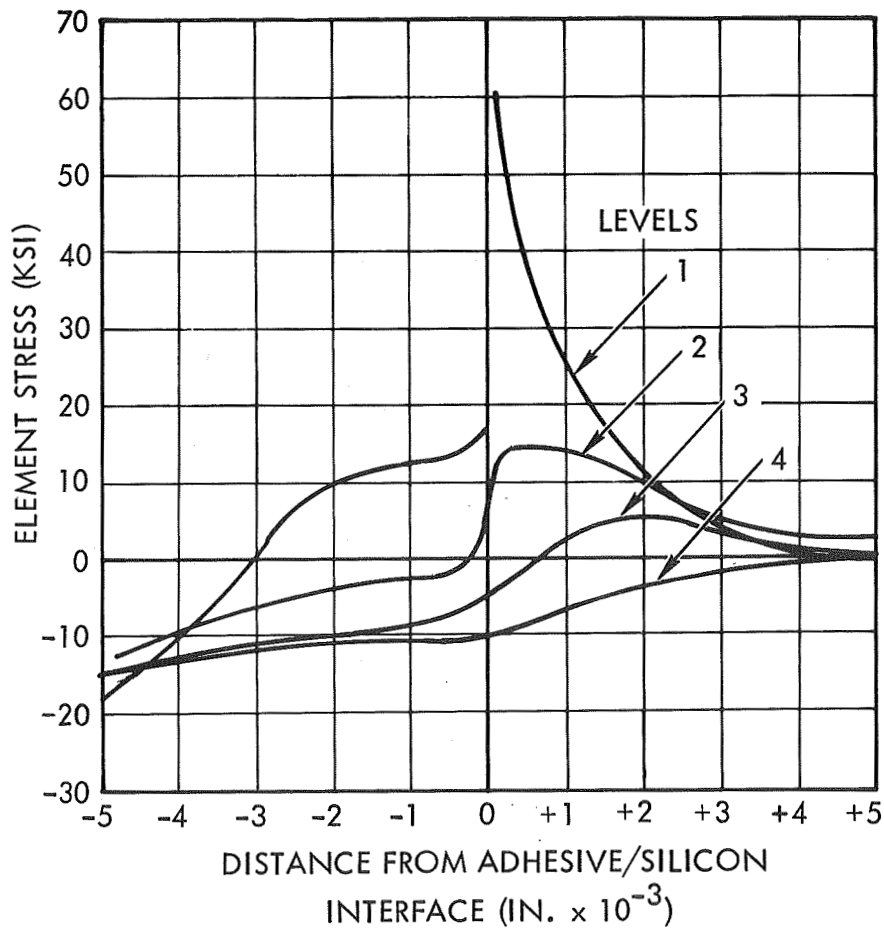


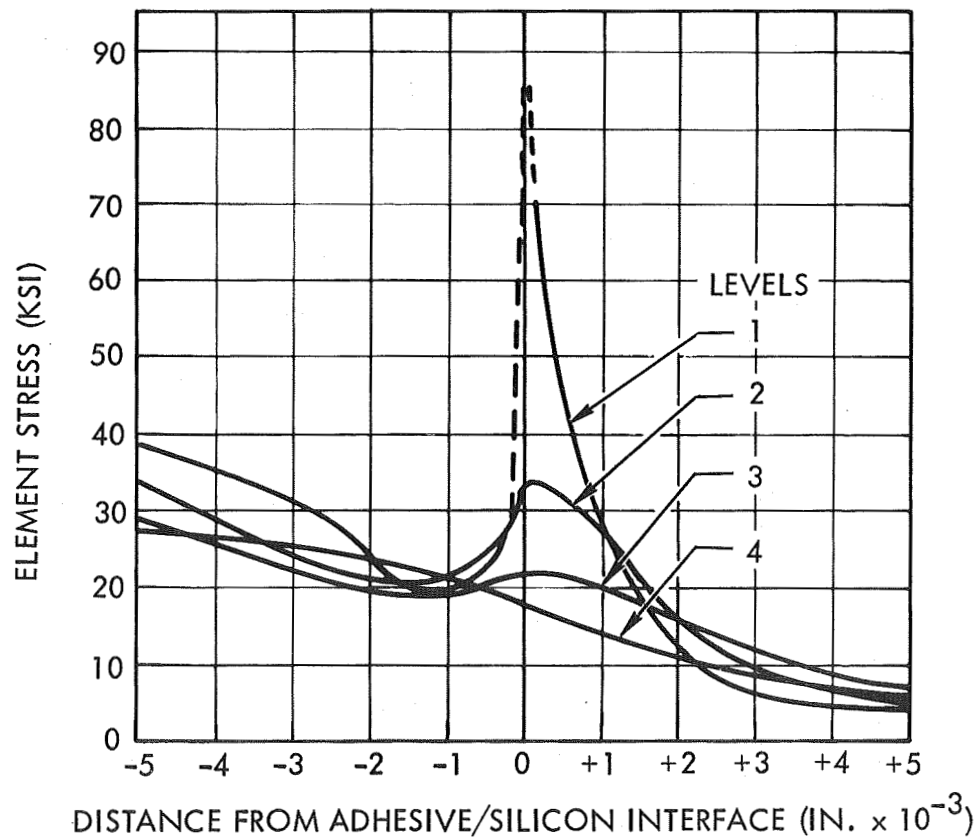
Figure 5.2 Model for Computer Analysis



LEVEL 1 IS 0.00017 FROM SURFACE
 2 IS 0.00067 FROM SURFACE
 3 IS 0.00133 FROM SURFACE
 4 IS 0.00267 FROM SURFACE

$E_2 = 0.5 \times 10^6$ PSI
 $\alpha_2 = 163 \times 10^{-6}$ IN/IN/ $^{\circ}$ C
 $t_2 = 0.020$ IN.

Figure 5.3 Silicon Cell Axial Stress Distribution



LEVEL 1 IS 0.00017 FROM SURFACE

2 IS 0.00067 FROM SURFACE

3 IS 0.00133 FROM SURFACE

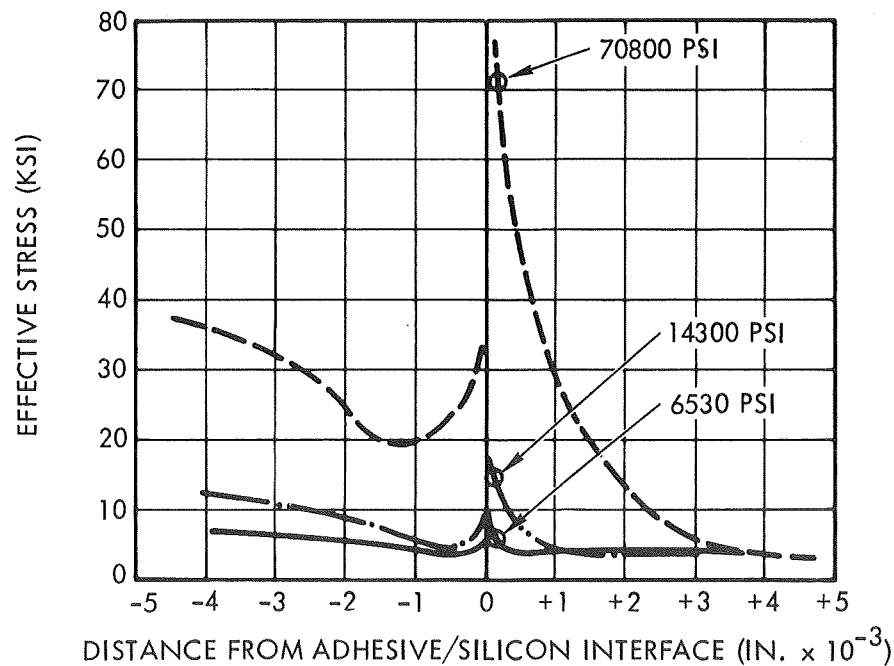
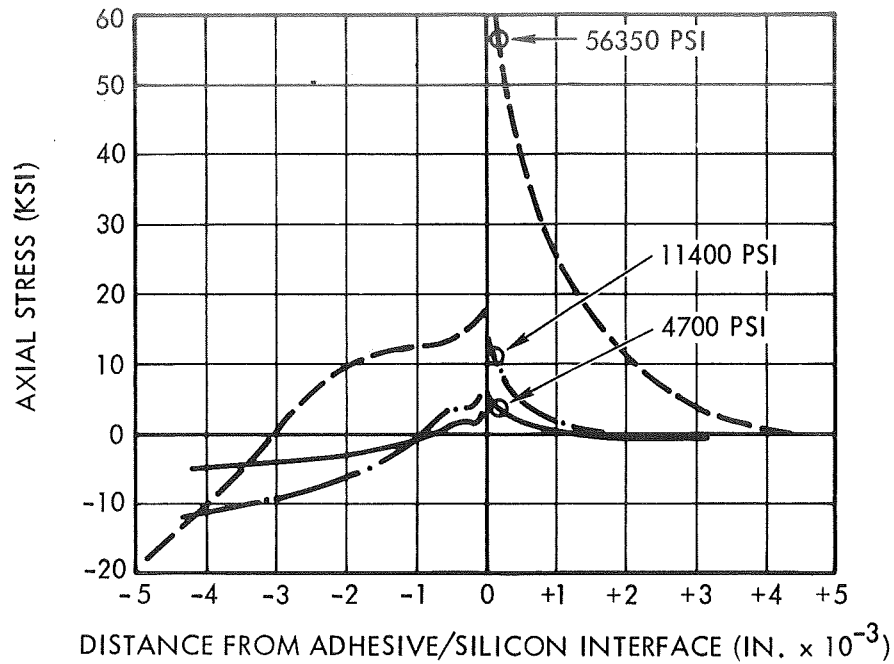
4 IS 0.00267 FROM SURFACE

$$E_2 = 0.5 \times 10^6 \text{ PSI}$$

$$\alpha_2 = 163 \times 10^{-6} \text{ IN/IN/}^\circ\text{C}$$

$$t_2 = 0.020 \text{ IN.}$$

Figure 5.4 Silicon Cell Effective Stress Distribution



LEGEND:

- RTV MODULUS AT 0.5×10^6 PSI
- · - RTV MODULUS AT 0.1×10^6 PSI
- RTV MODULUS AT 0.4×10^5 PSI

Figure 5.5 Longitudinal Silicon Cell Stress at a Level 0.00017 Inch from Interface Surface

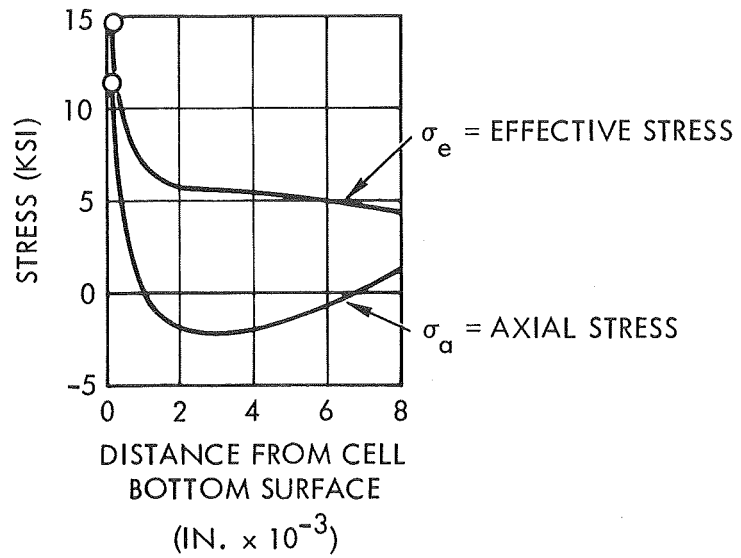


Figure 5.6 Stress Distribution Through Solar Cell Thickness - Modulus of Elasticity of Adhesive = 1×10^5 psi

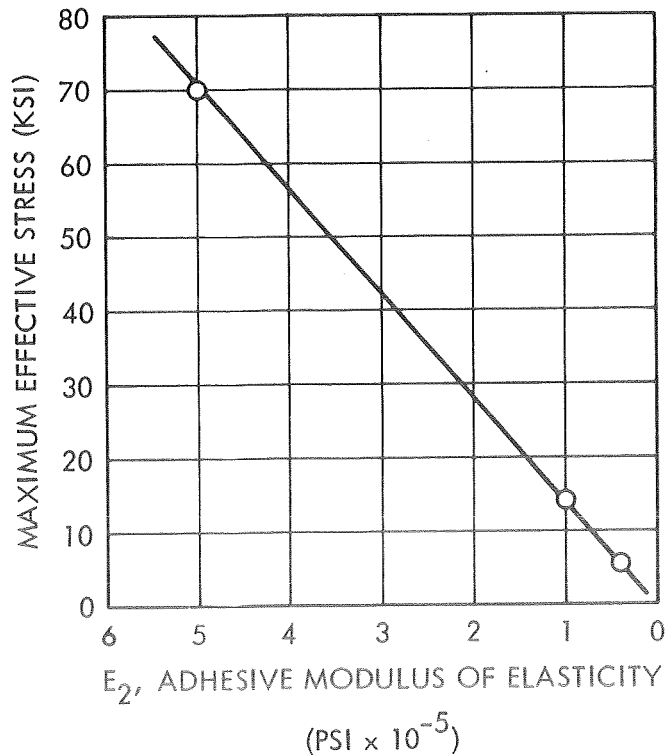


Figure 5.7 Effect of Adhesive Modulus of Elasticity on the Maximum Computed Stress

may be rewritten to obtain the change in cell stress due to a change in adhesive modulus;

$$\frac{\delta N}{\delta E_2} = \frac{1}{1 + \frac{E_1}{E_2}}$$

where all the other parameters are held constant. The plot of Figure 5.7 uses the computed peak effective stress for $E_2 = 1 \times 10^5$ psi as a focal point and shows close agreement for stresses at the other selected moduli for the range under consideration. Thus, this equation can be used to extrapolate the parametric effect of material property changes once the peaking stress has been determined by a computer analysis.

5.2.5 Additional Parametric Analyses of Spalling Failures

The initial investigation of silicon/RTV thermal stress was completed and documented in Paras. 5.2.1 to 5.2.3. An additional analysis to investigate the effects of RTV stiffness (E_2 , Young's Modulus) on silicon cell stresses was also completed and the results summarized in Para. 5.2.4. These studies predict the occurrence of stresses in the silicon higher than the ultimate tensile strength, of 19,000 psi, at -173°C . The highest stress occurred at the edge of the RTV dot due to shear lag of the differential expansion thermal load. This phenomenon is typical of a bimetallic strip, in which the thermal load, N , can be expressed by the following equation:

$N = \frac{(\alpha_1 - \alpha_2) \Delta T}{\frac{1}{E_1 t_1} + \frac{1}{E_2 t_2}}$	α_1, E_1, t_1 are properties of silicon
$N = [\text{lb. load/in. width}]$	α_2, E_2, t_2 are properties of RTV
$\alpha \Delta T = [\text{in/in thermal strain}]$	ΔT is uniform temperature re- lative to room temperature = $(-173^\circ\text{C} - 20^\circ\text{C}) = -193^\circ\text{C}$
$Et = [\text{lb/in stiffness per1" wide strip}]$	

The silicon stress, f , is directly related to the thermal load, N , and should be relatively insensitive to overall geometry, because of the local nature of the highest stress (see Figures 5.3, 5.4 and 5.5). The ratio of maximum effective stress to thermal load is defined as a constant, γ , which is discussed in References 1.4 and 1.5. The stress is found by using the TRW Systems AS 165 Plane Strain Finite Element Program. This program utilizes an elastic matrix solution to solve the strain compatibility relationships for a grid of triangular elements.

The constant, $\gamma \equiv f/N$, is summarized in Table 5.1, below for the cases previously investigated:

Table 5.1 - Silicon Stress Summary

Case	RTV - E_2 (10^6 psi)	RTV - α_2 (10^{-6} in/in/ $^{\circ}$ C)	N , lb/in	f , psi*	$\gamma \equiv f/N$
1	0.50	141	249.8	70800	284
2	0.10	122	45.8	14300	312
3	0.04	122	18.5	6500	351
*NOTE: These maximum effective stresses are taken at a position near the edge of the RTV dot circle, at a distance .00017 inch inside the edge surface.					

These results are based on the following supplementary data:

$$\begin{aligned} \Delta T &= -193^{\circ}\text{C} & E_1 &= 16.1 \times 10^6 \text{ psi} \\ t_2 &= .020 \text{ in} & \alpha_1 &= 1.5 \times 10^{-6} \text{ in/in}/^{\circ}\text{C} \\ & & t_1 &= .008 \text{ in} \end{aligned}$$

5.2.5.1 Scope of Parametric Study

This investigation of silicon cell stress versus RTV adhesive properties at -173°C was conducted for the following range of variables for the adhesives:

$t_2 = 0.005$ to 0.020 inch thickness

$E_2 = 0.04$ to 0.50×10^6 psi Young's Modulus

$\alpha_2 = 1.8$ to 220×10^{-6} in/in/°C thermal expansion coefficient

The range of Young's Modulus and thermal expansion coefficient for the adhesive bond (an elastomer compound) was intentionally large to account for the extreme temperature sensitivity of its mechanical properties to low temperatures. The thermal stress level in the silicon is dependent on the average value of the particular adhesive mechanical property (averaged over the temperature range of +20 to -173°C).

The solution for silicon stress was accomplished using a time-share program to solve the following simplified equation, with $\gamma(N_0)$ plotted in Figure 5.8.

$$f = [N_0] [\gamma(N_0)] \left[\frac{1 - \beta}{1 + \eta} \right] \quad \left| \begin{array}{l} N_0 = \alpha_2 E_2 t_2 (-\Delta T) \\ \beta = \alpha_1 / \alpha_2 \\ \eta = t_2 E_2 / t_1 E_1 \end{array} \right.$$

5.2.5.2 Results of Analyses

The maximum effective stress in the silicon cell versus adhesive thickness, Young's Modulus, and thermal expansion coefficient have been plotted in Figures 5.9, 5.10, 5.11, 5.12, and 5.13.

Values representing the maximum combined limits for adhesive mechanical properties (averaged over the temperature range of +20 to -173°C) which will not exceed the silicon strength of 19000 psi are summarized in Table 5.2.

The acceptable temperature - averaged mechanical properties for the adhesive represents material property controls that must be imposed on the adhesive bond to prevent silicon failure at -173°C. Future programs should consider material tests designed to determine the process control variables affecting adhesive stiffness and expansion coefficient at low temperatures. These variables should then be controlled to maintain the temperature - averaged properties at acceptable values for the

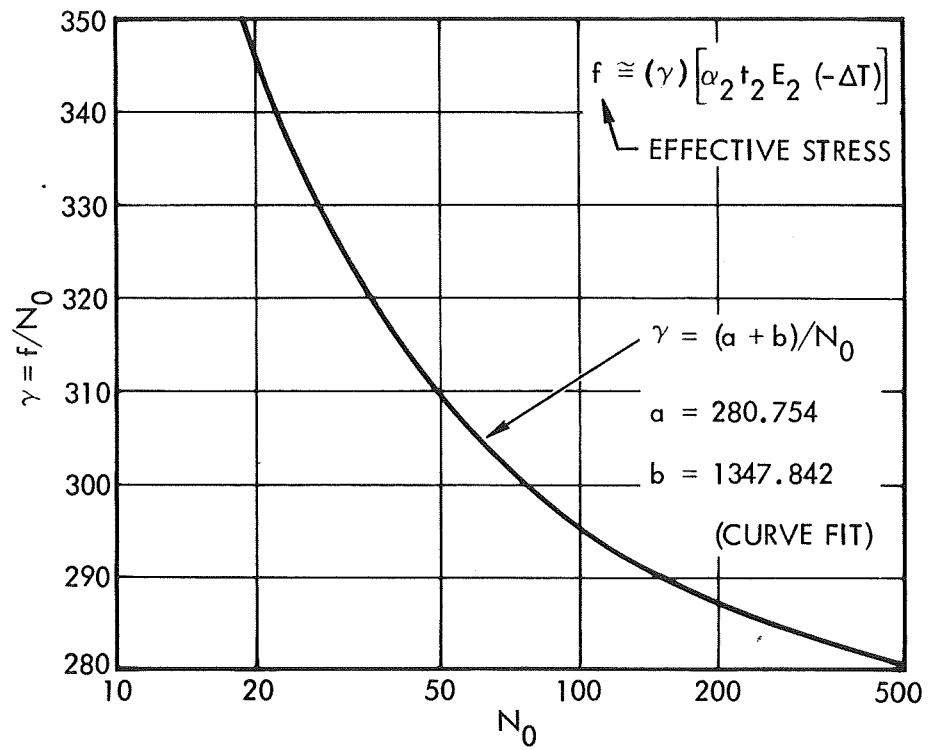


Figure 5.8 Plot of Function $\alpha = f/N_0$ for Simplified Stress Equation

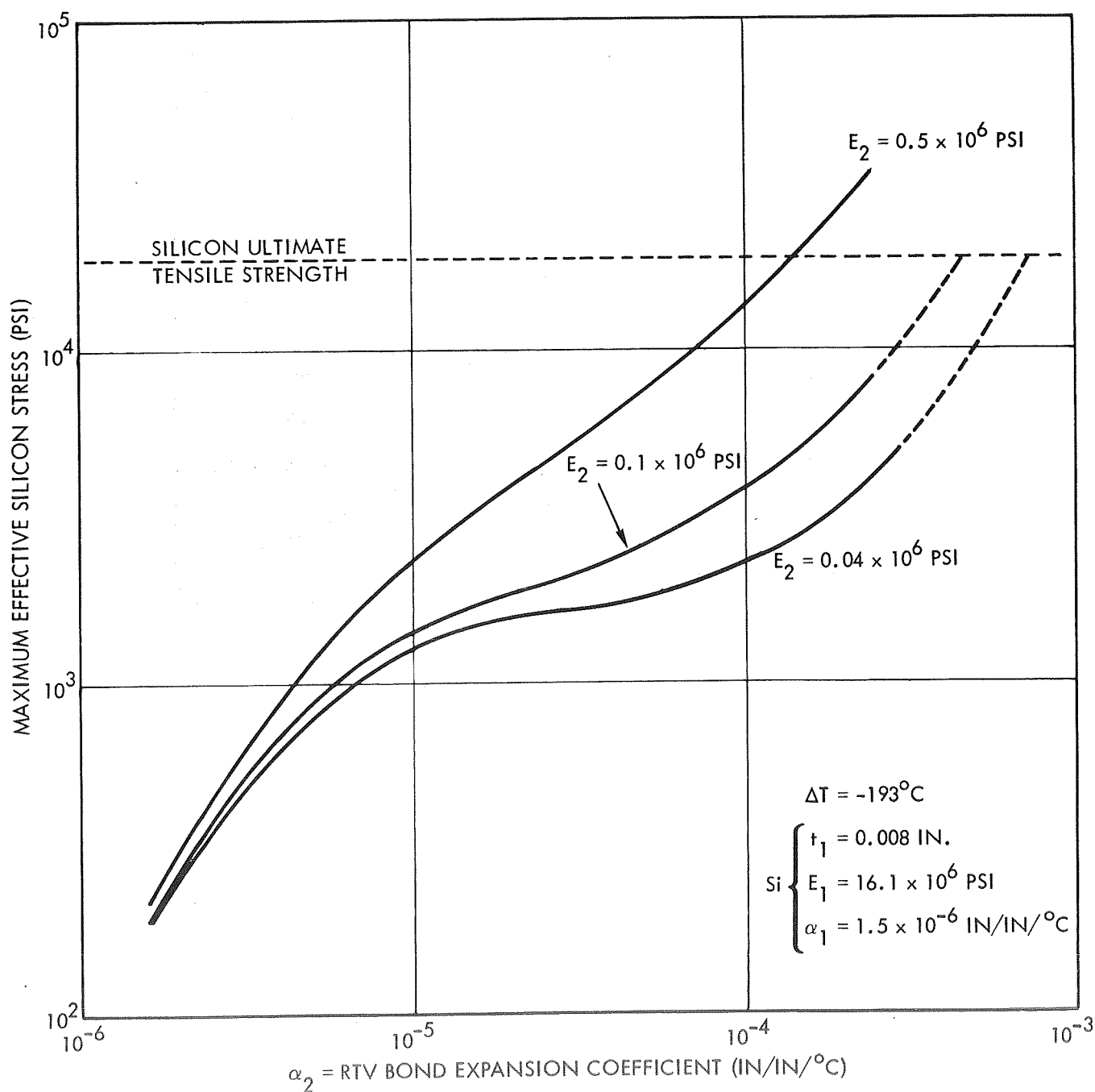


Figure 5.9 Silicon Thermal Stress - RTV Adhesive Thickness,
 $t_2 = 0.005$ in., at 0.00017 Stress Level

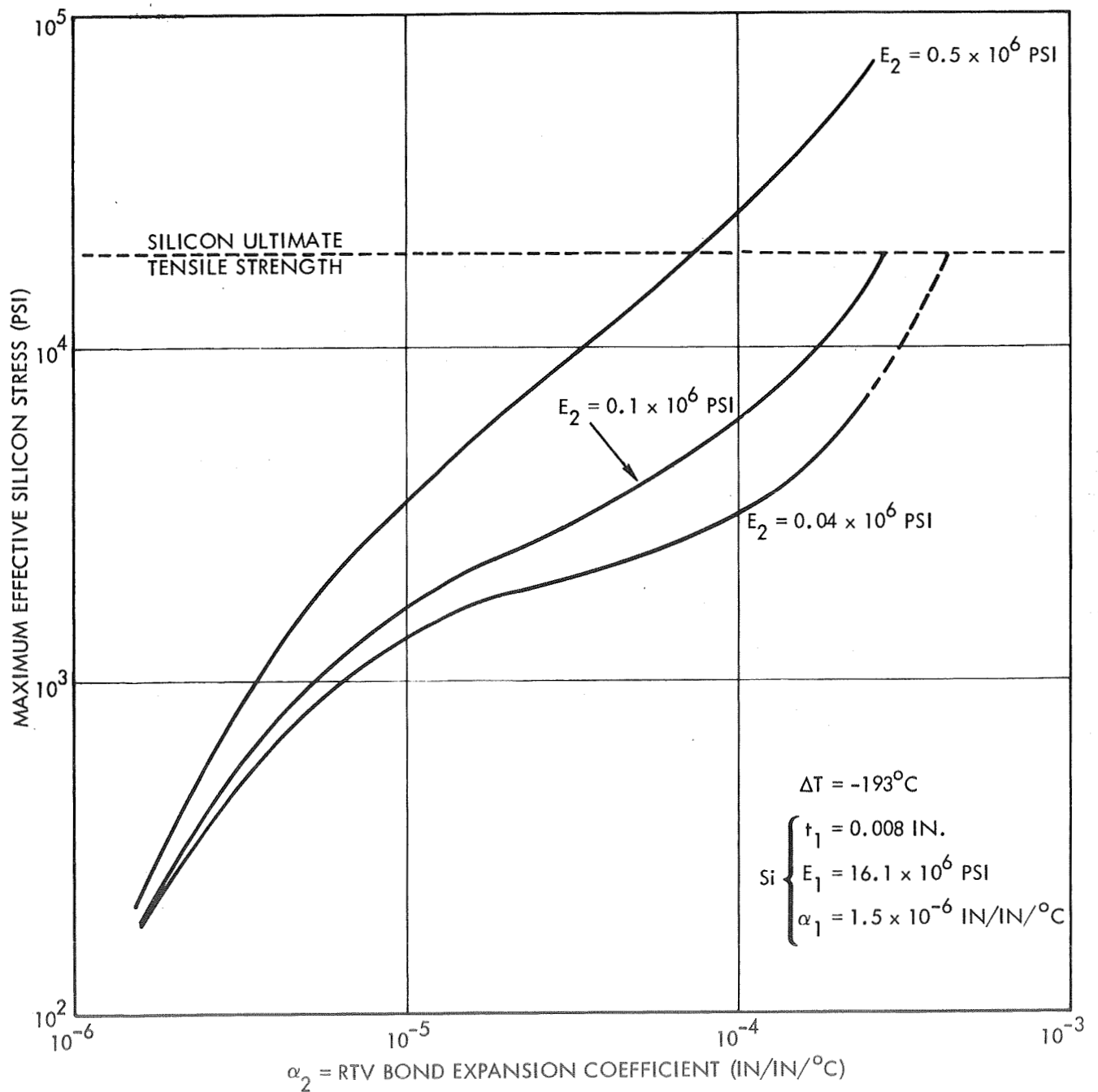


Figure 5.10 Silicon Thermal Stress - RTV Adhesive Thickness, $t_2 = 0.010$ in., at 0.00017 Stress Level

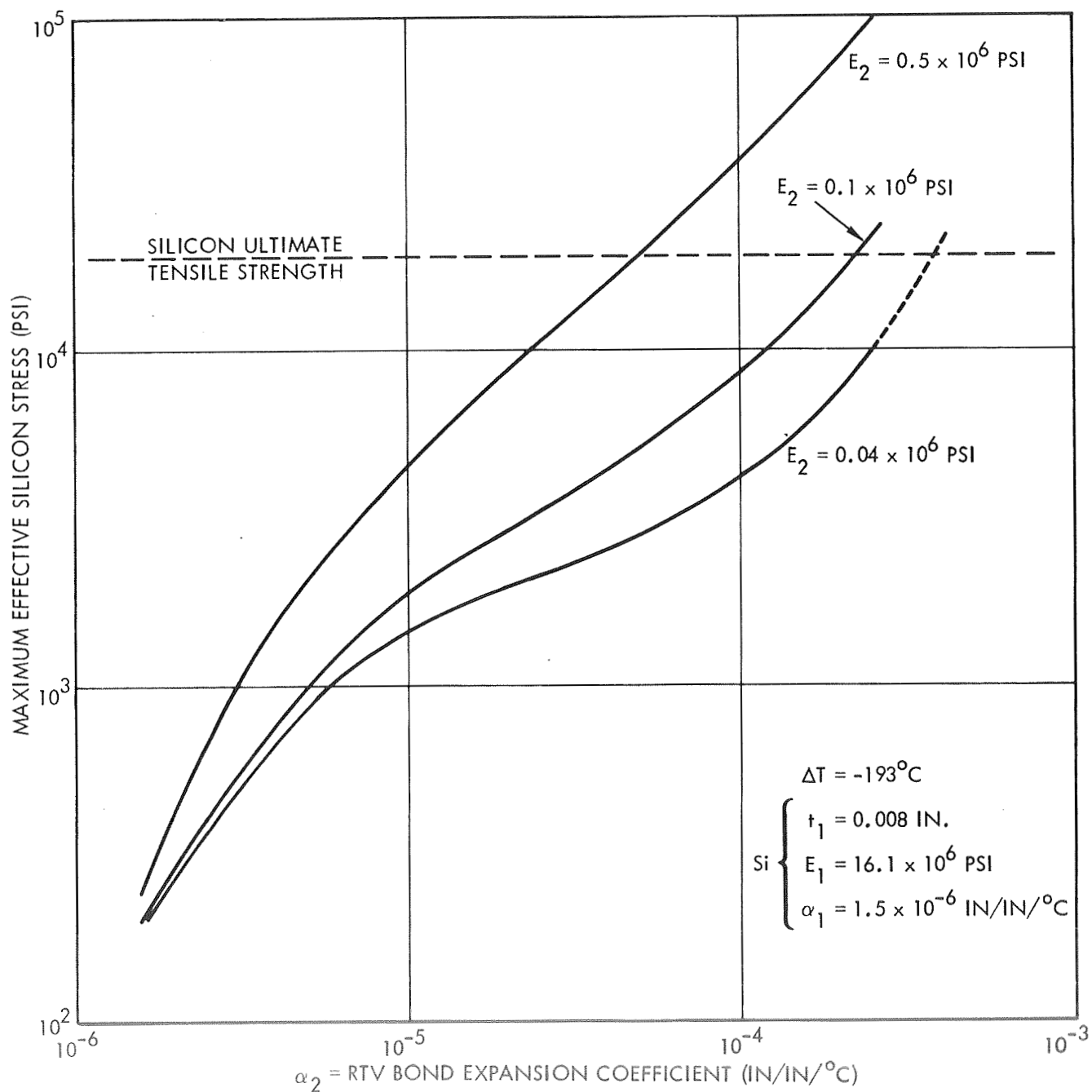


Figure 5.11 Silicon Thermal Stress - RTV Adhesive Thickness,
 $t_2 = 0.015 \text{ in.}$, at 0.00017 Stress Level

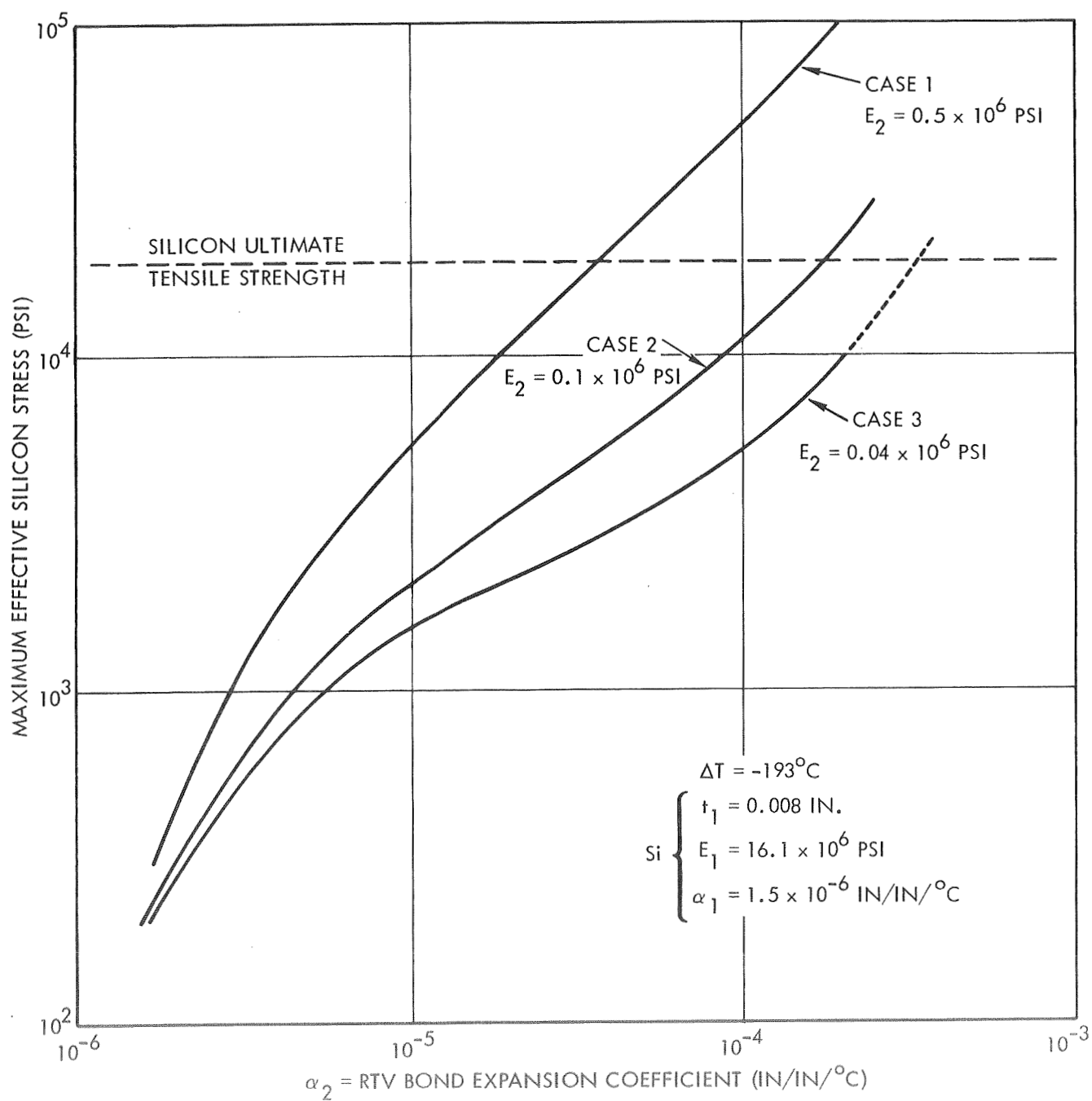


Figure 5.12 Silicon Thermal Stress - RTV Adhesive Thickness,
 $t_2 = 0.020$ in., at 0.00017 Stress Level

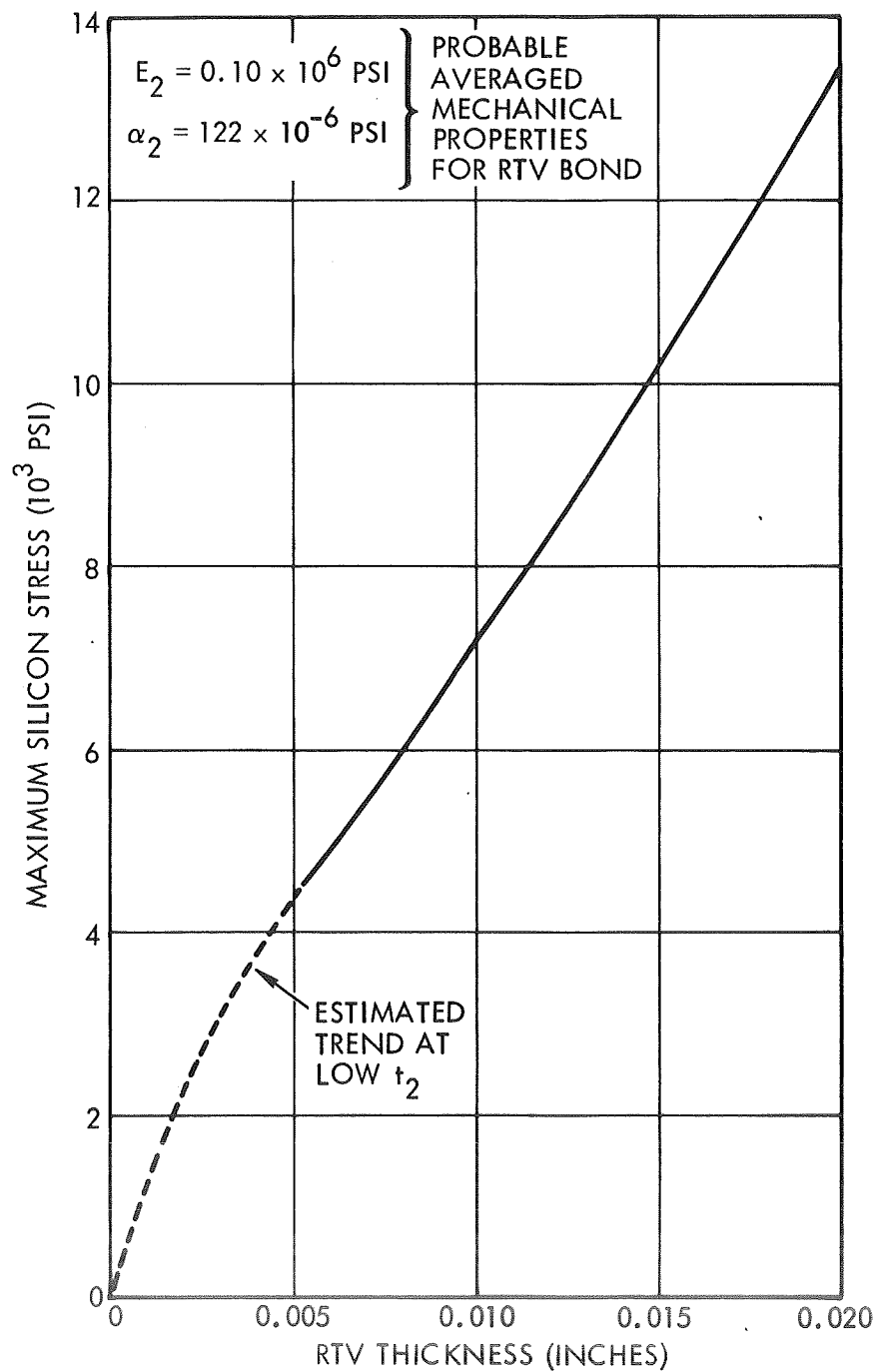


Figure 5.13 Maximum Effective Stress in Silicon
as Function of RTV Adhesive Thickness

thickness chosen. Variation of silicon stress with adhesive thickness for representative averaged properties of adhesives ($E_2 = 0.10 \times 10^6$ psi; $\alpha_2 = 122 \times 10^{-6}$ in/in/°C) are shown in Figure 5.13. Maximum effective silicon stress varies between 4300 psi and 13400 psi for the thickness range of 0.005 to 0.020 inches. These averaged properties should represent acceptable material limitations to prevent silicon spalling at -173°C, the minimum design temperature for the Lunar Based Solar Array.

Table 5.2 Allowable Adhesive Properties Versus t

RTV Thickness	Max. Ave. Adhesive Properties	
t_2 , in.	E_2 , 10^6 psi	α_2 , in/in/°C
0.005 (Fig. 5.9)	0.04	7.5×10^{-4}
	0.10	4.6×10^{-4}
	0.50	1.4×10^{-4}
0.010 (Fig. 5.10)	0.04	4.3×10^{-4}
	0.10	2.7×10^{-4}
	0.50	7.3×10^{-5}
0.015 (Fig. 5.11)	0.04	3.8×10^{-4}
	0.10	2.2×10^{-4}
	0.50	4.9×10^{-5}
0.020 (Fig. 5.12)	0.04	3.3×10^{-4}
	0.10	1.7×10^{-4}
	0.50	3.7×10^{-5}

6. SUBSTRATE DESIGN CRITERIA

The substrates that were designed for this program phase were similar to those utilized during Phase II. However, the emphasis during this phase was primarily to duplicate the facesheet materials so that the effect, if any, on the spalling phenomena could be ascertained. The ETM's designed during Phase II were 30 inches x 48 inches in overall dimensions. The Phase III substrates were approximately 20 inches x 20 inches. The latter size was selected to accommodate the various cellstack configurations included in the ETM Cellstack Bonding Matrix (Figure 8.1). Provisions were also made for subjecting the modules to acceleration and vibration testing. This required that the module frames incorporate a mounting surface together with properly spaced mounting holes and inserts. For the flexible Kapton substrate, it also included the addition of aluminum honeycomb endplates, hinges, spacers, and vibration pads (simulated skirting per Reference 1.2).

6.1 FIBERGLASS - ALUMINUM FRAME CONFIGURATION FOR ETM IA

The criteria established for this substrate design was to use the same epoxy fiberglass facesheet material as was used on the ETM I configuration of Phase II. This was done to obtain the same coefficient of linear expansion for the facesheet. No attempt was made to duplicate the pre-tensioned fiberglass tape lattice, since considerable difficulty was experienced with this design in accurately locating the tape intersections. However, it was necessary to pre-stress the fiberglass diaphragm. This was required to insure that the facesheet still remained taunt down to -173°C . In addition, for structural dynamic testing it was important that the natural frequency of the fiberglass diaphragm be maintained at 40 Hz or greater. This was accomplished by applying a uniform tension of 20.4 lb/in. in both directions of the fiberglass diaphragm as it was being installed on the aluminum box beam frame. A calculated natural frequency of 124 Hz was obtained. The analysis is shown in Appendix C. The final design of this substrate is shown on Figure 8.2.

6.2 ALUMINUM - HONEYCOMB END PLATES WITH INTERMEDIATE FLEXIBLE KAPTON MODULE FOR ETM IIA

The criteria established for this substrate design was to use the same materials that had been previously used on the ETM II configuration

of Phase II. These were depicted in Figure 6.2 of Reference 1.2. The major modification to the ETM IIA design was that only one flexible Kapton module was utilized rather than the two flexible modules fabricated during Phase II. This was done for several reasons. First, the ability for the silicon cells to survive the launch environment when clamped to the endplate with the polyurethane foam vibration pad in between was established in the earlier phase of this program (Reference 1.2). Secondly, the 19.5 inch x 19.5 inch Kapton module was made similar in size to the other two ETM's so that the same experimental matrix of cells could be used on all three configurations. Finally, the emphasis during this phase was on evaluating the spalling failures associated with thermal vacuum testing, so that maintaining the same coefficient of expansion material was the critical parameter.

The only significant design change in ETM IIA was to eliminate the stress concentration in the joint between the Kapton module and the aluminum spacer bar. This had caused some cracking of the Kapton module and the flat cable hinge during vibration testing during the earlier phase. In addition, all holes cut in the Kapton to permit the passage of the hold down bolts were reinforced with a doubler layer of 0.003 inch Kapton. The final design of this substrate is shown on Figure 8.3.

6.3 ALUMINUM HONEYCOMB - GRAPHITE/EPOXY COMPOSITE SUBSTRATE FOR ETM IIIA

The criteria established for this substrate design was identical to that previously used on the ETM III. The facesheets were made for Morganite Type II. Each facesheet consisted of two plies of 0.003 inch thick unidirectional graphite fibers perpendicularly cross laid with one ply of 0.003 inch thick No. 112 fiberglass cloth between the graphite filament plies. Whittaker Corporation - NARMCO No. 5505 epoxy impregnation was used to make the graphite plies and NARMCO No. 252 adhesive was used to bond the facesheets to the aluminum honeycomb core. Because the graphite filaments are an electrical conductor, 0.001 inch Kapton sheets of insulation were placed on the side of the substrate to which the silicon cells were to be attached. The Kapton insulator strip was sized to match the 2 cells in parallel by 5 cells in series sub-modules. Holes were punched in these insulators to match the diameters of the adhesive spots. The final design of this substrate is shown on Figure 8.4.

7. MATERIAL PROPERTIES EXPERIMENTAL PROGRAM

7.1 ADHESIVE MATERIALS TEST PLAN

Upon initiation of this Phase III program, an assessment was made of the adhesive material properties that are essential for evaluation of the spalling phenomenon. It was agreed that the most critical parameters were coefficient of linear expansion, Young's modulus of elasticity, ultimate tensile strength, ultimate shear stress, and to a lesser degree, shear modulus of elasticity. In addition, general agreement was reached that the main load producing effect was the thermal differential expansion stresses induced during the low temperature thermal cycling testing during Phase II of this program.

The thermal conductivity of the adhesive was not considered to be a critical parameter, as far as contributing to the spalling failure. This conclusion was drawn after a review of the Reference 7.1 data. This technical paper indicated that spalling type failures could occur in silicon cells due to thermal stresses induced by temperature gradients. Under the conditions outlined in Reference 7.1, namely the rapid insertion of thin silicon slices into a 1000°C furnace, temperature differences across the wafers as high as 50° to 100°C were experienced. This created a thermal stress of from 4-8 kg/mm², which is sufficiently large to cause plastic deformation of the silicon at its elevated (1000°C) temperature. For this condition, it was concluded that the thermal stresses induced by the comparatively large temperature gradients (50°-100°C), could exceed the strength of the material at its elevated temperature and cause permanent deformation of the silicon wafers. However, this failure effect does not appear to be applicable to the spalling phenomenon which occurred during the low temperature (-173°C), long duration (14 hour) thermal cycling test of Phase II. First, the total temperature differential between room temperature and at the extreme of low temperature thermal testing is only approximately 200°C. In addition, the temperature in the thermal-vacuum chamber was reduced slowly (per Reference 7.2), so that the possibility of inducing large temperature differentials is highly improbable. Finally, the strength of silicon at low temperatures is not diminished as is the case at 1000°C. Because of the foregoing, it was not deemed necessary to

obtain experimental data for the thermal conductivity of the candidate adhesive materials.

This Phase III Adhesive Material Test Plan encompassed an experimental test program which provided, as a minimum, Young's modulus of elasticity, ultimate tensile strength, and ultimate shear stress of four (4) elastomeric adhesive systems. These included:

- Dow Corning RTV 3145
- General Electric RTV 511/577 (50-50 mix)
- General Electric RTV 118
- Products Research PR 1538

RTV 602, and Sylgard 182, originally suggested in Reference 1.4 were eliminated since these are non-structural adhesives which are not suitable for cell-to-substrate bonding. Silastic 140 is very similar to RTV 118 and hence the urethane base PR 1538 adhesive was substituted for it.

The above designated material properties were obtained over a range from room temperature ($\sim 25^{\circ}\text{C}$) to -173°C . The coefficient of thermal expansion was also determined over the entire range between room temperature and -173°C so that a continuous curve for this parameter could be established. Only limited data was obtained on the shear modulus of elasticity of these adhesives, since this is a less critical parameter and the scope of this program did not permit detailed evaluation of all material properties.

Various testing techniques were utilized to obtain the adhesive material property data. Young's modulus and ultimate tensile strength were obtained using cast adhesive specimens approximately 1/8 in. thick, 1/4 in. wide, with a two-inch gauge length. The specimens were straight, rectangular sections rather than the dumbbell shape normally utilized for elastomeric tensile specimens so that stress-strain data could be taken directly from the test machine head travel. This greatly simplified testing at cryogenic temperatures. Each test point was represented by five specimens for each adhesive. Both individual and average values were documented. The test set-up for these tests is shown on Figures 7.1 A and B. The test specimens are shown on Figures 7.2 and 7.3.

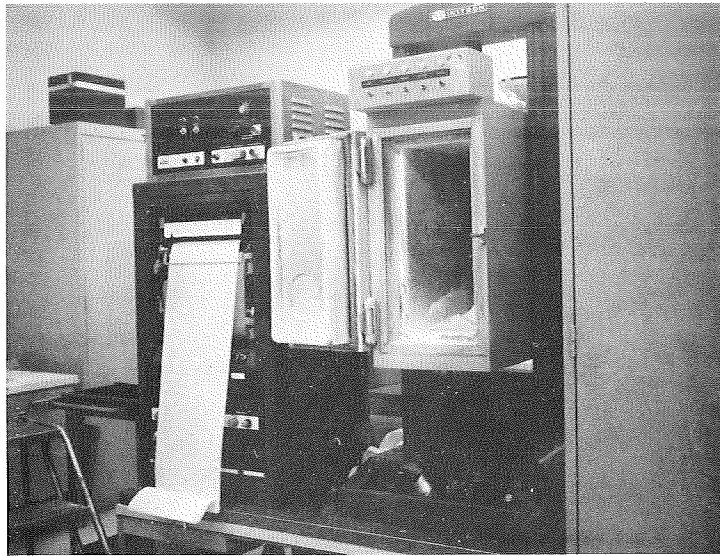


Figure 7.1 A

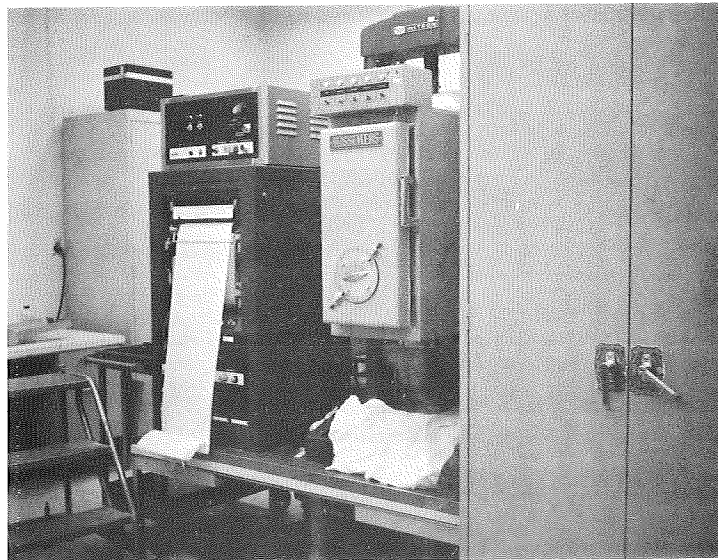


Figure 7.1 B Test Set-up for Obtaining Ultimate Shear and Tensile Strength

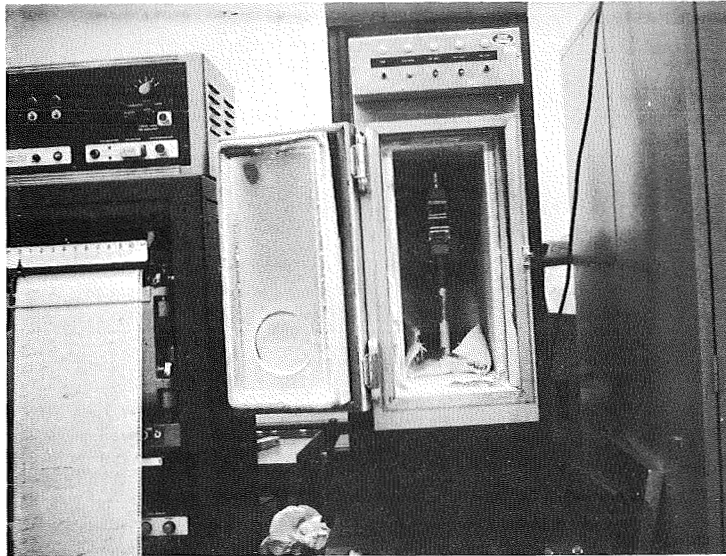


Figure 7.2 Test Set-up for Obtaining Ultimate Tensile Strength

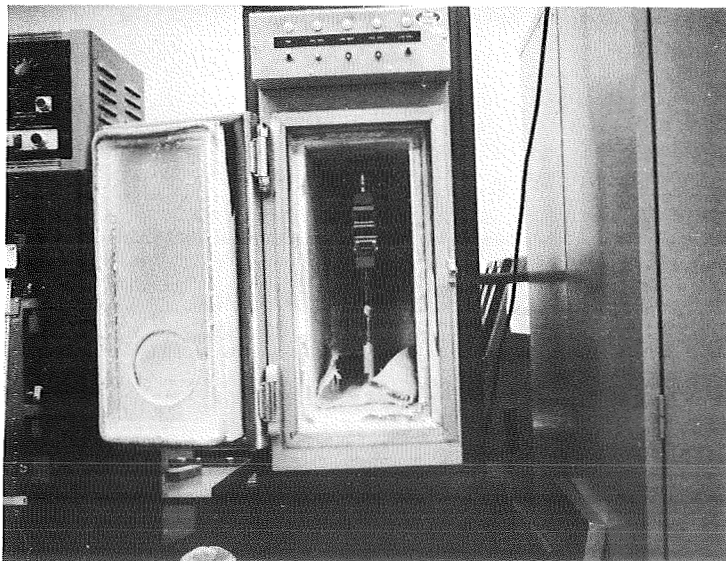


Figure 7.3 Test Set-up for Obtaining Ultimate Tensile Strength

Previously obtained experimental data (Reference 1.2) indicated that a time function (cold soak time) greater than that required to reach equilibrium temperature at -173°C exists which may affect measured material properties. Definitization of the variation of adhesive properties during this transition phase was beyond the scope of the Phase III effort. However, during this test program, a cold soak time was selected which was in excess of the time required to permit crystalline transitions of the material to occur. This data would become available during the course of linear coefficient of expansion determinations. Preliminary data indicated that this transition period was at least one hour.

Ultimate overlap shear strength was obtained using specimens (Figure 7.4) similar to those described in ASTM Test Method D 1002. It is probable that specimen failure occurred as a result of exceeding the adhesive strength of the material, i.e. at the interface between the adhesive and substrate. Therefore, the specimens were fabricated such that the adherence obtained is representative of high quality solar array module construction. Again, each test point was represented by five test specimens. Individual and average values were documented. The test set-up for these tests is shown on Figures 7.5 and 7.6.

The coefficient of linear expansion measurements were made using the test set-up shown on Figure 7.7 which included a quartz tube dilatometer in accordance with ASTM Test Method D 646 (Figure 7.8). The measurements were made continuously over the temperature range from room temperature to -173°C and for a period of time of at least one hour after reaching -173°C . A minimum of two complete determinations were made with each adhesive material and data points were continuously plotted on the X-Y plotter shown on Figure 7.9.

Shear modulus of elasticity values were obtained by the torsion method described in ASTM D 1043 at appropriate temperatures between room temperature and -173°C . The test set-up used is shown on Figure 7.10.

A test matrix listing the candidate adhesives and critical material properties that were to be obtained are shown in Table 7.1.

The outgassing characteristics of the candidate adhesives were also to be provided. In general, this was based upon test data previously obtained at TRW Systems. The technique used to evaluate this characteristic

TABLE 7.1 TEST MATRIX OF CRITICAL ADHESIVE MATERIAL PROPERTIES

Candidate Adhesive Material	Temperature, T , ($^{\circ}\text{C}$)	Adhesive Material Property				
		Young's Modulus of Elasticity, E , (lb/in^2)	Ultimate Tensile Strength, σ_{tu} , (lb/in^2)	Ultimate Shear Strength, σ_{su} , (lb/in^2)	Coefficient of Expansion, α , ($\text{in/in}/^{\circ}\text{C}$)	Shear Modulus of Elasticity, G , (lb/in^2)
Dow Corning RTV 3145	$T_1 = +25$ $T_2 = \text{intermediate value}$ $T_3 = -173$				(Sufficient data will be obtained for plotting a continuous	
General Electric RTV 511/577 (50/50 mix)					curve between $+25^{\circ}$ & -173°C)	
General Electric RTV 118						
Products Research PR 1538						

is to determine the weight loss of the adhesive volatiles as a function of time and temperature in a vacuum. Since these weights are measured in a vacuum for a given temperature, curves for weight loss as a function of time can be drawn. A weight loss that does not exceed 2 to 3% is considered acceptable. The initial weight loss is predominantly evaporation controlled since the surface volatiles are lost first. Subsequently, the weight loss is diffusion controlled and the rate of weight loss decreases rapidly to an insignificant value.

7.2 OTHER MODULE MATERIALS TEST PLAN

Similar data for the other module materials was desired in order to investigate the spalling failure mode. These include the module substrates, interconnectors, solder joints and silicon cells. This data was obtained primarily by a survey of existing literature and material properties documentation available at TRW Systems Materials and Processes Department or in industry. A matrix of the data that was to be assembled is listed in Table 7.2.

Every effort was made to provide data for all these materials over the specified temperature range of $+25^{\circ}\text{C}$ to -173°C . In those cases where the data was lacking (particularly at cryogenic temperatures), estimates had to be made. These values were compared with the cellstack design analysis and their impact upon the results evaluated in Section 5.

7.3 MATERIALS PROPERTIES TEST EVALUATION

The following data documents the experimental results of the material properties evaluated during this program phase. Because of the plastic characteristics of the four elastomeric adhesives, considerable difficulty was encountered in preparing adequate test specimens to insure uniformity. For example, it proved to be quite difficult to prepare completely void (bubble) free specimens. A large quantity of potential test specimens were prepared and closely examined in order to obtain the relatively few specimens which were ultimately tested. Those that were selected were representative of the quality of adhesive that would be obtained during normal solar cell bonding operations.

7.3.1 Coefficient of Expansion - Adhesives

The coefficient of expansion for the four candidate adhesives was

TABLE 7.2 DATA MATRIX OF DESIRED MODULE MATERIAL PROPERTIES

Candidate Material	Temperature, T , (°C)	Module Material Property				
		Young's Modulus of Elasticity, E , (lb/in ²)	Ultimate Tensile Strength, σ_{tu} , (lb/in ²)	Ultimate Shear Strength, σ_{su} , (lb/in ²)	Coefficient of Linear Expans- (in/in/°C)	Shear Modulus of Elasticity, G , (lb/in ²)
Dupont Kapton (0.001" Thick)	$T_1 = + 25$ $T_2 = \text{intermediate}$					
Fiberglass Laminate	$T_3 = - 173^\circ\text{C}$					
Graphite Composite						
Kovar						
Aluminum						
Sn 62/2% Silver Solder						
Silicon cell (preferred crystal orientation)						
Silicon cell (random Crystal orientation)						

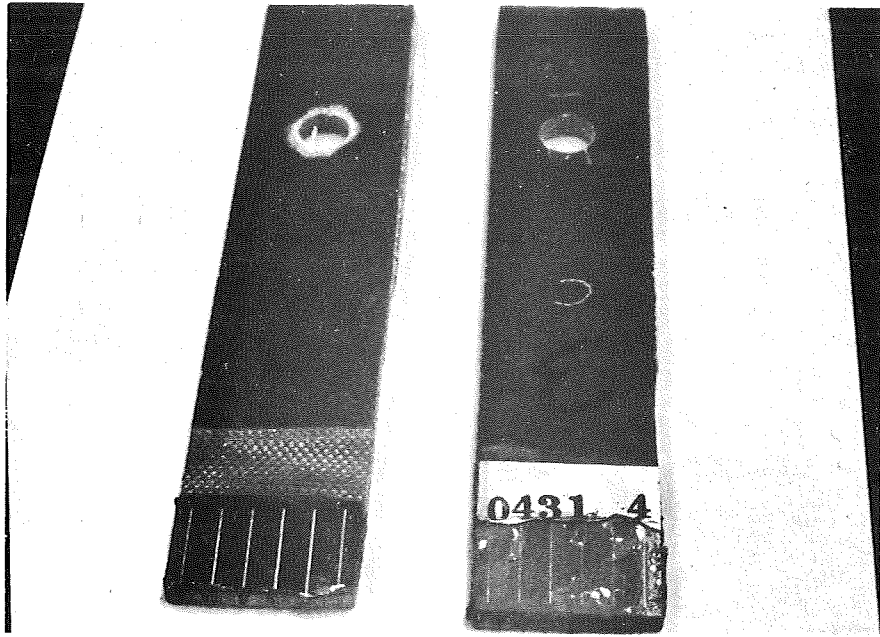


Figure 7.4 Lap Shear Specimen Configuration

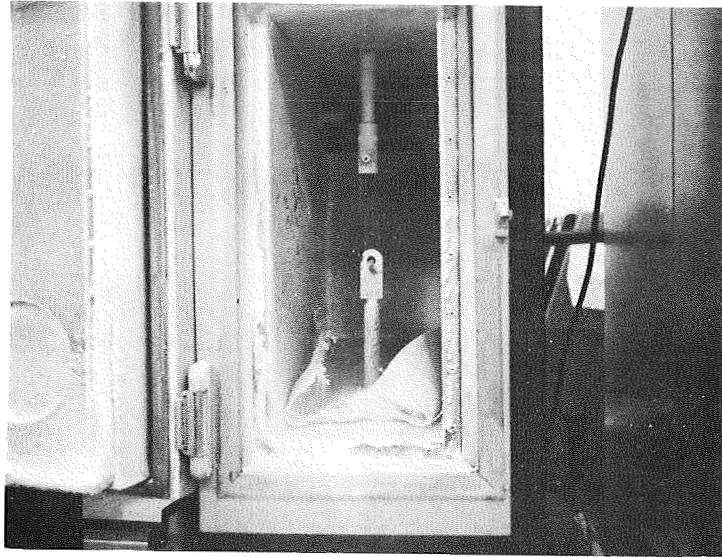


Figure 7.5 Test Set-up for Obtaining Ultimate Overlap Shear Strength

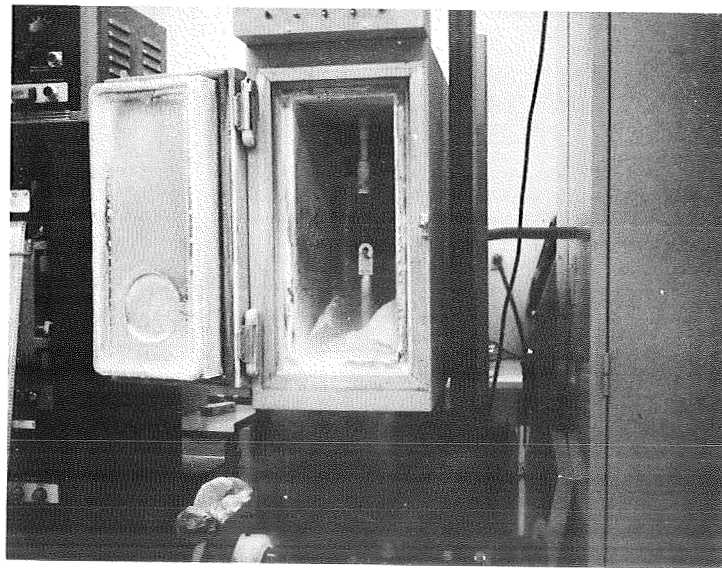


Figure 7.6 Test Set-up for Obtaining Ultimate Overlap Shear Strength

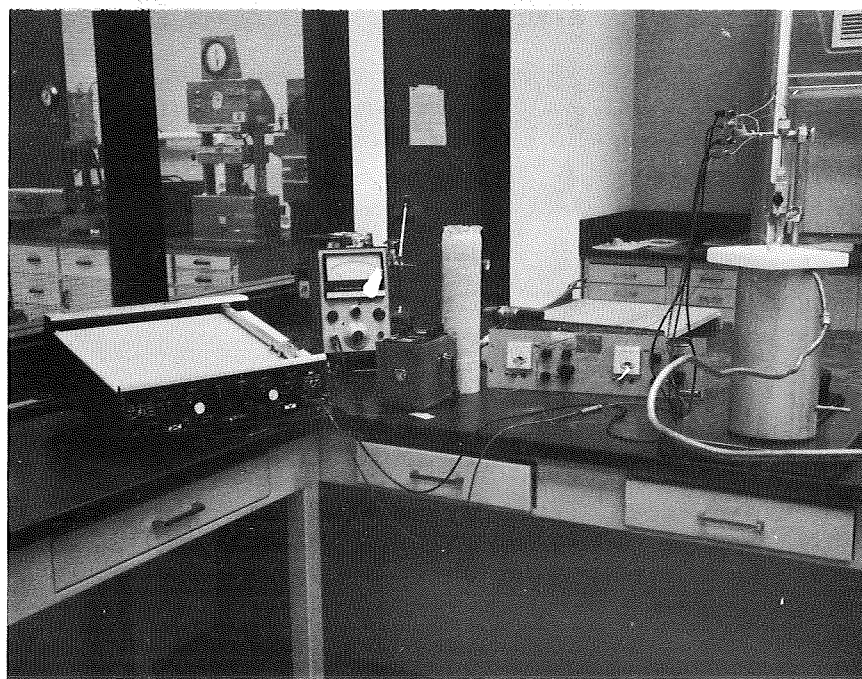


Figure 7.7 Test Set-up for Obtaining
Coefficient of Thermal Expansion

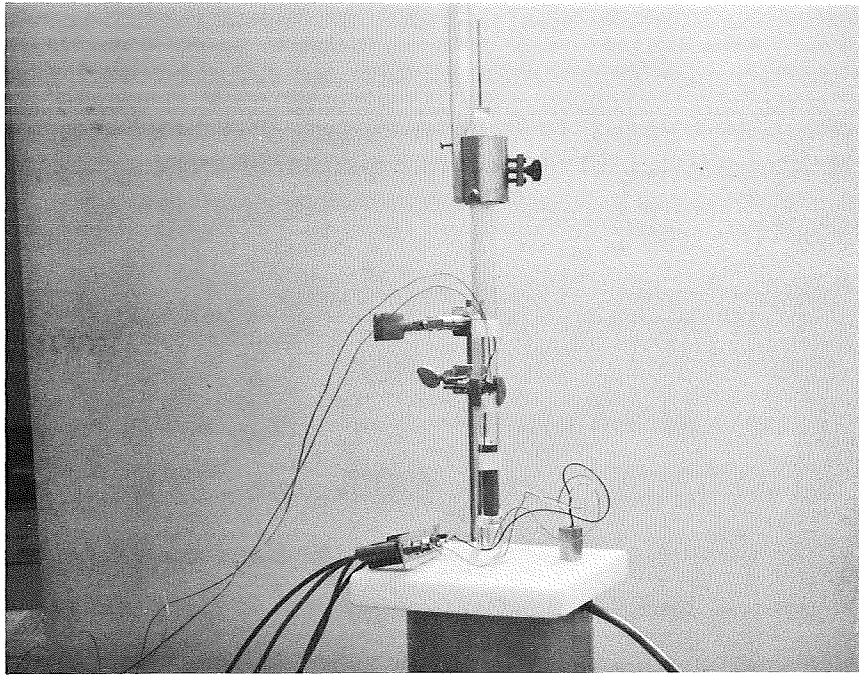


Figure 7.8 Dilatometer Used for Obtaining Coefficient of Thermal Expansion

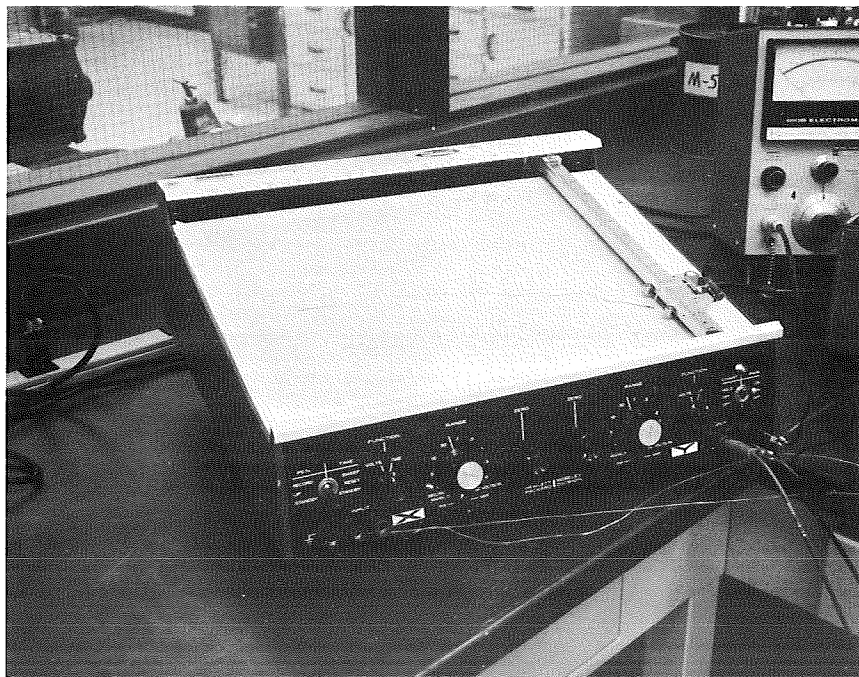


Figure 7.9 X-Y Plotter Used in Conjunction with Coefficient of Thermal Expansion Testing

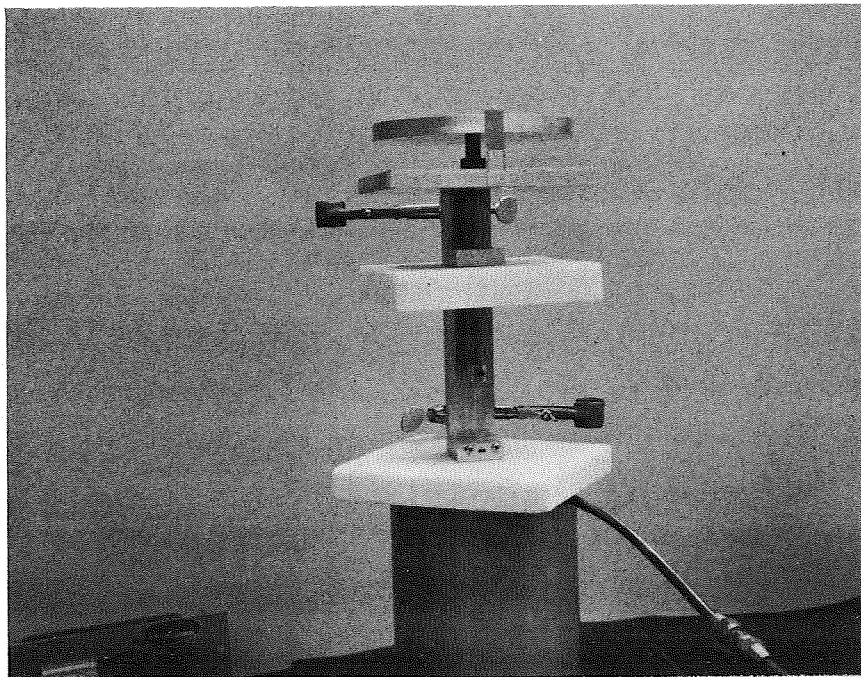


Figure 7.10 Test Set-up for Obtaining Shear Modulus in Torsion

determined over a temperature range from + 25°C (+ 77°F) to -173°C (-280°F). The test set-up was in accordance with that shown on Figures 7.7 and 7.8. The test specimens had a nominal gauge length of 2 inches (5.08 cm). The procedure that was followed was to place the specimen in the dilatometer (Figure 7.8). The specimen was then placed in a chill-down capsule (Figure 7.7) with the upper portion of the apparatus exposed to room temperature. A copper-constantan thermocouple reference junction (32°F or 0°C) was utilized to insure accurate temperature readings. A fifteen minute chilldown period was utilized to bring the test sample down to - 173°C. A three hour warm-up period was used to measure the change in specimen length as a function of temperature. A continuous readout was obtained and plotted on the X-Y plotter (Figure 7.9). Two test runs were made for each adhesive specimen. This data has been incorporated in Appendix B. Utilizing this data, Figures 7.11 to 7.14 were prepared. These charts show the amount of contraction which occurred to each of the four adhesive test specimens as a function of temperature. These measurements were made using the quartz tube dilatometer in accordance with ASTM Test Method D 646, except that a linear differential transformer was used to measure the movement of the specimen with temperature. The output from this transformer and the thermocouple attached to the test specimen were plotted on the X-Y recorder. Two separate determinations were made for each adhesive. It was found that the second run in each case did not identically duplicate the values from the first run. In all cases, the amount of contraction experienced by the sample on the second run was less than that experienced during the initial run.

It is postulated that the specimen cooldown rate was always faster during the second run. This was attributed to the fact that the mass of the test chamber was much colder at the initiation of the second run. With this faster cooldown rate, it was assumed that the brittle point characteristics were reached sooner and this material property change reduced the contraction rate on all of the second runs.

During this adhesive properties experimental test work a specially prepared test sample of RTV 3145 was obtained from Dow Corning. This sample was 2.24 inches (5.69 cm) long. It had been prepared by subjecting it to a pressure of 10,000 psi. This was done to provide as void-free a sample as possible. Data from these tests have been included in Appendix

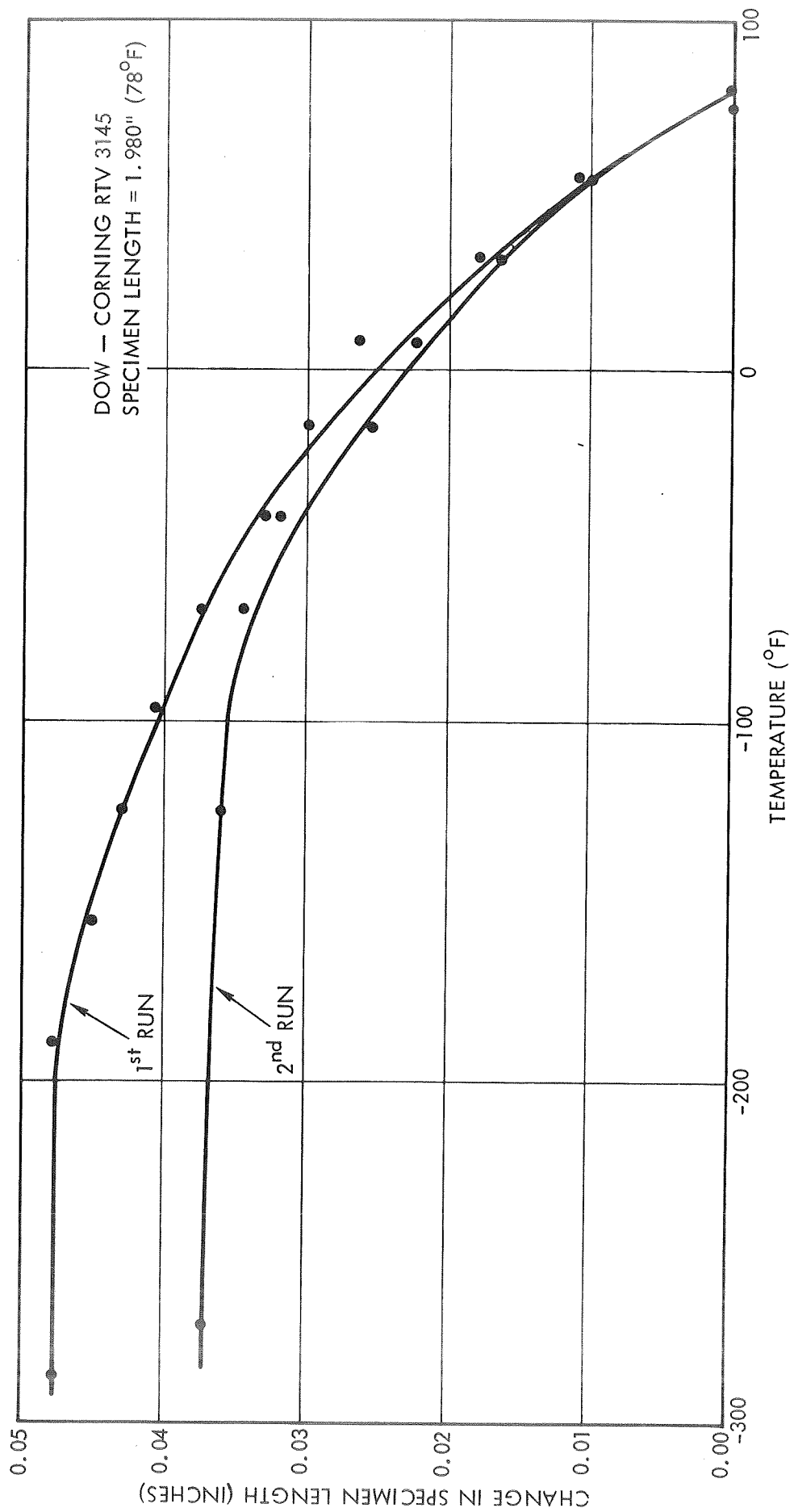


Figure 7.11 Change in Specimen Length as Function of Temperature - RTV 3145 Adhesive

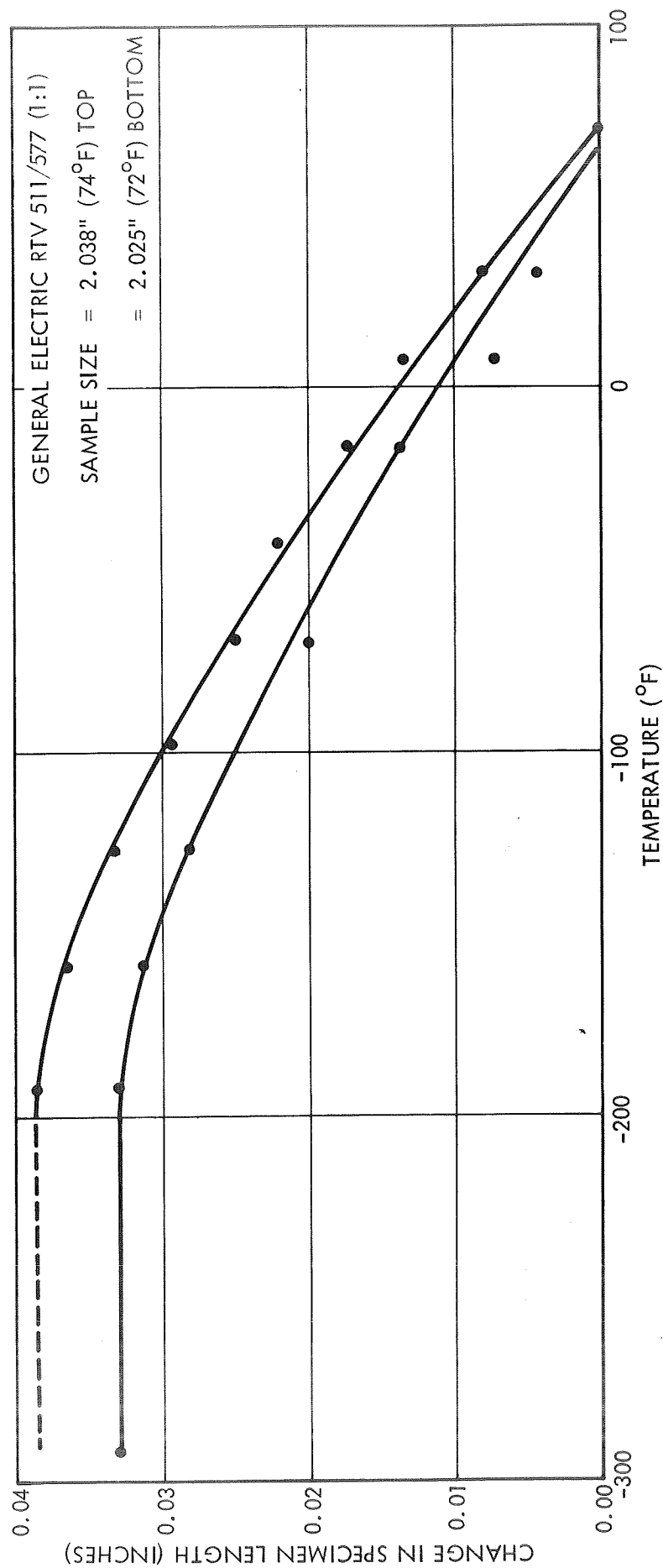


Figure 7.12 Change in Specimen Length as Function of Temperature - RTV 511/577 (1:1)

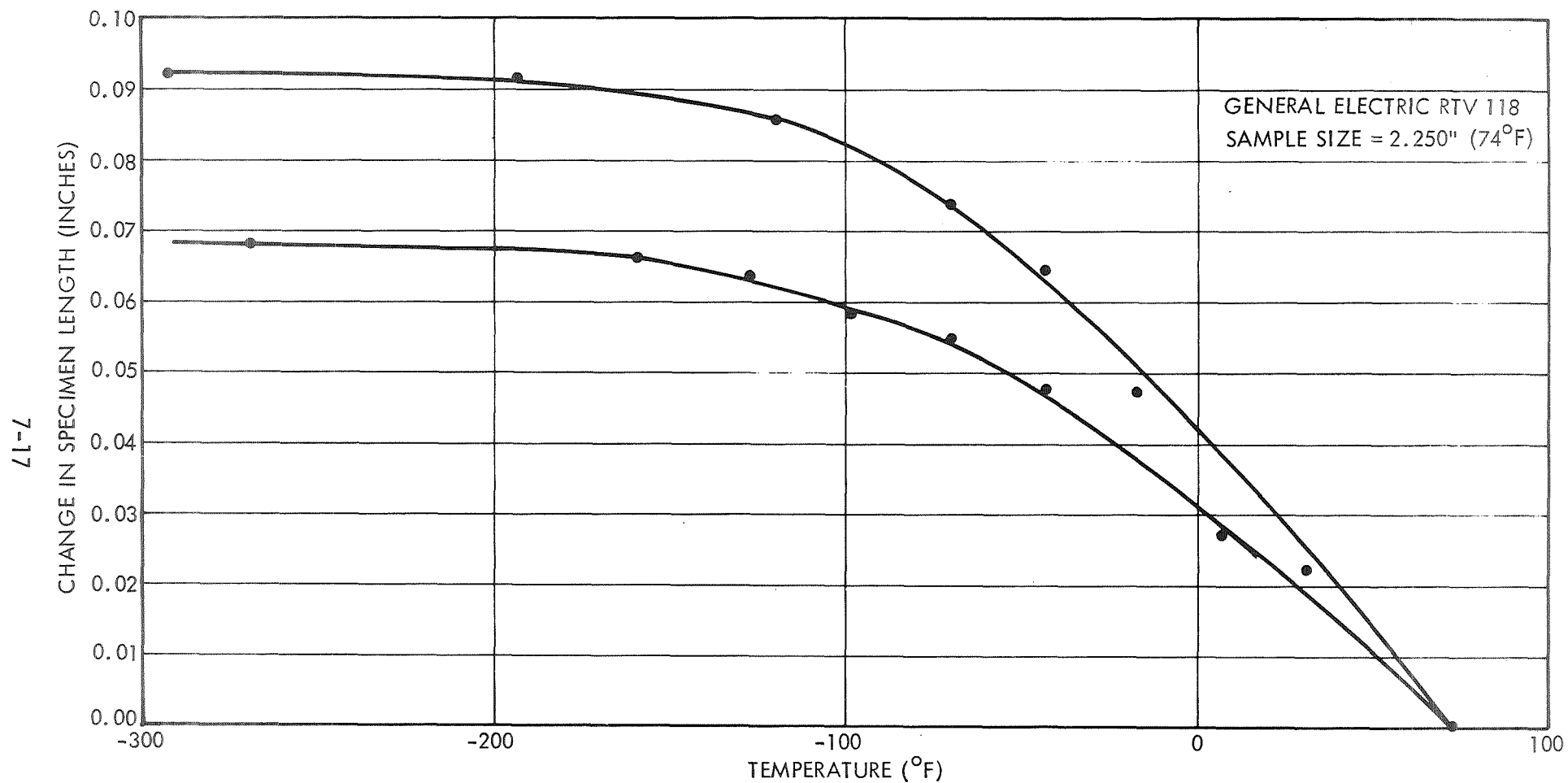


Figure 7.13 Change in Specimen Length as Function of Temperature - RTV 118

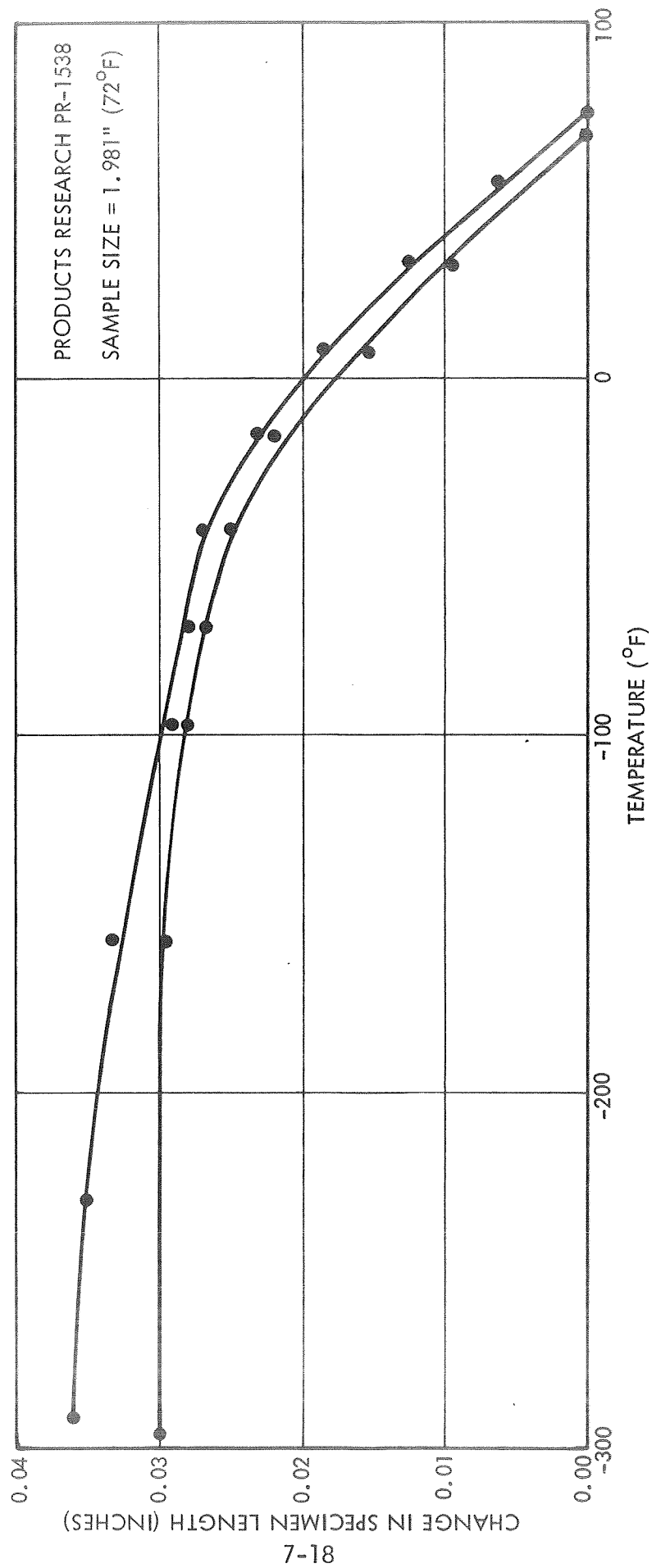


Figure 7.14 Change in Specimen Length as Function of Temperature - PR T538

B. In general, the values for coefficient of expansion were in the same range as for those samples prepared by TRW Systems. This was also true despite subjecting the Dow Corning sample to a 24 hour aging process at 260°F. It was noted, however, that in the temperature range from approximately - 22°F to - 70°F that a repeatable, marked change in the coefficient of expansion occurred. It was felt that this was due to a crystalline transition which occurs in the RTV 3145 adhesive in this temperature range and is only discernable on a comparatively void-free sample. This crystalline transition occurrence had been noted previously at TRW Systems during earlier testing.

The value of the coefficient of expansion over the temperature range varied considerably. For example, for Dow Corning RTV 3145, the values varied from 130×10^{-6} (+80°F to -60°F) to 2.4×10^{-6} (-160°F to -300°F). In addition, these represented average values over the temperature ranges involved since the temperature versus specimen contraction curves (Figures 7.11 to 7.14) for all the adhesive samples were non-linear. In any assessment of the spalling problem, it is important to take this variation into account.

The experimental values for the coefficient of linear expansion for the four adhesives evaluated are summarized in Table 7.3. Since the values also varied from Run No. 1 to Run No. 2 on the same specimen, it is suggested that the average of the two values be utilized for thermal differential expansion and stress analyses determinations.

7.3.2 Ultimate Tensile Strength and Modulus of Elasticity-Adhesives

The ultimate tensile strength and modulus of elasticity for the four adhesive types were obtained. The results are given in Table 7.4. Both of these values increased in magnitude as the temperature was reduced. A drop-off in ultimate tensile strength was noted at -275°F for both RTV-3145 and PR-1538. This however, may have been due to the lack of homogeneity in the preparation of the specimens. This could produce an internal, local stress concentration, which under the brittle characteristics that exist in these adhesives at low temperature could cause a premature tensile failure.

TABLE 7.3 EXPERIMENTAL VALUES OF COEFFICIENT OF LINEAR EXPANSION, IN/IN/°F

ADHESIVE TYPE	RUN NO.	TEMPERATURE RANGE		
		27°C to -51°C (+ 80°F to - 60°F)	- 51°C to - 107°C (- 60°F to - 160°F)	- 107°C to - 185°C (- 160°F to - 300°F)
Dow Corning RTV 3145	1	130×10^{-6}	48×10^{-6}	8.3×10^{-6}
	2	120×10^{-6}	19×10^{-6}	2.4×10^{-6}
General Electric RTV 511/577	1	84×10^{-6}	63×10^{-6}	6.0×10^{-6}
	2	70×10^{-6}	56×10^{-6}	6.7×10^{-6}
General Electric RTV 118	1	220×10^{-6}	84×10^{-6}	8.3×10^{-6}
	2	160×10^{-6}	62×10^{-6}	5.1×10^{-6}
Product Research PR 1538	1	100×10^{-6}	24×10^{-6}	12×10^{-6}
	2	94×10^{-6}	18×10^{-6}	1.8×10^{-6}

However, since this lack of homogeneity in the adhesives could also occur during actual production operations, the use of the lower values is recommended to be conservative. Additional data obtained for these adhesives included the room temperature Shore A hardness. These hardness measurements were obtained using the ASTM D 1706 testing procedures. These values are also shown in Table 7.4.

7.3.3 Lap Shear Ultimate Strength and Shear Modulus of Elasticity - Adhesives

The lap shear ultimate strength for the four candidate adhesives was obtained using the specimen configuration shown in Figure 7.4 and the test set-up shown in Figures 7.5 and 7.6. The results are given in Table 7.5. Two types of cells were used to obtain the effects of random and preferred crystal orientation. The "Heliotek" cell is a preferred crystal orientation type and the "Centralab" cell is of the random crystal orientation type. There were four typical failure modes as follows:

- (1) Adhesive Failure (Bonding)
- (2) Cohesive Failure (Adhesive Shear)
- (3) Cell Breakage (Cell Shear)
- (4) Entire Cell (top) pulled off with no breakage of cell (Adhesive Shear of SiO Bond)

These failure modes, together with their corresponding lap shear ultimate values are depicted in Table 7.5. As can be noted, in most cases the failure was due to a cohesive failure (shearing of the adhesive) or cell breakage). The only adhesive failures occurred with RTV 511/577 in the -150°F and -250°F ranges. It should be noted that the fourth failure mode was an adhesive bond or Silicon Oxide coating failure of the top of the cell. Each solar cell was bonded face down to MIL-P-18177, Type GE epoxy laminate test coupons. A similar test coupon was then bonded with the candidate adhesive to the back of the solar cell to a distance of approximately 1/2 of the length of the cell. It was intended that this approach would ensure that the shear failure would occur at the back of the solar cell. However, many of the test specimens failed in tension during test or the adhesive failed on the top surface of the solar cell. Since a cohesive failure or an adhesive failure at the test specimen - substrate interface represents the true bond strength of the candidate

TABLE 7.4 EXPERIMENTAL VALUES OF ULTIMATE TENSILE STRENGTH & MODULUS OF ELASTICITY, LB/IN²

ADHESIVE TYPE	TYPE OF TEST	SPECIMEN TEMPERATURE			HARDNESS ** SHORE A 22.2°C (72°F)
		22.2°C (72°F)	- 101°C (- 150°F)	- 170.5°C (- 275°F)	
Dow Corning RTV-3145	Ult. Tensile Strength	437	* 1,440	1,300	28 - 35
	Modulus of Elasticity	40	*15,600	*39,500	
General Electric RTV-511/577	Ult. Tensile Strength	273	790	4,790	45 - 50
	Modulus of Elasticity	89	114	108,000	
General Electric RTV-118	Ult. Tensile Strength	234	2,190	10,200	25 - 30
	Modulus of Elasticity	29	30,400	173,800	
Product Research PR-1538	Ult. Tensile Strength	1,055	7,250	4,530	70 - 72
	Modulus of Elasticity	500	33,000	37,900	
Average of 5 specimens, except as noted.					
*Average of 4 specimens.					
**Range of 10 separate readings.					

TABLE 7.5 EXPERIMENTAL LAP SHEAR ULTIMATE STRENGTH, LB/IN²

ADHESIVE TYPE	CELL TYPE*	22.2°C (72°F)	FAILURE MODE	- 101°C (- 150°F)	FAILURE MODE **	-170.5°C (-275°F)	FAILURE MODE **
Dow Corning RTV-3145	H	211	2	635	3	450	3
	H	205	3	910	3	1400	3
	H	293	2	455	4	155	4
	C	203	2	745	3	900	3
	C	187	2	615	3	1000	3
	C	-	-	990	3	-	-
Average Values	H	236	-	667	-	668	-
	C	190	-	783	-	1000	-
General Electric RTV-511/577 (1:1)	H	362	2	165	1	200	1
	H	178	2	177	1	65	1
	H	261	3	155	1	75	1
	C	260	2	340	1	-	-
	C	138	2	575	1	50	1
	C	176	2	380	1	-	-
Average Values	H	267	-	166	-	113	-
	C	192	-	432	-	50	-
General Electric RTV-118	H	128	2	1700	3	1400	3
	H	113	2	-	-	-	4
	H	104	2	750	3	450	4
	C	237	2	870	3	600	3
	C	183	2	830	3	500	3
	C	156	2	645	3	500	3
Average Values	H	115	-	1225	-	925	-
	C	192	-	782	-	533	-
Product Research PR-1538	H	343	3	1300	3	110	4
	H	400	3	1650	3	850	4
	H	211	3	900	3	1600	4
	C	364	2	900	3	1050	1
	C	272	2	1200	3	1100	3
	C	375	2	1100	3	1100	1
Average Values	H	318	-	1283	-	1183	-
	C	337	-	1067	-	1083	-

* CELL TYPE

** FAILURE MODE

H - Heliotek Cell
C - Centralab Cell1. Adhesive Failure
2. Cohesive Failure
3. Cell Breakage4. Entire Cell (top)
pulled off with no
breakage of cell.

TABLE 7.6 OTHER MODULE MATERIAL PROPERTIES

Material	Young's Modulus of Elasticity; psi	Ultimate Tensile Strength; psi	Ultimate Shear Strength; psi	Coefficient of Expansion; in/in/°F	Shear Modulus of Elasticity, psi
Kapton (Dupont)	430,000 (+72°F) 510,000 (-319°F)	25,000 (+72°F) 35,000 (-319°F)	-----	1.1×10^{-5} (100°F to + 7°F)	-----
Epoxy Laminate- 120 Glass Cloth	3.0×10^6 (+72°F)	35,000 (+72°F)	11,800 (+72°F) (Panel Shear)	5.5×10^{-6} (200°F to -100°F)	580,000 (+72°F) (Panel Shear)
Graphite Composite- Morganite Type II (0/90 Orientation)	11.0×10^6 (+72°F) 18 - 23×10^6 (+72°F) (Graphite Filaments only)	100,000 (+72°F) 350,000 (+72°F) (Graphite Filaments only)	15,000 to 16,500 (+72°F) (Graphite Filaments only)	2.0×10^{-6} (+72°F) 0.3 to 1.8×10^{-6} (212°F to - 300°F)	-----
Kovar	25×10^6 (+72°F)	77,500 (+72°F)	-----	3.4×10^{-6} (+72°F to 932°F)	-----
Aluminum - 2024 - T 81	10.6×10^6 (+72°F) 10.6×10^6 (-297°F)	65,000 (+72°F) 75,000 (-279°F)	41,000 (+72°F)	9.4×10^{-6} (0°F to -250°F)	3.3×10^6 (+72°F)
2% Silver Solder (Sn 62, Pb 36)	3.3×10^6 (+72°F)	3,000 (+ 212°F) 6,700 (+72°F) 14,200 (- 220°F)	3,000 (+ 212°F) 6,060 (+72°F) 14,200 (-220°F)	2.5×10^{-5} (+72°F) 1.7×10^{-5} (148°F)	-----
Silicon (Preferred Crystal Orientation)	16×10^6 (+72°F)	19,000 (+72°F) ⁽¹⁾ 28,000 (+72°F) ⁽²⁾	-----	-0.17×10^{-6} (-279°F) 0.83×10^{-6} (-100°F) 1.3×10^{-6} (+72°F)	-----

(+72°F = Room Temperature = 22.2°C)
(1) Centralab - random crystal orientation - Zone Soldered
(2) Heliotek - preferred crystal orientation - Solder Dipped

adhesive, all values given in Table 7.5 which are noted to be other than failure modes 1 or 2 represent minimum (i.e. conservative) values. Failure of the upper surface bond was attributed to the notch sensitivity of the PR 1538 adhesive that was used or poor bonding of the silicon oxide coating.

The scope of the program did not permit a complete evaluation of the shear modulus of elasticity for all the candidate adhesives. However, a test apparatus was fabricated to obtain this data for two of the adhesives. The test apparatus that was fabricated to obtain this data was in accordance with ASTM D 1043 and is shown in Figure 7.10. The modulus of the adhesives at room temperature was too low to be recorded by the test equipment. Two determinations were made at cryogenic temperatures, as follows:

- GE RTV 511/577 - 825 psi at -150°F (- 101°C)
- PR 1538 - 137,000 psi at -130°F (- 90°C)

Using this test apparatus it was not possible to obtain adhesive specimen temperatures below those indicated above. A large mass of aluminum in the test apparatus remained outside of the low temperature chamber. Due to the high thermal conductivity of the aluminum, the test equipment could not achieve lower temperatures. A different type of test apparatus or better methods of insulation are required before readings to - 275°F (- 171°C) can be obtained.

7.3.4 Outgassing Characteristics - Adhesives

The outgassing characteristics for the four candidate adhesives was obtained with respect to the steady - state rate of weight loss. The data is shown on Figures 7.15 to 7.18. The test temperature was 200°F (93.3°C) which is slightly lower than that prescribed in Section 3 of Reference 7.3. This slightly lower temperature was not considered to be significant in view of the very low values of steady-state rate weight losses obtained. These are tabulated as follows:

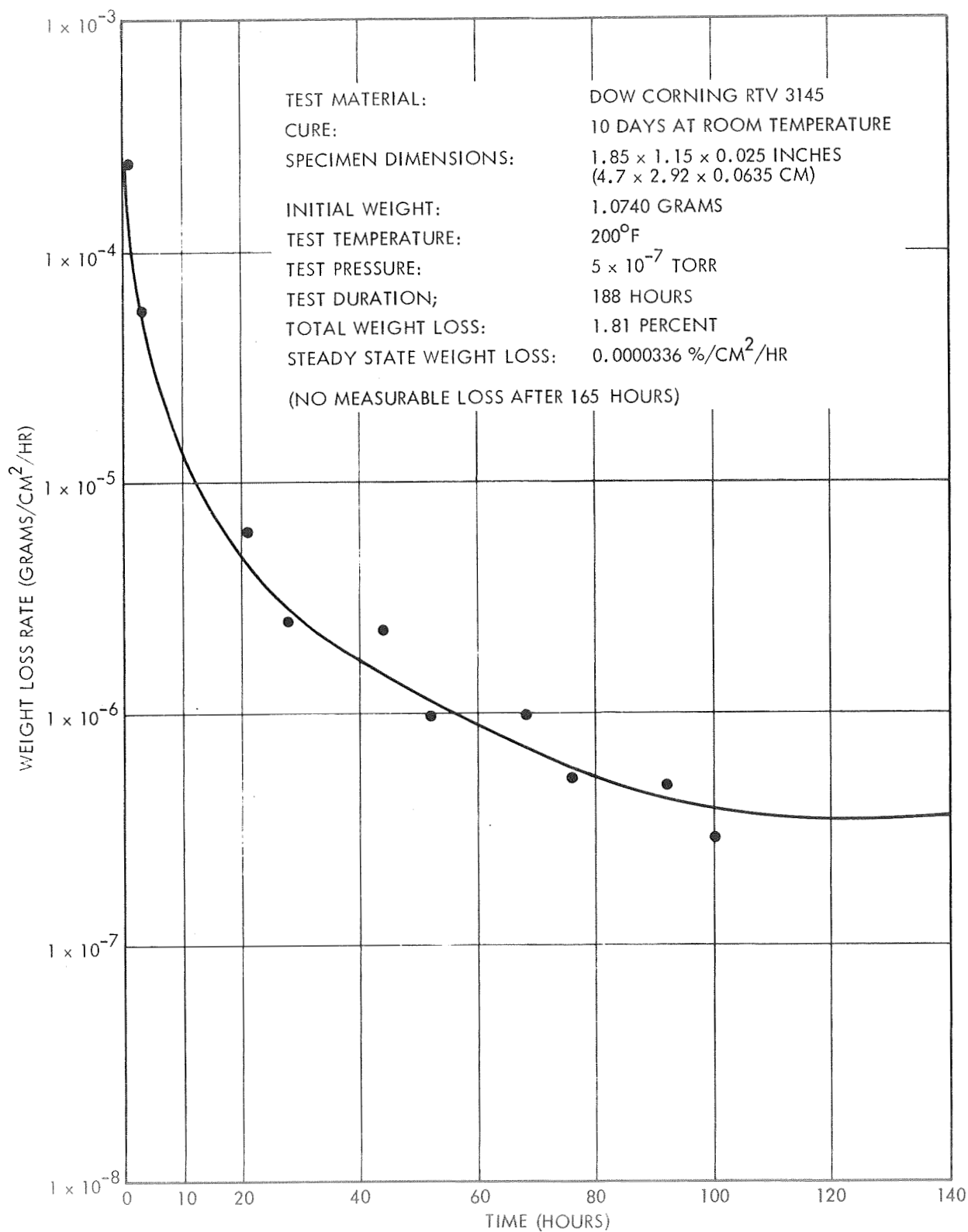


Figure 7.15 Weight Loss Rate Vs. Time
for RTV 3145

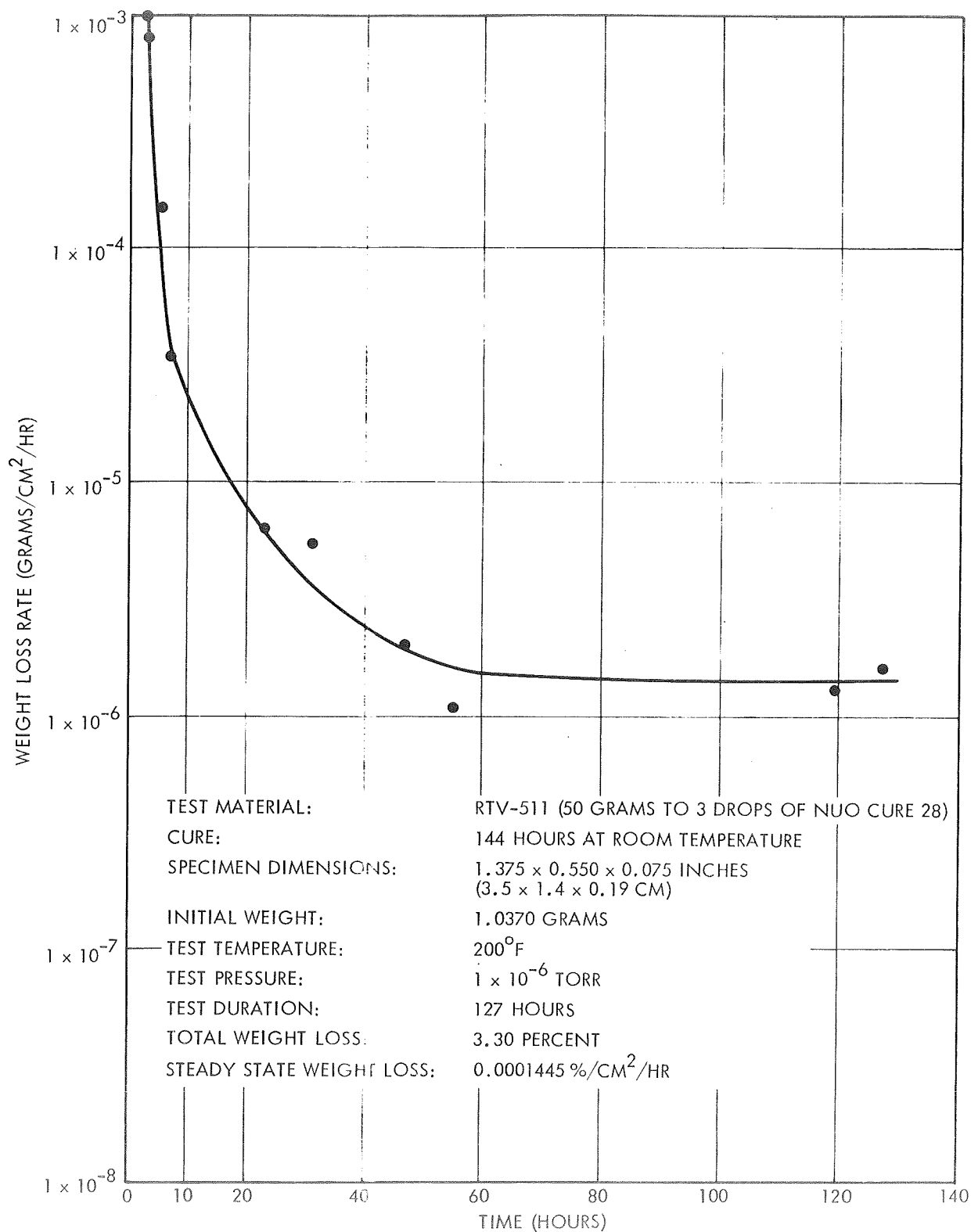


Figure 7.16 Weight Loss Rate Vs. Time
for RTV 511/577

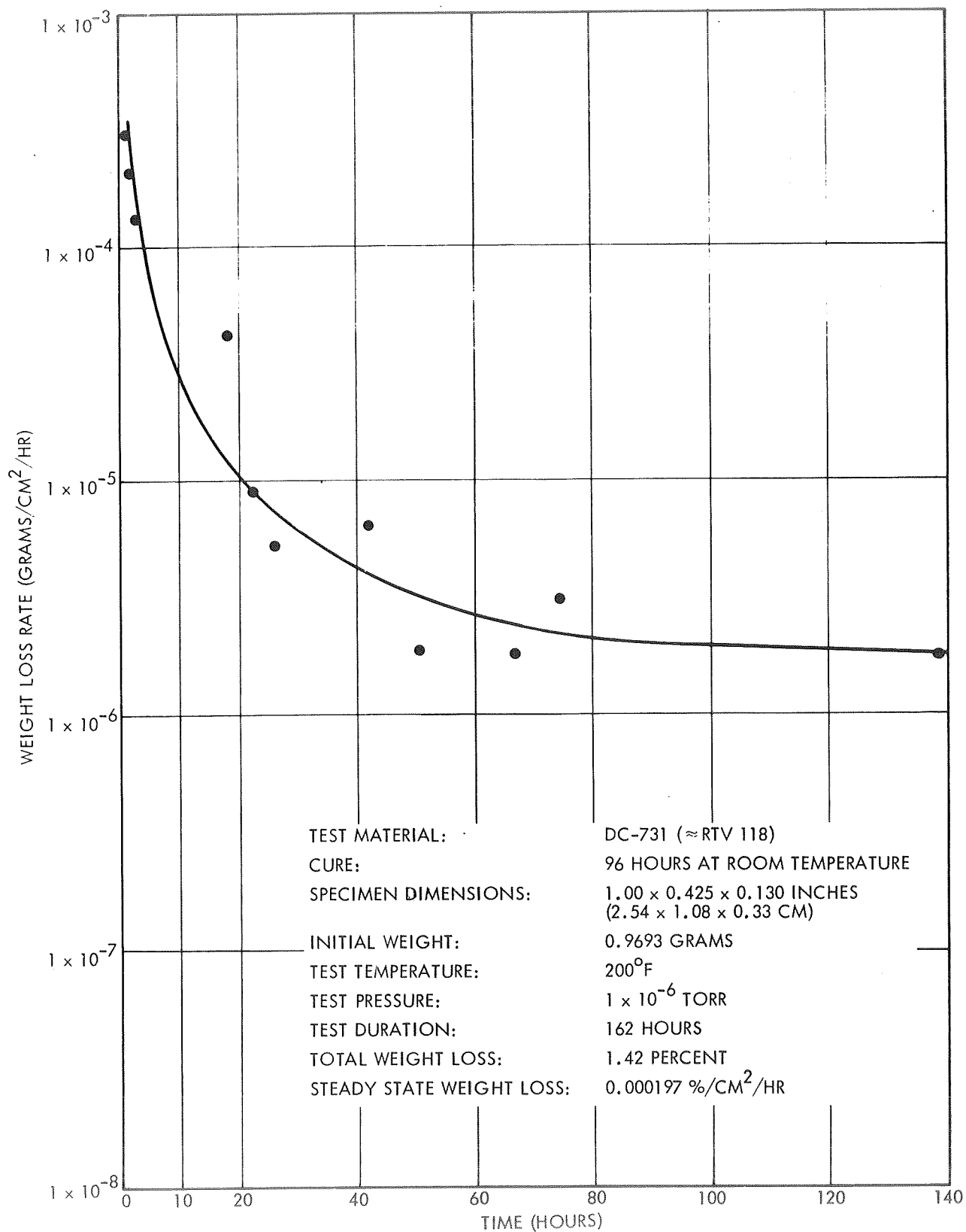


Figure 7.17 Weight Loss Rate Vs. Time
for RTV 118

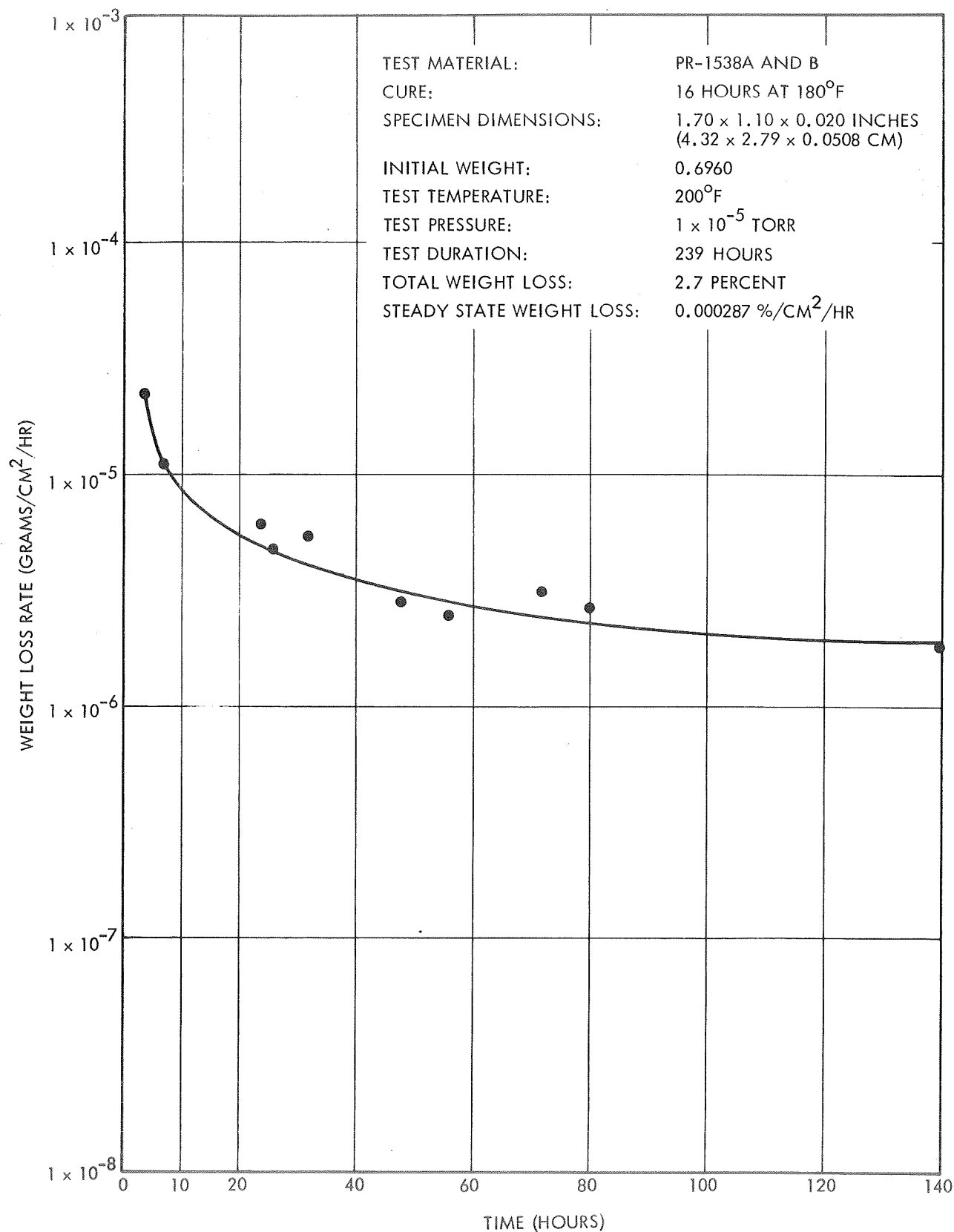


Figure 7.18 Weight Loss Rate Vs. Time
for PR 1538

<u>Test Specimen</u>	<u>Steady-State Weight Loss (%/cm²/hr.)</u>
--	0.04 (Allowable Value per Ref. 7.3)
RTV 3145	0.0000336
RTV 511 (RTV 511/577 similar)	0.0001445
DC-731 (RTV 118 similar)	0.000197
PR 1538	0.000287

As may be noted all the candidate adhesive were found to be well below the maximum allowable value. It is noted that for the Apollo Telescope Mount (ATM) program that Reference 7.3 rates RTV-118 as acceptable and RTV-511 or RTV-577 as unacceptable. RTV-3145 and PR 1538 were not evaluated in Reference 7.3. However, based upon the limited outgassing testing conducted during this program, all four candidate adhesives should prove satisfactory for most applications including the lunar surface case.

7.3.5 Other Module Material Properties

The properties for the other typical materials used in solar array modules were obtained by a survey of existing data. These other material properties have been listed in Table 7.6. The table provides that data which was available and considered to be representative for the temperature conditions specified. Because of the crystalline structure of single crystal silicon cells, it is possible to get quite a wide range of ultimate tensile strengths (19000 to 28000 psi). This material property is very sensitive to the method used in growing the silicon ingot and also the etching technique utilized. The value shown in Table 7.6 is the minimum estimated one and hence should be conservative for design use. The analysis of Section 5.2 utilized this lower value in establishing the spalling failure mode. The graphite composite - Morganite Type II material properties are influenced by the fiberglass epoxy matrix that the filaments are bonded to. In addition, the techniques and processes used to make these composite substrate facesheets can also influence the overall material properties. In both instances, selective material sample testing is recommended to insure that the required minimum material properties have been obtained.

8. ENGINEERING TEST MODULE DESIGN

Three Engineering Test Modules were designed and designated ETM IA, ETM IIA, and ETM IIIA. Three substrate facesheet materials were represented, namely; Fiberglass, Kapton, and graphite composite.

In order to accommodate all of the possible combinations of cell type, solder status, interconnects, bond spot thickness and area, and bond adhesive type, each module contained a matrix of 400 cells arranged to provide a cross-matrix of characteristics as shown in Figure 8.1.

The cells covered an area of 16.37 x 16.70 inches on substrate panels that are either 19.5 x 19.5 inches or 20 x 20 inches, allowing a rim around the edge without cells for handling and mounting to the structural-dynamic test fixture.

A summary of characteristics represented in the matrix is as follows:

Cell Type	2 cm x 2 cm x 0.010 in. thick
Cell Material	Silicon-Random Crystal Orientation Silicon-Preferred Crystal Orientation
Solder Status	Solder Backed Non-solder Backed
Interconnect Status	Interconnected Non-interconnected
Bond Spot Area	8% Cell Area 18% Cell Area 32% Cell Area 70% Cell Area
Bond Spot Thickness	0.005 inch 0.010 inch
Adhesive Compounds	RTV 3145 RTV 511/577 (50-50 mix) RTV 118 PR 1538

8.1 ALUMINUM BOX BEAM FRAME/FIBERGLASS FACESHEET MODULE (ETM IA)

This module concept utilizes a Fiberglass facesheet substrate consisting of an aluminum extrusion box beam frame welded at the corners. The Fiberglass facesheet is put under tension and bonded to the aluminum box beam frame with adhesive and a riveted aluminum cap plate. The silicon

cells are bonded to the facesheet in the pattern shown on Figure 8.1. The overall ETM IA design is shown on Figure 8.2.

8.2 FLEXIBLE KAPTON SUBSTRATE - ALUMINUM HONEYCOMB ENDPLATES (ETM IIA)

This module concept utilizes a flexible Kapton sheet substrate with aluminum honeycomb endplates to provide for support and stowage during structural dynamic testing.

The solar cells, arranged in orthogonal rows, are bonded directly to the Kapton substrate with bond spots dimensioned as outlined in Figure 8.1. The overall ETM IIA design is shown in Figure 8.3.

8.3 ALUMINUM HONEYCOMB-GRAPHITE/EPOXY COMPOSITE (ETM IIIA)

This module concept utilizes an aluminum honeycomb core and a graphite/epoxy composite facesheet substrate panel.

In this substrate concept, the facesheets are theoretically electrically self-insulating by virtue of the epoxy resin matrix. However, in actual practice, the presence of sufficient thickness of epoxy on the surface graphite filaments to prevent some contact and electrical leakage is not sufficiently reliable. Therefore, a Kapton film dielectric sheet as described in Section 4.4.3 was used to insulate the silicon cells from the facesheet. The solar cells are similarly arranged in accordance with the matrix shown on Figure 8.1. The overall ETM IIIA design is shown in Figure 8.4.

8.4 SOLAR CELL SUB-MODULE CELLSTACK DESIGN

The candidate solar cell sub-module cellstack design consisted of two 2 x 2 cm cells in parallel by five 2 x 2 cm silicon cells in series for a total of ten cells per sub-module. The cell dimensions are nominally 0.788 x 0.788 inches and have an active area of 0.589 in² (3.80 cm²). The cells have a thickness of 0.010 \pm 0.002 inches. The base resistivity of these cells was not considered to be a critical parameter during this program phase. Hence, both 2 ohm-cm and 10 ohm-cm cells were considered acceptable and the use of either type was based upon their availability.

Typical electrical power characteristics for these 2 x 2 cm silicon cells at 28°C and AMO conditions are 470 mv x 124 ma (2 ohm-cm) and 430 mv x 128 ma (10 ohm-cm). With both 5% glassing losses degrading the voltage

output and an additional 5% assembly loss assumed for the current, the nominal electrical output for the candidate submodule would be 2.35 v x 228 ma (2 ohm-cm) and 2.15 v x 235 ma (10 ohm-cm) respectively. The beginning-of-life (BOL) power output for each 10 cell sub-module would range from 0.506 to 0.535 watts. For the configuration shown on Figure 4.12, this corresponds to a BOL power density of 11.0 to 11.6 watts/ft².

The interconnector design for the sub-module is also shown on Figure 4.12. It consists of a common U-shaped configuration (Figure 4.13) to connect the inner sub-module cells. A positive and negative bus bar (Figures 4.14 and 4.15) is provided for each solar cell sub-module. By grouping these sub-modules in series the desired overall module voltage can be obtained. The interconnect configuration has been designed so that the soldering pattern for both the U-shaped connectors and the bus bars are amenable to the use of automated soldering techniques. This is an important cost reduction consideration where large area solar arrays are involved. Thus, while the bus bar tooling creates eight solder holes in each element, only six of these holes will be solder to the cell solder zone.

A thermal stress analysis of the sub-module common interconnectors was conducted (Appendix A). The results indicated that the expansion loops incorporated in this design were adequate to prevent any occurrence of thermal differential stresses. Stresses in the bus bars and the solder joints in the region lacking expansion loops were found to be acceptable. A design margin in excess of 2 was estimated to exist for both the Kovar-silicon thermal interaction and the interconnect induced load on the solder joint. However, due to the statically indeterminant configurations associated with the overall interconnector design, the thermal vacuum tests are required to ultimately confirm the adequacy of this design.

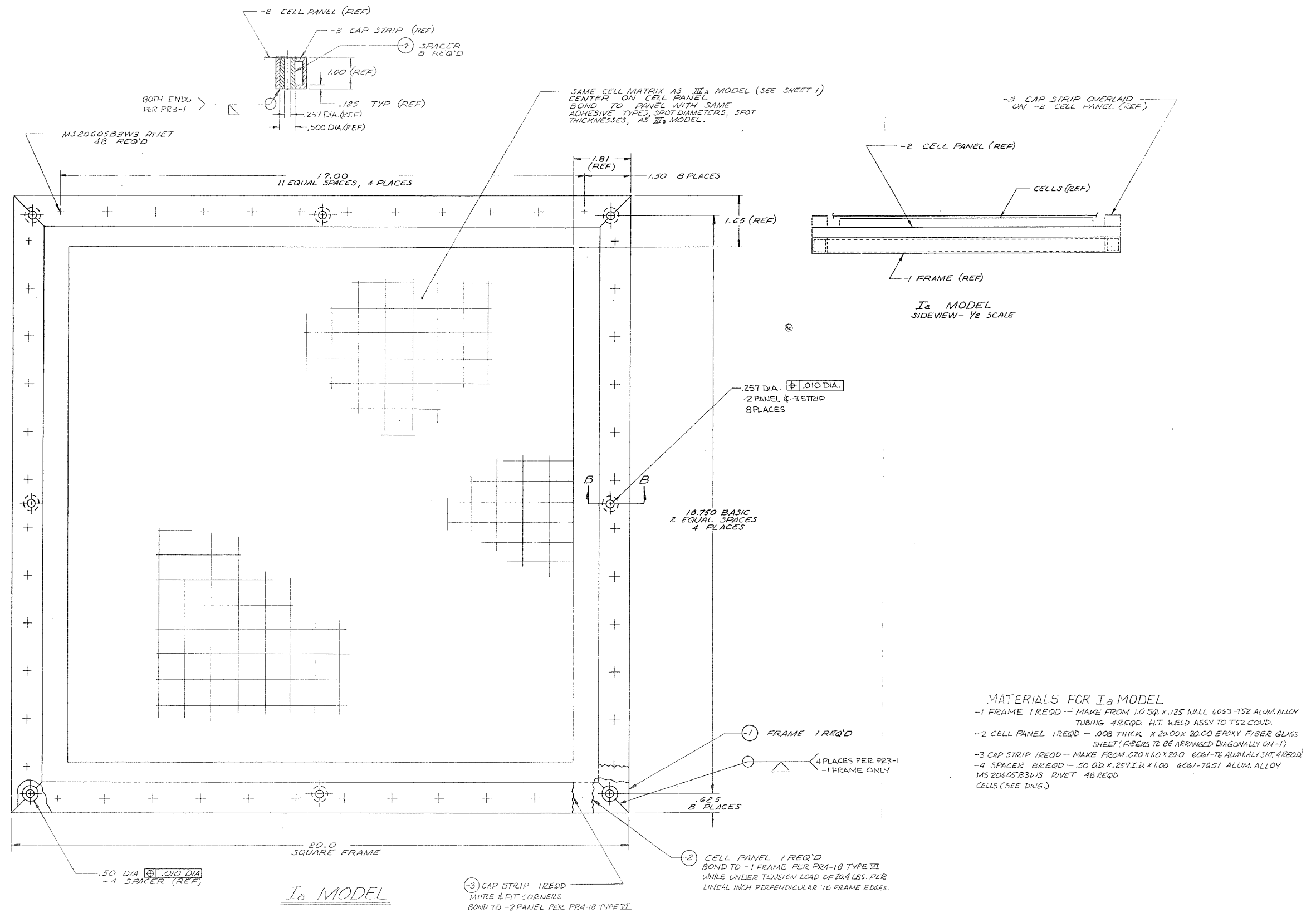
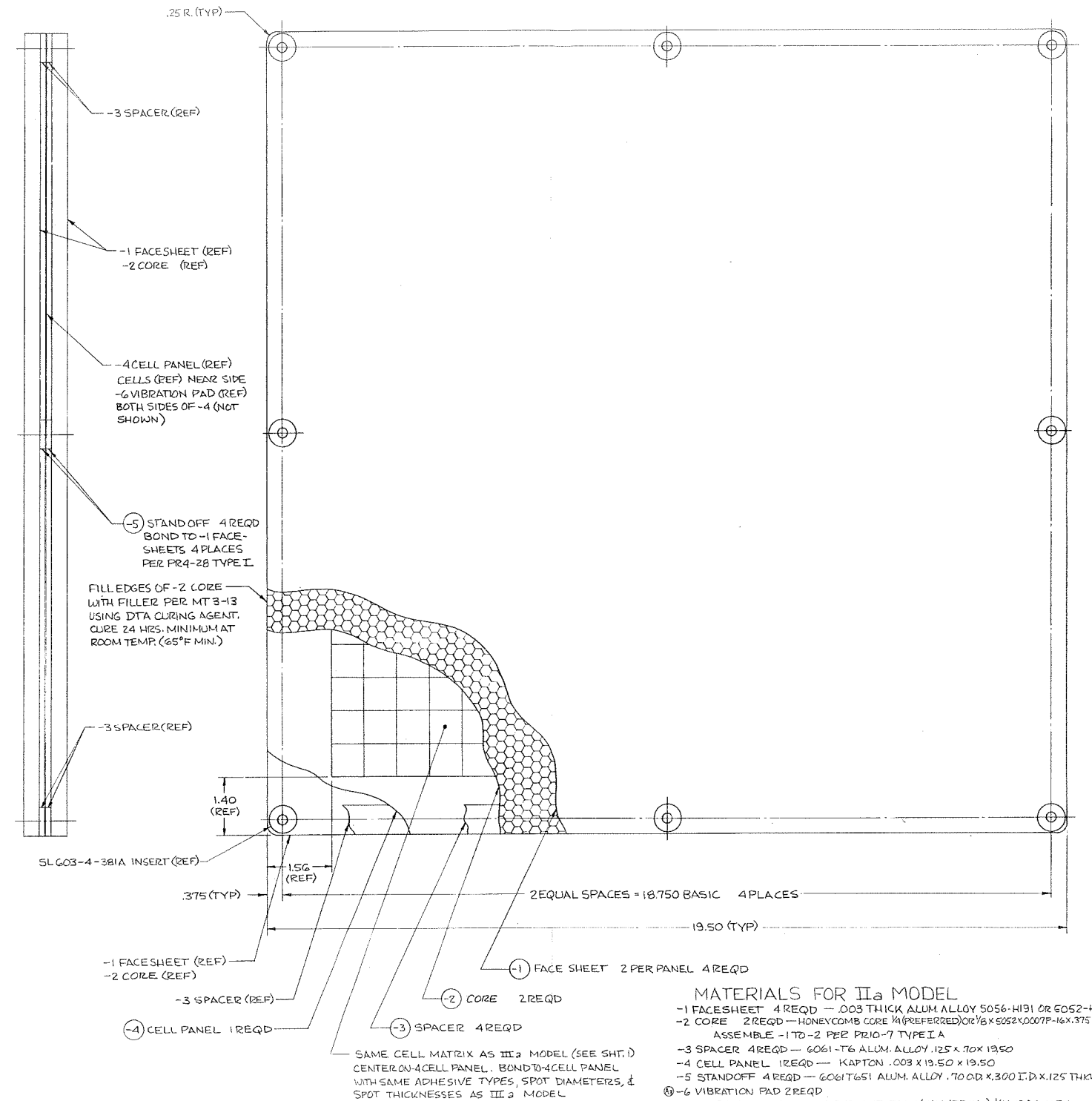
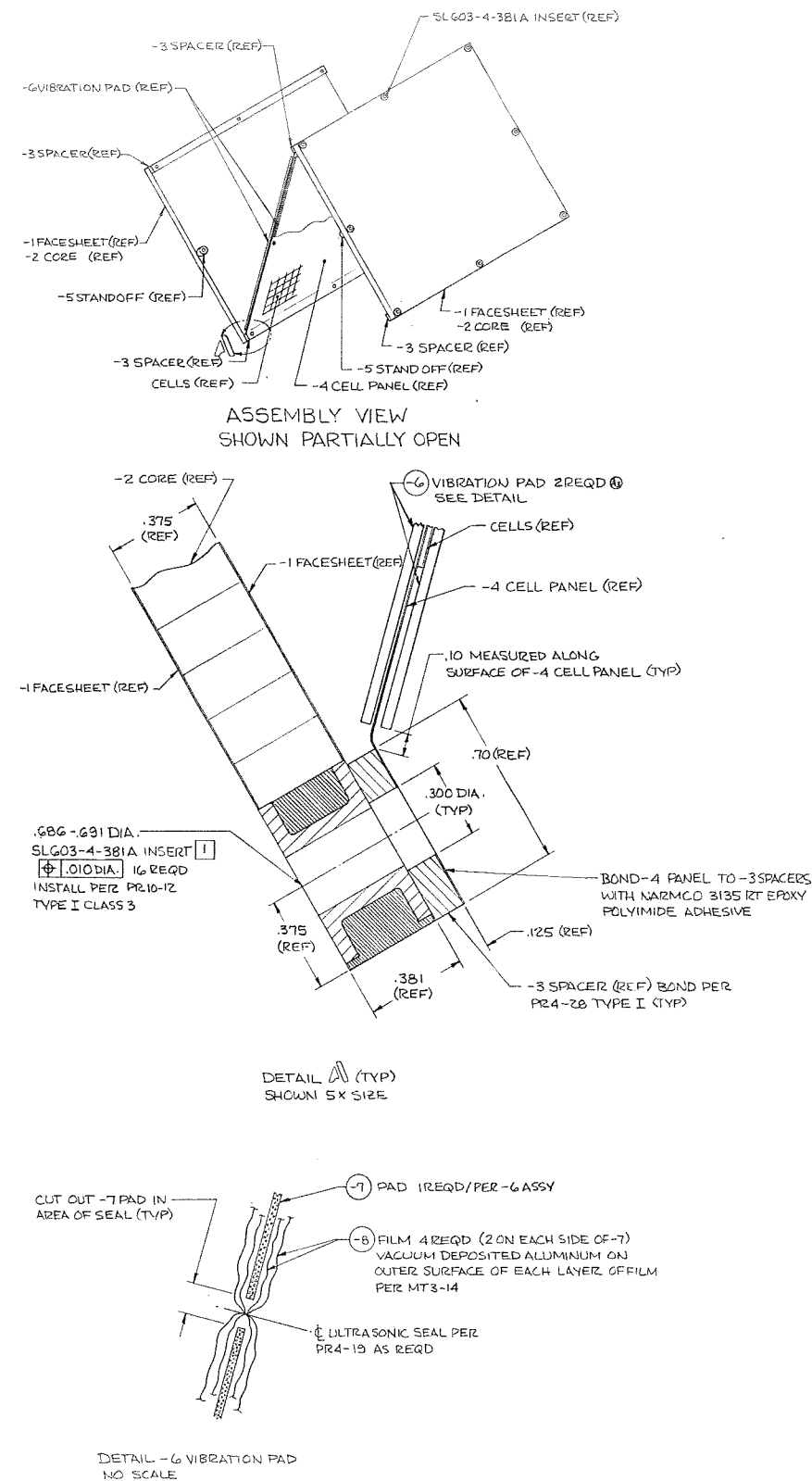


Figure 8.2 Aluminum Box Beam Frame/Fiberglass Facesheet Module Design (ETM IA)



IIa MODEL

- MATERIALS FOR IIa MODEL**
- 1 FACESHEET 4 REQD - .003 THICK ALUM. ALLOY 5056-H191 OR 6052-H19
 - 2 CORE 2 REQD - HONEYCOMB CORE 1/8" (PREFERRED) OR 1/8" X 5052 X 0007P-16 X .375 THK ASSEMBLY -1 TO -2 PER PR10-7 TYPE I A
 - 3 SPACER 4 REQD - 6061-T6 ALUM. ALLOY .125 X .70 X 19.50
 - 4 CELL PANEL 1 REQD - KAPTON .003 X 19.50 X 19.50
 - 5 STANDOFF 4 REQD - 6061-T6 ALUM. ALLOY .70 OD X .300 I.D. X .125 THK
 - ⑥ -6 VIBRATION PAD 2 REQD
 - 7 PAD 1 REQD - POLYURETHANE FOAM (COMMERCIAL) 1/4 X 17.90 X 17.90
 - 8 FILM 4 REQD - CRINKLED PLASTIC FILM .00025 THICK
 - ① SLG03-4-381A INSERT 8 REQD
 - SUGGESTED VENDOR: SHUR-LOK CORP., SANTA ANA CALIF. CORP. IDENT. 97393
 - ALTERNATE: FAB. FROM 6061-T6 ALUM. ALLOY PER SHUR-LOK CATALOG DIMS.
 - CELLS - SEE DWG.

Figure 8.3 Flexible Kapton Substrate-Aluminum Honeycomb Endplates (ETM IIA)

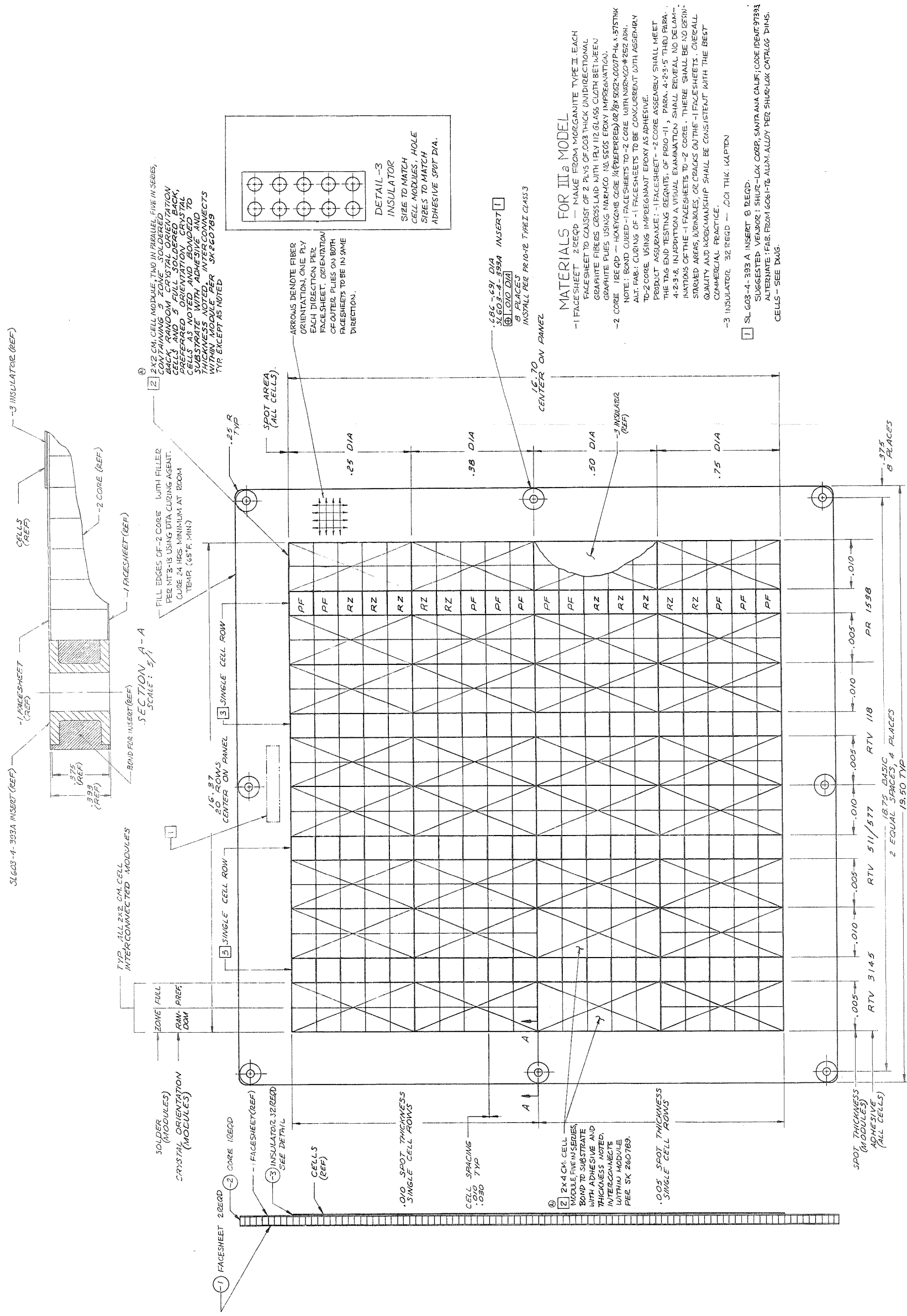


Figure 8.4 Aluminum Honeycomb - Graphite Epoxy Composite (ETM IIIA)

9. ENGINEERING TEST MODEL FABRICATION

9.1 MANUFACTURING CONSIDERATIONS

The three Engineering Test Models (Figure 8.2, 8.3, and 8.4) fabricated during this program phase utilized similar materials and manufacturing techniques as employed during Phase II. However, the standard 30 inches x 48 inches (76.2 cm x 123 cm) module built during this earlier phase was reduced to a nominal 20 inches x 20 inches (50.8 cm x 50.8 cm), to stay within the scope of this Phase III effort.

The main emphasis during this phase was to evaluate the spalling failure mode which occurred during thermal-vacuum testing in Phase II. However, it was also found desirable to evaluate the design integrity of the cellstack interconnects and solder joints as depicted in Figures 4.12 to 4.15. These designs differed from those used in Phase II (Reference 1.2) and confirmation of their ability to meet lunar surface power system environments was considered essential for total evaluation of the cellstack design. In addition, because 2 cm x 4 cm cells have been found cost-effective for use on large area solar arrays, two sub-modules using these size cells were added to each Engineering Test Model cell matrix in the regions where RTV 3145 adhesive was to be employed.

The process methods and procedures utilized in fabricating the ETM's were similar to those that would be utilized in standard TRW Systems solar array manufacturing operations. However, because of the great variety of adhesives types, thicknesses and dot diameters, as well as cell size (2 cm x 2 cm and 2 cm x 4 cm), cell mounting (flat laydown and overlap) and cell interconnecting (both interconnected and non-interconnected types), these standard production techniques were modified to be compatible with these configurations.

9.1.1 Factors Effecting ETM IA

The ETM IA built during this program phase was similar to the aluminum box-beam/fiberglass lattice diaphragm configuration (ETM I - Appendix C of Reference 2), built during Phase II with the following exceptions:

- (a) a one piece fiberglass diaphragm was substituted for the fiberglass tape lattice

- (b) the box beam frame was made from 1.0 in x 1.0 in x 0.125 in wall thickness 6063-T52 aluminum alloy tubing instead of 1.50 in x 0.75 in x 0.025 in wall thickness 6063-T6 aluminum alloy extrusions

These changes were made to be consistent with the scope of the program. The structural integrity of this design had been proven during Phase II and duplicating these more sophisticated fabrication techniques would unnecessarily increase manufacturing costs. The prime consideration in permitting these changes, was to assure utilization of a substrate material in the cell mounting area that had identical properties to the previously tested configuration (ETM I of Phase II).

The fiberglass diaphragm was bonded to the aluminum box beam frame using the adhesive and processes called out in TRW System Specification PR 4-18 Type VI. The diaphragm was kept under a tension load of 20.4 lbs. per lineal inch perpendicular to the box beam frame edges. A riveted cap strip was placed over the outer edges of the diaphragm. Finally, after sufficient time had been allowed for adhesive bond curing, the tensile loads were removed and the surplus diaphragm material was trimmed off. Under these conditions, the natural frequency of the pre-stressed diaphragm was estimated to be 124 Hz. (See Appendix C).

All the silicon cells were mounted to the fiberglass diaphragm in accordance with the cell matrix shown on Figure 8.4. All cells were individually numbered prior to bonding them to the substrate for future identification. The adhesive dot diameters were varied with four specific values utilized, namely; 0.25 in., 0.38 in., 0.50 in., and 0.75 in. dia. The drawing specified tolerance on these diameters was ± 0.03 inches. While it was not always possible to hold the nominal dot diameters to this tolerance due to variations in the viscosity of the adhesives, the tolerance that was maintained for the actual dot diameter in each of the cell matrix designated regions was ± 0.050 in. Similarly the nominal adhesive thicknesses (0.005 in. and 0.010 in.) were maintained to approximately ± 0.002 in., about a given "as fabricated" actual thickness.

The completed ETM IA is shown in Figures 9.1 and 9.2. The adhesive dot pattern is visible on Figure 9.2.

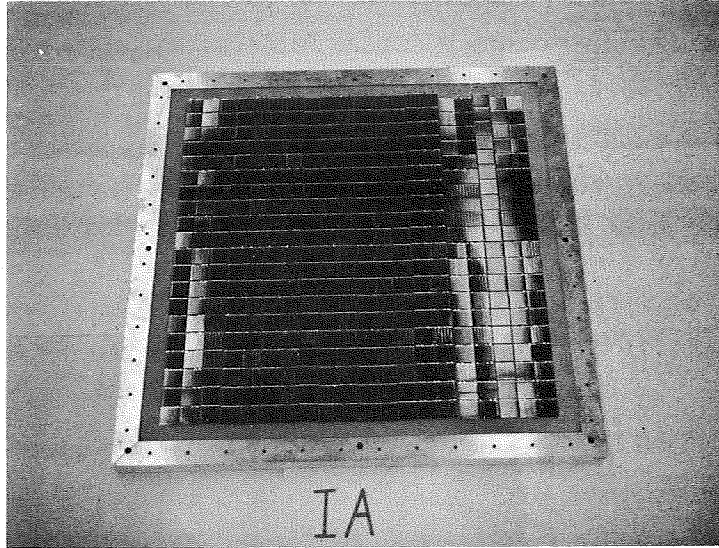


Figure 9.1 Front View of Engineering Test Model IA (Fiberglass Substrate)

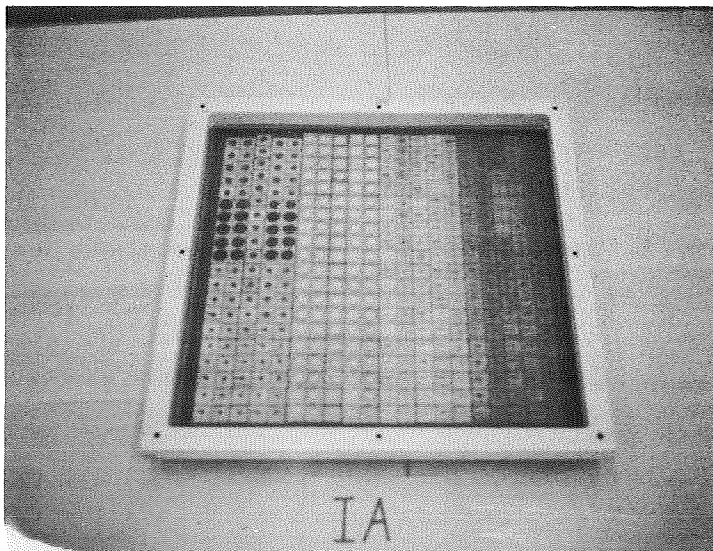


Figure 9.2 Rear View of Engineering Test Model IA (Fiberglass Substrate)

9.1.2 Factors Effecting ETM IIA

The ETM IIA built during this program phase was very similar to the flexible Kapton modules with the aluminum honeycomb endplates (ETM II - Appendix C of Reference 2), built during Phase II. The main difference were that one of the flexible Kapton modules was eliminated for economy reasons and the overall unfolded dimensions were nominally 19.5 in. x 58.5 in. (49.5 cm x 148.5 cm). The manufacturing techniques used were identical to those employed in Phase II and no difficulties were encountered.

Similar to ETM IA, all the silicon cells were mounted to the Kapton substrate in accordance with the cell matrix shown on Figure 8.4. Because of the flexibility of the Kapton, care was required in handling this configuration in the unfolded condition. The partially unfolded ETM is shown in Figure 9.3. The fully folded (stowed for launch operations) configuration is shown on Figure 9.4. This ETM is normally handled and shipped in the stowed condition. Polyurethane foam covered with aluminized mylar padding is placed on both sides of the Kapton module before it is clamped between the two aluminum endplates.

9.1.3 Factors Effecting ETM IIIA

The ETM IIIA built during this program phase utilized identical materials and manufacturing processes that were employed in fabricating the graphite composite module (ETM III - Appendix C of Reference 1.2) built during Phase II. The manufacturing and process control experience gained during this earlier phase resulted in the production of high quality, uniform textured graphite composite facesheets. This can be seen in Figures 9.5 and 9.6 where the uniformity can be judged by the black appearance of the high density of graphite filaments in the fiber-glass epoxy matrix. The completed ETM module is shown in Figure 9.7.

9.1.4 Factors Effecting the Interconnect and Bus Bars

The interconnects and bus bars used during this program phase were entirely redesigned from the configuration used during Phase II (Figure 7.15 of Reference 1.2). The common interconnect used between individual cells (Figure 4.13) were made from 0.001 in. thick Kovar (iron-nickel-cobalt alloy). This configuration was used on all the flat laydown cells. The 2 cm. x 4 cm cells were assembled in an overlap fashion and

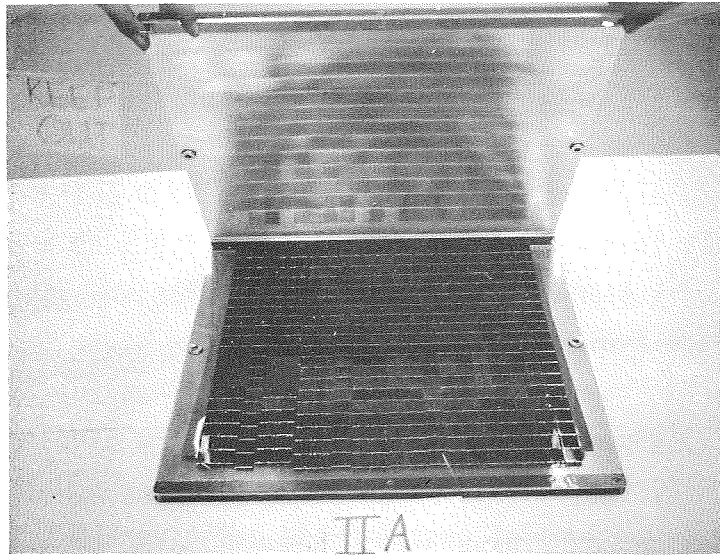


Figure 9.3 Front View of Engineering Test Model IIA (Kapton Substrate)

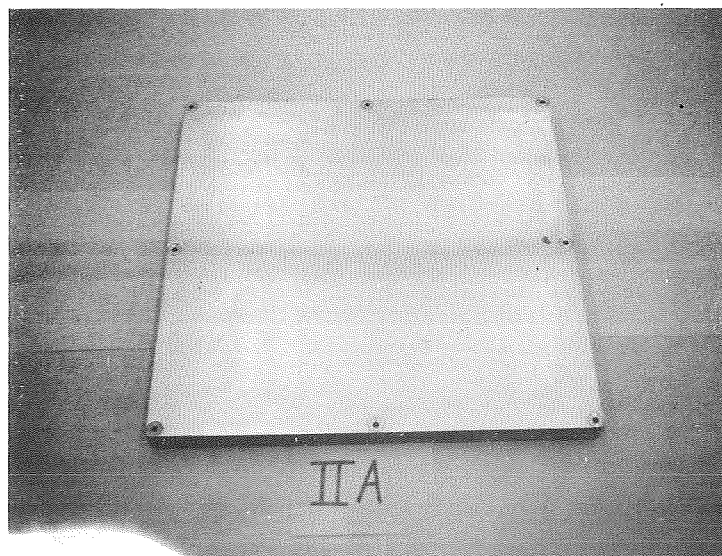


Figure 9.4 Top View of Engineering Test Model IIA Endplate (Aluminum Honeycomb with Aluminum Facesheets)

used a similar interconnect (Figure 9.8). Because of the overlap configuration, the length of the common interconnect in this case was shortened from 0.22 in. to 0.153 in. In addition, an expansion loop was added to compensate for the reduced length.

The positive and negative bus bars used for the 2 cm x 2 cm cells are as shown on Figures 4.14 and 4.15. These were designed to connect groups of sub-modules together, which consisted of 2 cells in parallel and five (5) cells in series. The bus bars for the 2 cm x 4 cm cells which consisted of sub-modules of 1 cell in parallel by five (5) cells in series were made from the same tooling as those shown on Figures 9.9 and 9.10. These bus bars had been used on a previous TRW Systems program (Project 777) and with minor modifications were used for this program. Finally, while not used on this program, Figures 9.11 and 9.12 represent improved versions of negative and positive bus bars suitable for use with either 2 cm x 2 cm or 2 cm x 4 cm cells. These improved configurations use a reduced height, soldering tab (from 0.110 in to 0.080 in) and a new stress relief loop to limit solder wicking action and to assure maintenance of flexibility required for thermal differential expansion requirements.

Because for certain applications (flexible foldup or roll-up arrays), the soldering tabs on the bus bars may not be desirable, it is possible to replace the bus bar configurations of Figures 9.11 and 9.12 with a multiple number of U-shaped interconnects as shown on Figure 9.8. For these latter cases, consideration should be given to this substitution in both the design and fabrication stages.

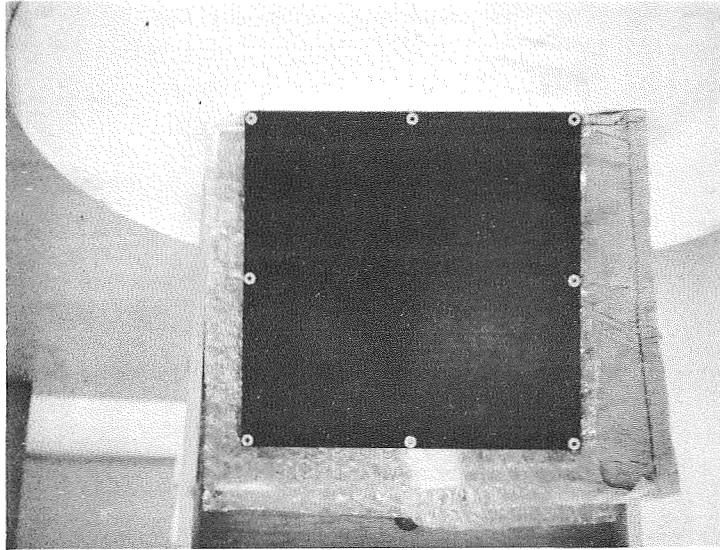


Figure 9.5 Front View of Graphite Composite Substrate for Engineering Test Model IIIA

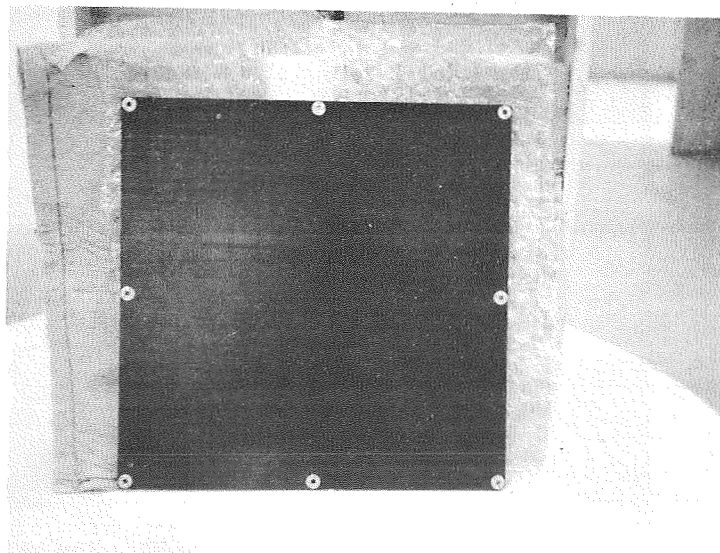


Figure 9.6 Rear View of Graphite Composite Substrate for Engineering Test Model IIIA

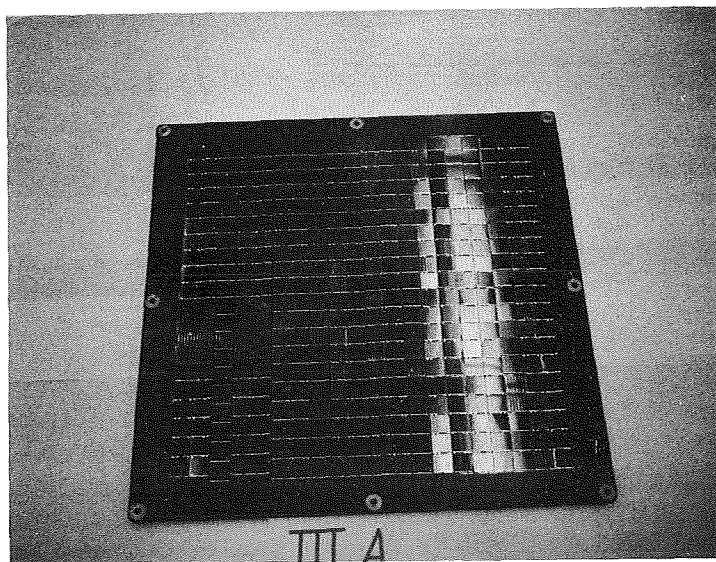
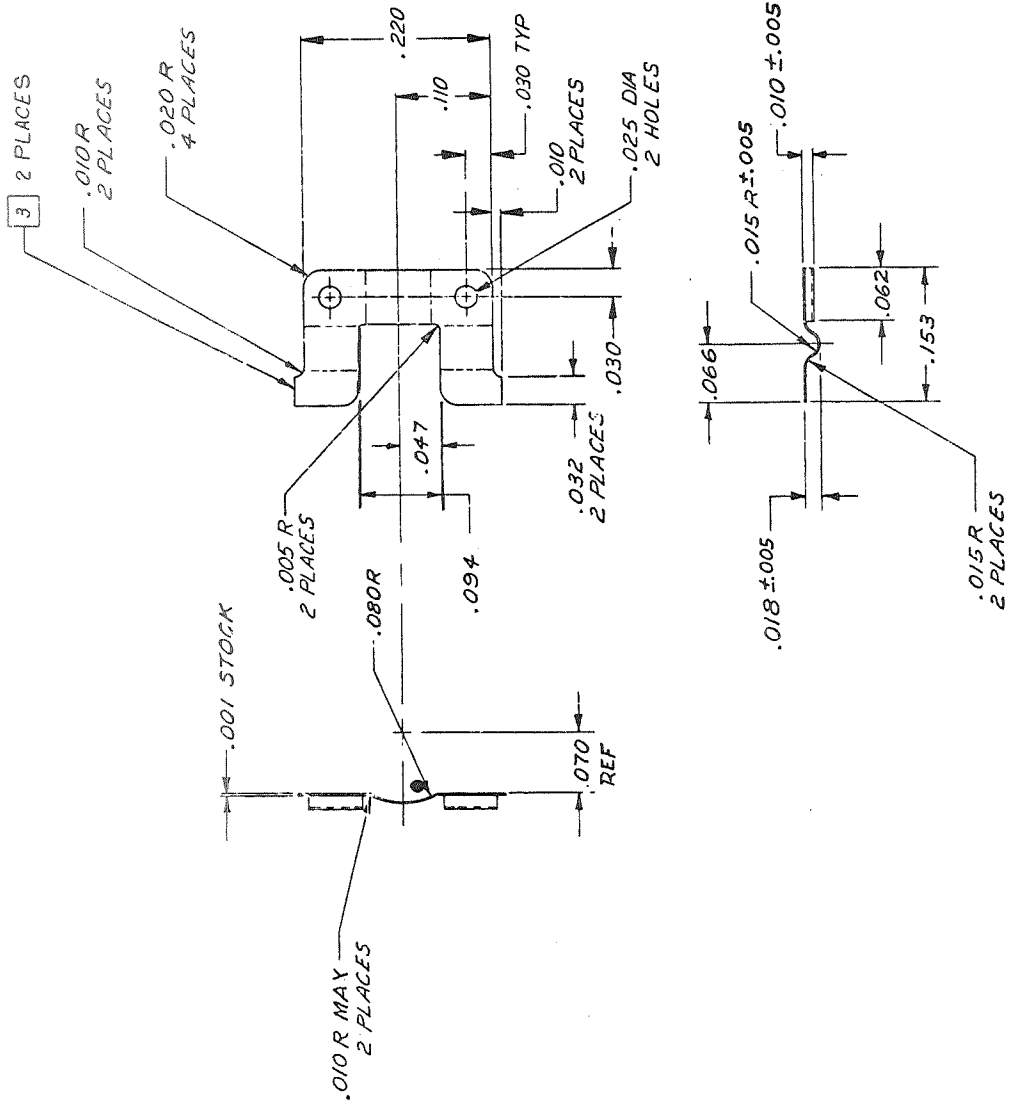


Figure 9.7 Front View of Engineering
Test Model IIIA (Graphite
Composite Substrate)



REFERENCE PRINT
CONFIGURATION & DATA MANAGEMENT
ISSUED

OCT 13 1970

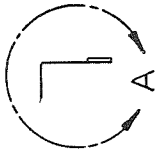
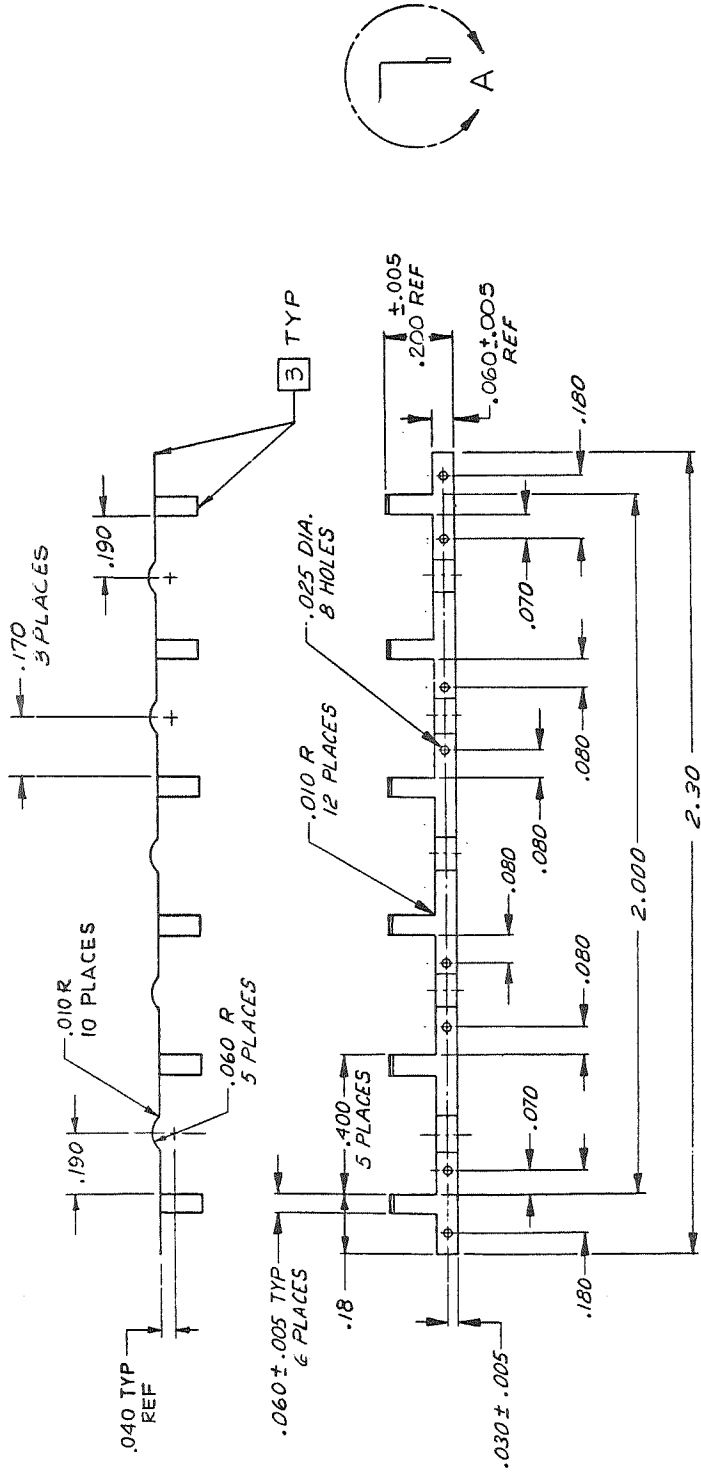
WILL NOT BE MAINTAINED CURRENT

1. NO PHASE TRANSFORMATION SHALL OCCUR IN THE MAT'L BETWEEN 1100°C AND -190°C.
2. ONLY PIECE PART SEPARATION EDGES MAY REMAIN UNPLATED
3. SOLDER PLATE & FUSE PER PRG-5 TYPE II EXCEPT PARA 3.3.4 PARA 3.4.2, NICKEL STRIKE .00003 MAX & COPPER PLATE .00005 TO .00015 PER MIL-C-14550 USING CYANIDE TYPE PYROPHOSPHATE OR ROCHELLE COPPER UNDER PLATING BATH, SOLDER PLATE .00008 TO .0002 MEASURED BEFORE FUSING.

1. IDENTIFICATION MARKING PER PR 1231
TYPE 2 CLASS 16 PART NUMBER _____

NOTES: UNLESS OTHERWISE SPECIFIED

Figure 9.8 Common Interconnect for
2 cm x 2 cm Silicon Cells
(3 in Parallel)



REFERENCE PRINT
CONFIGURATION & DATA MANAGEMENT
ISSUED

OCT 13 1970

DETAIL A
SCALE: 10/1

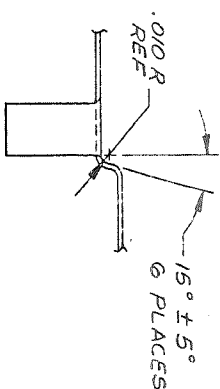
WILL NOT BE MAINTAINED CURRENT

- 4 NO PHASE TRANSFORMATION SHALL OCCUR
III THE MATERIAL BETWEEN 1100°C AND -190°C.
- 3 ONLY PIECE PART SEPARATION EDGES MAY REMAIN UNPLATED
- 2 SOLDER PLATE & FUSE PER PRG-5, TYPE II, EXCEPT PARA. 3.3 & PARA 3.4.2, NICKEL STRIKE .00003 MAX & COPPER PLATE .00005 TO .00015 PER MIL-C-14550 USING CYANIDE TYPE PYROPHOSPHATE OR ROCHELLE COPPER UNDER PLATING BATH. SOLDER PLATE .00008 TO .0002, MEASURED BEFORE FUSING.

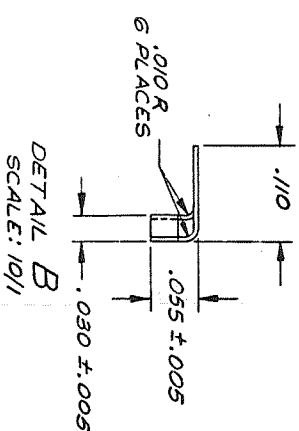
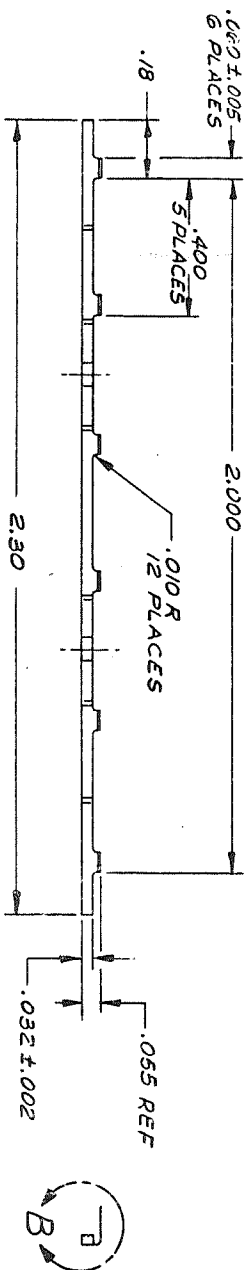
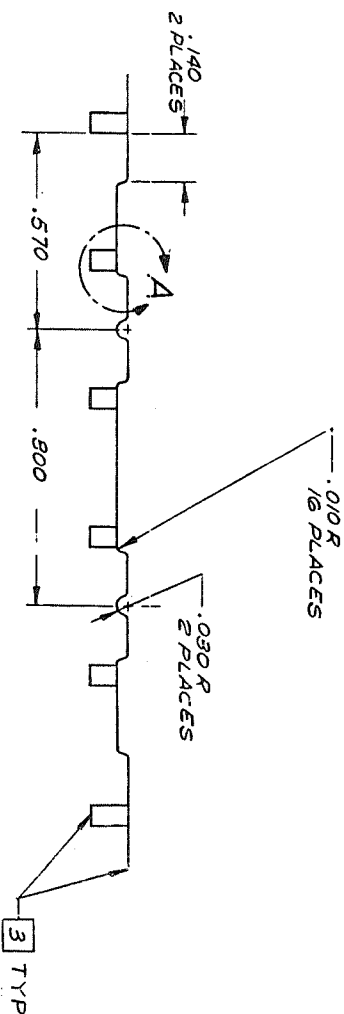
1. IDENTIFICATION MARKING PER PR 123
TYPE 2 CLASS 15 PART NUMBER

NOTES: UNLESS OTHERWISE SPECIFIED

Figure 9.9 Positive Bus Bar for
2 cm x 2 cm Sub-Modules
(3 in Parallel)



DETAIL A
SCALE: 10/1



DETAIL B
SCALE: 10/1

1. NO PHASE TRANSFORMATION SHALL OCCUR IN THE MATERIAL BETWEEN 1100°C AND -190°C
2. ONLY PIECE PART SEPARATION EDGES MAY REMAIN UNPLATED.
3. SOLDER PLATE & FUSE PER PRG-5, TYPE II, EXCEPT PARA. 3.3 & PARA. 3.4.2. NICKEL STRIKE .00003 MAX & COPPER PLATE .00005 TO .00015 PER MIL-C-14550 USING CYANIDE TYPE PYROPHOSPHATE OR ROCHELLE COPPER UNDER PLATING BATH. SOLDER PLATE .00008 TO .0002 MEASURED BEFORE FUSING.

1. IDENTIFICATION MARKING PER PR 121
TYPE 2 CLASS 45 PART NUMBER

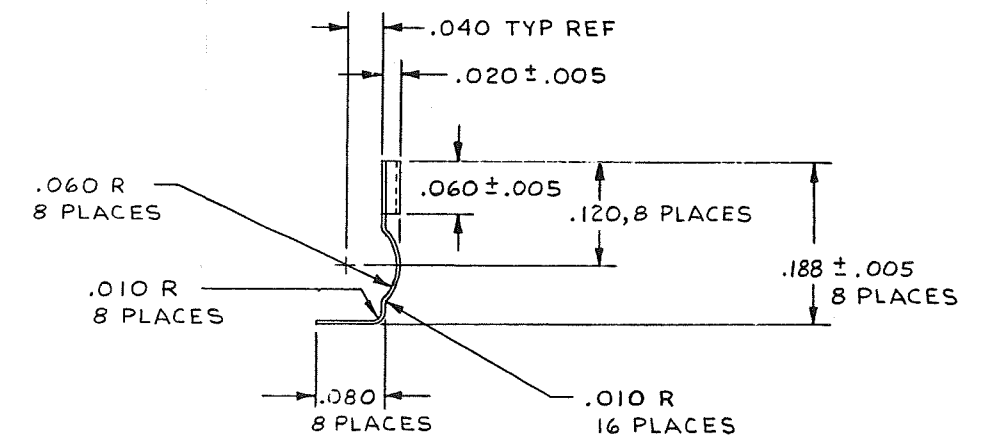
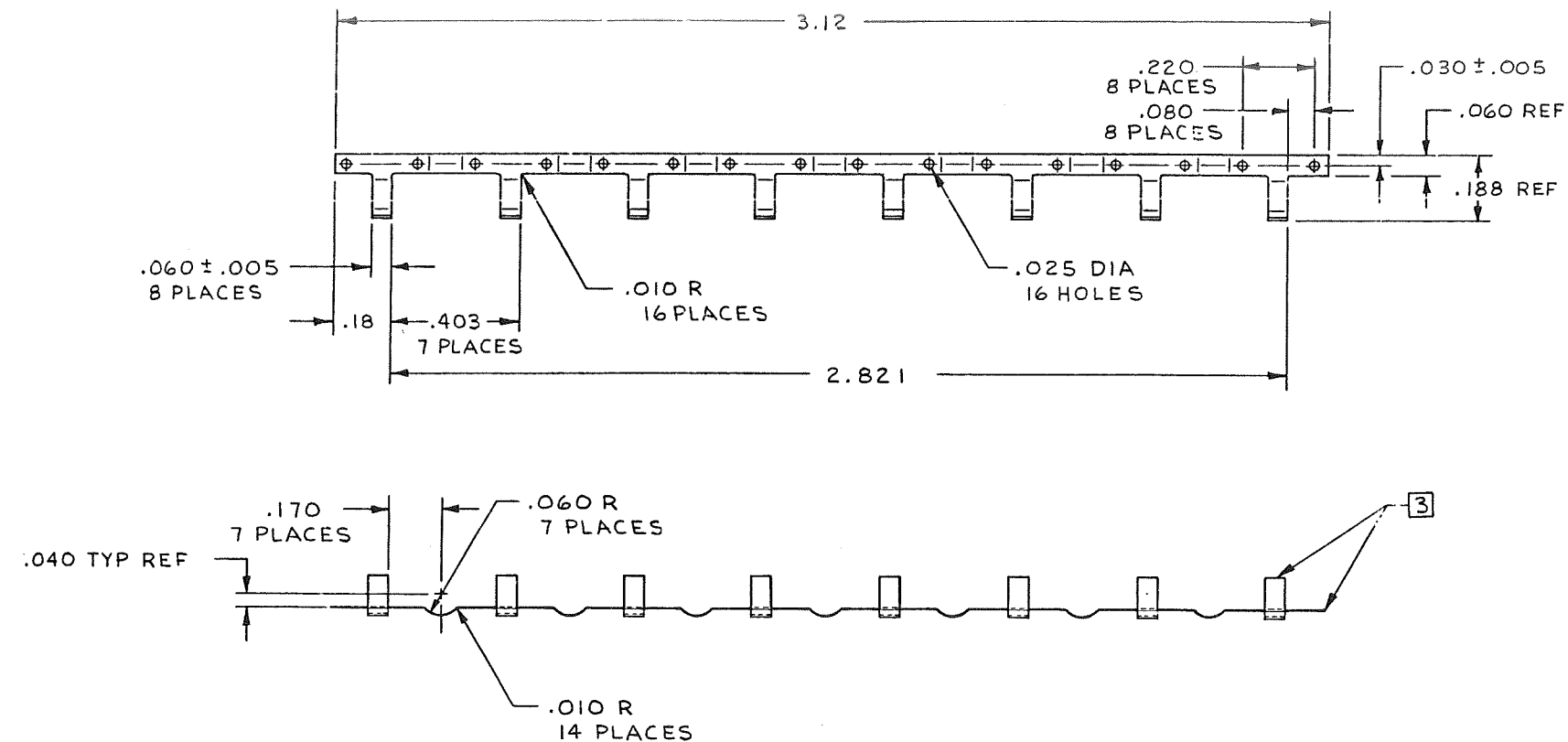
APPLICATION DATA WILL
NOT BE MAINTAINED

NOTES: UNLESS OTHERWISE SPECIFIED

REFERENCE PRINT
CONFIGURATION & DATA MANAGEMENT
ISSUED
OCT 13 1970

WILL NOT BE MAINTAINED CURRENT

Figure 9.10 Negative Bus Bar for
2 cm x 2 cm Sub-Modules
(3 cells in Parallel)



DETAIL A
SCALE: 10/1

REFERENCE PRINT
CONFIGURATION & DATA MANAGEMENT
ISSUED

OCT 13 1970

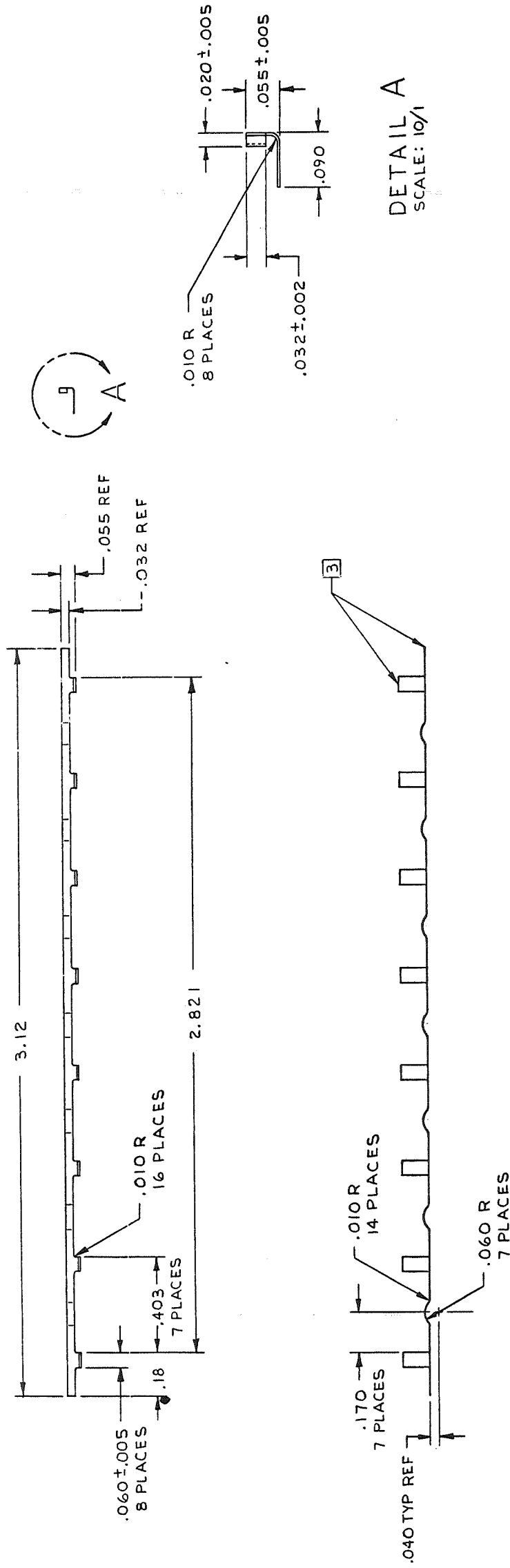
WILL NOT BE MAINTAINED CURRENT

- [4] NO PHASE TRANSFORMATION SHALL OCCUR IN THE MATERIAL BETWEEN 1100°C AND -190°C
- [3] ONLY PIECE PART SEPARATION EDGES MAY REMAIN UNPLATED
- [2] SOLDER PLATE AND FUSE PER PRG-5-2, EXCEPT PARA 3.3 AND PARA 3.4.2, NICKEL STRIKE .00003 MAX AND COPPER PLATE .00005 TO .00015 PER MIL-C-14550 USING CYANIDE TYPE PYROPHOSPHATE OR ROCHELLE COPPER UNDER PLATING BATH. SOLDER PLATE .00008 TO .0002, MEASURED BEFORE FUSING

1. IDENTIFICATION MARKING PER PR 12-1
TYPE 2 CLASS 1G PART NUMBER

NOTES: UNLESS OTHERWISE SPECIFIED

Figure 9.11 Improved Positive Bus Bar for 2 cm x 4 cm (2 in. Parallel) Silicon Cells



REFERENCE PRINT
CONFIGURATION & DATA MANAGEMENT
ISSUED

OCT 13 1970

SHALL NOT BE MAINTAINED CURRENT

- 4 NO PHASE TRANSFORMATION SHALL OCCUR IN THE MATERIAL BETWEEN 1100°C AND -190°C
- 3 ONLY PIECE PART SEPARATION EDGES MAY REMAIN UNPLATED
- 2 SOLDER PLATE AND FUSE PER PR6-5-2, EXCEPT PARA 3.3 AND PARA 3.4.2. NICKEL STRIKE .00003 MAX AND COPPER PLATE .00005 TO .00015 PER MIL-C-14550, USING CYANIDE TYPE PYROPHOSPHATE OR ROCHELLE COPPER UNDER PLATING BATH. SOLDER PLATE .00008 TO .0002 MEASURED BEFORE FUSING

1. IDENTIFICATION MARKING PER PR 12-1
TYPE 2 CLASS 1G PART NUMBER

NOTES: UNLESS OTHERWISE SPECIFIED

Figure 9.12 Improved Negative Bus Bar for 2 cm x 4 cm (2 in Parallel) Silicon Cells

10. ENGINEERING TEST MODEL TEST EVALUATION

10.1 TEST OBJECTIVES

The primary purpose of the test program, during this phase of the development effort, was to attempt to correlate the analytical model for the spalling failure mode with experimental data. The three Engineering Test Module cellstacks, each consisted of a sufficient number of variations in materials and material properties to span the range of parameters assessed in the analytical model. These included all the material variables depicted on the ETM cellstack matrix (Figure 8.1). In addition, the effect of three substrate materials (fiberglass, Kapton, and graphite composite) was also evaluated. The previous spalling failures had occurred during thermal-vacuum testing (Reference 7.2). The temperature profile used simulated the array temperature range on the lunar surface (Figure 4.11).

An additional test objective was to check the structural integrity of the common interconnects, positive and negative bus bars and their solder joints. Both structural-dynamic and thermal-vacuum testing (Reference 7.2) were conducted to evaluate these components of the cellstack design.

As in Phase II, the structural-dynamic test operations preceeded the thermal-vacuum testing. In addition, electrical performance characteristics (I/V curves) were obtained for all the electrically interconnected sub-modules on each ETM, before and after completion of the vibration tests. This was done to check for any malfunctions of the interconnects during these vibration tests.

10.2 TEST OPERATIONS

The three Engineering Test Models (ETM's) were received in the NASA/MSFC solar simulator test trailer July 7, 1970.

Electrical tests were performed July 9, 1970 on the as received modules. An I/V curve was recorded for each of the 32 interconnected cell groups (modules) of each ETM. Informal visual inspection revealed a few cracked or chipped cover slides; ETM IA had three, ETM IIA has six, and ETM IIIA had seven, but the electrical integrity of all test modules was intact.

Vibration tests were performed July 10 and 13, 1970. Sinusoidal, random high level, and random low level tests were performed on each of the three ETMs. The vibration survey was conducted in each of three mutually perpendicular axes (see Figure 10.1), using the levels specified in TRW Systems Test Plan No. 09681-6004-R000 (Ref. 7.2). No damage to the test articles was observed during these test runs. However, small bits of loose solder were seen bouncing on the surface of the ETMs during some of the runs. (See Figures 10.2 to 10.5).

Post vibration electrical tests and visual inspection of the ETMs were performed while preparation was made to run the thermal-vacuum tests. Several additional cracked or chipped cover slides were observed; ETM IA had five more than before testing, ETM IIA had possibly three more (although these could have been overlooked previously or could have occurred during electrical testing), and ETM IIIA had approximately twelve more. Electrical performance I/V curves revealed that four modules on ETM IA had developed malfunctions during the vibration tests. Two of the modules had failed completely open, and two had intermittent malfunctions. Within three of the failed groups, approximately 25 broken common interconnects were found using magnification aided inspection techniques, (see Figures 10.6 and 10.7), but none was found in modules that had passed electrical tests. Most (19) of the broken interconnects occurred in the RTV-118, 0.25 in. spot, diameter region while the remainder (6) appeared in the RTV-118, 0.375 in. region. However, interconnects showing work-hardened areas occurred throughout the modules. The fourth failed module had no broken common interconnects but did have a broken positive bus bar which occurred in the 0.75 in., RTV-3145 region. In addition to the broken interconnects, one solder joint between positive bus bars had separated. No broken interconnects or bus bars were found on ETM IIA or ETM IIIA, but one separated solder joint between bus bars was found on ETM IIA. The I/V curves for all modules on ETMs IIA and IIIA satisfactorily compared with the original curves.

Thermal-vacuum tests were performed August 17 thru 22, 1970. Each of the ETMs was instrumented with five thermocouples, (see Figure 10.8). On ETM's IA and IIA three sensors each were bonded on the back side of the fiberglass or Kapton sheets with RTV-3145. One sensor was bonded and one sensor was

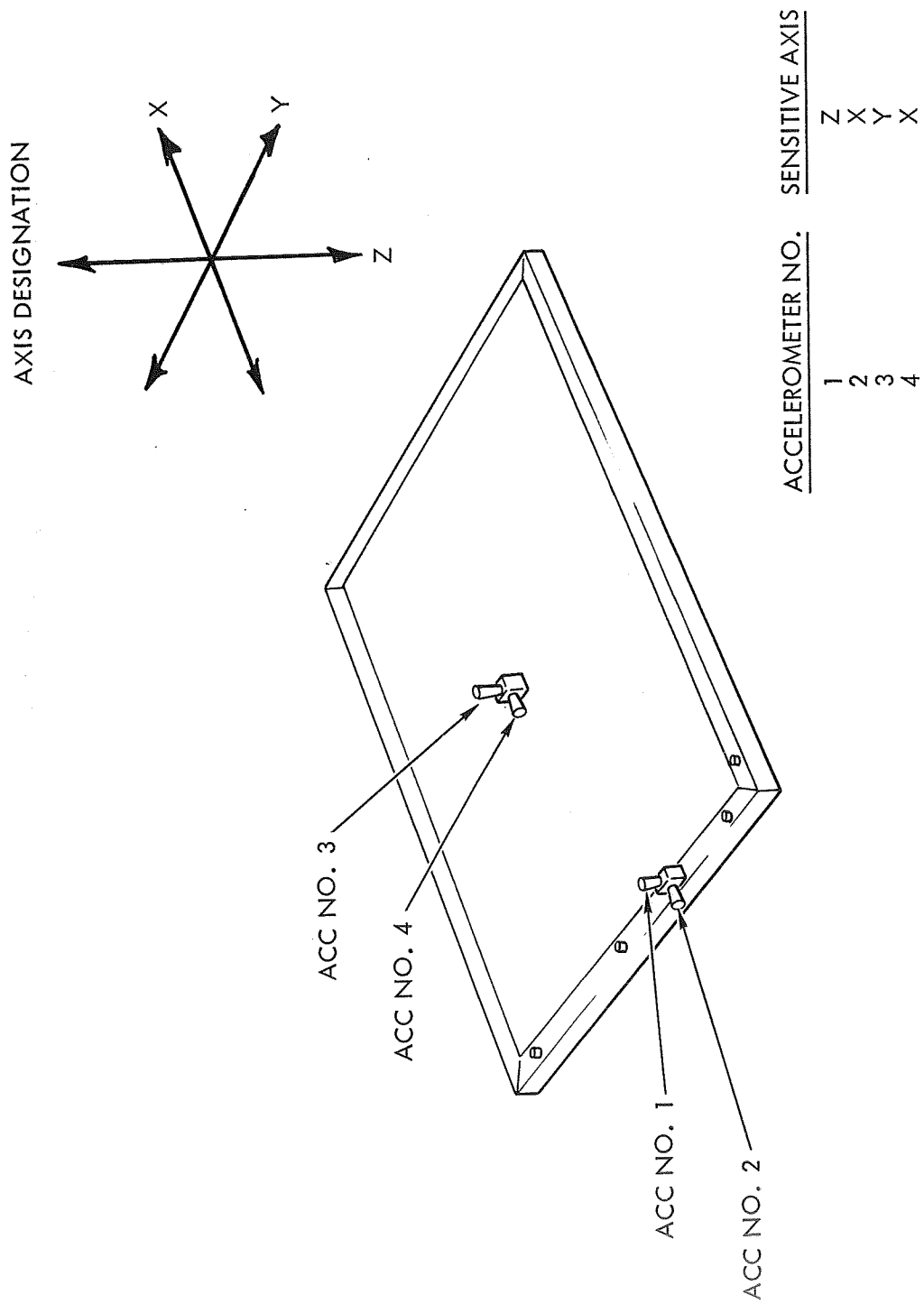


Figure 10.1 Typical Location and Orientation of Accelerometers on ETM Modules during X, Y, and Z Axes Vibration Testing

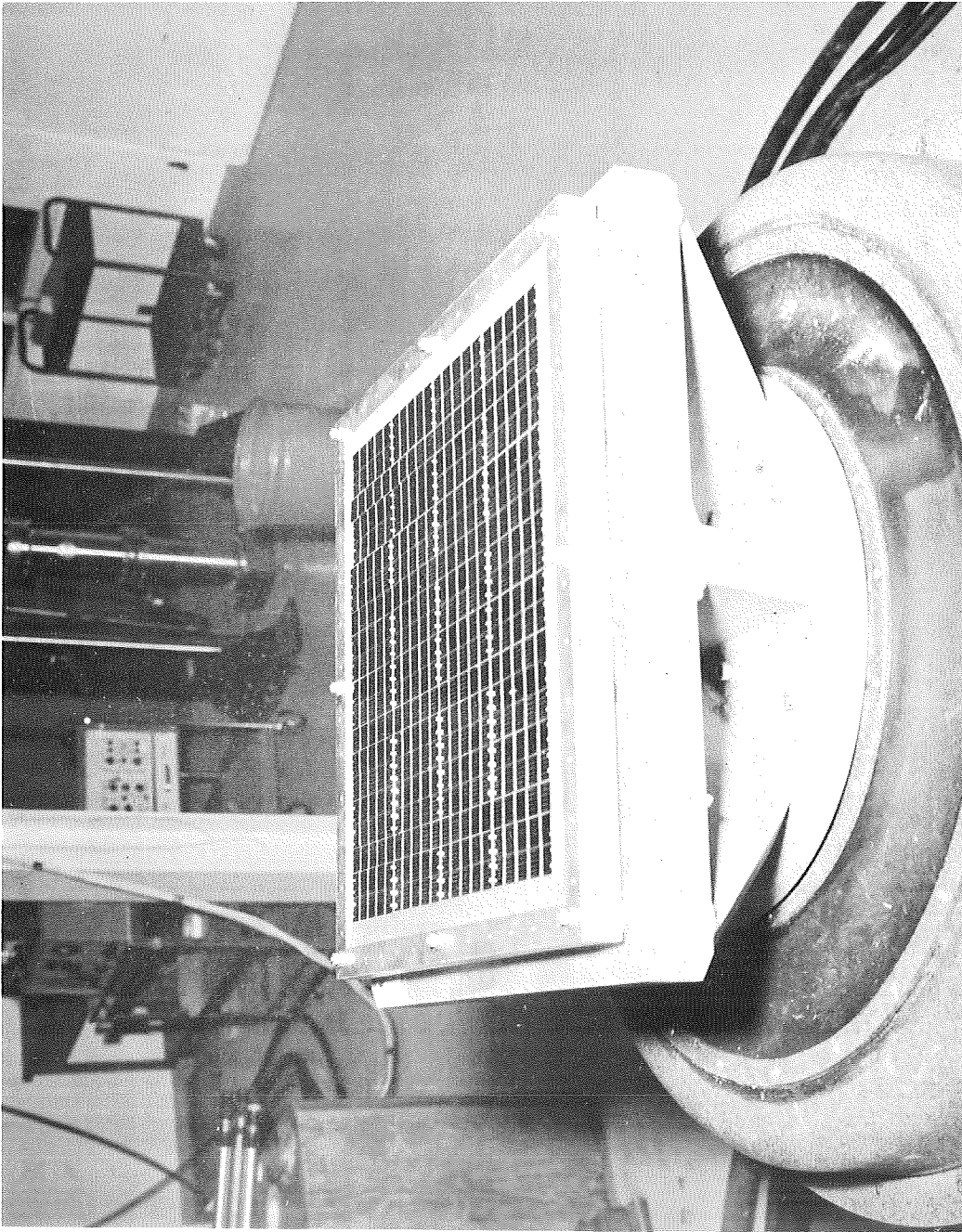


Figure 10.2 ETM IA Mounted on Shake Table Fixture
Before Being Subjected to Z-Axis Vibration

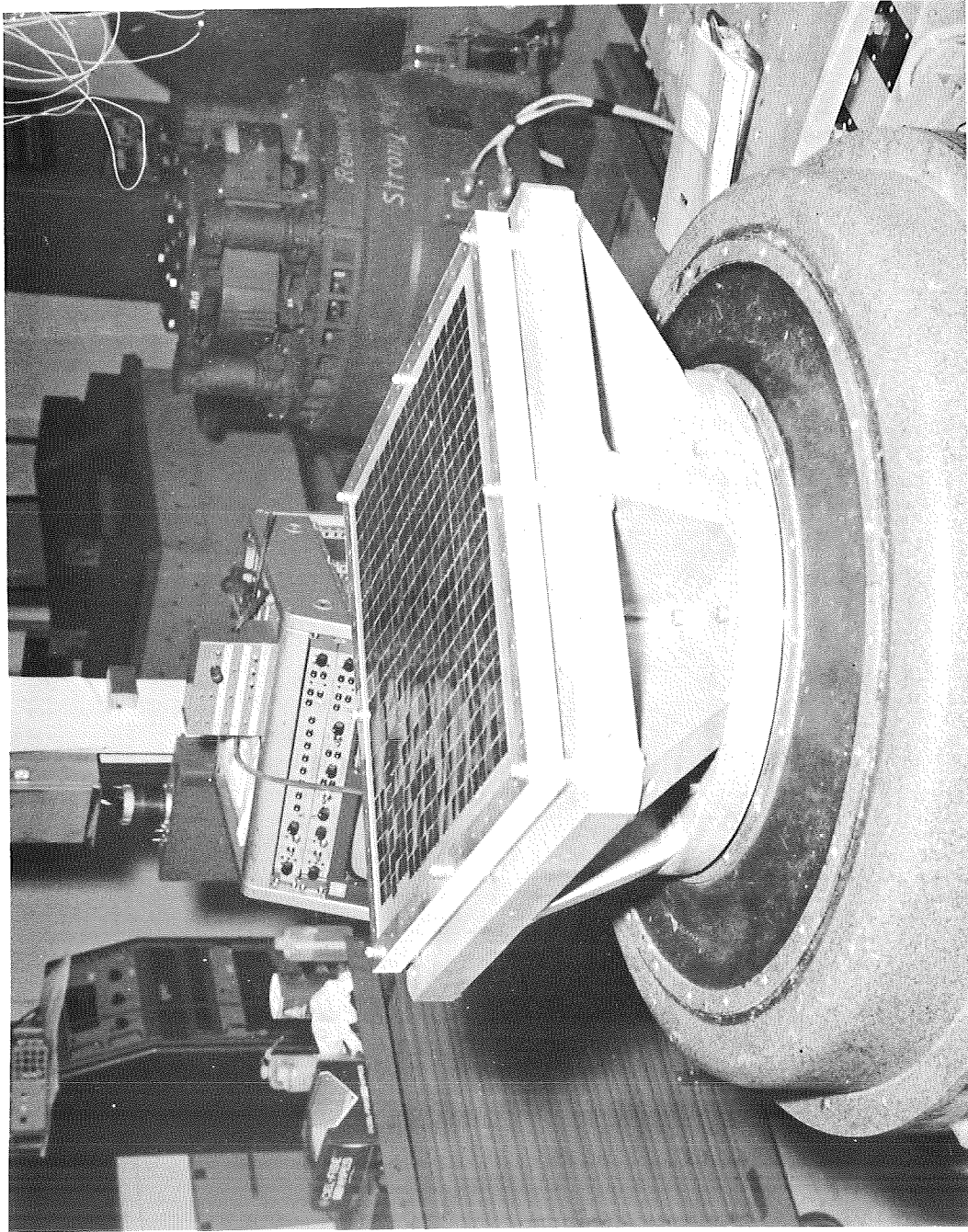


Figure 10.3 View of ETM IA Mounted on Vibration Test Fixture After Completion of Z-Axis Testing

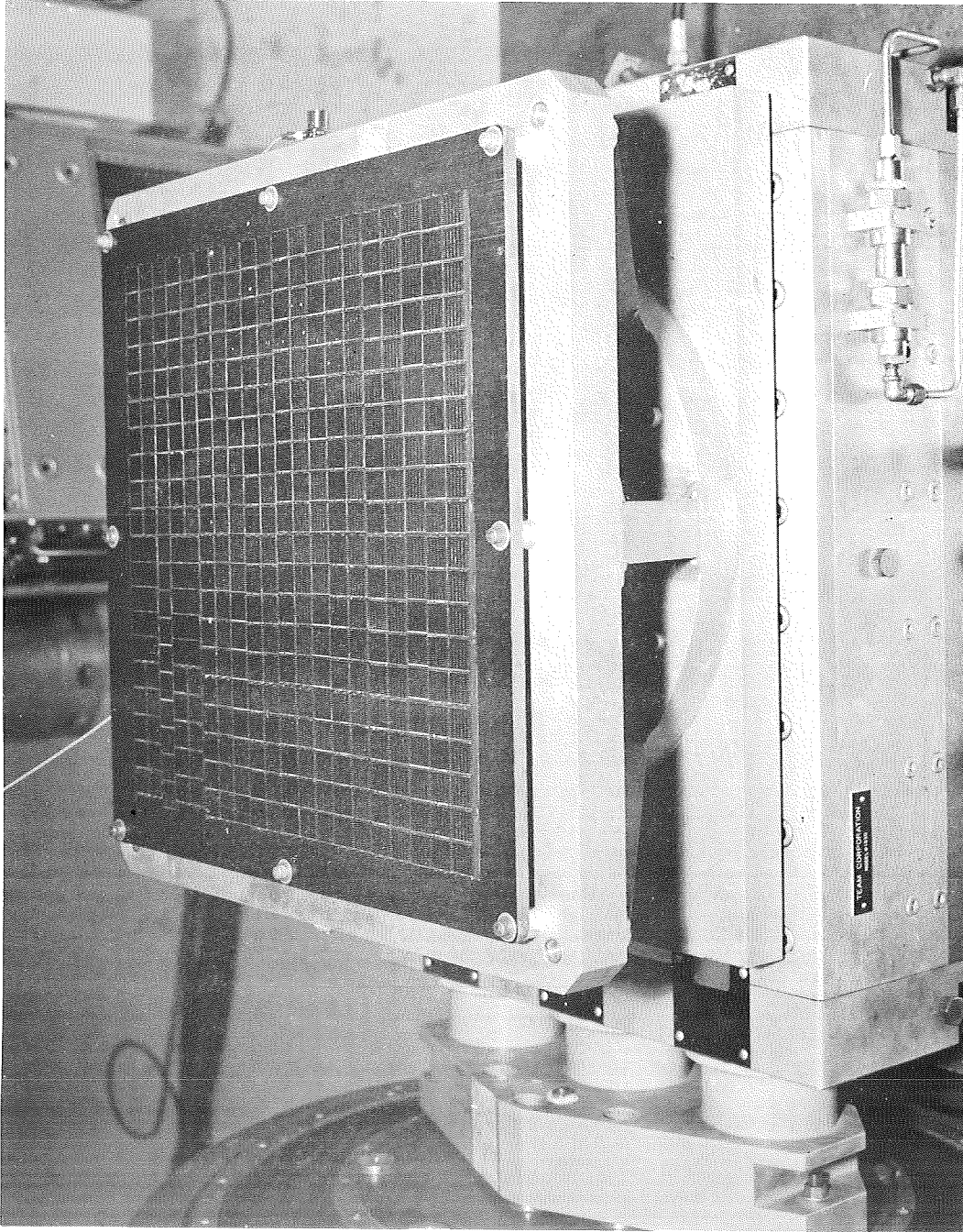


Figure 10.4 ETM IIIA Mounted on Shake Table Fixture
Before Being Subjected to X and Y Axes
Vibration

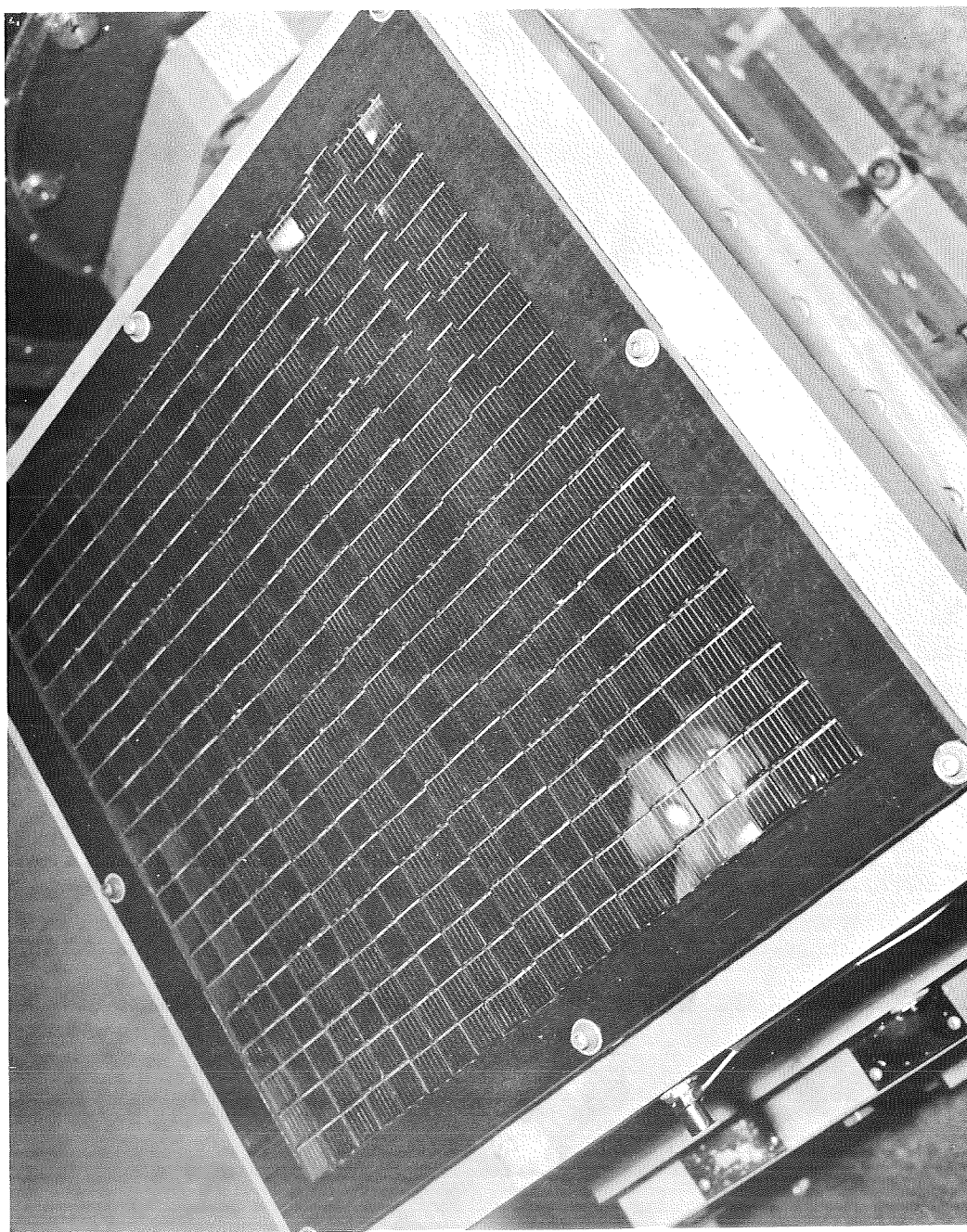


Figure 10.5 ETM IIIA Mounted on Shake Table Fixture
After Being Subjected to X and Y Axes
Vibration

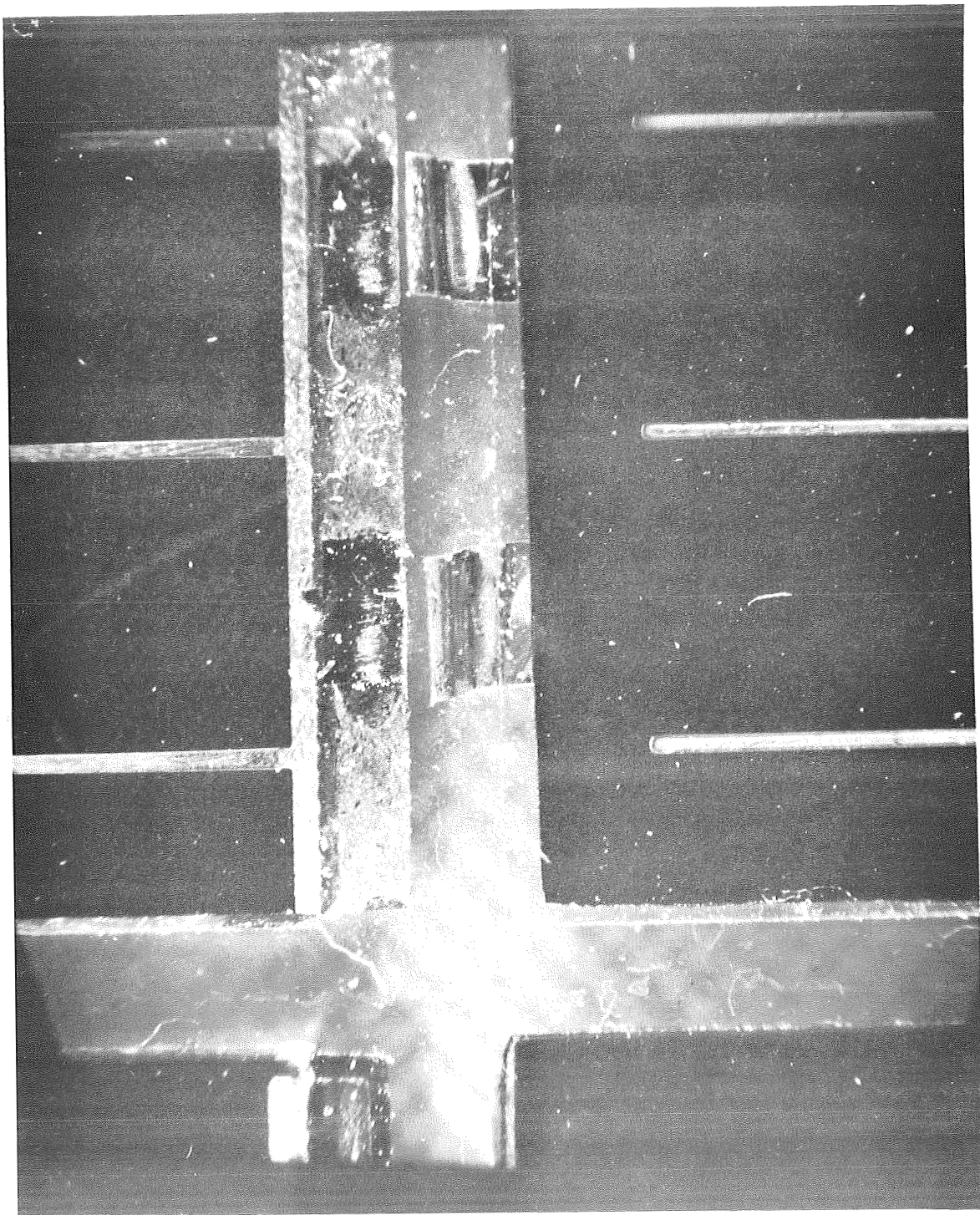


Figure 10.6 Enlarged View of Failed Common
Interconnects after Completion of
Z-Axis Vibration Testing on ETM IA

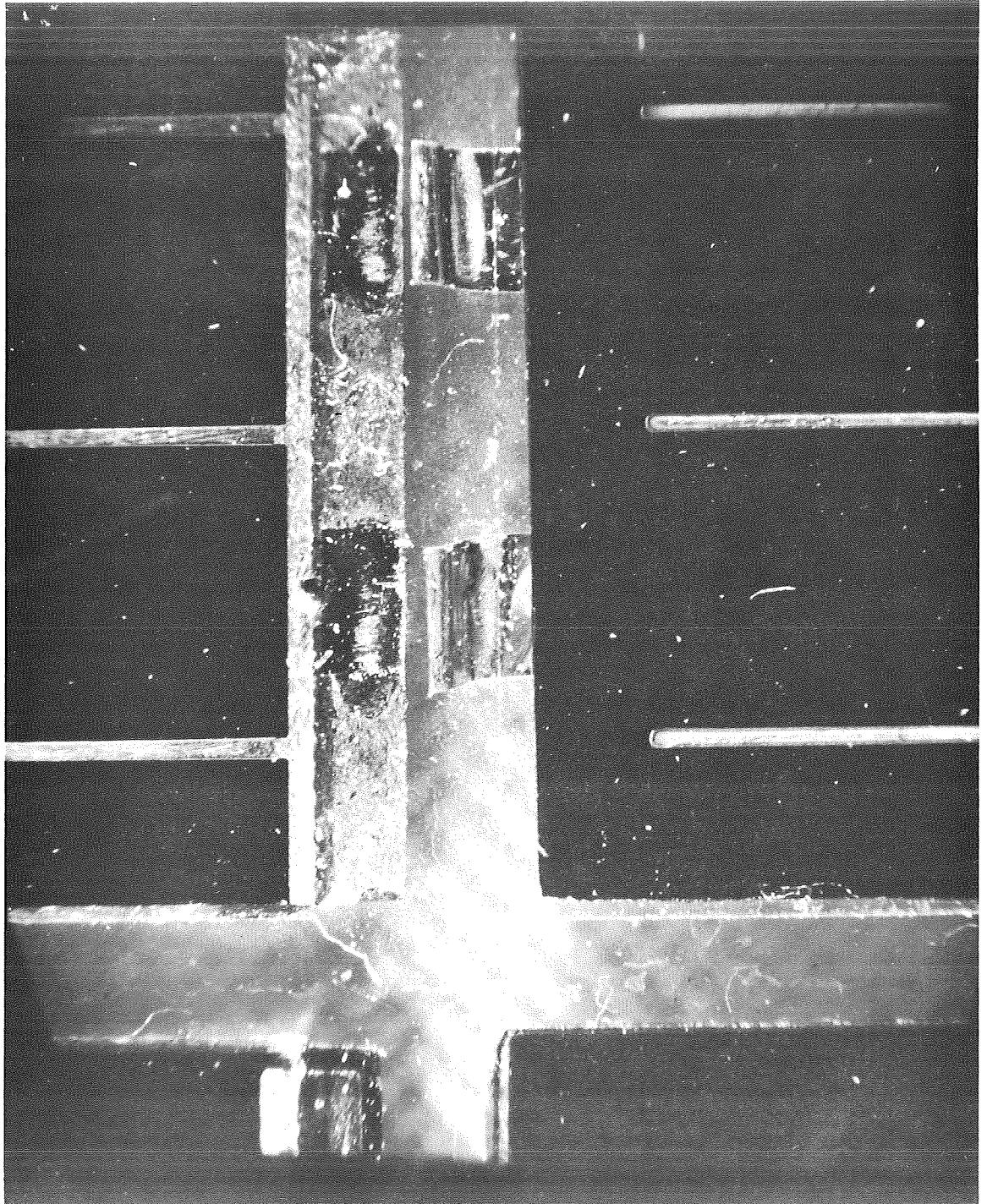


Figure 10.7 Magnified View of Failed
Common Interconnector on ETM IA
at Completion of Vibration Test

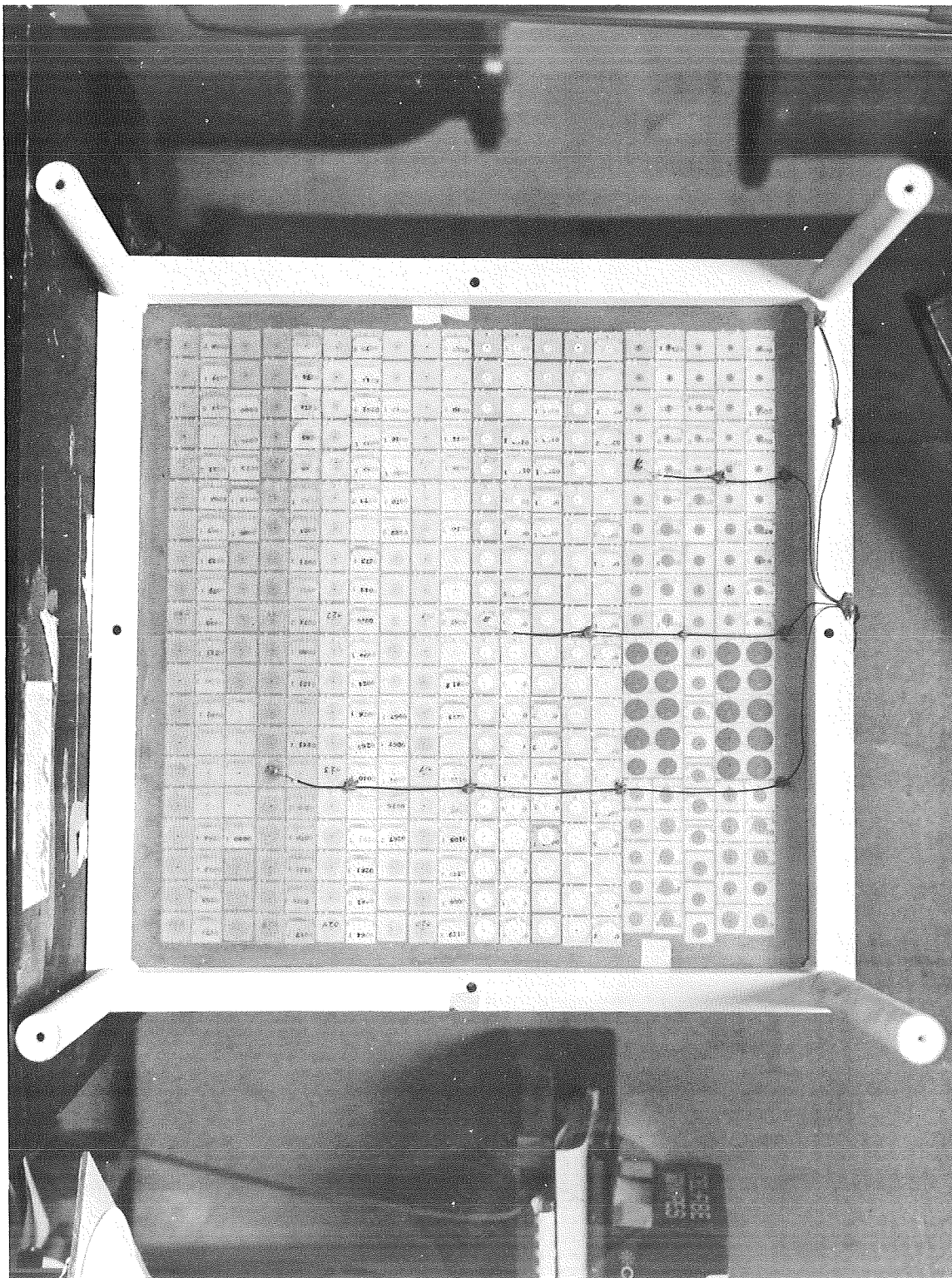


Figure 10.8 Back of ETM IA Showing the Location of Temperature Sensors

bolted to the metal frame in each case. On ETM IIIA three unconnected cells were lifted and rebonded with thermocouples in the adhesive spots. Three separate test runs were made, one for each of the ETM's. Seven channels of temperature data were recorded for each ETM test; two chamber shroud channels and five channels from sensors located on the ETM. Twenty-one computer generated plots of the data show that the ETM temperature was varied between the agreed upon limits of +120°C to -173°C. Two complete cycles with two hour soak times at each temperature extreme were achieved. An attempt was made to limit temperature changes to less than 4°C per minute. however this goal was exceeded in some cases. Figures 10.9 to 10.12 depict typical test set-ups in the thermal-vacuum chamber.

Post thermal-vacuum test I/V curves recorded for all modules of each ETM compared satisfactorily with those taken prior to the thermal-vacuum tests. No gross electrical failure of a module was detected in this manner; however, visual inspection of the common interconnects and positive bus bars revealed some damage. Solder joints between positive bus bars constituted the largest electrical failure mode as follows:

ETM IA	- 44 separated tabs
ETM IIA	- 1 separated tab
ETM IIIA	- 6 separated tab

On ETM IA two common interconnect solder joint failures and two additional broken interconnects were noted. Two broken interconnects were also found on ETM IIIA.

Failure of adhesive bonding was evident on all ETM's after thermal-vacuum tests. Tables 10.1, 10.2, and 10.3, shows the number of loose and spalled cells found for each of the adhesive types and spot diameters.

Multiple spalling occurred on ETM IA and IIA but only one case was noted on ETM IIIA. Spalling occurred on both the zone soldered and solder dipped cells. The 2 cm x 4 cm cell sub-modules exhibited considerable spalling (Figure 10.12A).

Several spots on the 2 cm x 4 cm cells were measured in an attempt to correlate the spot thicknesses to spalling. The spots measured all had diameters greater than 0.5 inch and less than 0.75 inch. The un-spalled spots ranged in thickness from 0.013 to 0.022 on the thin side and 0.022 to 0.031 on the thickest side. The spalled spot measurements fell within the same thickness ranges.

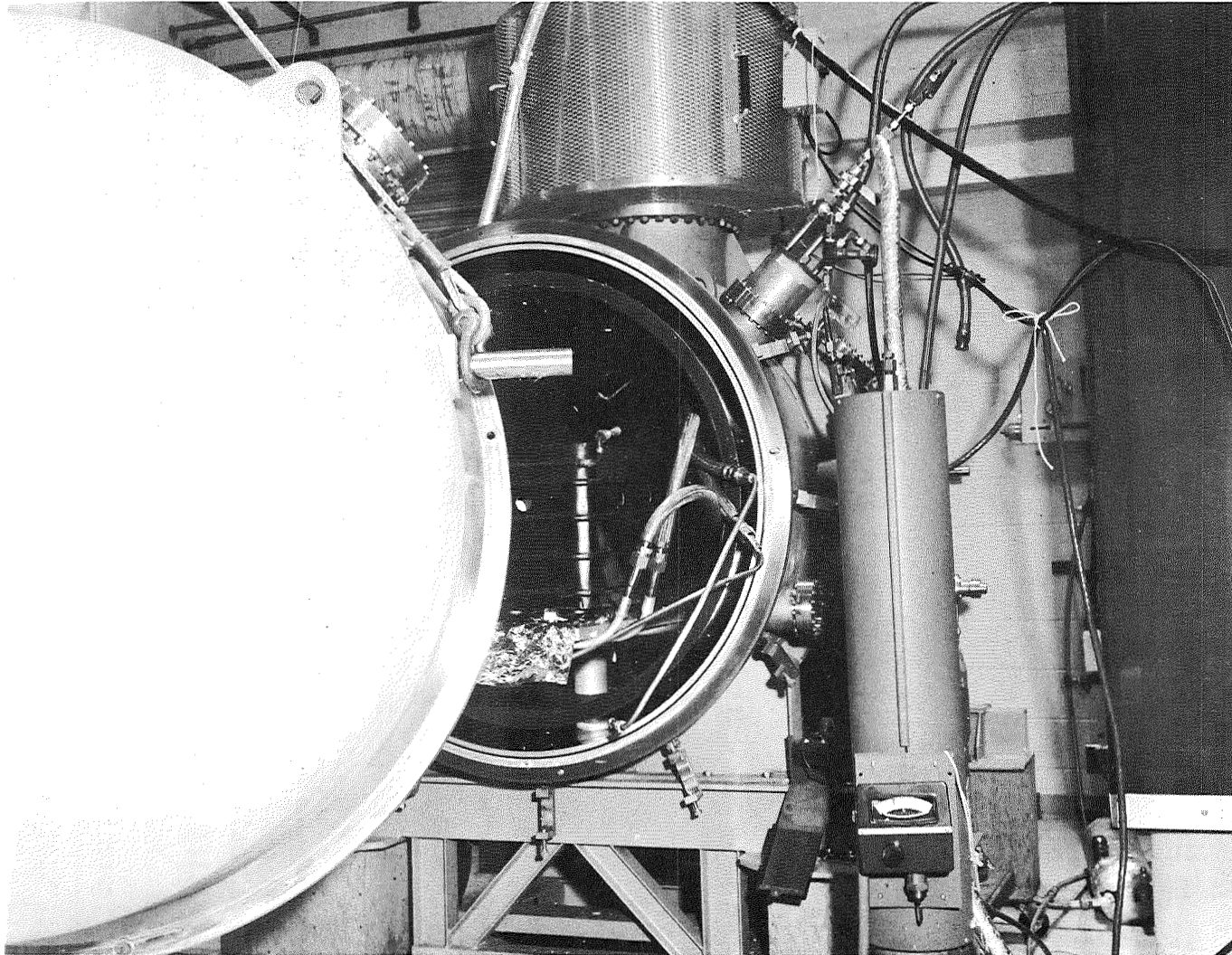


Figure 10.9 Internal View of Thermal-Vacuum Chamber
Showing LN₂ Cooled Test Fixture

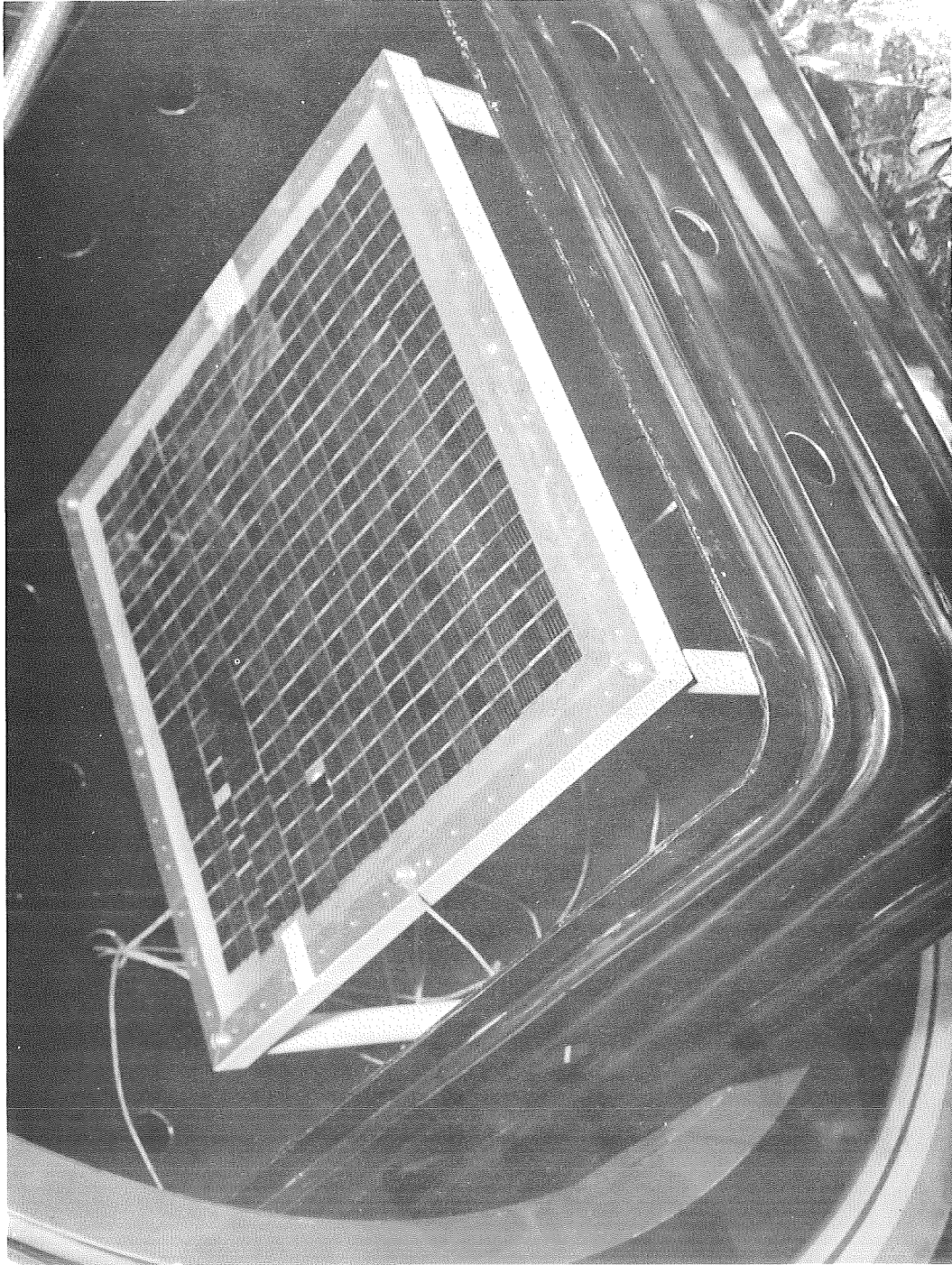


Figure 10.10 View Showing ETM IA Mounted in LN₂ Cooled - Radiatively Coupled Fixture During Thermal Vacuum Testing

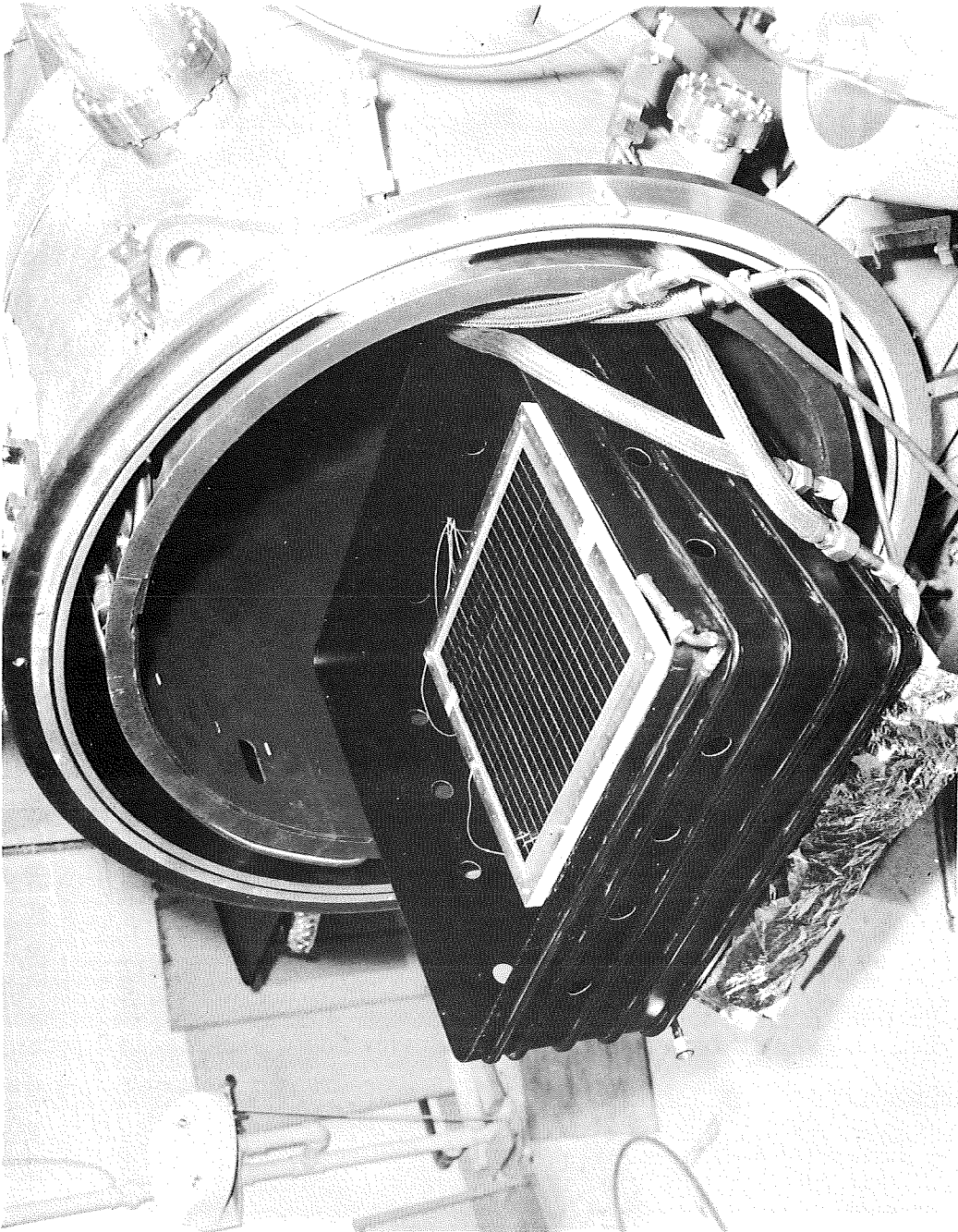


Figure 10.11 View of ETM IA In Thermal-Vacuum Chamber Radiatively Coupled Test Fixture

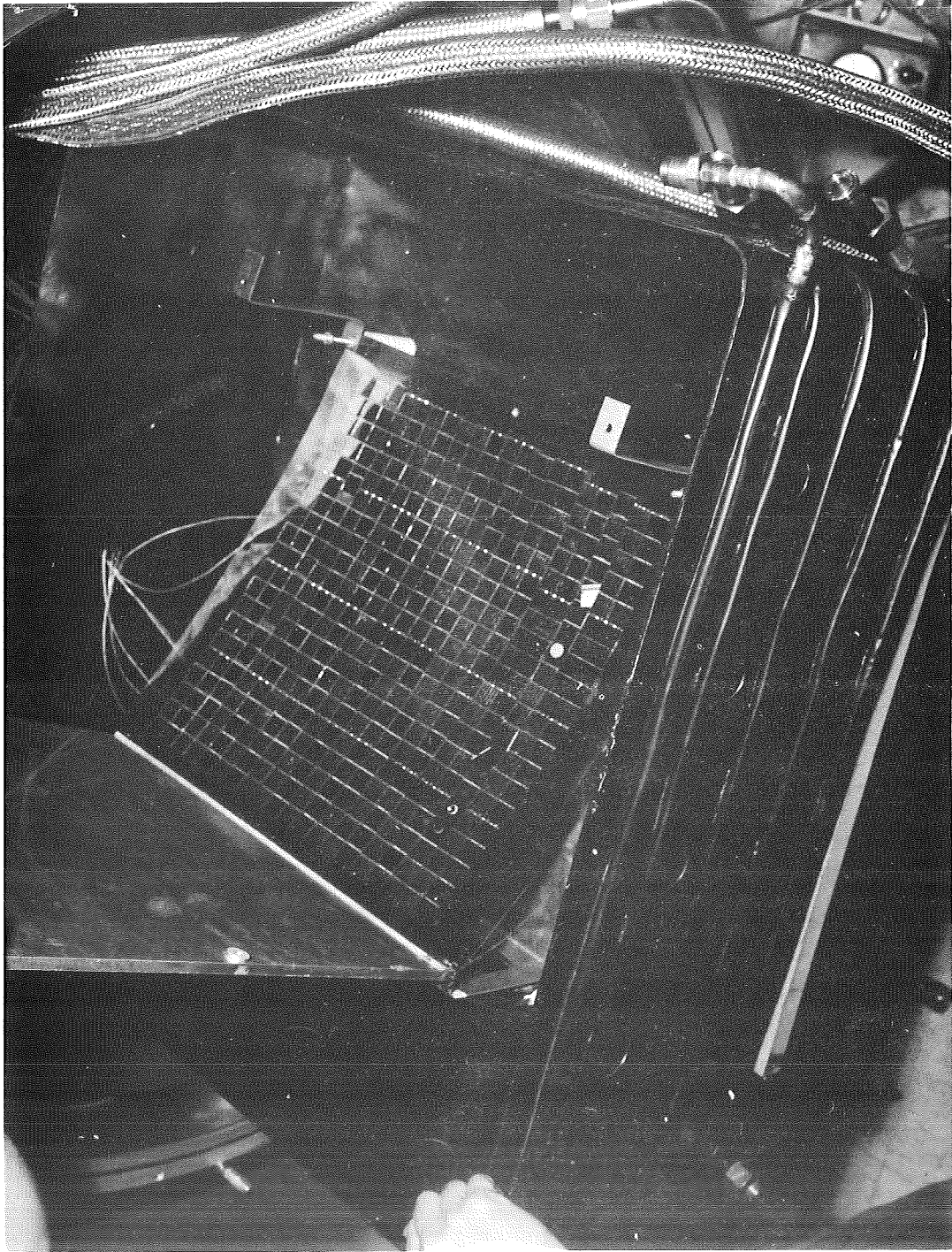


Figure 10.12 View Showing ETM IIA (unfolded) Mounted in LN₂ Cooled - Radiatively Coupled Fixture During Thermal-Vacuum Testing

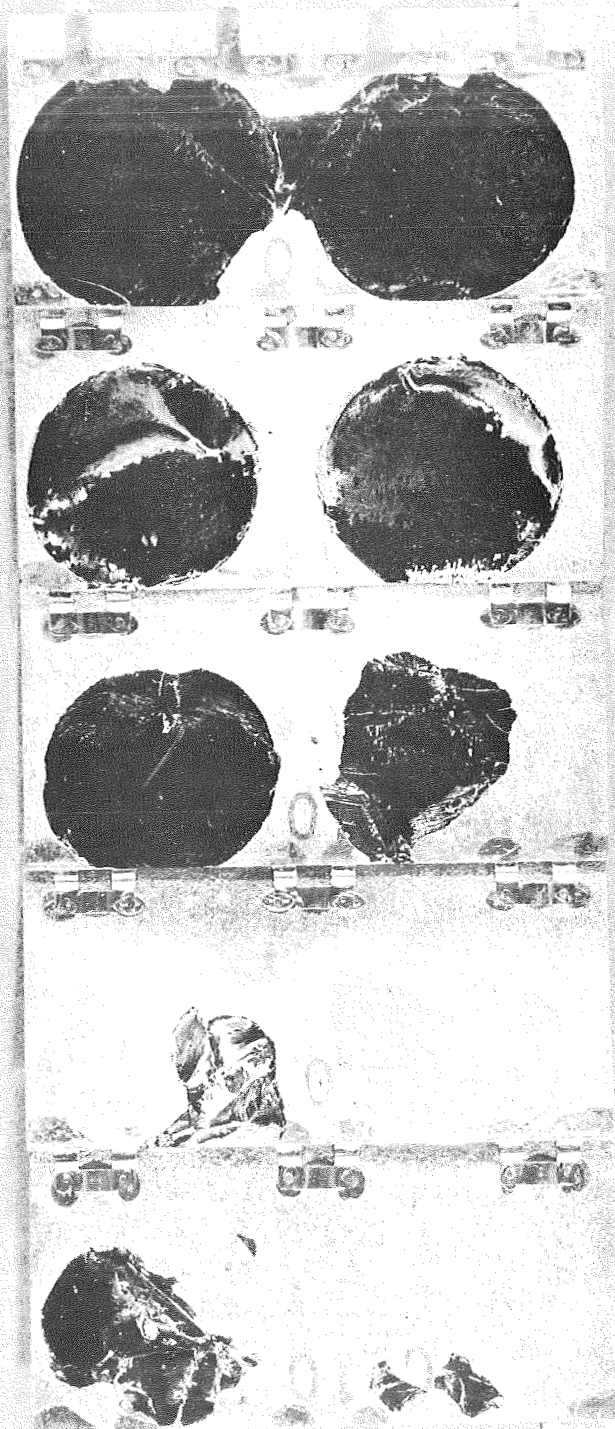


Figure 10.12A Enlarged View of Spalling Failures on 2 cm x 4 cm Silicon Cells (Random Crystal Orientation-Solder Dipped)

Adhesive Spot
Diameter - inches

7F	2F	0F	13F	0.25
6F	1F	0F	20F	0.375
5F 3S	2F	0F	19F	0.50
7F 1S	1F	0F	21F 1S	0.75
RTV 3145	RTV 511/577	RTV 118	PR 1538	

F= Total failed cells
(including cells
with spalling)

S= Cells which had evidence of spalling

This area contained
2 cm x 4 cm cells
with 2 spots per
cell (numbers indi-
cate adhesive spot
failures)

Adhesive Type

Table 10.2 ETM IIA Thermal-Vacuum Test Bonding Failures

Legend					Adhesive Spot Diameter - inches		
F= Total failed cells (including cells with spalling)							
S= Cells which had evidence of spalling					0.25		
This area contained 2 cm x 4 cm cells with 2 spots per cell (numbers indi- cate adhesive spot failures)	11F 2S	3F	1F 1S	9F	0.375		
	11F 3S	0F	1F 1S	14F 1S			
	19F 18S	2F	2F 2S	19F	0.50		
	20F 7S	1F	0F	22F 5S	0.75		
Adhesive Type →							
RTV 3145					RTV 511/577	RTV 118	PR 1538

Table 10.3 ETM IIIA - Thermal-Vacuum Test Bonding Failures

				Adhesive Spot Diameter - inches
<p><u>Legend</u></p> <p>F= Total failed cells (including cells with spalling)</p> <p>S= Cells which had evidence of spalling</p> <p>This area contained 2 cm x 4 cm cells with 2 spots per cell (numbers indicate adhesive spot failures)</p>	2F	2F	0F	12F
	9F 1S	3F	0F	12F
	2F	0F	0F	6F
	10F	0F	0F	9F
Adhesive Type →				
RTV 3145				PR 1538
RTV 511/577				RTV 118

Pull tests were performed on the unconnected cells of each ETM after all other post environmental inspections were completed. The values recorded ranged from less than one pound pull to over eighteen pounds, but the majority of the cells that had not already fallen off withstood several pounds of pull. One additional spalled cell was found during the pull tests (See Tables 10.4, 10.5, and 10.6).

The following comments were recorded during post-test inspection of the ETM's.

- (a) The 2 cm x 4 cm cell interconnects could not be inspected without lifting the module from the substrate.
- (b) Where zone soldered cells spalled and the adhesive spot was large enough to cover the solder zone, the cell did not fall off the substrate, but had to be pulled away for inspection.
- (c) The fiberglass substrate on ETM IA showed signs of deterioration after the thermal-vacuum tests. The cloth grain was more noticeable and the sheet was distorted in several areas.
- (d) Adhesives used to bond the cells (or primers) in some cases flowed onto the front surface of the cells.
- (e) Some of the adhesive spots were noticeably off center.
- (f) A non-uniformity of the adhesive spots was noted during inspection after thermal-vacuum tests. Some of the RTV-3145 spots on ETM IIIA from which cells had become unbonded had a fractured or granular appearance. The spots could be easily lifted from the substrate and were found to have varying characteristics for different segments of the same spot. The spot could be easily pulled apart in some places, but some of the pieces exhibited considerable residual strength and elasticity. The PR 1538 adhesive was found to have many bubbles in the spots from which cells came loose.
- (g) Damage to cells (spalling, loose cells, degraded interconnects, cracked cells, etc.) could not be detected by performance of electrical tests except in cases where total interconnect (all redundant) failure occurred. Visual inspection revealed much of the damage that occurred during testing of the ETM's.

Table 10.4 ETM IA - Results of Pull Tests on Unconnected Cells

Legend

X= Cells that come loose during Thermal-Vacuum tests

5+ Indicates more than 5 lbs. pull was required to lift cell, or that pull attachment failed before a valid reading could be made

Numbers in blocks indicate the pull in lbs. required to lift cell in that location on ETM

Legend									
X= Cells that come loose during Thermal-Vacuum tests									
5+ Indicates more than 5 lbs. pull was required to lift cell, or that pull attachment failed before a valid reading could be made									
Numbers in blocks indicate the pull in lbs. required to lift cell in that location on ETM									
Adhesive Type →									

Adhesive Spot Diameter - inches									
0.25									
0.375									
0.50									
0.75									
RTV 3145									
RTV 511/577									
RTV 118									
PR 1538									

Table 10.5 ETM IIA - Results of Pull Tests on Unconnected Cells

Legend

X= Cells that come loose during Thermal Vacuum tests

5+ Indicates more than 5lbs. pull was required to lift cell, or that pull attachment failed before a valid reading could be made

Numbers in blocks indicate the pull in lbs. required to lift cell in that position

Adhesive Spot Diameter - inches												Adhesive Type →	
0.25		5+	5+	5+	X	5+	X	1	X	5+	X	RTV 3145	PR 1538
		5+	5+	5+	X	5+	X	1	X	5+	X		
		5+	5+	5+	X	5+	X	1	X	5+	X		
		5+	5+	5+	X	5+	X	1	X	5+	X		
		5+	5+	5+	X	5+	X	1	X	5+	X		
0.375		5+	5+	5+	X	5+	X	2	4	5+	5+	RTV 118	PR 1538
		5+	5+	5+	X	5+	X	2	4	5+	5+		
		5+	5+	5+	X	5+	X	2	4	5+	5+		
		5+	5+	5+	X	5+	X	2	4	5+	5+		
		5+	5+	5+	X	5+	X	2	4	5+	5+		
0.50		5+	5+	5+	X	5+	X	5+	5+	5+	5+	RTV 511/577	PR 1538
		5+	5+	5+	X	5+	X	5+	5+	5+	5+		
		5+	5+	5+	X	5+	X	5+	5+	5+	5+		
		5+	5+	5+	X	5+	X	5+	5+	5+	5+		
		5+	5+	5+	X	5+	X	5+	5+	5+	5+		
0.75		5+	5+	5+	X	5+	X	5+	5+	5+	5+	RTV 3145	PR 1538
		5+	5+	5+	X	5+	X	5+	5+	5+	5+		
		5+	5+	5+	X	5+	X	5+	5+	5+	5+		
		5+	5+	5+	X	5+	X	5+	5+	5+	5+		
		5+	5+	5+	X	5+	X	5+	5+	5+	5+		

Legend

X= Cells that come loose during Thermal Vacuum tests

5+ Indicates more than 5lbs. pull was required to lift cell, or that pull attachment failed before a valid reading could be made

Numbers in blocks indicate the pull in lbs. required to lift cell in that position

Adhesive Type →

Legend

5+ indicates more than 5 lbs. pull was required to lift cell, or that pull attachment failed before a valid reading could be made

Numbers in blocks indicate the pull in lbs. required to lift cell in that position

Shaded blocks indicate cells that were sacrificed to mount Thermocouples

Adhesive Type —

10-22

10.3 TEST EVALUATIONS

The evaluation of the test results obtained during this program phase is divided into several segments. Assessments have been made of the following Engineering Test Model design characteristics:

- a) structural integrity of substrates
- b) common interconnector fatigue strength
- c) sub-module bus bar solder joints
- d) cell-to-substrate adhesive bond strength
- e) silicon cell spalling

While the main emphasis during this program phase was directed at evaluating the silicon cell spalling phenomena, during thermal-vacuum testing, it was possible to draw various qualitative conclusions regarding items (a) to (d) above during both structural-dynamic and thermal vacuum testing. These are discussed in the following paragraphs.

10.3.1 ETM IA Substrate Evaluation - Effects of Structural-Dynamic Tests

The ETM IA (fiberglass diaphragm - aluminum box-beam frame) substrate successfully passed all the structural-dynamic tests it was subjected to. This can be seen from Figure 10.3. The natural frequencies of the frame were in the 1500 Hz to 2000 Hz range based upon the outputs from accelerometers 1 and 2 (Z axis and X axis respectively). Amplified acceleration loads were as high as 100 g's in the region but no deleterious effects to the frame was noted. Accelerometers Nos. 3 and 4, were not mounted on the pre-tensioned fiberglass diaphragm, because the mass of the accelerometers would increase the amplitude of deflections that would occur. It was visually noted, during Z-axis vibration testing, that deflections as high as approximately $\pm 1/2$ inch were being experienced. At the completion of this test no adverse effects were discernible on the diaphragm. The pretensioned condition of the diaphragm appeared to be intact. No warping or fraying of the diaphragm was evidenced. In addition, the aluminum box beam frame retained its original structural configuration and no permanent sets were noted.

10.3.2 ETM IA Cellstack Evaluation - Effects of Structural-Dynamic Tests

A close, magnified examination of the U-shaped common interconnects, at completion of structural-dynamic testing, revealed that several had

failed in the central region of the diaphragm where the maximum deflections occurred (See Figures 10.6 and 10.7). From the crystalline appearance of the material at the interconnect crack, it appeared evident that failure had been due to the combined effects of work hardening and fatigue. However, these limited failures were not considered to be significant since in the actual stowed condition of the array, during launch ascent, the diaphragms of this ETM would be supported with either vibration pads (per the skirting recommended in Reference 1.1) or bumper/spacers located at the center of the diaphragm. Either of these arrangements would sufficiently damp out the diaphragm deflections to eliminate the possibility of the work hardening, fatigue failure mode in these interconnects.

In assessing this common interconnect failure mode, it became evident that it would be important to determine if solder "splash" or "wicking" could have contributed to some of the common interconnect failures. With a different interconnect design this problem had been noted and reported in Paragraph 8.4.4.3 of Reference 1.2. It was not evident that any "wicking action" had occurred, of the type that was indicated in the photographs of Figures 8.38, 8.39 and 8.40 of Reference 1.2. However, it appeared that some "solder splash" did occur which resulted in small globules of solder being deposited on the stress relief loop of the common interconnect. Upon investigation (Reference 10.3) it was found that if the solder splash leaves an open chord length of at least 0.060 inches, the large stress relief loop will not be adversely effected for a maximum temperature excursion of 87°C. For this temperature excursion a displacement of approximately 0.003 inch was calculated in Reference 10.4. It was further determined that the stress relief loop in the common interconnector could absorb up to 0.004 inch deflection without inducing large forces in the solder joint. This four mil limit on displacement was based upon a minimum solder free chord length of 0.060 inches. The improvements made in the common interconnect from that shown on Figure 4.13 to Figure 9.8 encompassed the flexibility to take care of all the thermal differential expansion requirements over this range. For this lunar surface application, however, because of the larger temperature excursion (approximately 193°C), it is obvious that considerably more care must be taken to minimize or eliminate solder splash on the stress relief loops of the common interconnect. In addition, as was determined during the Phase II testing,

globules of excess solder deposited on the interconnect expansion loops could produce high tensile stresses during Z-axis vibration testing. If these tensile stresses exceed the allowable fatigue stress for the number of cycles experienced by an interconnector loop during vibration testing, failure of the interconnector could result. Because this hypothesized failure mode may have caused the failures depicted in Figures 10.6 and 10.7, a more comprehensive analysis and test program to evaluate these effects is suggested for future cellstack development programs.

Upon completion of these structural-dynamic tests on the ETM I A module, visual inspection indicated that all silicon cells (both 2 cm x 2 cm and 2 cm x 4 cm) had satisfactorially passed these tests. There was no evidence of structurally induced cracks in either the coverglass or cells and the bond between the cells and the substrates remained intact for all the different type adhesives and adhesives geometries (diameters and thicknesses) employed. This applied to the non-interconnected, as well as the interconnected cells. In addition, by limiting the adhesive dot diameter to a minimum of 0.25 inches, and carefully controlling the dot eccentricity during the manufacturing operation, no torsional vibration of the silicon cells was experienced. This confirmed the test evaluation analysis conducted during Phase II and summarized in the "Silicon Cell Adhesive Dot Design Chart" (Figure 8.33 of Reference 1.2).

The interconnected sub-modules were subjected to pre-test and post-test electrical performance checks. Typical current/voltage curves were generated at a constant temperature of 28°C. Except for those few cases where the common interconnector had failed, no change in sub-module electrical performance characteristics was detected.

The negative and positive bus bars used with this cellstack were also unaffected by the vibration testing. This was considered to be indicative of a high structural design margin for these configurations, since considerable deflections were experienced by the pre-tensioned fiberglass diaphragm used in this ETM design during Z-axis vibration testing.

10.3.3 ETM II A Substrate and Cellstack Evaluation-Effects of Structural-Dynamic Tests

The basic ETM II A substrate consists of 0.003 inch thick "Kapton" (polyimide H film). It is attached to two rigid end panels made from an

aluminum honeycomb core (1/8 in. x 5052 x 0.0007 P- 3.1 x 0.500 thick) and 0.003 inch aluminum facesheets (Al. alloy 5056-H191 or 5052-H19). Prior to subjecting the ETM II A to structural-dynamic testing, it is folded together (see Figure 10.13) and two vibration pads are placed on either side of the flexible Kapton module before clamping them to the rigid end panels. (See Figure 10.14). This configuration was designed in this fashion so the flexible substrate and cellstack would be capable of surviving the launch and lunar descent environments.

The ruggedness of this configuration in the stowed configuration is evidenced by the fact that the structural integrity of the substrate/cellstack combination was maintained throughout all the three axes structural dynamic tests to which it was subjected. This was true despite the fact that amplified g-loads as high as 80 g were occasionally experienced. Visual and electrical performance checks conducted at the completion of these tests confirmed the structural adequacy of the ETM II A design.

10.3.4 ETM III A Substrate Evaluation - Effects of Structural Dynamic Tests

The ETM III A (graphite composite facesheet on aluminum honeycomb core) successfully passed all the structural-dynamic tests it was subjected to. This can be seen from Figure 10.5. The natural frequencies of the substrate were in the 500 Hz to 750 Hz range based upon the outputs from accelerometer 1 (Z axis). Amplified acceleration loads in this axis were as high as 80 g (sinusoidal) and approximately 250 g (random). At the completion of these tests no adverse effects were discernible on any portion of the substrate or the mounting holes.

10.3.5 ETM III A Cellstack Evaluation - Effects of Structural-Dynamic Tests

Post vibration electrical and visual inspection of the ETM III A cellstack revealed that the structural and electrical (I/V curves) integrity of the module had been maintained. Informal, visual inspection had revealed a few cracked or chipped cover slides (seven) on ETM III A. Since non-flight quality coverslides had been used on this program for economy reasons, this was considered acceptable. At the completion of vibration testing approximately 12 additional coverslides had developed minor cracks. Since this had no effect on the electrical performance of the sub-modules

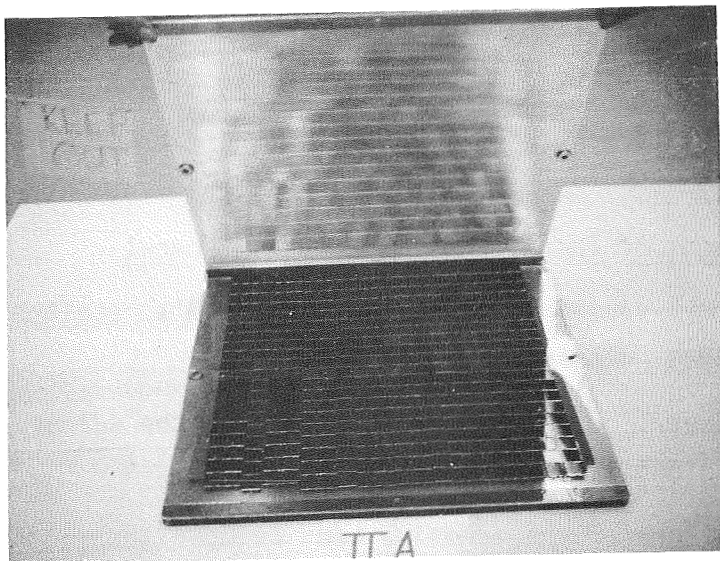


Figure 10.13 Partially Folded ETM II A Configuration

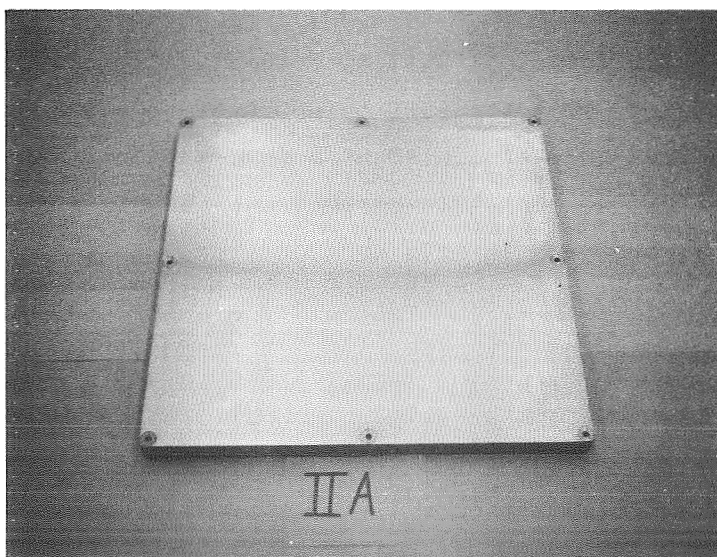


Figure 10.14 Fully Folded ETM II A Configuration

and only a minor effect on the appearance of the module, no further evaluation of this failure mode was conducted. It has been determined that by the use of flight quality coverslides only, use of a proper coverglass/cell adhesive such as Dow Corning R63-489 (equivalent to XR6-3489), proper post curing (8 hrs. at 150°C and 10^{-5} torr) for outgassing, and the use of proper fixturing and sciving tooling to control application of and to clean off excess adhesive, no problems with coverglass cracking or chipping will be encountered.

10.3.6 Effects of Thermal-Vacuum Tests - General

The thermal-vacuum tests on the three ETM's resulted in three types of failure modes. These were:

- a) separation of the vertical tabs on the solder joints between the negative and positive bus bars
- b) failure of the adhesive bond between the silicon cell and adhesive spot or the adhesive spot and the substrate
- c) Spalling of the silicon cell at the interface between the underside of the silicon cell and the adhesive spot.

The first two failure modes were not specifically under investigation during this program phase. Hence, no pre-test analytical effort was undertaken. However, in this section, some qualitative assessments have been made in these areas, as well as recommendations for design improvements. The silicon cell spalling phenomenon, had been analyzed in Section 5 and this failure mode predicted as a function of various critical material properties and geometric parameters. A detailed evaluation of the failure mode is included in this section also.

10.3.7 Evaluation of Bus Bar Tabs - Effects of Thermal-Vacuum Tests

The temperature excursion from + 120°C to - 173°C experienced by the ETM bus bars during thermal vacuum testing is quite large. This not only produces large thermal differential expansion deflections in the cellstack configuration, but also results in considerable changes in the properties of the solder, Kovar, silicon, and substrate facesheet. Only limited material property data was available for most of these cellstack elements (see Table 7.6) and in many instances it varies with data from

other sources (see Reference 10.5). However, it is fairly evident that the 2% silver solder (Sn 62/Pb 36) used in making cellstack interconnect solder joints does vary from a value as low as 3,000 psi at + 212°F to as high as 14,200 at - 220°F. The Reference 10.6 and 10.7 reports indicated that for a three-member rigidly bonded system [substrate, silicon cell, (10 mils) interconnector (3 mils)], stresses could be induced in the solder joints due to thermal cycling that could produce solder cracks (up to 92% cracked solder joints when using copper interconnects and for 350 thermal cycles). For a molybdenum interconnector system essentially no cracks were detected. The test data used compared the behavior of the molybdenum and copper interconnect systems for a ΔT of 250°C (+ 75°C to - 175°C). Under these conditions, the theoretical average solder stresses for the molybdenum tab was approximately 9600 to 9900 psi (see Table 10.7). The thermal coefficient of expansion of Kovar is very close to that of molybdenum (see Table 10.8), so that the solder stresses for the interconnector material should be similar. During the thermal cycling tests conducted during this program a greater temperature excursion was experienced (+ 120°C to - 173°C). This ΔT of 293°C would undoubtedly produce even higher solder stresses (approximately 11,250 to 11,600 psi). Furthermore, an examination of the bus bar tabs (Figures 4.14 and 4.15) indicates that a "sissor-like" action could occur between the negative and positive bus bar tabs due to thermal differential expansion effects. This would produce a stress concentration in the solder joint due to the re-entrant geometry of the connection. The use of stress relief loops in these vertical tabs tends to alleviate this condition somewhat, but solder wicking into the relief loop region could easily offset this. Hence, two possible causes for the failure of the bus bar tab solder joints can be surmised for this lunar surface application. At the elevated temperature (+ 120°C) during thermal cycling, the strength of the solder material is so greatly reduced (less than 3,000 psi), that the induced thermal differential expansion stresses for a ΔT of 100°C (+ 20°C to + 120°C) are large enough to cause solder joint failure. Similarly, at the minimum thermal cycling temperature of - 173°C, despite the increase in the solder material strength (up to 14,200 psi) the combination of the larger ΔT (i.e. + 20°C to - 173°C = ΔT of 193°C) and the effects of the stress concentration, are sufficient to produce stresses high enough

TABLE 10.7 THEORETICAL THERMAL STRESS

Interconnector Material and Thickness	Stresses (p.s.i.)		
	Interconnector	Solder	Solar Cell
0.5 mil Molybdenum	6,500	9,900	1,900
1.0 mil Molybdenum	6,000	9,800	2,000
2.0 mil Molybdenum	4,300	9,600	2,600
0.5 mil Copper	18,400	9,600	2,400
1.0 mil Copper	17,100	9,300	3,400
2.0 mil Copper	15,100	8,700	4,900
4.0 mil Copper	12,100	7,900	7,200
6.0 mil Copper	10,100	7,300	8,700
1.0 mil Silver	18,700	9,600	2,970

TABLE 10.8 NOMINAL VALUES FOR THERMAL COEFFICIENT OF LINEAR EXPANSION FOR VARIOUS CELLSTACK MATERIALS

Materials	Thermal Coefficient of Linear Expansion at 30°C (10 ⁻⁶ in/in/°C)
Aluminum	23.0
Polyimide	20.0
Silver	19.0
Copper	16.8
Be-Copper	16.0
Nickel	13.1
Molybdenum	5.2
Kovar	5.0
Silicon	3.5
60/40 Solder	22.5 approximate
Kapton	6.1
Graphite Composite	1.1
Fiberglass (Epoxy Laminate/ 120 Glass Cloth)	3.1

to cause tab solder joint failure.

This effect has been of concern to TRW Systems on other programs. As a result an improved negative and positive bus bar design has been developed. This is shown in Figure 9.11 and 9.12 and includes a larger stress relief loop in the vertical tabs. Tests on these tabs over a temperature excursion of up to $100^{\circ}\text{C}-\Delta T$ resulted in no solder joint failures. For this lunar surface application, however, it is recommended that an additional assessment be made of these improved bus bar design for the anticipated $193^{\circ}\text{C}-\Delta T$ before they are utilized on a flight configuration. A preliminary review has indicated that replacement of the negative and positive bus bars with a modified version of the U-shaped common interconnector may be a more satisfactory approach for the lunar surface temperature extremes.

10.3.8 Evaluation of Adhesive Bond - Effects of Thermal-Vacuum Tests

Approximately 260 out of 1200 silicon cells came loose from the three ETM's during thermal vacuum testing. Of these, 169 were from the region where the polyurethane adhesive-primer system, PR 1538 was utilized. This adhesive system was selected almost entirely because many polyurethane materials exhibit a comparatively low modulus of elasticity at low temperatures (see Table 7.4) which is desirable for this application. All the other adhesive materials were silicone based "polymers" which tend to have similar low temperature properties. The selection of this specific polyurethane material was made with the limited knowledge that its room temperature adhesive properties appeared good for this application and that this material had been satisfactorily utilized as a low temperature connector potting system.

As a result of this adhesive bond failure an investigation was conducted. It was found that on a previous program, a silicon cell adhesive bond (primer) failure was experienced under similar conditions (min. temperature -162°C) during engineering development tests on a solar array. The adhesive in this case was a mixture of methyl-penyl RTV compounds (i.e. 50/50 mixture of G. E. RTV 511 and 577 silicone compounds). A silane primer was used. The thermal environment during thermal-vacuum testing ranged from -260°F (-162°C) to $+140^{\circ}\text{F}$ ($+60^{\circ}\text{C}$). An investigation of this failure led to the conclusion that the primer thickness, which

normally required little control, became extremely critical at very low temperatures (-140°C and below). The adhesive bonds which failed during these thermal cycling tests consisted of an adhesive dot, approximately 0.375 inches in diameter and 0.020 inches thick (Figure 10.15). The 2 cm. x 2 cm. silicon cells were bonded to test substrates of pyrex glass or magnesium which had been treated with a conversion coating and then coated with an epoxy paint. Bond failures occurred at the adhesive interface of both these substrates as well as at the adhesive interface at the solar cell. The silicon cell surface had been coated with a vacuum deposition of silicon monoxide. These failures were completely adhesive in nature, i.e., the adhesive dot separated cleanly from the adherend in each case. In most instances some of the primer (G. E. SS 4004) remained on the adhesive dot indicating that the failure was in primer adhesion rather than adhesion of the RTV compound to the primer. Approximately 50% of a total of 342 adhesive dots failed on at least one side of the bond.

A microscopic examination of the thermally exposed primer surfaces revealed that the primer film had "mudcracked" in a manner normally associated with a film shrinkage due to a solvent loss. This cracking (Figure 10.16) was found to occur regardless of the apparent process-controlled film thickness on the test assemblies. Rebonding of these failed assemblies with greater control of primer application and cure and subsequent thermal cycling resulted in additional bond failures except that a much lower percentage of the bonds failed. The failed assemblies were once again rebonded with even greater control of the primer application and cure and again thermally cycled. No further bond failures occurred. Because the test schedule did not permit a verification of the failure mechanism prior to rebonding the specimens, the greater control referenced could only utilize such information as could be gleaned by the apparent state of primer adjacent to those adhesive bonds which had survived the initial thermal cycling. This gross observation indicated that the surviving bonds had apparently been made over a thinner primer application than those that had failed. Additionally, the knowledge of the chronological order in which the specimens had been bonded seemed to indicate that those which had been bonded last exhibited a higher level of survival. Since all specimens were primed within a very short time period, it appeared that the primer cure time for the first specimens bonded may

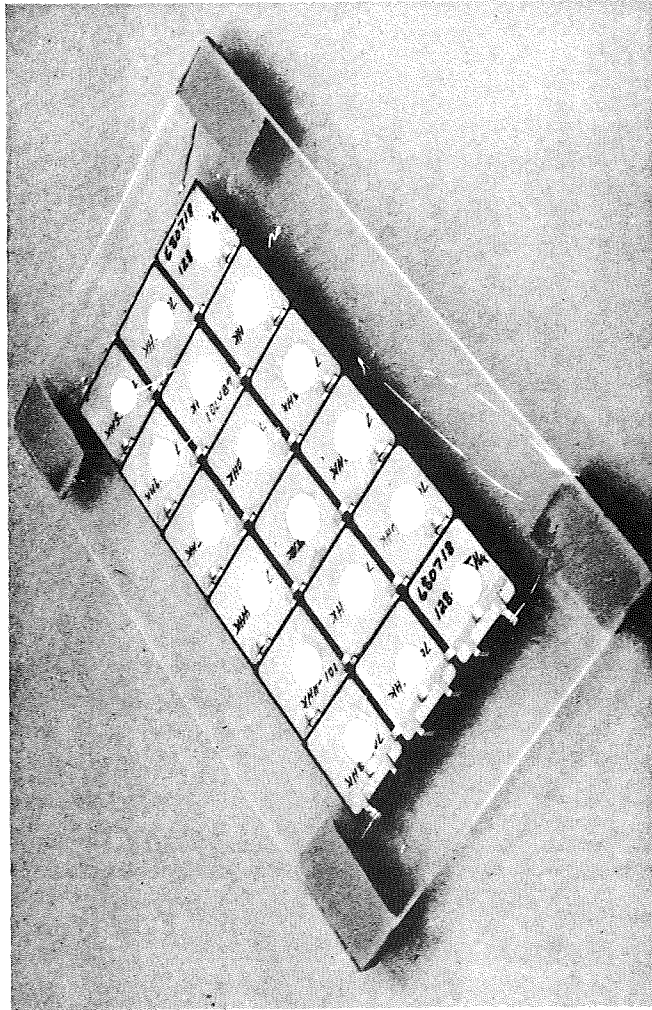


Figure 10.15 Solar Module Assembly Showing Configuration of Adhesive Bonds

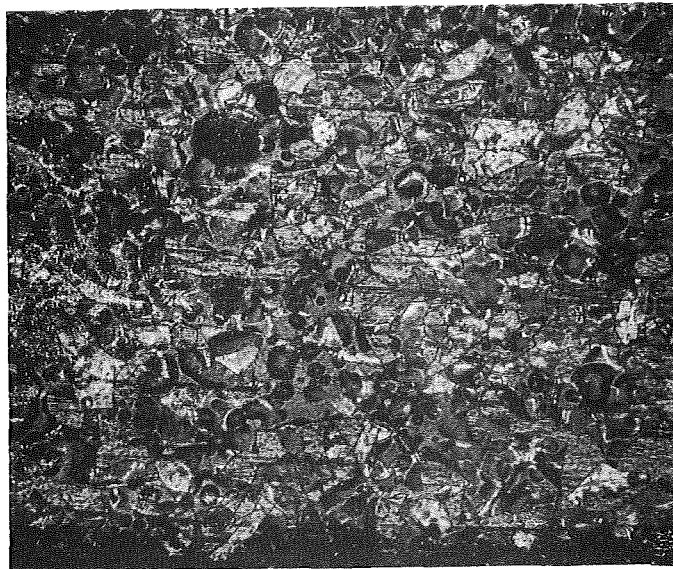


Figure 10.16 Photomicrograph (100X) of Mudcracked Primer.

have been inadequate. With these observations an experiment was designed to explore some of the variables of the primer-adhesive bond process. This experiment was a 3 x 3 x 3 factorial design with three fixed levels in cure time; namely: E_1 (1 hr.), E_2 (2 hrs.) and E_3 (3 hrs.), three levels of primer thickness, f_1 (thinnest primer), f_2 (medium), f_3 (thickest), and three fixed levels of temperature cycle, i.e., 0, 15, and 30 cycles. The order of experiment was completely randomized. The mathematical model to represent this experiment is:

$$x_{ijkm} = \mu + E_i + C_j + EC_{ij} + T_k + ET_{ik} + CT_{jk} + ECT_{ijk} + e_{ijk(m)}$$

where:

x_{ijkm} = the measured variable, i.e., peel bond strength (in pounds)

μ = the true mean of the population from which all the data came

E_i = cure time

C_j = temperature cycle

T_k = primer thickness

EC_{ij} , ET_{ik} , CT_{jk} and ECT_{ijk} are interactions between variables in question.

$e_{ijk(m)}$ = random error in the experiment

The specimen used to obtain the desired data was a "T-peel" specimen consisting of a 1" x 6" piece of magnesium substrate material (finished with Dow 17 and epoxy paint) bonded to a piece of 0.005" x 1" x 6" aluminum sheet. Peel strength values were obtained after conditioning the specimens with the required number of cycles by pulling back the end of the aluminum adherend and monitoring the load required to peel the entire specimen apart.

The results of analysis of variance are shown pictorially in Figure 10.17. These data show that:

(1). Peel strength is highly dependent upon primer thickness. The effects due to primer thickness f_2 and f_3 are definitely better than thickness f_1 .

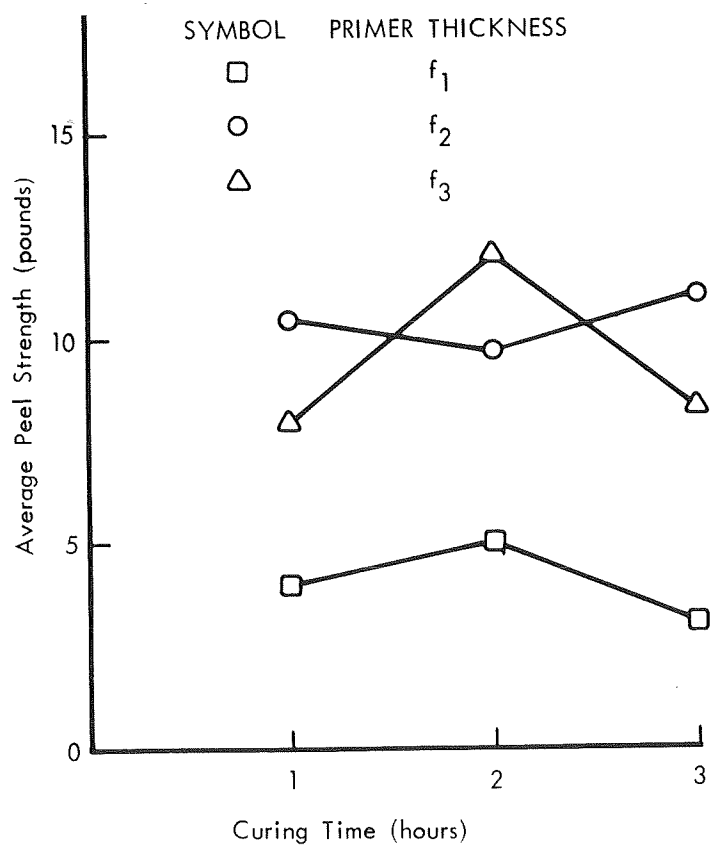


Figure 10.17 Average Peel Strength of Primer Test Samples as a Function of Curing Time for Three Thickness of Primer

(2). There is a minor effect due to cure time which may be attributed to random error. In order to determine more precisely the cure time effect, one more test was conducted which is presented below.

(3). There exists a minor interaction between primer thickness and cure time which again may be due to random errors.

In explanation of the significance of primer thickness it should be noted that f_1 (thinnest) was somewhat thinner than that normally considered as the minimum acceptable thickness, f_2 thickness was average, and f_3 was near the normal maximum thickness. Primer thickness is usually not measured, but indicated by the depth of color. Primer thickness f_3 was near, but not duplicate the primer thickness noted on those assemblies upon which bond failures were first experienced.

Even though the experiment did not indicate a significant relationship between cure time and bond strength, it was known that it had to exist. It was, therefore, assumed that the levels of cure time selected had been excessively long and that partially uncured primer had not been captured in the one to three hour range of the experiment. Recognizing that the primer cure was a function of both time and humidity, a second experiment was designed.

In this experiment, one more variable was included, that was humidity with three fixed levels: 10%, 30% and 50%. However, primer thickness f_3 was dropped from the test leaving only two fixed levels of primer thickness: A, approximately equal to the previous f_1 and B, approximately equal to the previous f_2 .

Temperature cycles were also excluded as a variable and all specimens were exposed to 15 thermal cycles.

The mathematical model is:

$$X_{ijkm} = \mu + H_i + T_j + HT_{ij} + E_k + HE_{ik} + TE_{jk} + HTE_{ijk} + e_{(m)ijk}$$

Where:

H_i = humidity and other symbols are the same as before.

Based upon the results of the analysis of variance, the following conclusions were obtained.

(1). The effect of humidity is highly significant. Figure 10.18 shows that 50% humidity provides higher peel strength than 30% and 30% humidity provides higher peel strength than 10%.

(2). The effect of thickness of primer is highly significant. Figure 10.19 shows that primer thickness B (thicker than A) has higher peel strength than A.

(3). The effect of cure time is also highly significant. From figure 10.20, it can be concluded that one hour cure time is better than 0.5 hour cure time. Although no significant difference between cure time of 0.5, 1.5 and 2.0 hours is indicated, knowledge of the curing mechanism would indicate that once the primer is cured (1.0 hour) the peel strength values should remain high. The one exception to this is the value plotted for 1.5 hour cure time and 30% humidity, which is abnormally low and assumed to be incorrect. The scatter of data above values of 8 pounds is meaningless for this test since the failure mode changes from adhesive to cohesive at this point. The data point plotted for 10% humidity at 1.5 hour is considered invalid since it has been previously shown that 10% humidity will not produce satisfactory bonds. The shaded area of Figure 10.20 is, therefore, defined as a "safe" area without respect to data values.

A third experiment was performed to verify that the apparent conditions of primer thickness B and cure time of greater than one hour at 50% or greater relative humidity would produce the desired bond strength. An additional purpose of the test was to establish the upper primer thickness limit. This test did indeed verify the previously indicated acceptable conditions, but also indicated a greatly reduced bond strength for primer thicknesses only slightly greater than the primer thickness B.

As previously mentioned, primer thickness is usually not measured, but estimated by the depth of color. Throughout these experiments the thickness control was assured through the use of color standards which had been prepared with primer on substrates identical to those of the test specimens. The failure of the thicker primer in the last experiment had indicated a very narrow acceptable primer thickness range, so narrow, that it seemed questionable that color could be used as an acceptance criteria for production spraying of primer.

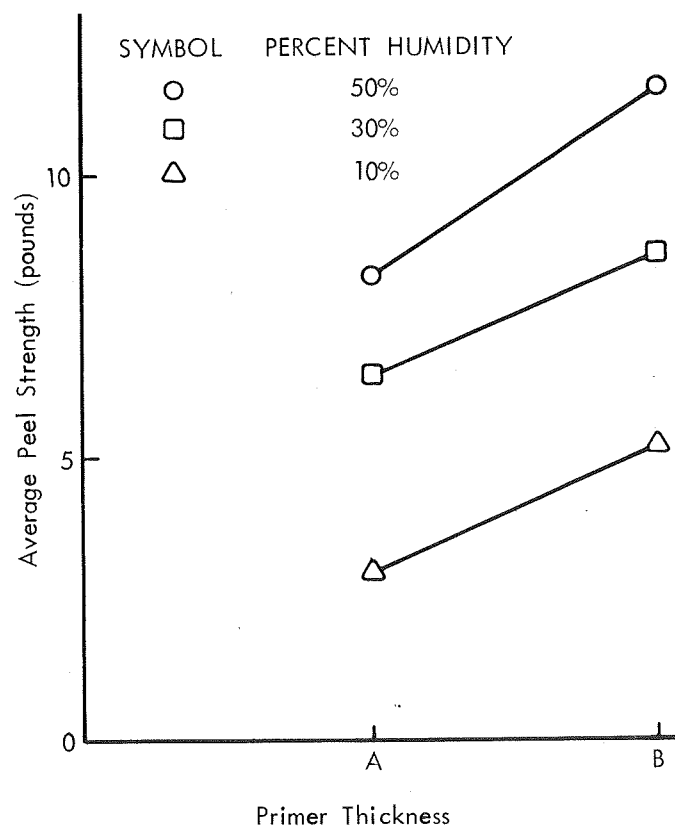


Figure 10.18 Average Peel Strength of Primer Test Samples as a Function of Two Primer Thicknesses for Three Humidity Levels

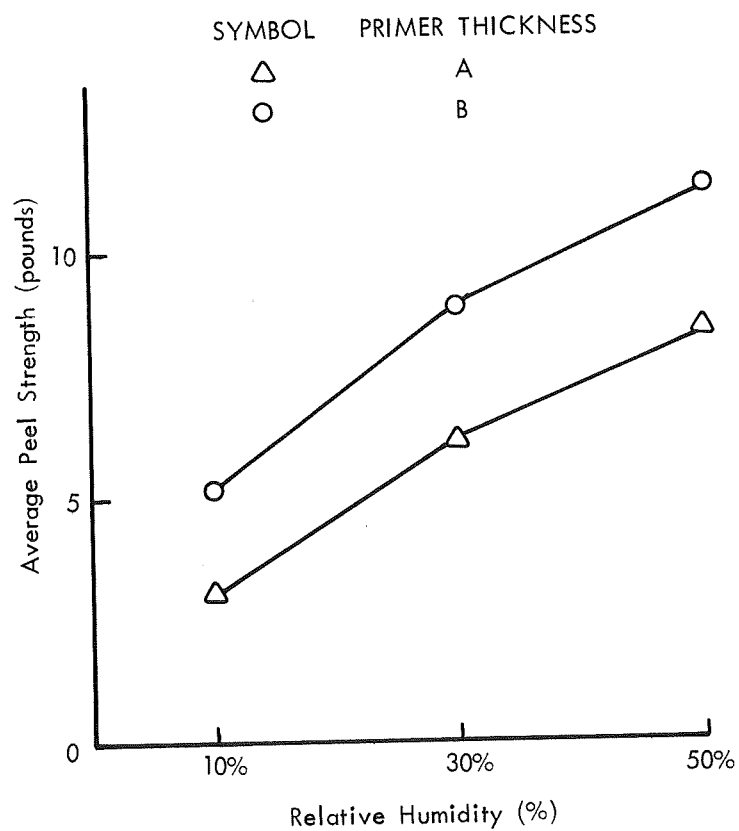


Figure 10.19 Average Peel Strength of Primer Test Samples as
a Function of Relative Humidity for Two Primer
Thicknesses

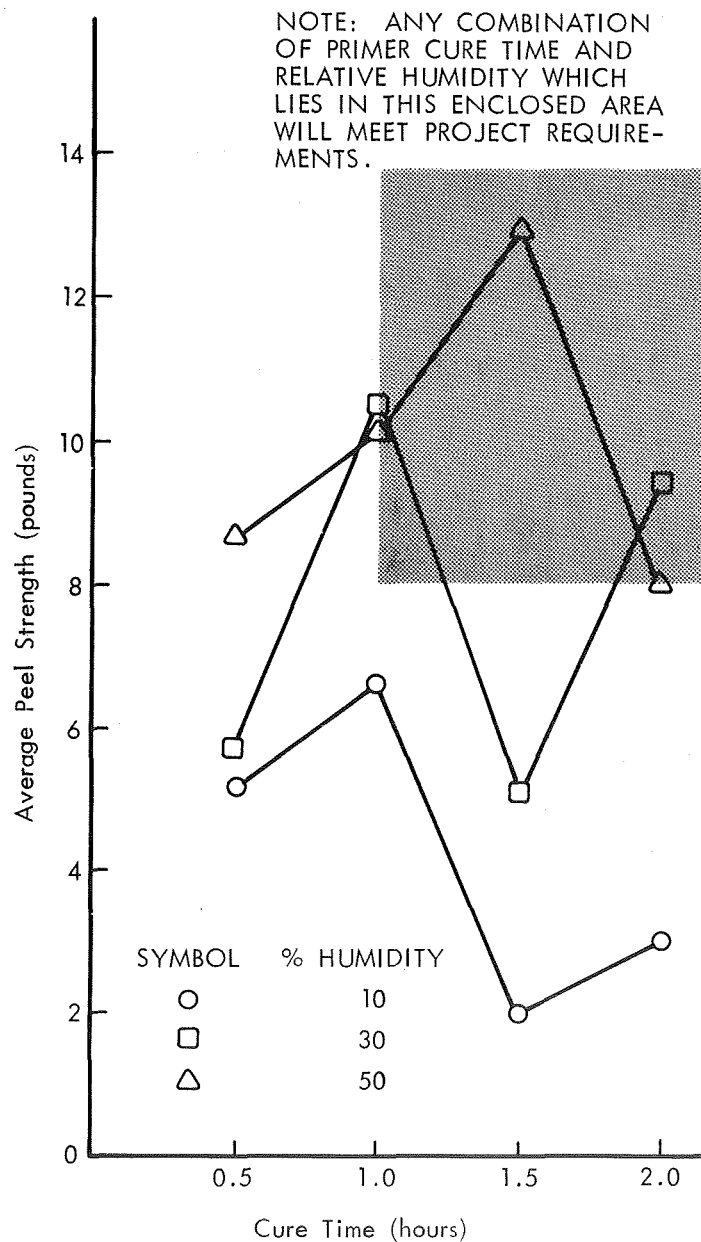


Figure 10.20 Average Peel Strength of Primer Test Samples as a Function of Cure Time for Three Conditions of Relative Humidity (Both Adhesive Thicknesses Combined)

Microscopic examination of the acceptable primer coatings and those considered to represent the margins of the acceptable thickness range revealed that the optimum coatings were comprised of many small unconnected droplets of primer.

A photomicrograph of specially dyed primer of the optimum thickness is shown in Figure 10.21. At the lower thickness margin, the drops became so far separated that the loss of primer area was responsible for the loss of bond strength. The upper margin thickness level approached the formation of a continuous film of primer. Thermal cycling of this coating produced the "mudcracks" previously observed and shown in Figure 10.16.

At this point it was obvious that production use of the primer for the intended application would require a high degree of operator and inspector training unless a simple method of application and/or inspection could be developed. An alternate to this was considered to be a material substitution for the primer. Parallel programs for the development of the simple primer application method and alternate primer were initiated.

Even though the acceptable primer thickness range was narrow, the test had indicated that color could be used as a thickness control device. Thus, an initial effort was made to prepare permanent color standards. The primer itself, which had been used to prepare standards for the early testing, faded too rapidly when exposed to light to be considered an acceptable medium for the standard preparation. Optimally coated specimens and their chromaticity values, obtained on a spectrophotometer, were transmitted to color specialists to determine whether the required standards could be prepared. The response was negative. The transparency of the primer color itself along with the substrate showing between the primer droplets made the color unreproducible on the light background required for the necessary subtle shade discrimination.

Lacking the ability to easily control the primer application, an attempt was made to develop a rapid post-application test to verify the adequacy of the primer coating. It was thought that the "mudcracking" failure mode of too thick primer could be easily detected with a coupon which could be sprayed simultaneously with the production hardware. This



Figure 10.21 Photomicrograph (100X) of Optimum Thickness Primer

was quickly verified and made even more positive by testing the adherence of the primer with masking tape after dipping the primed coupon in liquid nitrogen.

This test, however, did not alert the inspector to primer applications which were too thin. It was, of course, also undesirable in that it imposed a "trial and error" application method which would inevitably result in cleaning and repriming of a large amount of production hardware. It was considered unacceptable. An important fact was discovered during this test evaluation, however. In preparation and examination of the many specimens it was discovered that it was possible to produce a primer coating which, upon microscopic examination, appeared to be satisfactory, but which was not. This was the result of a "dry" spray application. With these disappointing results it was obvious that the only alternative was the installation of equipment capable of delivering the desired primer application with a high degree of reproducibility. Semiautomatic equipment was designed, fabricated, and installed to perform this function. It is shown in Figure 10.22. A trigger release of the pendulum mounted gun actuates both the primer delivery and the gun travel. An adjustable weight on the pendulum is used to control the gun velocity. Standard pressure, fluid flow and spray pattern adjustments are made on the gun and the distance from the gun nozzle to the surface to be sprayed is controlled by adjusting the height of the table holding the work.

This equipment was calibrated by preparing a series of T-peel specimens similar to those used in earlier tests. It now consistently provides optimum primer applications which require no inspection. The equipment is routinely certified on a monthly basis with the preparation, thermal cycling and testing of T-peel specimens. Since its installation a second 300 thermal cycle test has been performed using specimens sprayed with this equipment. All adhesive bonds survived the test.

The program undertaken to determine whether the requirement for high level control of primer application could be circumvented through use of another primer was conducted in the following manner.

The commercially available primers were surveyed to determine their compatibility with the RTV 511/577 adhesive. Among those tested were:

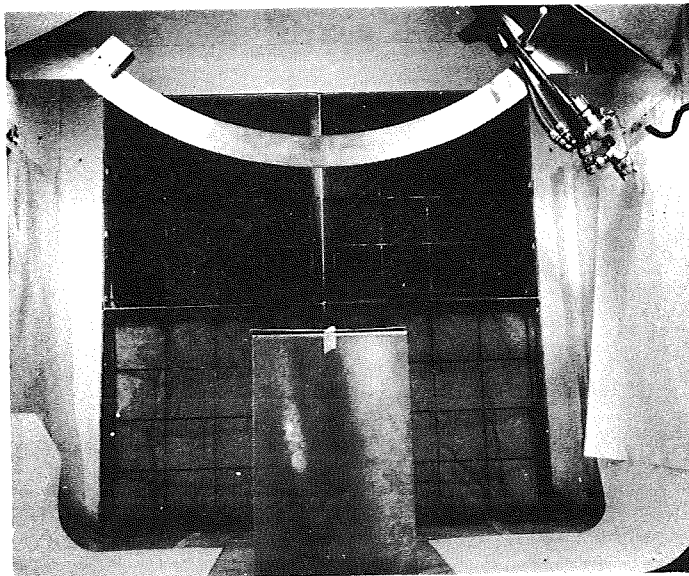


Figure 10.22 Semiautomatic Primer Spray Equipment

Dow Corning Primers

- 1200
- 1201
- A4094
- 90-198
- XR6-3466

Dow Corning Self-priming Elastomers used as primers

- DC 732
- DC 3140
- 92-007

General Electric Primers

- SS 4101
- SS 4155
- SS 4004 (thinned)

Union Carbide Primer

- A 1100

Three of these primers were initially incompatible with the adhesive. They were XR6-3466, DC 3140, and 92-007. Bonded assemblies were made with the remaining systems and thermally cycled to progressively lower temperatures producing the failure of four more primer systems: 1201, 90-198, 4101, and A-1100.

Subsequent tests to obtain quantitative bond strength data with the remaining primers yielded inconsistent results with two of them, 1200 and 4094, and these two were dropped from further testing. Primer 4155 was also dropped when it was discovered that bond strength results were dependent upon whether or not the powdery surface of the dried primer coating was brushed.

The remaining two primers, 732 and 4004, were further evaluated in a series of peel tests to determine the effect of process variables. Both of these primers were thinned for this application. The 4004 primer was thinned with acetone to an 80/20 acetone/4004 ratio. This thinned primer can be brush applied to produce a film which will survive low temperature cycling without cracking and adhesion loss. The 732 adhesive also required thinning so that it could be used as a primer. For brushing, it was mixed with an equal weight of methyl i-butyl ketone (MIBK)

and for spraying it was mixed in an 80/20 Freon TF/732 ratio.

Both the thinned 4004 and thinned 732 primers could be applied to surfaces with much less control than required for unthinned 4004 and still produce peel specimens which would survive thermal cycling and fail cohesively (in the adhesive, not at an interface) when destructively tested.

On further testing of these systems with solar array configurations it was observed that the success of thinned 4004 was specific to certain surfaces. Failures occurring during thermal cycling at the back of solar cells with silicon monoxide coated silver-titanium contacts, but bonds to the substrate and solder coated cells survived.

Program requirements for use of the cells upon which the thinned primer had failed prohibited its use in this instance, however, all tests to date have indicated it is an adequate solution with compatible adherends.

The failure of RTV adhesive bonds, attributed to "mudcracking" of the primer at low temperatures, can be prevented through careful control of the primer application. The preferred primer application is a discontinuous film comprised of many small dots as illustrated in Figure 10.21. Since this acceptable primer thickness range is quite narrow and difficult to measure, the primer application is best made with calibrated, automatic spray equipment.

Solvent thinning of the primer for application by methods other than spraying and at least one alternate primer have also been shown to produce bonds which will survive low temperature thermal cycling. The success of these alternate methods is, however, not universal and is dependent on the nature of the adherend.

The foregoing evaluation indicates that with increased primer thickness control, and humidity and cure-time control, during cellstack production, this mode of failure can be eliminated for adhesive requiring primers (i.e. PR 1538 or RTV 511/577). The only cases where the adhesive bond failed despite the use of an adhesive not requiring primers, was that where RTV 3145 was used. A review of Tables 10.1 to 10.3 shows that no adhesive bond failures occurred with the use of unprimed RTV 118. Because of this, an investigation was conducted into how this particular adhesive is quality controlled at the vendor (Dow Corning), since it

appeared possible that a "batch-to-batch" variation might exist in the product. This survey revealed that each lot of adhesive material was subjected to a rather impressive list of quality control tests which included an assessment of the following material properties:

- Color
- Extrusion rate
- Flow
- Cure Time
- Hardness
- Specific Gravity
- Tear Strength
- Elongation
- Tensile Strength
- Dielectric Strength
- Dielectric Constant
- Dissipation Factor
- Volume Sensitivity

All these tests however, are conducted at ambient conditions. Initially, it seemed reasonable to assume that the adhesive properties at room temperature were the same from batch to batch, that they would not vary significantly from each other, at temperatures varying widely from room temperature. For example, flow, extrusion rate, and cure time would imply that all samples fell within a given molecular weight range. The specific gravity test would constitute a secondary check on filler content, volatiles, etc. However, TRW Systems has experienced difficulties in the past with the use of RTV 3145, in that it would not meet the extrusion rate specification. Dow Corning attributed this to entrapped air (moist) which could permit some advancement of the cure. It is suspected that this is the probable cause of adhesive extrusion rate variation and perhaps the major contributor to any lot-to-lot differences. In addition, from time to time, the occurrence of bubbles in the adhesive bond lines has been experienced. A third factor which could be affecting adhesive bond peel strength is outgassing. It has been found during tests conducted at NASA/MSFC that the weight loss experienced with RTV 3145 during outgassing tests was $0.3\%/cm^2/hr$. This compares with the allowable weight loss (see Reference 7.3) of $0.2\%/cm^2/hr$. It has been suggested by NASA/MSFC that if this adhesive is subjected to a $100^\circ C$ bake at 10^{-6} torr for a period of 8 hours, that the acceptable 2% weight loss rate could be achieved. However, this could also constitute another element which might contribute to some anomalous low temperature behavior. A fourth factor could be adhesive bond line thickness and area. While it has been established both analytically (Section

5) and to a degree experimentally (Section 10.3.9) that these adhesive dot geometric parameters do contribute to the spalling phenomenon, it is also possible that an adhesive bond failure could be masking a potential spalling failure due to the inadequacy of the adhesive bond strength itself. Finally, it has been found that occasionally the silicon oxide (SiO) coating on zone-soldered cells separates from the back of the cell together with the adhesive dot. In this case, the failed SiO coating could be masking either an adhesive bond failure or a spalling failure. It is interesting to note that for the majority of cells (50 out of 51) subjected to the post thermal-vacuum testing pull tests, (see Tables 10.4, 10.5, and 10.6) where RTV 3145 adhesive was used, a pull of 5 lbs. or greater was required to separate the cells from the substrate. Since all these non-interconnected cells were mounted at the same time, this would seem to indicate a lack of homogeneity within the individual adhesive batch used since nine cells in this region experienced an adhesive bond failure. This was further confirmed when an examination of failed RTV 3145 adhesive dots revealed a marked variation of material properties within an individual dot. For example, when examined at room temperature, portions of the dot were found to be quite elastic and resilient. Other portions of the same dot were hard and quite brittle. It appears evident that, despite the close environmental controls maintained during the cell to substrate bonding operation (see Figure 10.23), that variations in the consistency of individual batches of RTV 3145, as well as possible additional variations from batch-to-batch can lead to anomalous low temperature behavior of this adhesive. By contrast, the other non-primed adhesive, i.e. RTV-118, showed marked evidence of a much higher level of consistency with regard to its adhesive bond strength (see Tables 10.4, 10.5, and 10.6). Empirical manufacturing techniques on other programs, with less severe temperature extremes has undoubtedly contributed to the successful use of RTV 3145. However, currently there is insufficient data available to invoke any meaningful process controls for this adhesive for use down to temperatures of -173°C for long periods of time (14.75 days during lunar night). Until this is accomplished, the unprimed RTV-118 adhesive appears to be the superior candidate adhesive for assuring maintenance of an adequate adhesive bond for lunar surface applications.

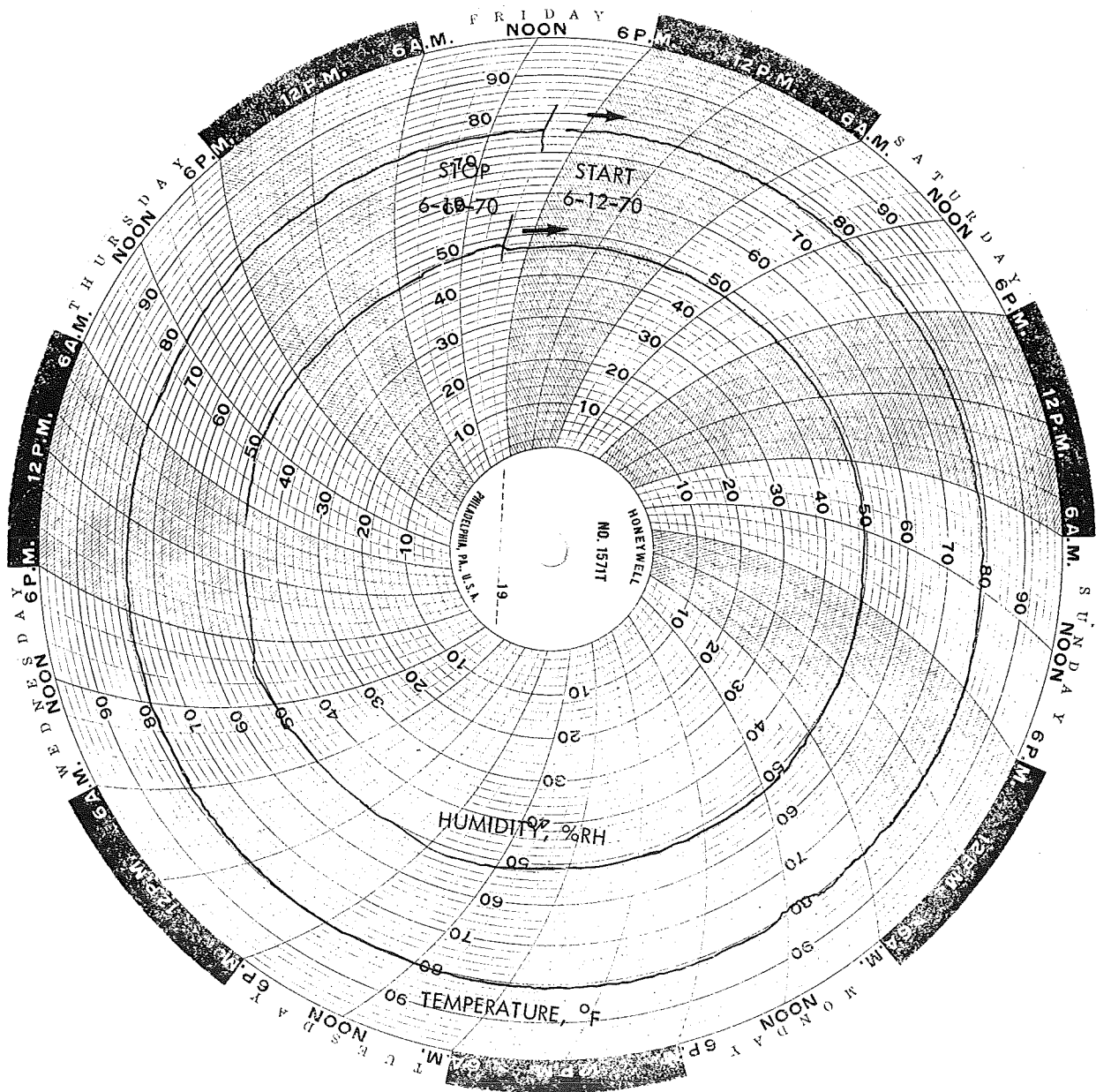


Figure 10.23 Typical Temperature and Humidity Plot of Module Assembly Room

10.3.9 Evaluation of Spalling Phenomena - Effects of Thermal-Vacuum Tests

Approximately 46 cells out of a total of 1200 showed evidence of spalling. Of the total of 46 spalled cells, 35 occurred with RTV 3145, 4 with RTV 118, and 7 with PR 1538). This small number (less than 4%) is attributed to the fact that all four candidate adhesives were selected because they exhibited attractive material properties at low temperatures (see Tables 7.3, 7.4, and 7.5). These were, reasonably high values of ultimate tensile strength, and lap shear, and comparatively low values of modulus of elasticity and coefficient of linear expansion at -173°C (-279°F). For all these room temperature vulcanizing (RTV) adhesives, these properties represent average values. These properties not only vary considerably from batch to batch, but depending upon the degree of moisture and/or air entrainment during the manufacturing process, can vary within a given batch. Some of these average values have been plotted as a function of adhesive temperature and are shown on Figures 10.24, 10.25, and 10.26. With respect to the spalling phenomena, the adhesive modulus of elasticity (E_2) and the linear coefficient of expansion (α_2) are the most significant. Furthermore, it is the low temperature properties (i.e. -100°C to -173°C), that constitute the critical regime for their selection. As may be noted for the selected adhesives, there is a considerable variation in these properties within this temperature regime. These ranges are listed in Table 10.9.

TABLE 10.9 CRITICAL LOW TEMPERATURE ADHESIVE PROPERTIES

Material Property or Parameter	Range of Values for Selected Adhesive	
	-100°C	-173°C
E_2 , Modulus of Elasticity, psi	0.114×10^3 to 33×10^3	37.9×10^3 to 173.8×10^3
α_2 , Coefficient of Linear Expansion, in/in/ $^{\circ}\text{C}$	6.0×10^{-6} to 28×10^{-6}	3.0×10^{-6} to 8.0×10^{-6}
$E_2 \alpha_2$; Adhesive Parameter [(lb/in ² (in/in/ $^{\circ}\text{C}$)]	0.0006 to 0.925	0.114 to 1.39

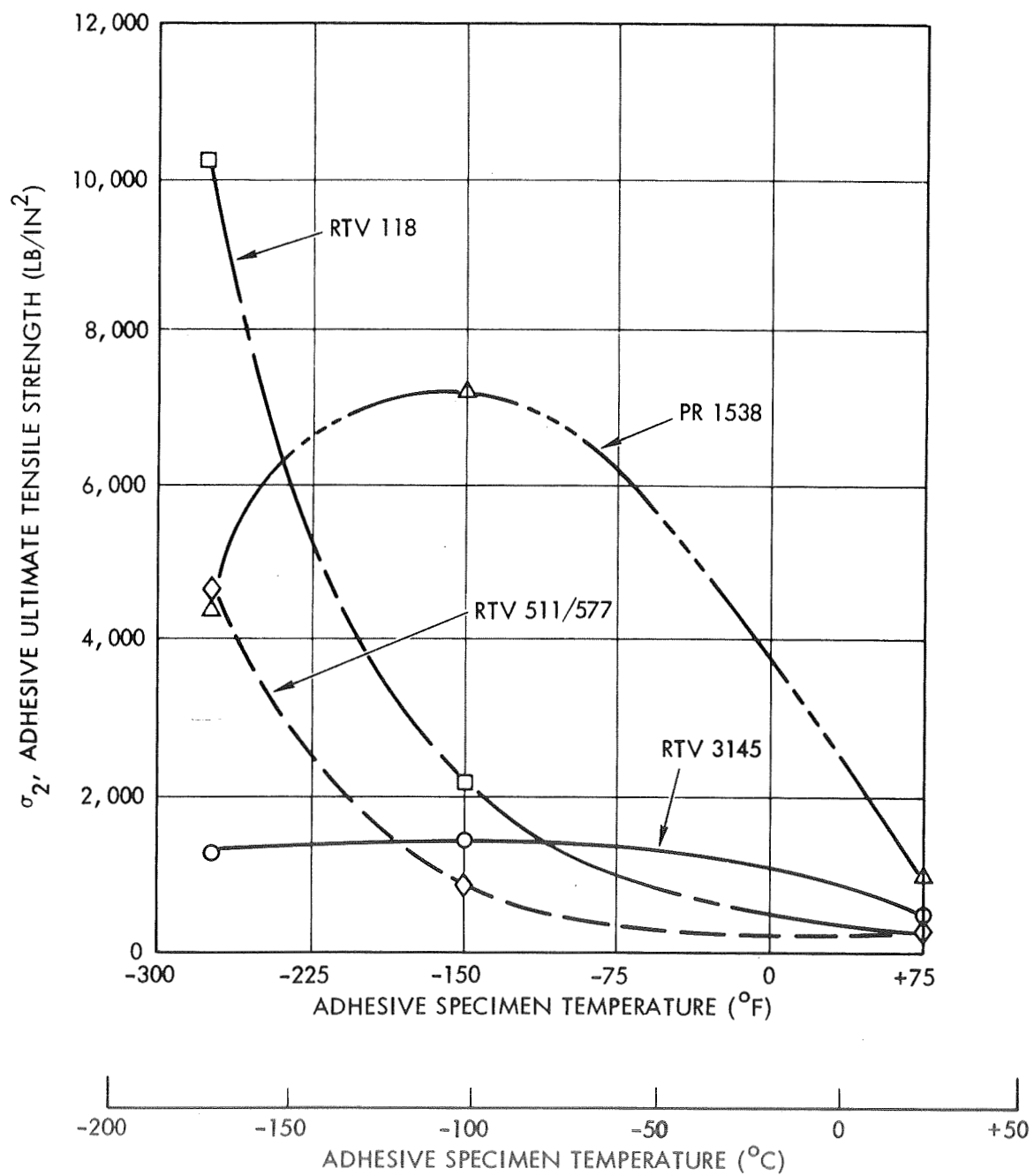


Figure 10.24 Variation of Adhesive Tensile Strength as Function of Specimen Temperature

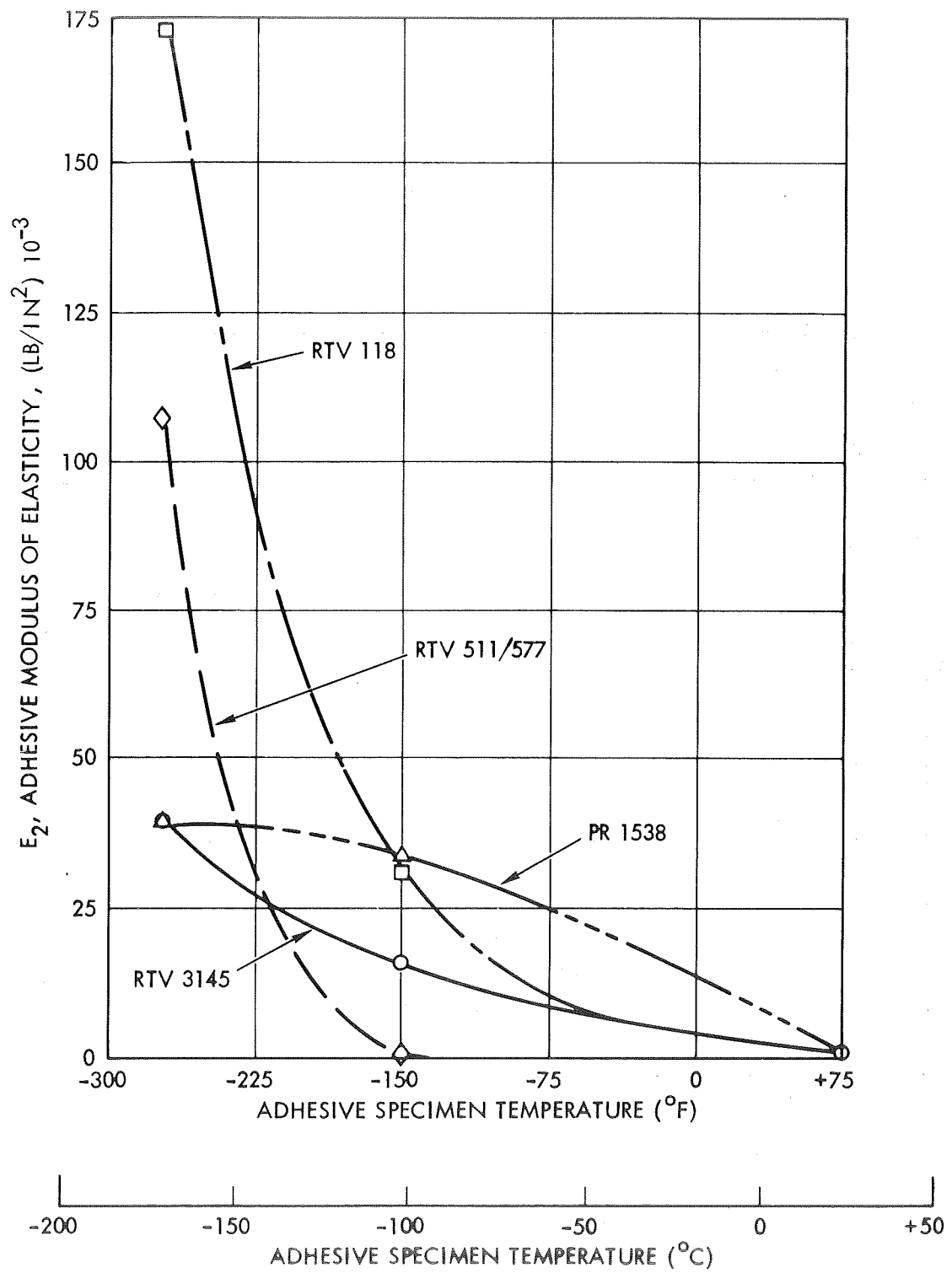


Figure 10.25 Variation of Adhesive Modulus of Elasticity as Function of Specimen Temperature

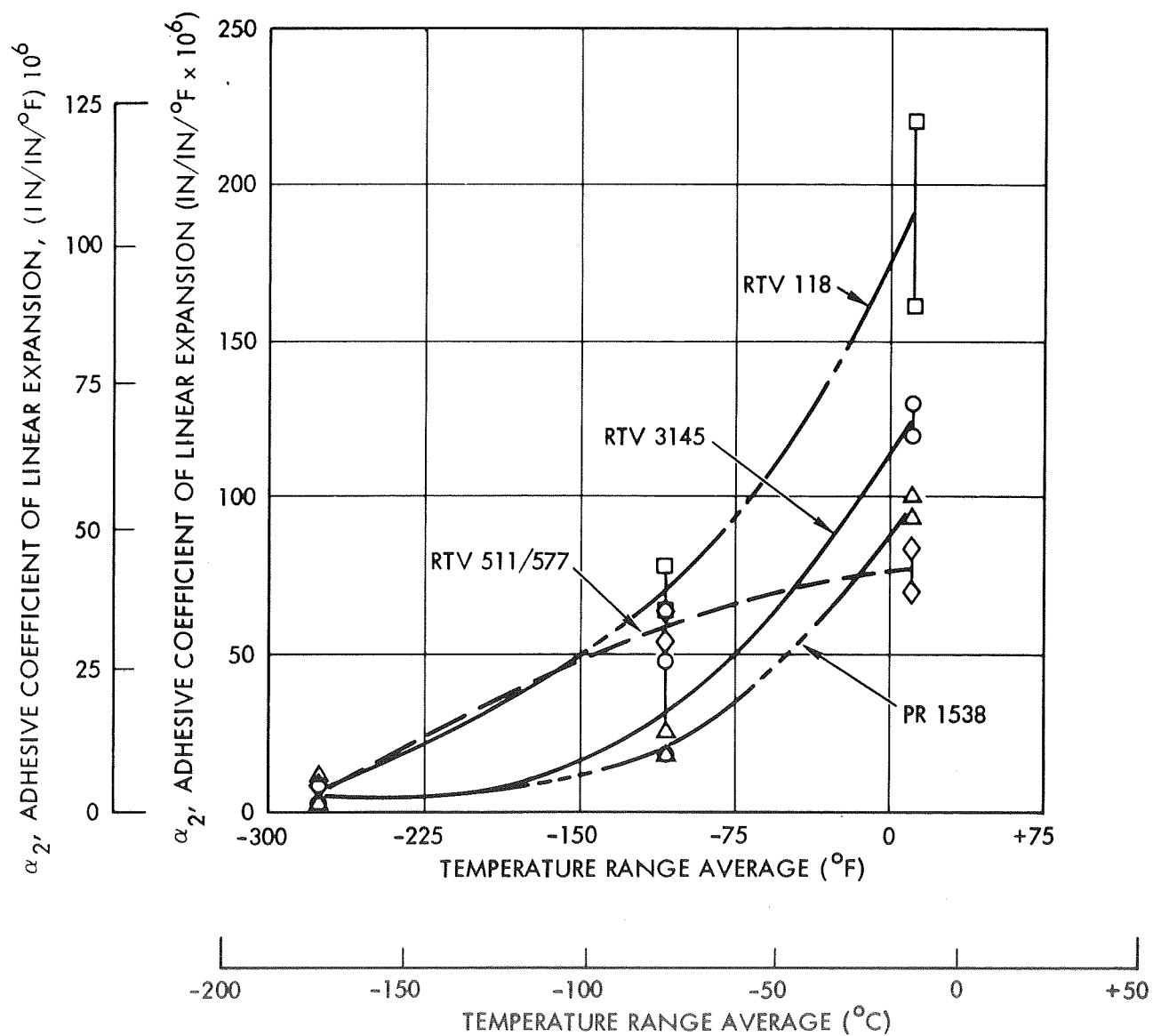


Figure 10.26 Variation of Adhesive Coefficient of Linear Expansion as Function of Average Temperature Range

Based upon these values and the parametric analyses conducted in Section 5, spalling of the silicon cells should not occur. This can also be seen by referring to Figures 10.27 and 10.28. In all cases these values are below the maximum allowable values which could cause spalling. This is true for the entire adhesive thickness range investigated (0.005 in. to 0.020 in.). However, there are several factors which could have lead to the spalling which did occur in the limited 46 out of 1200 cases. The first factor is the highly localized effect of maximum stress peaking (see Figures 5.3 to 5.6). This suggests the possibility of even higher surface stresses at values less than 0.00017 inches from the surface of the silicon cell. Should this be the case, then the maximum allowable values for E_2 and α_2 shown on Figures 10.27 and 10.28 could be considerably lower.

A second factor is the extremely high sensitivity of the peak axial and effective stresses to the adhesive modulus of elasticity (E_2). This can be seen in Figures 5.5 and 5.7. This is further compounded by the fact that three of the adhesives (RTV 3145, RTV 511/577, and RTV 118) have rapidly increasing values of E_2 in the low temperature regime (Figure 10.25). In addition, since both adhesive batch-to-batch and individual single batch non-homogeneity have been detected on previous programs, a high probability exists that these could contribute markedly to increasing the low temperature E_2 value for an individual adhesive dot. Finally, during simulated lunar surface thermal vacuum testing, the adhesive is subjected to both elevated (120°C) and low (-173°C) temperatures for long periods of time (up to 28 hours) and under hard vacuum (10^{-5} torr). Under these conditions outgassing of a portion of the adhesive volatile constituents, as well as possible phase changes in the elastomers may occur. These conditions could also produce a change in the adhesive modulus of elasticity. The assessment of a large statistical sample of each of the selected adhesives and under a variety of long duration environmental conditions was beyond the scope of this program. However, from the analyses conducted and the fact that spalling did occur in 4% of the cases investigated, leads one to conclude that significant changes in the value of E_2 could occur at the low temperatures to be expected on the lunar surface.

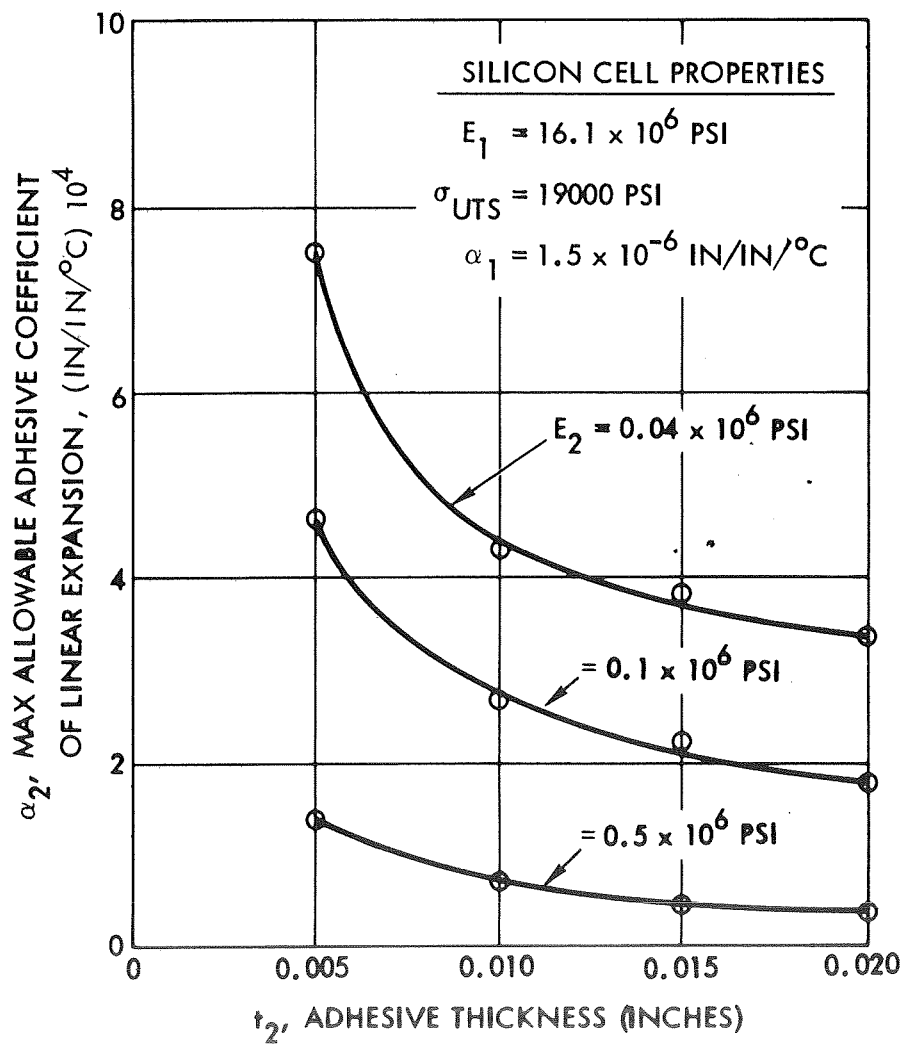


Figure 10.27 Maximum Allowable Value of Adhesive Coefficient of Expansion to Prevent Spalling ($\Delta T = -193^\circ\text{C}$)

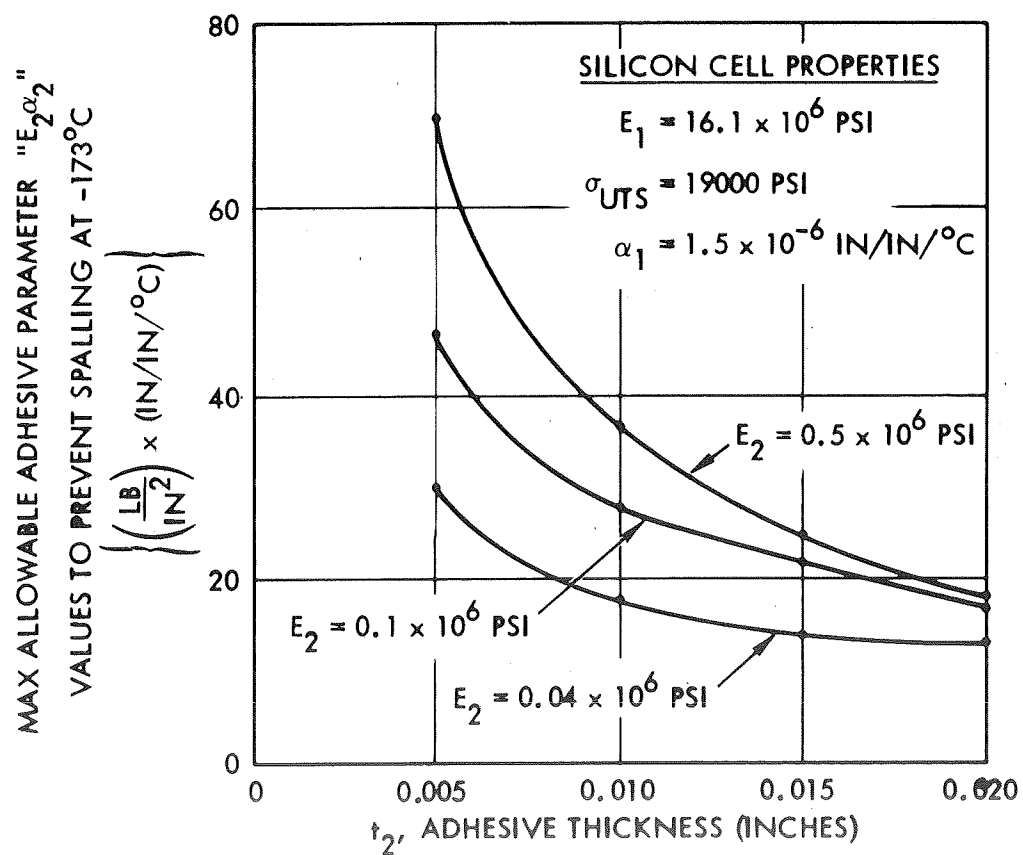


Figure 10.28 Maximum Allowable Value of " $E_2 \alpha_2$ " to Prevent Spalling ($\Delta T = -193^\circ\text{C}$)

A third factor is the large variation in the coefficient of linear expansion (Figure 10.26), α_2 , of the selected adhesives. The assessment of the resulting maximum effective silicon stress as a function of this parameter (Figures 5.9 to 5.12) not only indicates a high sensitivity to this value, but, as can be seen from Figure 10.27, to the adhesive dot thickness, t_2 , as well. The determination of the experimental values of α_2 for the various selected adhesives over the wide temperature range involved indicated variations as high as 50:1 from room temperature to -173°F . In addition, the accuracy of the determination of these values, particularly in the low temperature regime is highly dependent upon experimental technique and data reduction methods. Also, the inception of spalling, may actually occur at some temperature level higher than the minimum (-173°F) where the values of α_2 are considerably higher. Since for a given adhesive thickness, there is a maximum allowable value of the parameter, $E_2 \alpha_2$, and E_2 is increasing and α_2 is decreasing at different rates with decreasing temperature, it is possible to exceed these allowable values during the cool-down process.

Finally, it was noted in Table 7.6 that there can be a considerable variation in the ultimate tensile strength of silicon cells (σ_1). The generally accepted room temperature value for random crystal orientation, zone-soldered, cells (Centralab) is 19,000 psi. The equivalent value for the solder-dipped, preferred crystal orientation cells (Heliotek) is 28,000 psi. In conducting this spalling evaluation, the lower value was utilized to be conservative. However, because of this big difference in σ_1 , apparently based upon crystal orientation, it gives rise to the additional possibility that the silicon cell surface finish and potential micro-cracks in this surface generated by the manufacturing process could contribute to a marked reduction in σ_1 . For example, it was noted during an earlier program (Westinghouse Corporation) that there was several orders of magnitude (10^{-3}) less surface dislocations in polycrystalline, dendritic cells grown in the super-pure region of the silicon melt. This is in sharp contrast to the typical scratched surfaces obtained with random and preferred orientation single crystals grown and sawed-off from the Czochralski grown ingot. Furthermore, an assessment of the 46 spalled silicon cells revealed that approximately 76% of these failures occurred in the regions where either the random crystal oriented 2 cm x 2 cm or

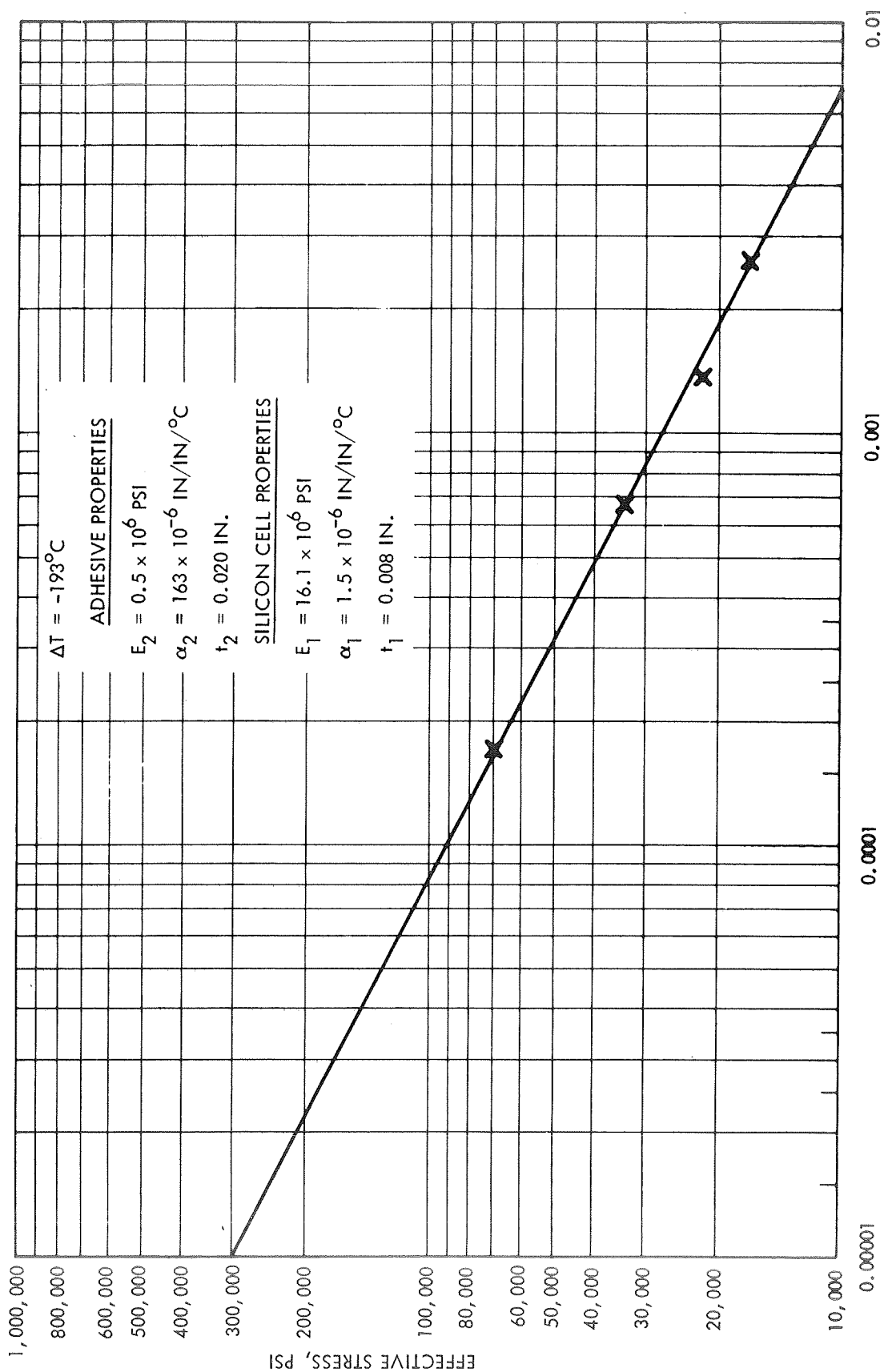


Figure 10.29 Extrapolation of Effective Stresses in Surface of Silicon Cells

2 cm x 4 cm cells were used. These cells were all considered to have the lower value of 19,000 psi as their ultimate tensile strength. In addition, many of the as manufactured 2 cm x 4 cm cells had a 0.010 inch bow in the 4 cm length. Upon further investigation, it was determined that to eliminate an alligatoring problem with these 2 cm x 4 cm cells, it was found necessary to squeegee away the excess solder on these solder-dipped cells. This operation would tend to flatten these slightly bowed cells and could produce micro-cracking of the under-surface. The occurrence of these micro-cracks could create stress concentration regions in the silicon cell surface and probably would result in considerably reducing its ultimate tensile strength. In addition, the maximum effective stresses in the silicon were calculated at a level 0.00017 inches from the adhesive/silicon cell interface (see Figure 5.5). The parametric data plotted in Figures 5.9 to 5.13 was based upon these maximum effective stresses. However, it is known that even higher stresses would result at levels in the silicon surface less than 0.00017. By extrapolating the data from Figure 5.4, it can be seen on Figure 10.29, that theoretically stresses as high as 300,000 psi could occur at a level of 0.00001 inches into the surface of the silicon cell. Since, the silicon material is not capable of sustaining such high stresses, the net result is to lower the allowable maximum values for the adhesive modulus of elasticity (E_2) and coefficient of linear expansion (α_2). Hence, if both of these factors are considered, the preponderance of spalling failures with the 2 cm x 4 cm silicon cells (i.e. lower ultimate tensile strength material and surface micro-cracks) can be explained. An additional factor which also probably contributed to these spalling failures was the average thickness of the adhesive dot used with the 2 cm x 4 cm cells. Since an overlap design was utilized, these adhesive dots were trapezoidal in cross-section. The maximum thickness of these dots varied from 0.025 in. to slightly over 0.030 in. The minimum thicknesses varied from 0.012 in. to 0.020 in. The range of values for the spalled 2 cm x 2 cm cells (0.010 in. to 0.030 in.) were also on the high side. The effect of these large adhesive thicknesses is to increase the maximum silicon stress (Figure 5.13) and to decrease the maximum allowable values of the adhesive E_2 and α_2 (Figures 10.27 and 10.28).

In view of the foregoing, it appears evident, that for lunar surface applications, where solar array temperatures as low as -173°C can be experienced, increased care must be taken in the design of the array cell-stack. While it is beyond the scope of this current program phase to establish detailed design criteria, since additional analyses and testing would be required, certain general recommendations can be made at this time. These are as follows:

- (a) The adhesive selected should have as low a value of modulus of elasticity (E_2) at low temperature (-173°C) as possible. Because of possible "batch-to-batch" differences, and potential lack of homogeneity within an individual batch, improved manufacturing process techniques and quality control procedures should be instituted for adhesives to be used for the low temperatures to be experienced on the lunar surface. For large area arrays, a sampling and material property testing control process should be initiated to insure that the low temperature property of E_2 of the adhesive is being maintained by the supplier.
- (b) The adhesive selected should have as low a value of coefficient of linear expansion (α_2) at low temperature (-173°C) as possible. However, because of the criticality of the " $E_2 \alpha_2$ " parameter with regard to spalling, and the rapid changing of the adhesive properties E_2 and α_2 with reduced temperatures, it may be important to select an adhesive whose " $E_2 \alpha_2$ " values stay below a maximum allowable value as the temperature is being reduced. In addition, similar to that stated for E_2 , improved process control and sampling techniques should be instituted to insure adequate quality control of this parameter.
- (c) Both the analytical and test data confirm the desirability of utilizing minimum adhesive thicknesses (t_2) to prevent spalling. For lunar surface applications a nominal thickness of 0.005 inches is preferred. Thus if a realistic manufacturing tolerance of ± 0.002 inches is allowed, an adhesive dot thickness range of 0.003 in. to 0.007 in. would result. By utilizing this range of thicknesses, increased design margins result with

regard to the selection and achievement of the low temperature adhesive E_2 and α_2 properties. In selecting these low adhesive thickness values, it should be recognized that this may preclude the use of a high packing factor overlap cellstack design. The latter design usually requires a thicker adhesive dot due to geometric considerations and in some instances to allow clearance space for interconnect expansion loops.

- (d) The use of silicon cells with as high an ultimate tensile strength (σ_1) as possible should be considered. This would imply that the preferred crystal orientation silicon cell with a σ_1 value of approximately 28,000 psi should be utilized for lunar surface applications. In addition, the adhesive/silicon cell surface of the cells should be as free from scratches and surface dislocations as is possible. It is recognized that both these requirements could result in increased silicon cell cost. However, this must be traded off against the gains achievable in cellstack design margins and increased reliability. In addition, if 2 cm x 4 cm or larger silicon cells are utilized, extreme care must be taken to avoid producing micro-cracks in the cell bonding surface. Minimization or elimination of cell bowing during its manufacture would be the desired approach. However, if this is not practical, then considerable care must be taken during the cell manufacturing operation (i.e. surplus solder squeegeeing) to avoid excessive flattening of bowed cells which could produce micro-cracks.
- (e) A review of the coefficients of linear expansion for the various substrates indicates that the graphite composite facesheet used on ETM IIIA more nearly matches the same silicon cell property at low temperatures (see Table 7.6). This, when coupled with the test results that only one cell out of 400 spalled on this configuration (see Table 10.3), would appear to indicate the desirability of using this material (or a 0 ± 60 orientation type which provides isotropic properties in the plane of the facesheet) for lunar surface applications. However, the benefits derived from this material property must be traded off with regard to other factors. For example, the graphite composite is

electrically conductive and a dielectric coating or material such as Kapton must be placed between the silicon cells and itself to prevent possible shorting. Secondly, the power to weight ratio of the ETM III module as developed during Phase II of this program was 15.5 watts/lb (34.1 watts/Kg) as indicated in Table 2.2 of Reference 1.2. This must be compared with 16.7 watts/lb (37.0 watts/Kg) for the fiberglass epoxy lattice design (ETM I) and 21.4 watts/lb (47.2 watts/Kg) for the Kapton substrate design (ETM II). In addition, where solar array stowage height may be critical, the Kapton substrate module thickness is approximately 0.025 inches while the minimum graphite composite module design would be 0.272 inches. Finally, if the array is to be subjected to multiple deployment and retraction operations, the lower specific weight Kapton substrate design may result in a lighter and simpler deployment mechanism in the 1/6 g environment that exists. Thus, all these factors, as well as minimization of spalling, must be taken into consideration when the selection of a candidate substrate design is being considered for a lunar surface application.

REFERENCES

- 1.1 "Study to Establish Criteria for a Solar Cell Array for Use as a Primary Power Source for a Lunar-Based Water Electrolysis System - Phase I Final Technical Report"; TRW Systems Report 09681-6002-R000, of 30 June 1968.
 - 1.2 "Study to Establish Criteria for a Solar Cell Array for Use as a Primary Power Source for a Lunar-Based Water Electrolysis System - Phase II Final Technical Report"; TRW Systems Report 09681-6005-R000, of 15 November 1969.
 - 1.3 RFP No. DCN-1-0-40-79268, "Study to Establish Criteria for a Solar Cell Array for Use as a Primary Power Source for a Lunar-Based Water Electrolysis System"; Modification 6 to Contract NAS 8-21189; NASA/MSFC, of 3 October 1969.
 - 1.4 TRW Systems Proposal No. 09681.003, "Study to Establish Criteria for a Solar Cell Array for Use as a Primary Power Source for a Lunar-Based Water Electrolysis System," Volume I, Technical Proposal, of 1 November 1969.
 - 1.5 "Study to Establish Criteria for a Solar Cell Array for Use as a Primary Power Source for a Lunar-Based Water Electrolysis System - Technical Plan - Phase III," TRW Systems Report 09681-6006-R000-Rev. 1, of 31 January 1970.
 - 1.6 "Study to Establish Criteria for a Solar Cell Array for Use as a Primary Power Source for a Lunar-Based Water Electrolysis System - Monthly Progress Report No. 32," TRW Systems Report 8210.1-70-48, of 15 May 1970.
-
- 5.1 Timoshenko, S., and Goodier, J., "Theory of Elasticity," McGraw-Hill Book Company 1951.
-
- 7.1 Morizane, K., and Gleim, P. S., "Thermal Stress and Plastic Deformation of Thin Silicon Slices," Journal of Applied Physics, Volume 40, Number 10, of September 1969.

- 7.2 "Test Plan - Engineering Test Model of LEPEPS Solar Array"; TRW Systems Report 09681-6004-R000, of 4 December 1968.
- 7.3 Robinson, J. C., and Cagle, E. H.; "ATM Material Control for Contamination Due to Outgassing," NASA/MSFC Report 50M02442, Rev. K, of 7 July 1969.
- 7.4 Runyan, W. R.; "Silicon Semiconductor Technology," McGraw-Hill, 1965.
- 7.5 Shamash, M. B., et al; "Development of Highly Reliable Soldered Joints for Printed Circuit Boards."
-
- 10.1 "Development of an Integrated Lightweight Flexible Silicon Solar Cell Array," Heliotek Report prepared for JPL under Contract No. 952560.
- 10.2 Yurk, J. F., "Extending the Thermal Range of RTV Adhesive Bonds"; 15th SAMPLE Exhibition; Los Angeles, California, of 1 May 1969.
- 10.3 Judkins, N. J.; "Common Interconnect-Effect of Solder Splash on the Allowable Displacement of the Large Stress Relief Loop"; TRW Systems Report 7415.2-1130, of 4 June 1970.
- 10.4 Judkins, N. J.; "M-35 Analytical Investigation of Solar Panel Interconnector"; TRW Systems Report 7415.2-575, of 28 August 1968.
- 10.5 Ralph, E. L., "Silicon Solar-Cell Array Interconnector Design," Textron, Inc., Heliotek Division, ASME Paper No. 70-Ay/SpT-30, Heat Transfer Conference, Los Angeles, California, of 21-24 June 1970.
- 10.6 Ralph, E. L., Zimmerman, E. F.; and Stella, P. M.; "Development of an Integrated Lightweight, Flexible Silicon Solar Cell Array - Final Report," Heliotek Division of Textron Inc.; JPL Contract No. 952560.
- 10.7 Luft, W., and Maiden, E.; "Temperature Cycling Effects on Solar Panels"; Fourth IECEC Conference, Washington D. C., 22-26 September 1970.
-

APPENDIX A

THERMAL STRESS ANALYSIS FOR SUB-MODULE

COMMON INTERCONNECTS

SUMMARY:

A thermal stress analysis was performed on the common interconnects of the Lunar-Based Solar Array Test Model. The analytical results indicated that the design of the solar array test model is such that the common interconnects will experience no thermal stress resulting from different coefficients of thermal expansion over the temperature range from 75°F (24°C) to -280°F (-173°C).

DISCUSSION:

The purpose of this simplified analysis was to determine whether or not the design of the common interconnects (Figure 4.13) are thermally adequate when they are subjected to a temperature range of 75°F (24°C) to -280°F (-173°C). In performing the analysis, the basic assumption was that the whole solar array is isothermal at any time. Hence, thermal stress caused by temperature gradients in the solar array were not investigated. Furthermore, the following simplifying assumptions were made:

- a) The distance between the center-lines of the cells is fixed.
- b) The cover glass and the cell expand or contract as one body with the coefficient of thermal expansion of the cell.
- c) The interconnect and the cell at the solder joint expand or contract with the coefficient of thermal expansion of the cell.
- d) The assumed values of coefficients of thermal expansion of the cell (silicon) and the common interconnect (Kovar) are shown on Page A-1.

No thermal stress analysis was performed on the bus bars. Based on the results of this analysis on the common interconnects, it appears that the sections of the bus bars where expansion/contraction loops are provided will experience no thermal stress resulting from different coefficients of thermal expansion over the temperature range from 75°F (24°C) to -280°F (-173°C). However, the sections where expansion/contraction loops are not provided may experience thermal stress. This was to be determined during thermal-vacuum testing.

Interconnect:

Material is Kovar.

$$\alpha = 2.26 \times 10^{-6} \text{ in/in } ^\circ\text{F at } 0^\circ\text{F, or } 4.06 \times 10^{-6} \text{ in/in } ^\circ\text{C at } -17.8^\circ\text{C}$$

$$\alpha = 1.88 \times 10^{-6} \text{ in/in } ^\circ\text{F at } -320^\circ\text{F, or } 3.38 \times 10^{-6} \text{ in/in } ^\circ\text{C at } -195.5^\circ\text{C}$$

Cell:

Material is Silicon.

$$\alpha = 3.0 \times 10^{-6} \text{ in/in } ^\circ\text{C at } 70^\circ\text{C to } 0^\circ\text{C}$$

$$\alpha = 1.7 \times 10^{-6} \text{ in/in } ^\circ\text{C at } -100^\circ\text{C}$$

$$\alpha = 0 \text{ (no change) at } -170^\circ\text{C}$$

NOTE: Values of α are obtained from G. R. Luckey (Adv. Systems Design)

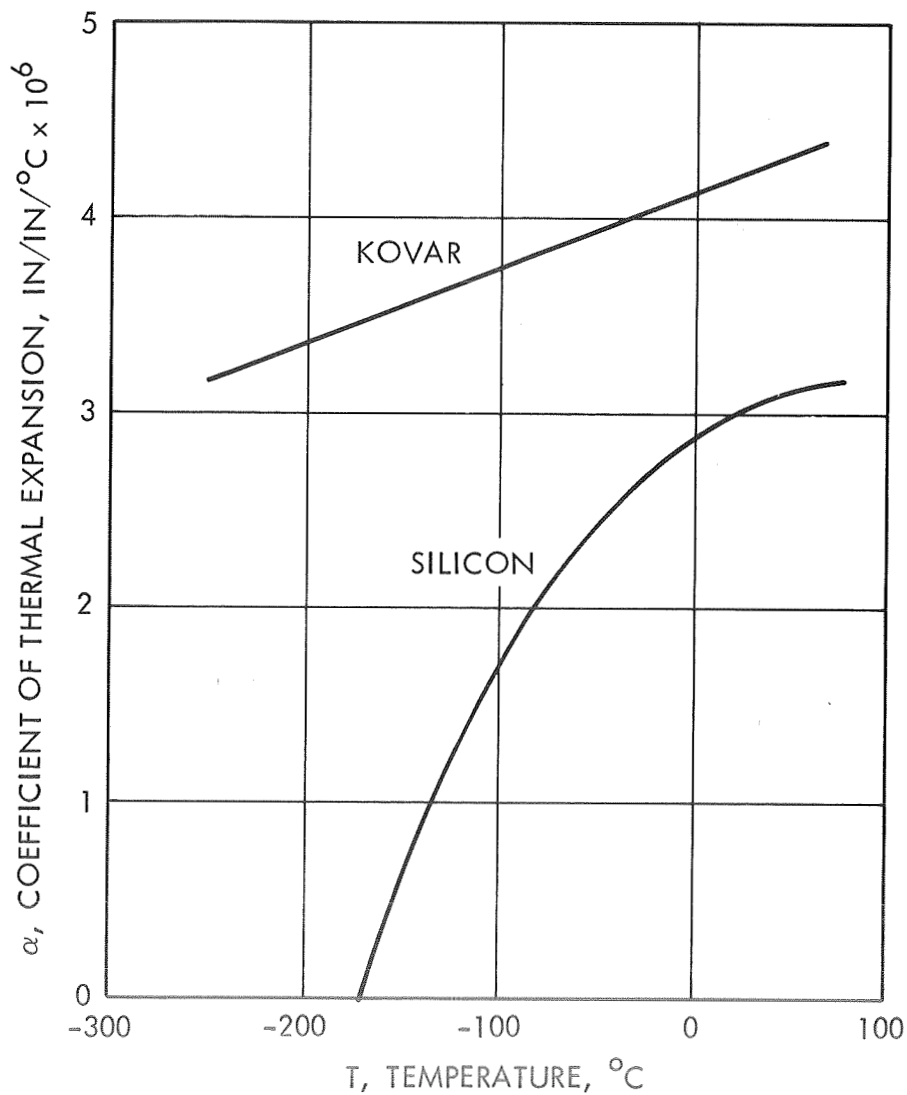
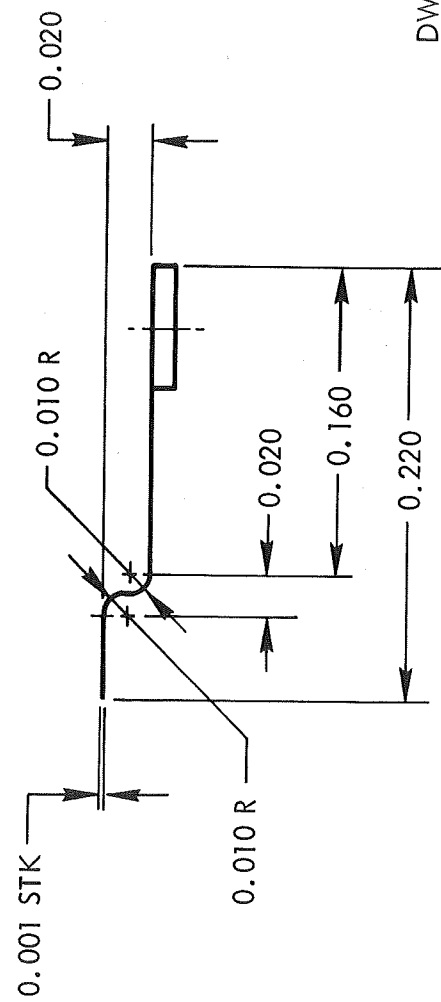
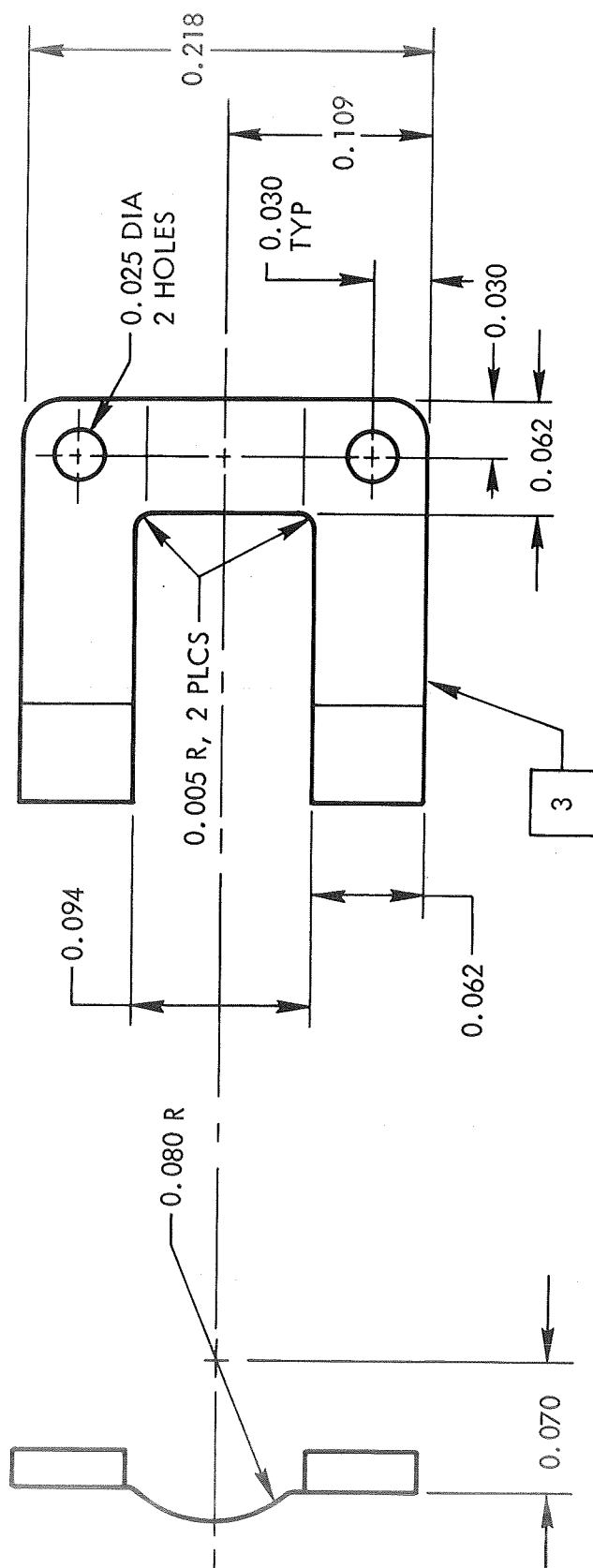


Figure A-1



DWG SK260790
Figure A-2

Assumptions:

1. Distance between center-lines of cells are fixed.
2. Cover glass and cell and adhesive expand or contract with α of the cell.
3. Interconnect and cell at solder joint expand or contract with α of the cell.

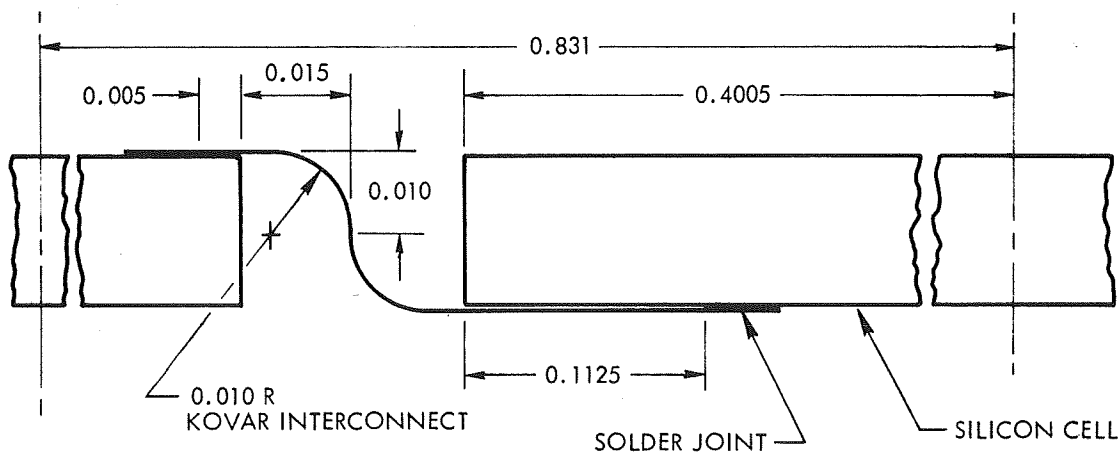


Figure A-3

$$(1) \quad L_{Kovar_{Allow}} = 2 \sqrt{(.010)^2 + (.015 + \Delta L_{Silicon})^2} + .1175 - 2\Delta L_{Silicon}$$

$$(2) \quad L_{Kovar_f} = L_{Kovar_i} (1 - \alpha_{Kovar} \Delta T) = .1589 (1 - \alpha_{Kovar} \Delta T)$$

If $L_{Kovar_{Allow}} > L_{Kovar_f}$, stress = 0

$$(3) \quad \Delta L_{Silicon} = L_{Silicon_i} \alpha_{Silicon} \Delta T = .4005 \alpha_{Silicon} \Delta T$$

$$L_{Kovar_i} = 2 \left(.010 \times \frac{\pi}{2} \right) + .1125 + .015 = .1589 \text{ in.}$$

From the curves, values of α are obtained:

T (°C)	α_{Silicon} (in/in -°C)	α_{Kovar} (in/in -°C)
0	2.9×10^{-6}	4.14×10^{-6}
-100	1.7×10^{-6}	3.75×10^{-6}
-173	0	3.47×10^{-6}

T = 0°C:

From Eq. (3), $\Delta L_{\text{Silicon}} = .4005 \times 2.9 \times 10^{-6} (24 - 0) = .0000279$ in.

$$\begin{aligned}
 \text{From Eq. (1), } L_{\text{Kovar}_{\text{Allow}}} &= 2 \sqrt{(.010)^2 + (.0150279)^2} + .1175 - 2 \times .0000279 \\
 &= 2 \times .018051 + .1175 + .000056 \\
 &= .153658 \text{ in.}
 \end{aligned}$$

$$\begin{aligned}
 \text{From Eq. (2), } L_{\text{Kovar}_f} &= .1589 \left[1 - 4.14 \times 10^{-6} (24 - 0) \right] \\
 &= .158884 \text{ in.}
 \end{aligned}$$

$$L_{\text{Kovar}_f} > L_{\text{Kovar}_{\text{Allow}}} ; \text{ o.k.}$$

T = -100°C:

$$\Delta L_{\text{Silicon}} = .4005 \times 1.7 \times 10^{-6} (24 - 100) = .0000843 \text{ in.}$$

$$\begin{aligned}
 L_{\text{Kovar}_{\text{Allow}}} &= 2 \sqrt{(.010)^2 + (.0150843)^2} + .1175 - 2 \times .0000843 \\
 &= 2 \times .018098 + .1175 + .000167 \\
 &= .153863
 \end{aligned}$$

$$L_{\text{Kovar}_f} = .1589 [1 - 3.75 \times 10^{-6} (24 + 100)]$$

$$= .158826 \text{ in.}$$

$$L_{\text{Kovar}_f} > L_{\text{Kovar}_{\text{Allow}}} \text{ o.k.}$$

$$T = -173^\circ\text{C:}$$

$$\Delta L_{\text{Silicon}} = .4005 \times 0 \times (24 + 173) = 0 \text{ in.}$$

$$L_{\text{Kovar}_{\text{Allow}}} = 2\sqrt{(.010)^2 + (.015)^2} + .1175$$

$$= .153556 \text{ in.}$$

$$L_{\text{Kovar}_f} = .1589 [1 - 3.47 \times 10^{-6} (24 + 173)]$$

$$= .158791 \text{ in.}$$

$$L_{\text{Kovar}_f} > L_{\text{Kovar}_{\text{Allow}}} \text{ o.k.}$$

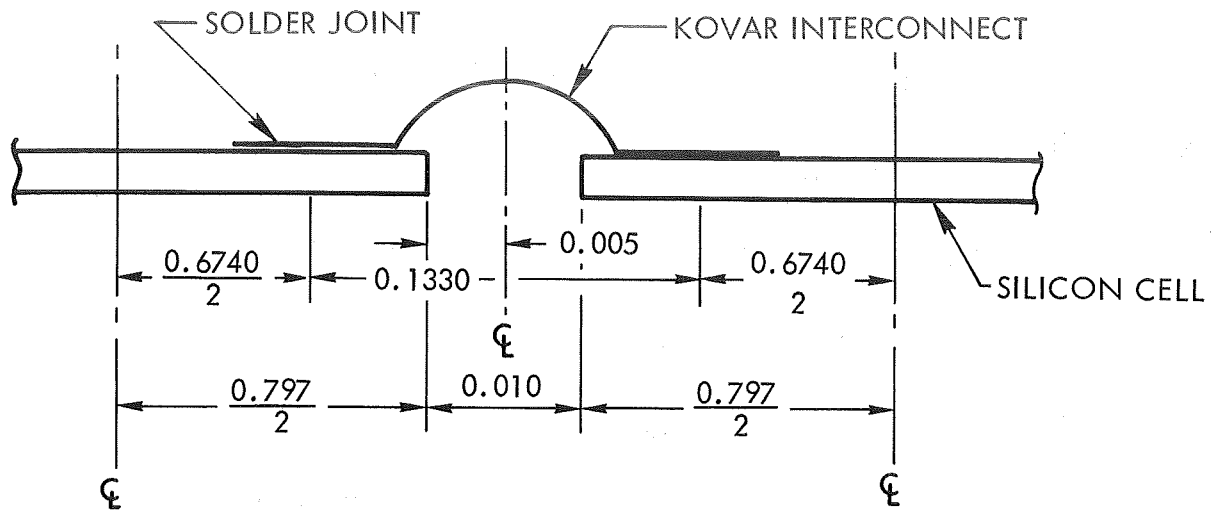


Figure A-4

For detail dimensions, see page 2.

$$(4) \quad L_{Kovar_{Allow}} = 2 [.109 - (.030 + .0125)] + \Delta L_{Silicon}$$

$$= .1330 + \Delta L_{Silicon}$$

$$(5) \quad L_{Kovar_f} = L_{Kovar_i} (1 - \alpha_{Kovar} \Delta T) = .13948 (1 - \alpha_{Kovar} \Delta T)$$

If $L_{Kovar_{Allow}} > L_{Kovar_f}$, stress = 0

$$L_{Silicon_i} = [2(.797/2) + .010] - 2 [.109 - (.030 + .0125)]$$

$$= .8070 - .1330 = .6740 \text{ in.}$$

$$(6) \quad \Delta L_{Silicon} = L_{Silicon_i} \alpha_{Silicon} \Delta T = .6740 \alpha_{Silicon} \Delta T$$

$$L_{Kovar_i} = 2 \left(\frac{.05024}{\sin \theta} + .062 \right) - 2 (.030 + .0125)$$

$$= .22448 - .085 = .13948 \text{ in.}$$

$$\theta = \sin^{-1} \frac{.047}{.080} = \sin^{-1} .587 = 36^\circ$$

$$\text{Arc Length} = R\theta = .080 \times 36^\circ \times \frac{2\pi}{360^\circ} = .05024 \text{ in.}$$

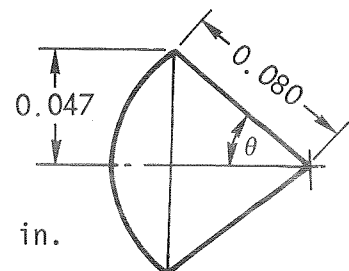


FIGURE A-5

T = 0 °C:

$$\text{From Eq. (6): } \Delta L_{\text{Silicon}} = .6740 \times 2.9 \times 10^{-6} (24 - 0) = .000047 \text{ in.}$$

$$\text{From Eq. (4): } L_{\text{Kovar}_{\text{Allow}}} = .1330 + .000047 = .133047 \text{ in.}$$

$$\begin{aligned} \text{From Eq. (5): } L_{\text{Kovar}_f} &= .13948 [1 - 4.14 \times 10^{-6} (24 - 0)] \\ &= .139466 \text{ in.} \end{aligned}$$

$$L_{\text{Kovar}_f} > L_{\text{Kovar}_{\text{Allow}}} \text{ o.k.}$$

$$T = -100^\circ\text{C: } \Delta L_{\text{Silicon}} = .6740 \times 1.7 \times 10^{-6} (24 + 100) = .000141 \text{ in.}$$

$$L_{\text{Kovar}_{\text{Allow}}} = .1330 + .000147 = .133141 \text{ in.}$$

$$\begin{aligned} L_{\text{Kovar}_f} &= .13948 [1 - 3.75 \times 10^{-6} (24 - 100)] \\ &= .139415 \text{ in.} \end{aligned}$$

$$L_{\text{Kovar}_f} > L_{\text{Kovar}_{\text{Allow}}} \text{ o.k.}$$

$$T = -173^\circ\text{C: } \Delta L_{\text{Silicon}} = .6740 \times 0 \times (24 - 173) = 0. \text{ in.}$$

$$L_{\text{Kovar}_{\text{Allow}}} = .1330 + 0. = .1330 \text{ in.}$$

$$\begin{aligned} L_{\text{Kovar}_f} &= .13948 [1 - 3.47 \times 10^{-6} (24 - 173)] \\ &= .139385 \text{ in.} \end{aligned}$$

$$L_{\text{Kovar}_f} > L_{\text{Kovar}_{\text{Allow}}} \text{ o.k.}$$

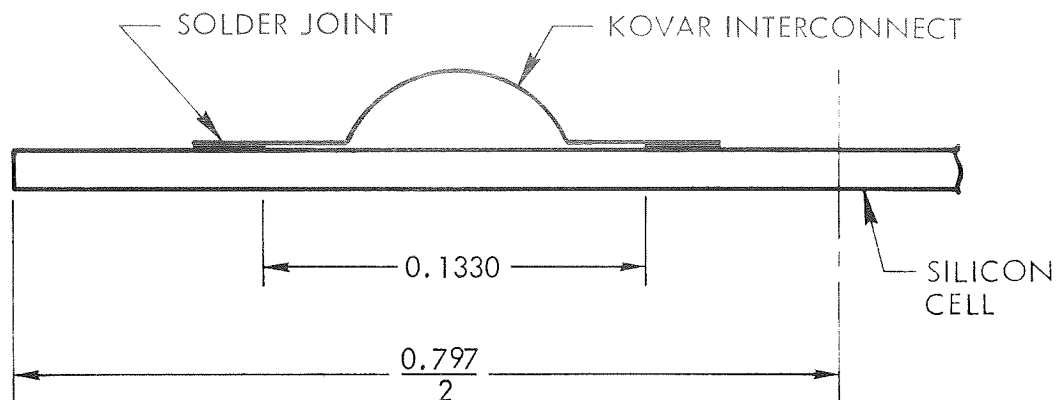


Figure A-6

For detail dimensions, see page 2.

$$(7) \quad L_{Kovar_{Allow}} = L_{Silicon_f} = L_{Silicon_i} (1 - \alpha_{Silicon} \Delta T)$$

$$L_{Silicon_i} = 2 [.109 - (.030 + .0125)] = .1330 \text{ in.}$$

$$(5) \quad L_{Kovar_f} = .13948 (1 - \alpha_{Kovar} \Delta T)$$

$$\text{If } L_{Kovar_f} > L_{Kovar_{Allow}}, \text{ stress} = 0$$

NOTE: L_{Kovar_f} are obtained from the previous page.

$$T = 0^\circ\text{C}: \quad L_{Kovar_{Allow}} = .1330 [1 - 2.9 \times 10^{-6} (24 - 0)] = .132991 \text{ in.}$$

$$L_{Kovar_f} = .139466 \text{ in.}$$

$$L_{Kovar_f} > L_{Kovar_{Allow}} \quad \text{o.k.}$$

$$T = -100^\circ\text{C}: \quad L_{Kovar_{Allow}} = .1330 [1 - 1.7 \times 10^{-6} (24 + 100)] = .132972 \text{ in.}$$

$$L_{Kovar_f} = .139415 \text{ in.} \quad L_{Kovar_f} > L_{Kovar_{Allow}} \quad \text{o.k.}$$

$$T = -173^\circ\text{C}: \quad L_{Kovar_{Allow}} = .1330 [1 - 0 (24 + 173)] = .1330 \text{ in.}$$

$$L_{Kovar_f} = .139385 \text{ in.} \quad L_{Kovar_f} > L_{Kovar_{Allow}} \quad \text{o.k.}$$

APPENDIX B

TEST CURVES FROM X-Y PLOTTER

FOR

DETERMINATION OF COEFFICIENT OF EXPANSION

FOR

FOUR CANDIDATE ADHESIVE MATERIALS

SUMMARY

The accompanying curves included in this appendix, (Figures B-1, B-2, B-3, and B-4) depict the experimental data as directly obtained from the X-Y plotter. This data was used in the determination of the coefficients of linear expansion for the four candidate cell-to-substrate adhesives used in this program. This data was reduced and incorporated into Figures 7.11 to 7.14 of Section 7. The values listed in Table 7.3 of that section were obtained from Figures 7.11 to 7.14 by determining the average slope to these curves (for both Run No. 1 and 2) in the temperature regions designated. The variations in the chilldown curve and the warm-up curve is a measure of the hysteresis in the test set-up. The slopes of the warm-up curves were used to determine the values in Table 7.3.

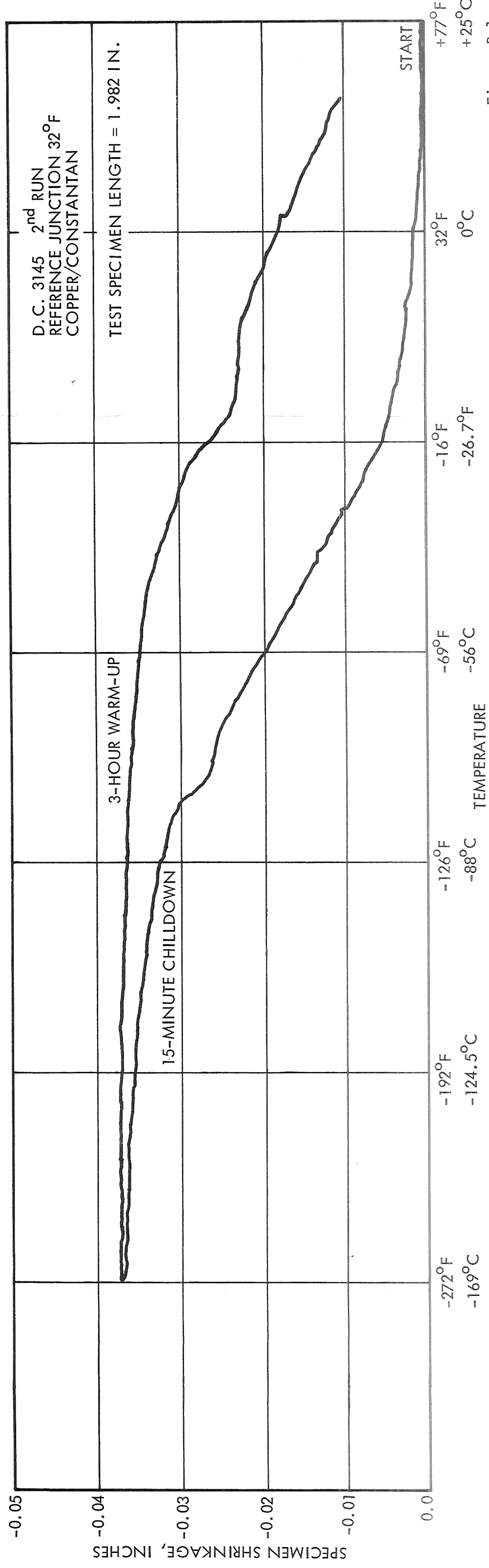
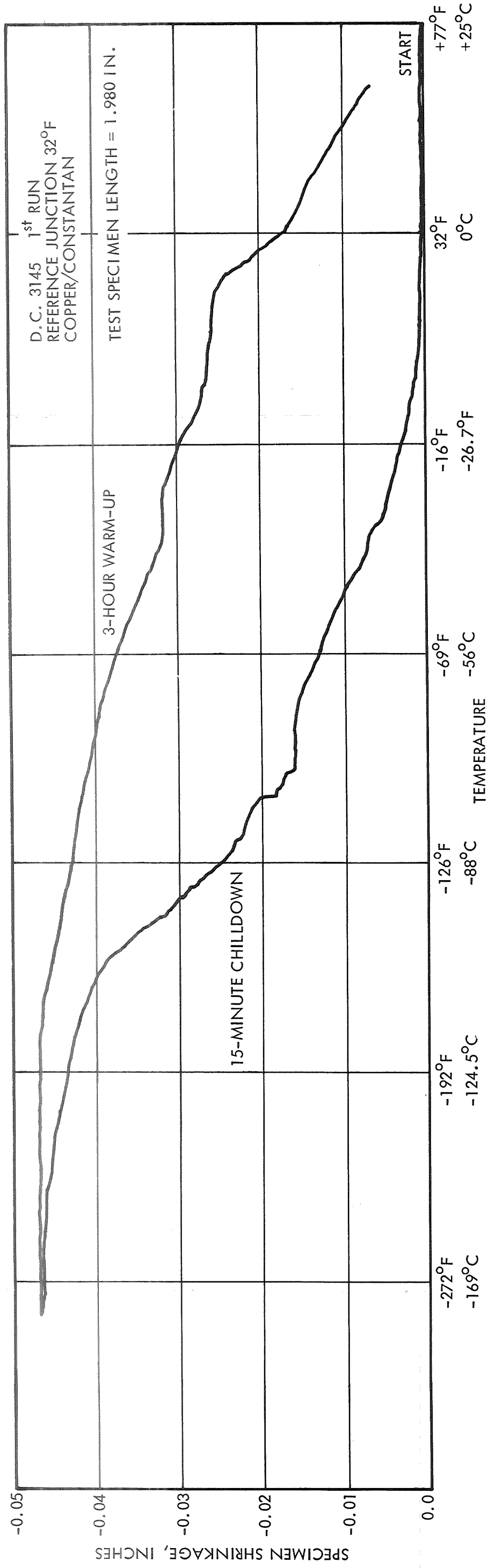


Figure B-1

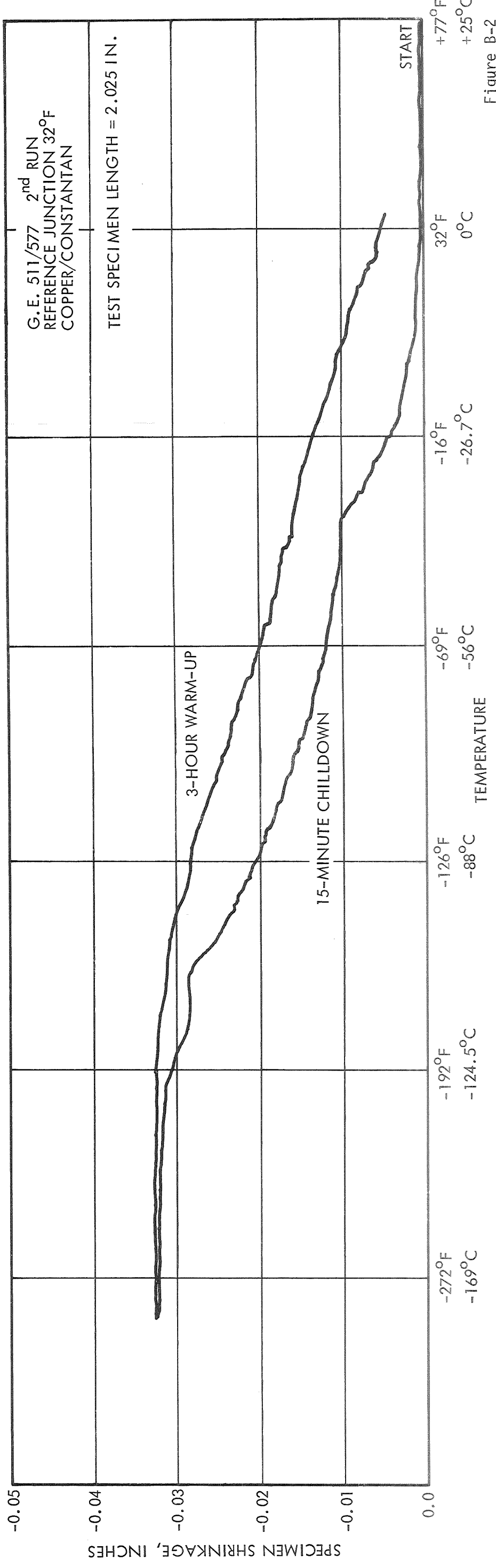
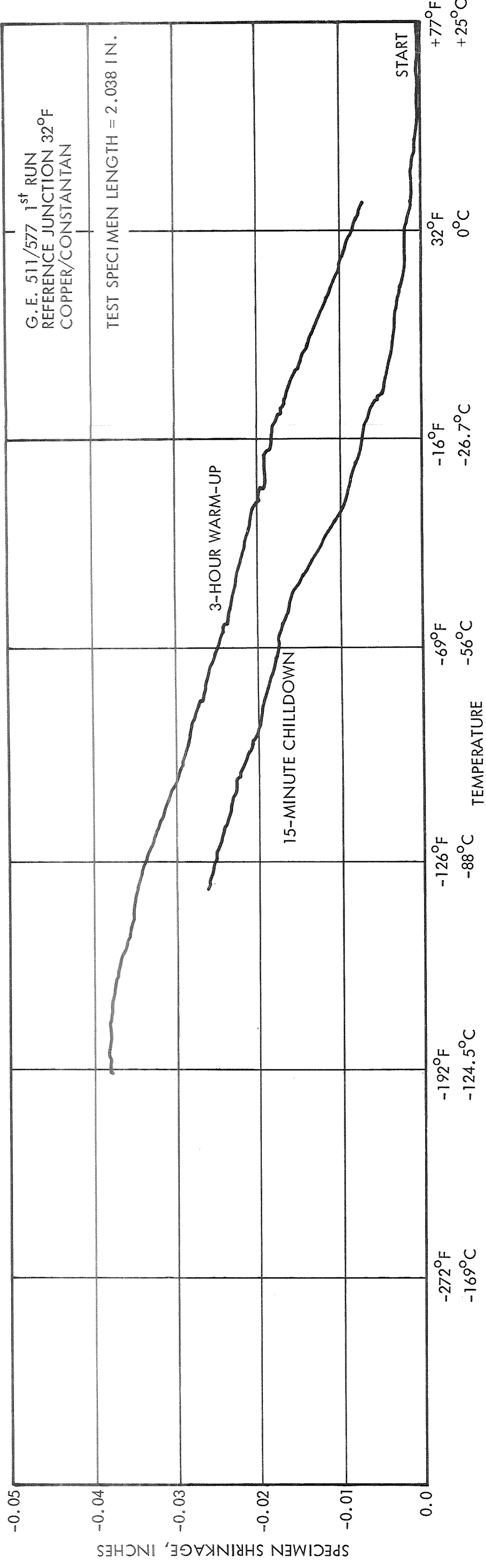


Figure B-2

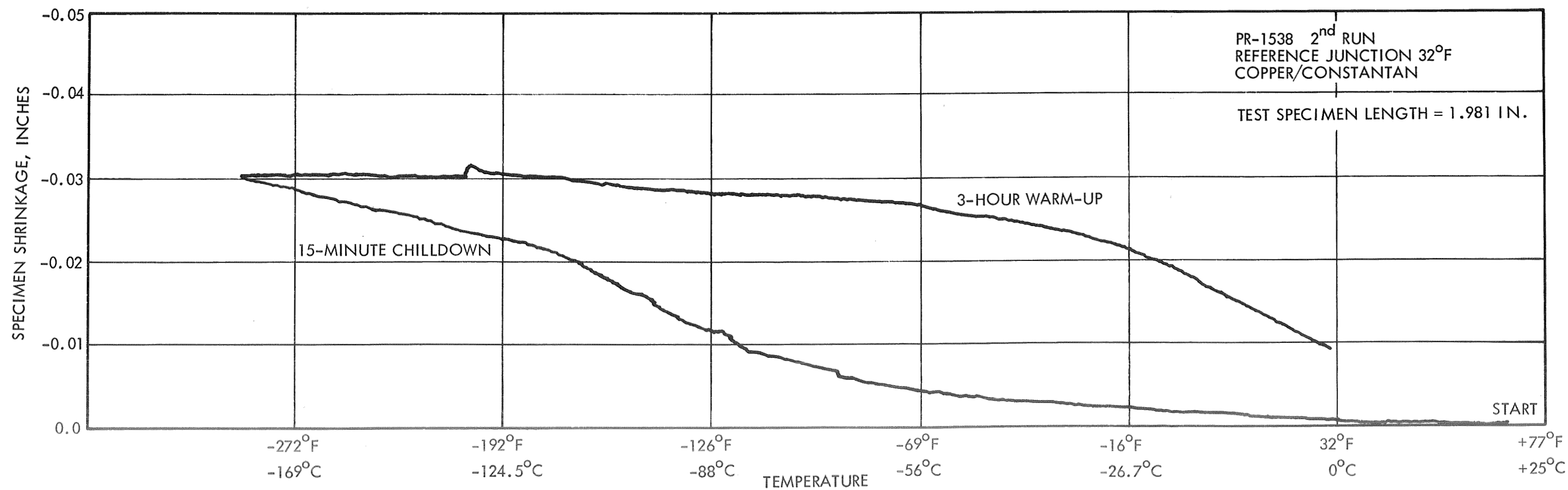
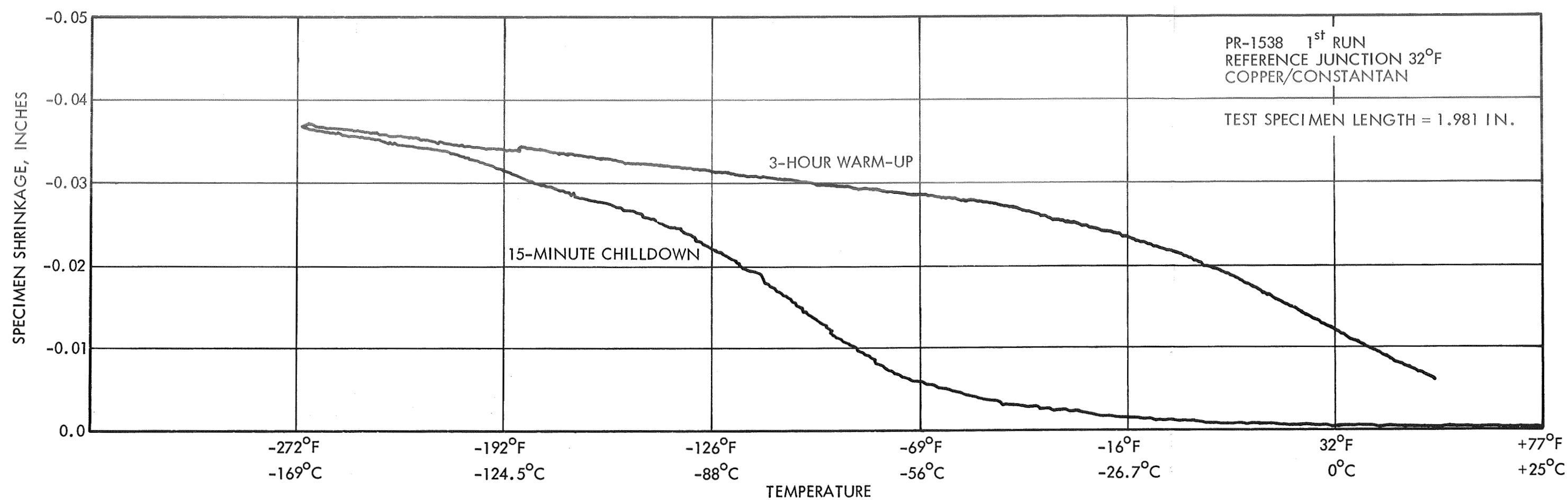


Figure B-3

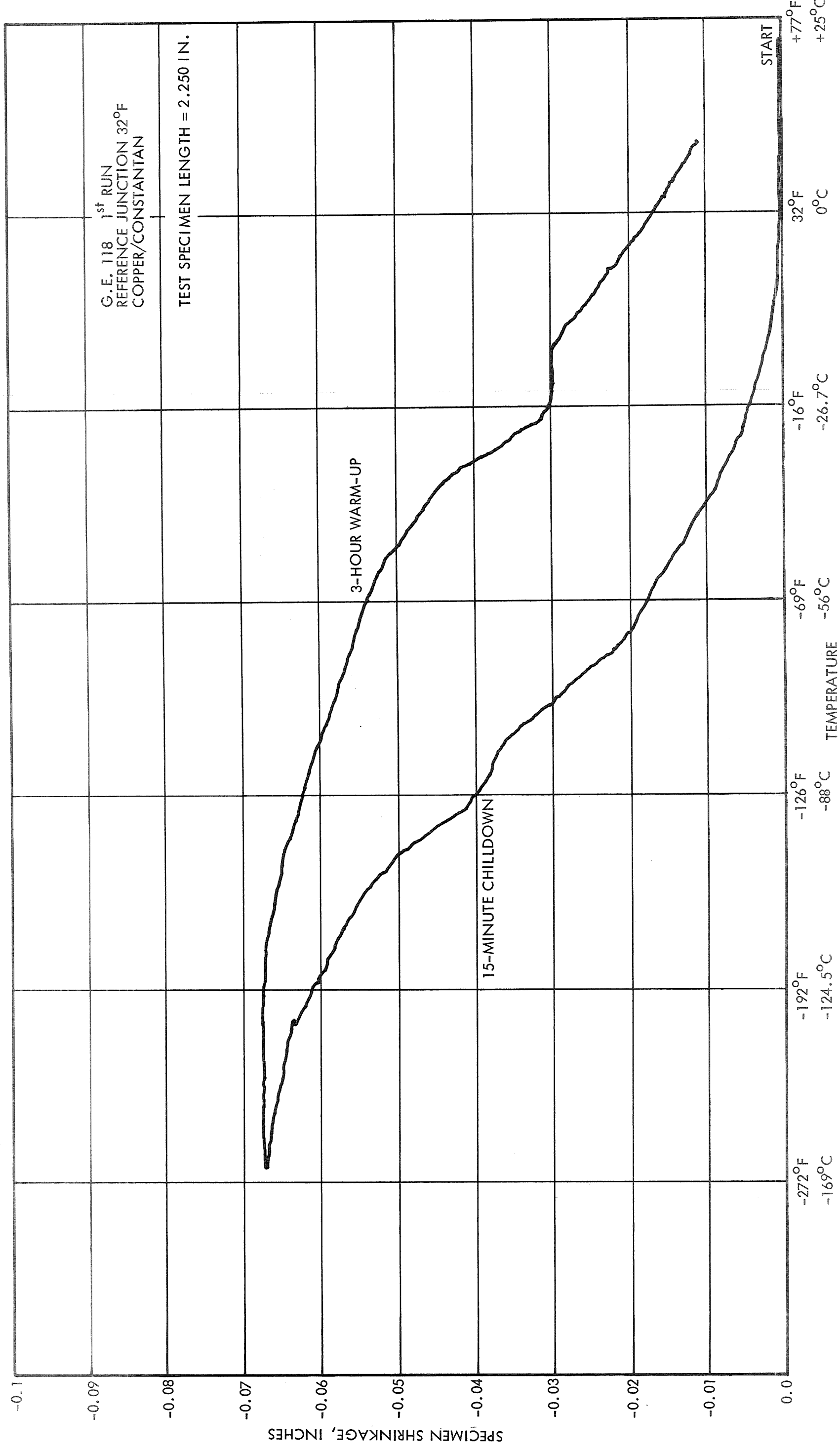


Figure B-4
B-5

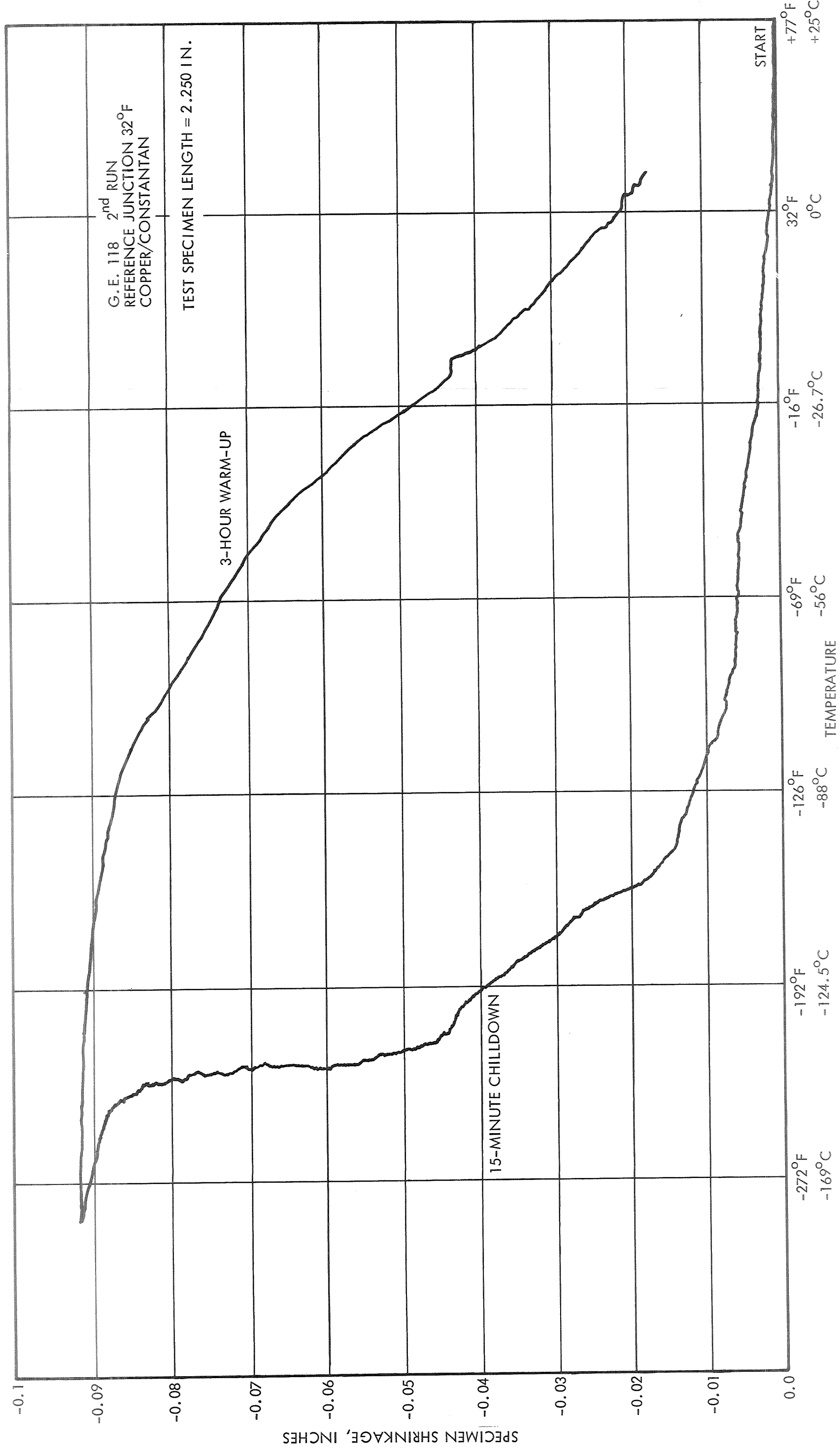


Figure B-5
B-6

APPENDIX C

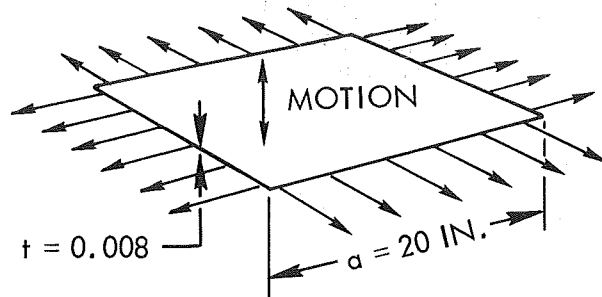
DYNAMIC AND THERMAL ANALYSIS FOR

PRE-STRESSED FIBERGLASS DIAPHRAM

FOR ENGINEERING TEST MODEL ETM IA

LUNAR BASED SOLAR ARRAY
PRE-STRESSED FIBERGLASS SHEET

Natural Frequency Estimate for Pre-Stressed Fiberglass Diaphragm



$$T = 20.4 \frac{\text{LB}}{\text{IN.}}$$

Figure C-1

$$w = 0.008 \left(.080 \frac{\text{lb.}}{\text{in.}^3} \right) = .00064 \frac{\text{lb.}}{\text{in.}^2} \text{ dist wt.}$$

$$\rho = (.64 \times 10^{-3} \frac{\text{lb.}}{\text{in.}^2}) / (.386 \times 10^3 \text{ in./sec}^2) = 1.66 \times 10^{-6} \frac{\text{lb.-sec.}^2}{\text{in.}^3}$$

Reference Sokonikoff and Redheffer, "Mathematics of Physics and Modern Engineering," Pg. 477

$$f = \frac{\alpha}{2} \left(\sqrt{\frac{2}{a}} \right) ; \gamma = \sqrt{\frac{T}{\rho}}$$

$$= \frac{3510}{\sqrt{2(20)}} = \sqrt{\frac{20.4}{1.66 \times 10^{-6}}} ; \frac{\text{lb./in}}{\text{lb.-sec}^2/\text{in}^3}$$

$$= \underline{124} \text{ Hz} \qquad = 3510 \text{ in./sec}$$

NOTE: Flexibility of side beams, which reduces the pretension, has not been included.

Deflection Check

$$\Delta_{\text{fiberglass}} = \frac{TL}{tE} = \frac{20.4 (20)}{.008 (4 \times 10^6)} = \frac{0.204 (.20)}{0.8 (4)}$$

$$= \underline{0.013} \text{ (Total)} / \underline{.0065} \text{ per side}$$

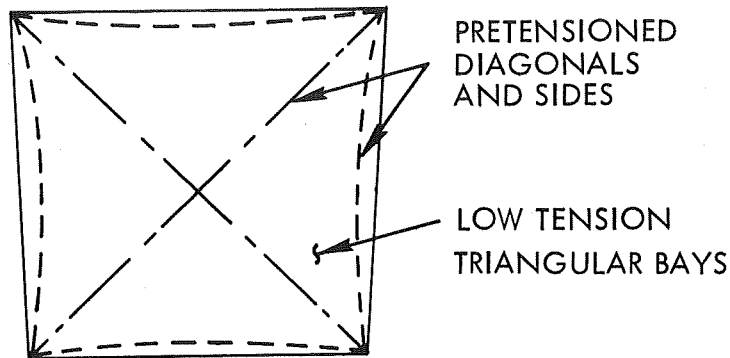
$$\Delta_{\text{beam}} = \frac{s}{384} \frac{wl^4}{EI} = \frac{5 (.204 \times 10^2) (2 \times 10^1)^4}{384 (10^7) (.570 \times 10^{-1})} = \underline{0.0746}$$

$$I = \frac{1}{12} (1^4 - .75^4) = 0.0570 \text{ in.}^4$$

.316
.684

Conclusion:

Beam flexibility will allow low-tension membrane vibration in four triangular bays bounded by the sides and diagonals



Coefficient of Exp.

1.5×10^{-5} in/in/°C Crosswise
 1.0×10^{-5} in/in/°C Lengthwise
 13.0×10^{-6} in/in/°F Aluminum

Temp. Range +130°C to -173°C
 266°F to -279.4°F

Assume Room Temp = 70°F or 21.1°C = t_0

$$\begin{aligned} \delta &= \alpha l (t - t_0) \\ \delta_{\text{glass}} &= (+21.1^\circ\text{C to } +130^\circ\text{C}) \\ \Delta t &= 130 - 21.1 = 108.9^\circ \\ \delta_{\text{gl}} &= (1.5 \times 10^{-5}) (20) (108.9) \\ &= .03267 \\ \delta_{\text{glass}} &= (+21.1^\circ\text{C to } -173^\circ\text{C}) \\ \Delta t &= -173 - 21.1 = -194.1^\circ \\ \delta_{\text{gl}} &= (1.5 \times 10^{-5}) (20) (-194.1) \\ &= -.05733 \\ \delta_{\text{alum}} &= (+70^\circ\text{F to } +266^\circ\text{F}) \\ \Delta t &= 266 - 70 = 196^\circ \\ \delta_{\text{al}} &= (13 \times 10^{-6}) (20) (196) \\ &= .05096 \\ \delta_{\text{alum}} &= (+70^\circ\text{F to } -279.4^\circ\text{F}) \\ \Delta t &= -279.4 - 70 = -349.4^\circ \\ \delta_{\text{al}} &= (13 \times 10^{-6}) (20) (-349.4) \\ &= -.09084 \end{aligned}$$

Figure C-2

Fiberglass

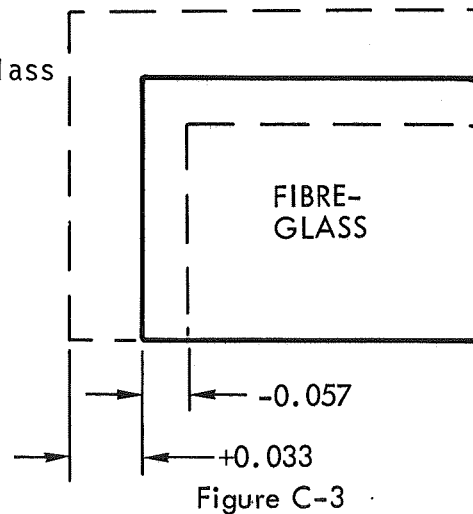


Figure C-3

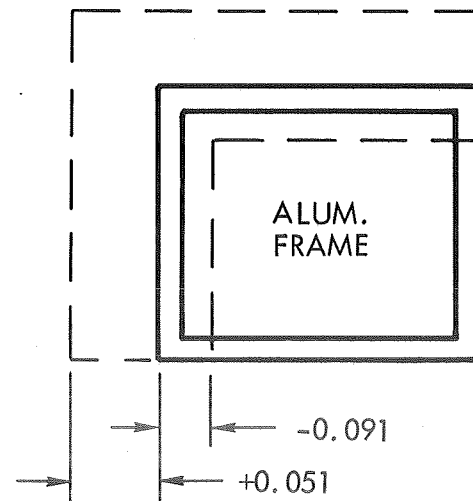


Figure C-4

$$\delta = \frac{PL}{AE} \quad \rho = \frac{\delta AE}{L}$$

$$A = (20)(.005) \\ = .10$$

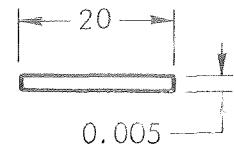


Figure C-5

Difference in Total Contraction
between Fiberglass and Aluminum is $.091 - .057 = .034$

$$\rho = \frac{\delta AE}{L} = \frac{(.034)(2.4 \times 10^6)}{20} = 408\#$$

$$\text{Pretension per Lineal Inch} = \frac{408}{20} = 20.4\#$$

$$\text{Total } \Delta\delta \text{ for Fiberglass} = .090$$

$$A_{gl} = .10 \quad E = 2.4 \times 10^6 \\ \rho = \frac{(.090)(.10)(2.4 \times 10^6)}{20} = 1080\#$$

$$S = \frac{\rho}{A} = \frac{1080}{.10} = 10800 \text{ psi}$$

$$F = \frac{45,000 \text{ psi}}{\text{allowable}}$$

$$S.F. = \frac{45000}{10800} = 4.17$$

$$\text{Total } \Delta\delta \text{ for Alum.} = .051 + .091 = .142$$

$$\rho = \frac{\delta AE}{L} = \frac{(.42)(2)(.2344)(10 \times 10^6)}{20}$$

$$= 33400 \text{ psi}$$

$$F = \frac{36000 \text{ psi}}{\text{allowable}}$$

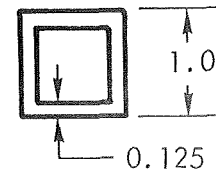


Figure C-6

$$A = (1)(1) - .875^2 \\ = .2344$$

$$SF = \frac{36000}{33400} = 1.078$$

APPENDIX D

TEMPERATURE REDUCTION

CONCEPT INVESTIGATION

RECOMMENDATIONS

Higher lunar based solar array performance per unit weight hinges on the temperature reducing schemes outlined in the Phase II report (Ref. 1.2) of this program. Specific proposals for future development activities are summarized below:

1.0 Optimization of the "Roof" Mirror Concept

The analytical optimization of the "roof" mirror concept includes the investigation of array performance as a function of mirror geometry, size, and type. As part of the study, parametric relations are required to indicate solar array performance as a function of weight and cost. (See Figures D-1 and D-2 for generalized performance curves).

Particular "roof" geometries which should be analyzed include the flat roof concept, the rippled roof concept, and the V-shaped roof concept. These concepts, illustrated in Figure D-3, should also be studied with respect to using different types of second-surface mirrors in order to investigate the cost-effectiveness of each idea.

A typical second-surface mirror source control specification is listed below in an effort to illustrate some of the specific requirements for the mirrored surfaces:

(1) Coating shall be 550 to 1000 Å of vacuum deposited silver overcoated with 300 to 600 Å of vacuum deposited inconel. Specifications:

(2) Vacuum metalized surface shall pass the following tape test: Using a length of 1/2-in. wide tape (scotch brand 610 or 250); apply the untouched sticky surface of one end to the inconel surface of the mirror leaving the other end free. The applied tape shall be set by firmly rubbing the back with a finger. Holding the mirror so it will not break, pull on the unapplied end of the tape at an angle approximately perpendicular to the mirror surface. At a measured force of between 6 and 8 ounces, the metal coating shall show no visual evidence of separation of the inconel from the silver surface or of the silver from the glass surface.

(3) Solar absorptance shall be 0.09 or less.

(4) Verification of solar absorptance to be accomplished on one part from each batch at time of receipt at TRW Systems. Supplier certification for this property is not required.

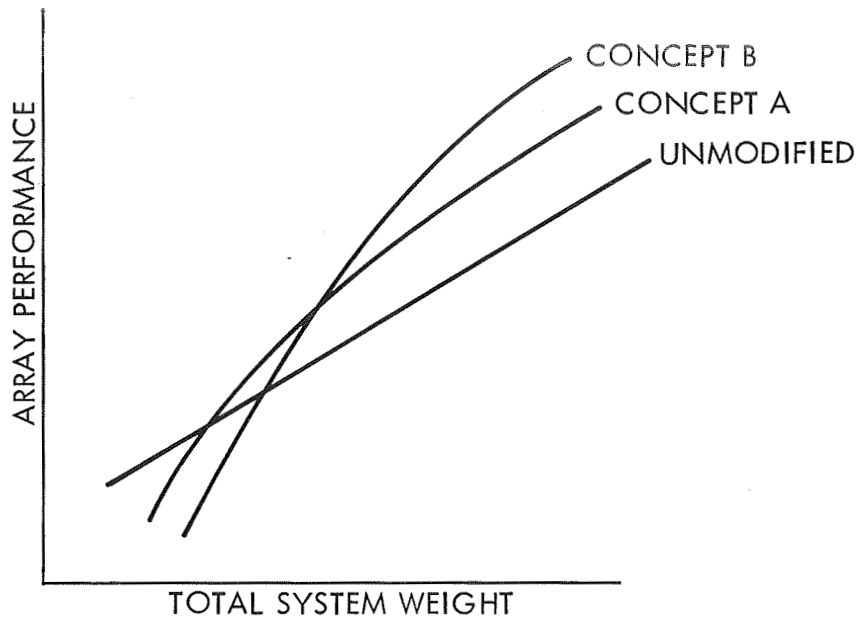


Figure D-1 Generalized Conceptual Solar Array Performance as a Function of Total System Weight

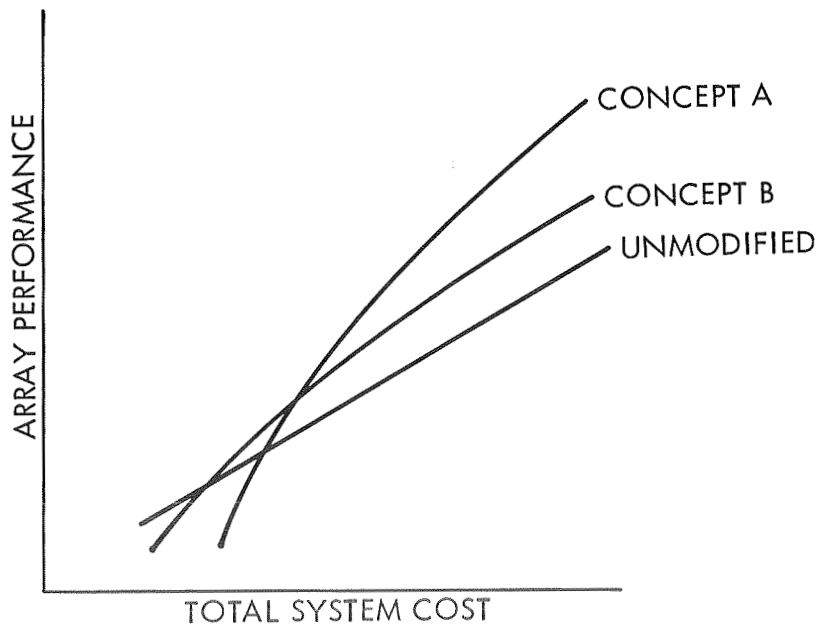


Figure D-2 Generalized Conceptual Solar Array Performance as a Function of Total System Cost

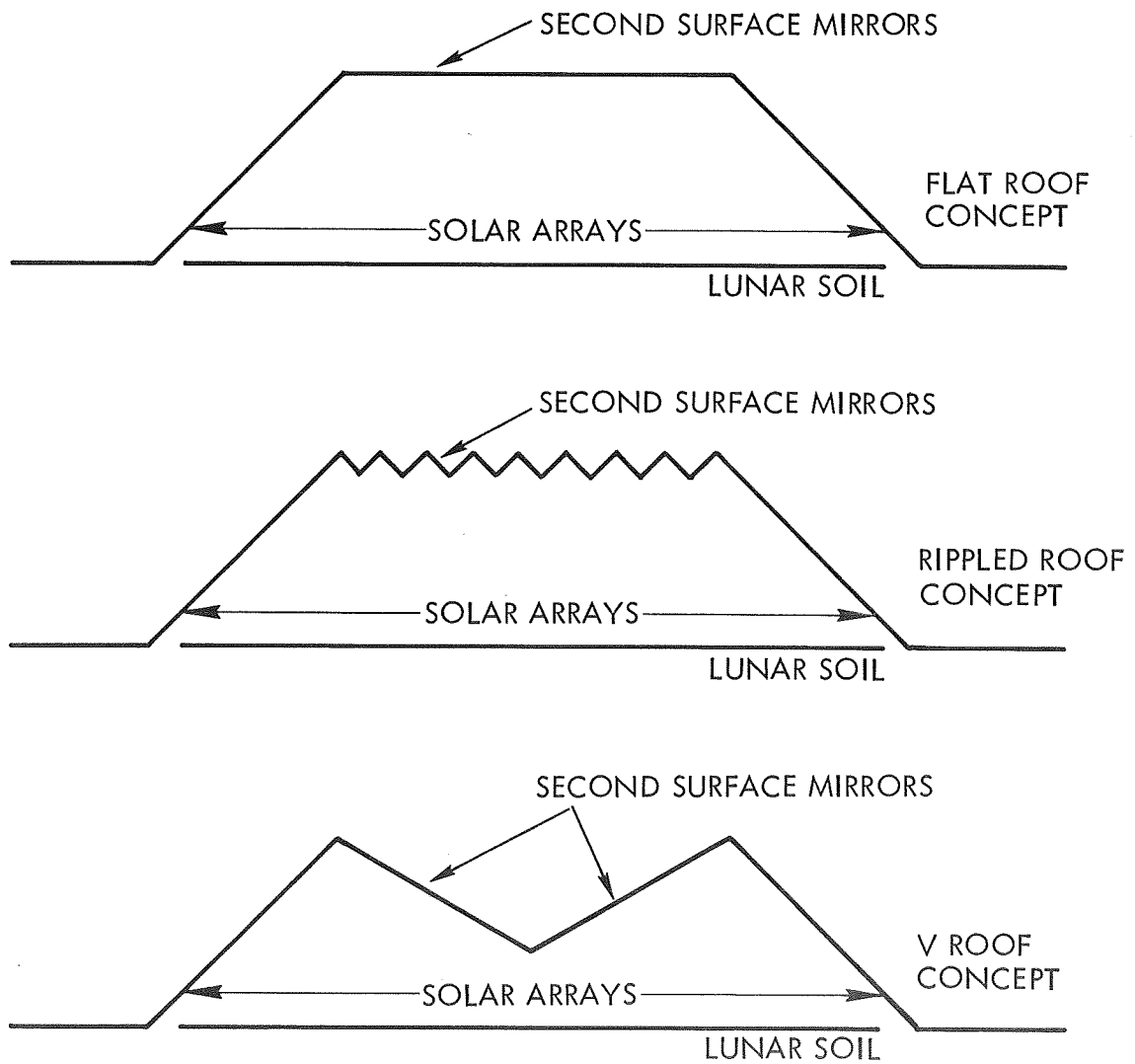


Figure D-3 "Roof" Type Concepts for Thermal Control for Lunar Surface Lean-to Solar Array Configuration

(5) Glass shall be Dow Corning microsheet , 0.0051 to 0.0063 inches thick. (1)

(6) The silver and inconel coatings shall be continuous and have a bright, specular, mirror-like, smooth uniform appearance. The silver coating shall exhibit a uniform silver color free from observable color change.

(7) Optical Properties Test (Face): The reflectance from the face (primarily from the silver surface plus some contribution from the glass) shall conform to the table below. Reflectance shall be measured at an angle of 30° or less from the normal and black paper shall be placed behind samples during measurement. Measurements shall be made with a spectrophotometer capable of measuring spectral reflectance to within ± 0.05 between 0.3 and 0.4 microns and $\pm .01$ from 0.4 to 1.0 microns.

Reflectance Requirements

<u>Wavelength-Microns</u>	<u>Minimum Reflectance - %</u>
0.380 \pm 0.001	87
0.475 \pm 0.005	94
1.00 \pm 0.02	97

(Failure to meet all of the requirements of the above table shall be cause for rejection only if the total integrated solar reflectance is less than 92%)

NOTE: (1) Possible source of supply Corning Glass Works, Corning, N. Y.

2.0 Optimization of the Array Mirror Concept

This temperature reducing scheme proposes the placement of second-surface mirrors side by side with solar cells in the plane of the solar array. Analysis of the concept should specifically predict increased array performance with larger mirror radiating areas. Total system weight and total system cost as related to electrical output should again be presented in the format of Figures D-1 and D-2. Also included in the analysis should be the temperature behavior (and power output) of the solar arrays as related to various mirrored surfaces.

3.0 Investigation of Complex Mirror Surface

As stated in the Phase II report, (Reference 1.2) the use of complex mirror surfaces placed on the lunar surface near the base of the solar array lean-to would significantly reduce array temperatures.

Because of the uncertainty of complex mirror surface analyses, it is recommended that laboratory investigations be conducted of the candidate surfaces in conjunction with the thermal analysis. These investigations would determine the spectral behavior of several complex surfaces with respect to solar array temperatures while the analysis would determine the optimum surface size and overall cost. The general type of surface under investigation would be constructed of mylar or aluminum foil, formed in such a fashion as to present a sawtooth cross section. Surface coatings to be investigated would include vacuum deposited aluminum, zinc oxide paints and ordinary white organic paints.

4.0 Final Design

Based upon the results of this experimental and analytical program, the best parameters from each temperature reducing method would be combined into a final solar array lean-to design. The combination of concepts should have a positive synergistic response on solar array output, and the performance to weight ratio would be significantly improved over the present unmodified array lean-to concept.